University of Liege

Faculty of Applied Sciences

ArGEnCo Department

Thesis submitted for the degree of

Doctor of Philosophy in Applied Sciences

Shallow geothermal energy: effect of in-situ conditions on borehole heat exchanger design and performance

by

Georgia Radioti

2016

JURY

Frédéric Collin (President)	Université de Liège
Robert Charlier (Supervisor)	Université de Liège
Frédéric Nguyen (Co-supervisor)	Université de Liège
Pierre Dewallef	Université de Liège
Bertrand François	Université Libre de Bruxelles
Fleur Loveridge	University of Leeds
Anh Minh Tang	Université Paris-Est
Vincent Vandenheede	Geolys SPRL

This research was funded by:

Acknowledgements

First, I would like to thank my supervisor Robert Charlier for his guidance, his advices and for the opportunities that he offered me during this thesis. I thank my co-supervisor Frédéric Nguyen for his significant contribution and the members of my thesis committee, Bertrand François and Frédéric Collin, for their interesting comments and suggestions. I also thank all the members of my Ph.D. jury for accepting revising my thesis.

Special thanks to Benjamin Cerfontaine for developing and implementing in LAGAMINE the 1D finite element formulation for borehole heat exchangers, to Simon Delvoie for his contribution in the geological interpretation of the site and to Kévin Sartor for providing the feeder pipe heat loss data. Without their contribution this work would not be possible. I also thank Pierre Illing for his assistance in the laboratory measurements.

I would like to acknowledge the financial support of the F.R.S.-FNRS (F.R.I.A. fellowship) and of the Walloon Region (GeoTherWal project, n° 1117492), as well as the company REHAU for providing the pipes and the commercial grouting materials and the University service ARI for their support in the installation of the BHEs. I thank our partners in the project, the ULB (Bertrand François and Selçuk Erol) and the companies Geolys (Vincent Lejeune, Vincent Vandenheede and Geoffrey Poulain) and OREX (Vincent Fiquet) for the fruitful collaboration.

Special thanks to Anne-Catherine, with whom we shared the office for four years, for her help and the joyful conversations, as well as to Sanae for the nice environment during the last months of this thesis. I would like to thank all the members of the group for their warm welcome, the friendly environment and the nice discussions. Τέλος, θα ήθελα να ευχαριστήσω την οικογένεια μου και τους φίλους μου για την συνεχή τους υποστήριξη κατά τη διάρκεια της εκπόνησης της εργασίας αυτής.

Abstract

The in-situ conditions are critical for the performance of Borehole Heat Exchangers (BHEs). However, in practise they are often not adequately considered, overwhelming the potential of these systems. This thesis focuses on the accurate estimation of the in-situ characteristics and on their influence on the design and the behaviour of BHEs based on an in-situ study of an heterogeneous bedrock in a semi-urban environment (campus of the University of Liege, Liege, Belgium). The experimental site consists of four double-U BHEs, of about 100 m long, installed over a surface area of 32 m² and equipped with fiber optic cables. Several temperature measurements and Distributed Thermal Response Tests (DTRTs) were conducted in situ in a period of four years, including a long-duration DTRT (heating phase of 7 months), during which temperature was measured by the fiber optics in all the four boreholes. These measurements create a unique data set, that allows to investigate the BHE behaviour for longer heating periods, to study the effect of various factors on the temperature field evolution at the heterogeneous bedrock at the in-situ scale and to evaluate the contribution of temperature borehole logging to the optimisation of BHEs.

The effect of urbanisation is studied based on the in-situ measurements and on 3D numerical modelling and its influence on the design is expressed in terms of the maximum extracted power. The subsurface characteristics are correlated with the measured fiber optic profiles and the potential of temperature borehole logging for optimising the design of BHEs in practise is presented. The accuracy of the thermal response test results in the case of insufficient test rig insulation is investigated and recommendations are provided regarding the interpretation of the data by the widely applied Infinite Line Source model. The in-situ measurements during the long-duration DTRT are presented and analysed, together with a 3D numerical model of the test. In this case-study, the possible variation of the effective thermal conductivity along the layers and the air temperature variations during the test do not seem to have a dominant effect on the BHE behaviour during the whole heating phase. The controlling factors for the temperature field evolution in the surrounding rock mass (bedrock heterogeneity, the air temperature variations, the distance to the heating source and the thermal effects at the borehole bottom end) are detected in the measured profiles and their influence is discussed.

Résumé

Les conditions in-situ sont cruciales pour la performance des forages géothermiques (borehole heat exchangers, BHEs). Néanmoins, dans la pratique elles ne sont souvent pas suffisamment prises en compte, limitant le potentiel de ces systèmes. Cette thèse se concentre sur l'estimation précise des caractéristiques in situ et sur leur influence sur la conception et le comportement des BHEs. Une étude in situ a été entreprise dans un bedrock hétérogène et dans un milieu semi-urbain (campus de l'Université de Liège, Liège, Belgique). Le site expérimental est constitué de quatre sondes géothermiques en double-U, d'une longueur de 100m, installées sur une surface de 32 m² et équipées de fibres optiques. Sur une période de quatre ans, plusieurs mesures de température ont été réalisées en tête de forage (test de réponse thermique, TRT) et le long de celui-ci grâce aux fibres optiques (DTRT). Elles incluent un DTRT de longue durée (phase de chauffage de 7 mois), au cours duquel la température a été mesurée par fibres optiques dans les quatre forages. L'ensemble de ces mesures forment une base de données unique, qui permet d'étudier le comportement des BHEs pour des périodes de chauffage plus longues, d'étudier l'effet de divers facteurs sur le champ de température dans le bedrock hétérogène à l'échelle in situ et d'évaluer la contribution de diagraphies thermiques à l'optimisation des BHEs.

L'effet de l'urbanisation est étudié sur base des mesures in situ et sur la modélisation numérique 3D. Son influence sur la conception est exprimée en termes de puissance extraite maximale. Les caractéristiques du sous-sol sont corrélées avec les profils de température et le potentiel de diagraphies thermiques pour optimiser la conception de BHEs dans la pratique est présenté. La précision des résultats des tests de réponse thermique dans le cas de l'isolation insuffisante du module est étudiée et des recommandations sont fournies en ce qui concerne l'interprétation des données par le modèle largement utilisé de la ligne source infinie (ILS). Les mesures in situ au cours du DTRT de longue durée sont présentées et analysées, ainsi qu'un modèle numérique 3D du test. Dans cette étude de cas, la variation possible de la conductivité thermique effective le long des couches et les variations de température de l'air pendant l'essai ne semblent pas avoir un effet dominant sur le comportement du BHE pendant toute la phase de chauffage. Les facteurs critiques de l'évolution du champ de température dans la masse rocheuse environnante (hétérogénéité, variations de température de l'air, distance à la source de chaleur et effets thermiques à l'extrémité inférieure du forage) sont détectés dans les profils mesurés et leur influence est discutée.

Contents

Chapter 3 - Fiber optic temperature measurements accuracy

Chapter 4 - Undisturbed ground temperature in a semi-urban environment

Chapter 5: DTRT measurements analysis: impact of heat input oscillations, in-situ grouting thermal conductivity and bedrock heterogeneity detection

Chapter 6: Long-duration DTRT and thermal plume in the surrounding bedrock

Chapter 7: Conclusions and perspectives

List of symbols and abbreviations

Latin symbols

A	annual oscillation amplitude of temperature (°C)
$c_{off.}$	offset factor (°C)
c_ρ	specific heat capacity (J/kgK)
D_h	hydraulic pipe diameter (m)
d	diameter (m)
f	Darcy friction factor (-)
f_{att}	attenuation ratio coefficient (°C/m)
h	convective heat transfer coefficient (W/m²K)
I	applied constant current (A)
L	length of the heater wire (m)
$\dot{m}$	mass flow rate (kg/s)
Nu	Nusselt number (-)
n	sample's porosity (-)
Pr	Prandtl number (-)
p_{electr}	electric power (W)
p_{pump}	power consumed by the pump (W)
q	heat flux per unit length (W/m)
q_{appl}	applied heating power (W)
q_{nom}	nominal heating power (W)
R	total resistance of the heater wire (Ω)
Re	Reynolds number (-)
R_b	borehole thermal resistance (Km/W)
r	radius (m)
T	T temperature (°C) or (K)
T_0	initial temperature (°C) or (K)
T_f	fluid temperature (°C) or (K)
T_{measur}	raw measured temperature (°C)
$T_{w,entrance}$	temperature at the entrance of the rig (°C)
$T_{w,exit}$	temperature at the exit of the rig (°C)
$T_{w,inlet}$	temperature at the pipe inlet (°C)
$T_{w,outlet}$	temperature at the pipe outlet (°C)
t	time (s)

Greek symbols

α	thermal diffusivity (m²/s)
γ	Euler's constant (-)
λ	thermal conductivity (W/mK)
ρc_ρ	volumetric heat capacity (J/m³K)

Abbreviations

BHE	Borehole Heat Exchanger
COP	Coefficient of Performance
DTRT	Distributed Thermal Response Test
DTS	Distributed Temperature Sensing
FLS	Finite Line Source
GSHP	Ground Source Heat Pump
GWHP	Ground Water Heat Pump
ICS	Infinite Cylindrical Source
ILS	Infinite Line Source
RTD	Resistance Temperature Detector
SEGI	General Service of Informatics
TRT	Thermal Response Test

Chapter 1 - Introduction

Geothermal energy consists in the heat stored in the Earth. Heat is stored by solar radiation and is also continuously generated inside the Earth mainly by the decaying of radioactive isotopes, such us potassium, uranium and thorium, and by the expansion of the Earth's core (latent heat). This heat, as well as the one remaining from the formation of the Earth, flows towards the Earth's surface (Clauser, 2006) (Figure 1.1). Given that this is a continuous process, geothermal energy is classified as a renewable source of energy. The continuous heat flow results in an increase of the temperature inside the Earth with depth. The rate of this temperature increase, the geothermal gradient, reaches an average value of 2.5 °C/km depth close to the surface in stable tectonic areas. At the Earth's surface, manifestations of geothermal energy include volcanic eruptions, geysers, hot springs etc.
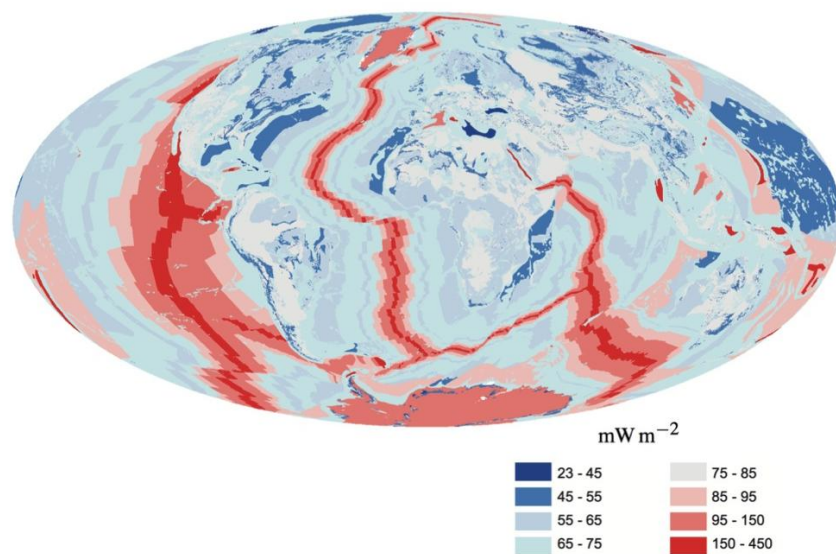
Figure 1.1 - Map of Earth's surface heat flux (mWm^{-2}) (Davies and Davies, 2010©)

1.1 Uses of shallow geothermal energy

The potential of geothermal manifestations was exploited in ancient times for cooking, bathing and health care (Kepinska, 2003). In South America, Incas developed bathing facilities close to hot springs areas and used pipes to supply hot and cold water. Balneotherapy (spa treatment) has been practised in Greece, New Zealand, China and Japan.

Roman natural and artificial baths (Figure 1.2, left) became the trademark of the roman period, reaching a number of 1.000 in the third century in Rome (Cataldi and Chiellini, 1995). Between the 13th and 16th century, thermal spas became popular all over Europe and the construction of the first geothermal heating district system started in France. In the following centuries, mining industry revealed the geothermal gradient effect on the underground temperature in several locations in Europe and America (Stober and Butcher, 2013). This, in combination with the rapid development of thermodynamics of the 19th century, opened up new horizons on the geothermal energy exploitation. In 1904, the first geothermal power plant was developed in Landerello, Italy, followed by others in New Zealand (1958), Mexico (1959) and USA (1960) (Quick et al., 2010) (Figure 1.2, right). In 1912, the idea of the ground source heat pump was documented in the patent by Heinrich Zoelly, where he proposed the use of a heat pump for extracting heat from the ground. Based on this idea, geothermal energy could be widely utilised for covering energy needs of individual and collective buildings. The first operational installation was recorded in 1940s, in Indianapolis (USA). In Europe, the first horizontal and vertical ground heat exchanger applications were documented in 1970s and 1980s (Sanner, 2001).
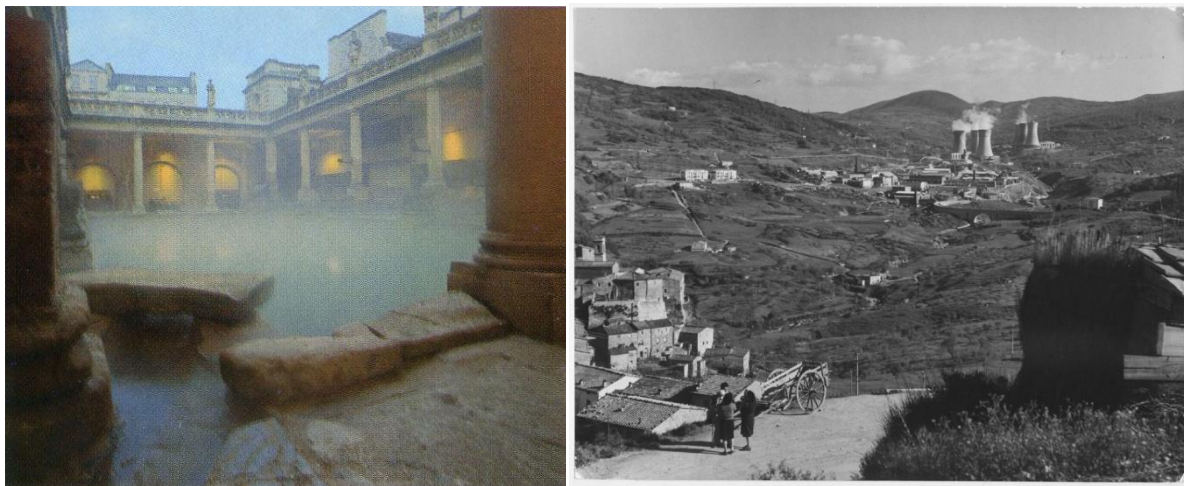
Figure 1.2 - Roman baths in Bath, England (left, wikepedia©) and geothermal power plant in Larderello, Italy, ca. 1950 (right, US. National Archives, ThinkGeoEnergy©)

Nowadays, geothermal energy is utilised for electricity production (indirect use) by taking into advantage great temperatures until great depths (a few km, deep geothermal energy). Direct utilisation of geothermal energy includes several applications, such as geothermal heat pumps, space heating, spas, balneology, green house heating and agricultural drying (shallow

geothermal energy). Shallow applications also include energy geostructures, where geothermal systems are embedded in concrete elements, such as piles, foundation slabs, retaining walls and tunnels (Brandl, 2006; Laloui and Di Donna, 2013; Barla et al., 2016). According to Lund et al. (2011), the increasing worldwide energy use of direct utilisation applications over the last decades is mainly attributed to the popularity and to the significantly increasing number of geothermal heat pumps installations. The equivalent number of installed units (12 kW) for 2005 was approximately 1.3 million, more than double of the one reported for 2000 (Lund et al., 2005). In a five year period (2005-2010), the corresponding number became 2.7 million with a worldwide installed capacity in the order of 33000 MW_t and annual energy use of 20000 TJ/yr.

Shallow geothermal heat pump systems (<400 m depth) exchange heat with the ground either by circulating the groundwater through two separate wells (Ground Water Heat Pumps, GWHPs) or by circulating a fluid in closed pipe loops embedded in the ground mass (Ground Source Heat Pumps, GSHPs) (Preene and Powrie, 2009; Florides and Kalogirou, 2007). In an open-loop system, the extracted water is usually reinjected into the aquifer (Figure 1.3). These systems are quite efficient for large power demands, such as for hospitals, airports or data centers. However, their applicability is limited by the local hydrogeological conditions (groundwater resources and aquifer capacity) and by environmental risks (potential impact on groundwater level, on water quality and on aquatic ecology).
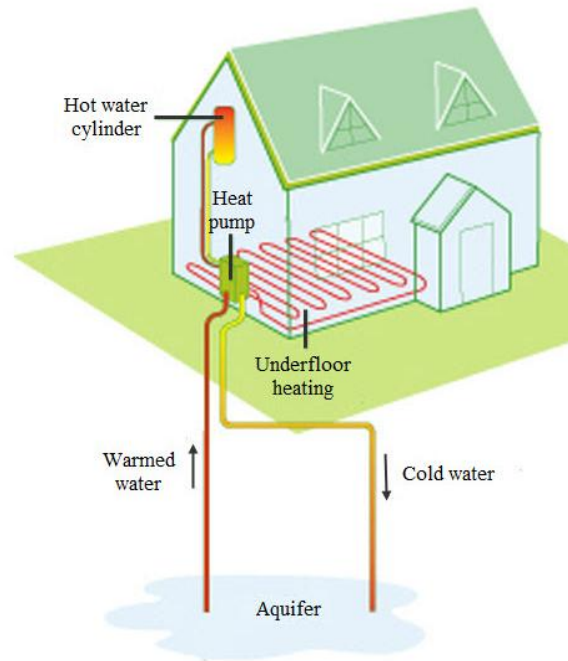
Figure 1.3 - Open-loop geothermal heat pump system (after Earthtest Energy©)

Contrary to open-loop systems, closed-loop systems do not require the presence of an aquifer and provide limited environmental risks, mainly associated with the potential leakage of the circulating fluid. There are two main categories of closed-loop systems: horizontal systems and vertical systems. Horizontal systems consist of pipe loops in various configurations (e.g. in series, in parallel, basket-type, "slinky"-type), embedded in the first meters of the ground (Figure 1.4). These systems are suitable for lower power demands such as individual houses and they have a limited capacity (typically required length of 35-60m per kW; Florides and Kalogirou, 2007). Vertical closed-loop geothermal systems, also known as Borehole Heat Exchangers (BHEs), consist typically of one or two U-pipe loops of high-density polyethylene installed in a borehole (Figure 1.5). Other configurations include concentric or coaxial pipes. A grouting material is injected in the borehole to enhance the heat transfer between the circulating fluid and the surrounding ground and to prevent environmental risks (e.g. aquifer contamination). It is also possible that the borehole is filled with groundwater (e.g. in Sweden). These systems are more efficient than horizontal systems, since they take into advantage the annual constant ground temperature at depth. Their capacity varies between 20 W/m - 80 W/m, depending on the ground thermal properties (VDI 4640). They are widely used for heating and cooling of individual and collective buildings (Bayer et al., 2012), since they can be applied in many hydrogeological contexts, are more efficient than horizontal systems and have a small footprint at the ground surface.

4
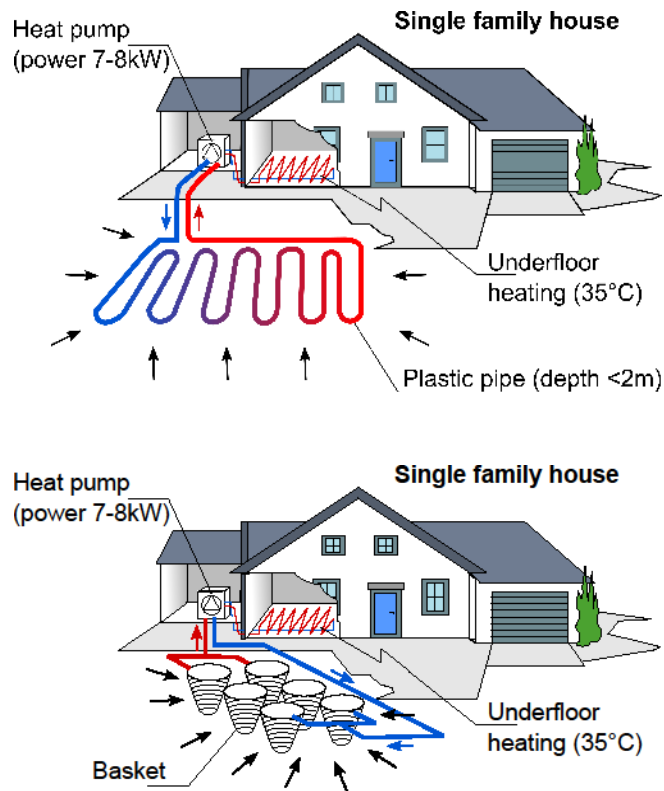
Figure 1.4 - Horizontal closed-loop geothermal systems (after CREGE©)
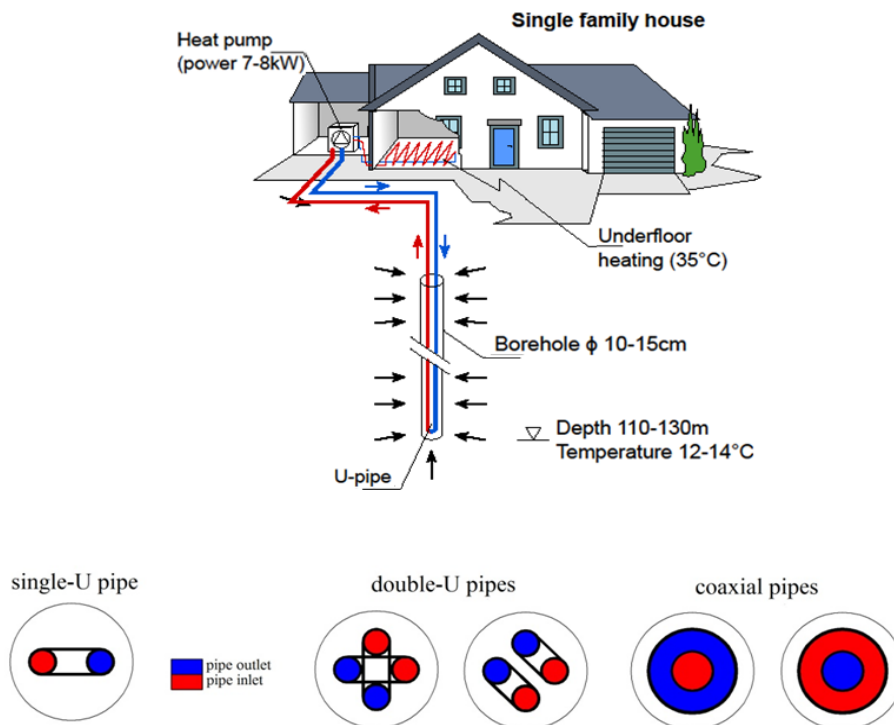
Figure 1.5 - Vertical closed-loop geothermal systems (after CREGE©)

The geothermal pipes are connected to the heating system through a heat pump, installed inside the building. During operation, heat is transferred from the ground to the circulating fluid and the heat pump increases the fluid temperature at levels suitable for heating purposes. This is achieved by changing the state of the working fluid inside the heat pump (evaporation, compression, condensation and expansion) (Figure 1.6). The procedure is inversed for cooling purposes. The efficiency of the heat pump is expressed by the coefficient of performance (COP), defined as the ratio of the heat delivered by the pump to the (electrical) power required for its operation (Banks, 2009).
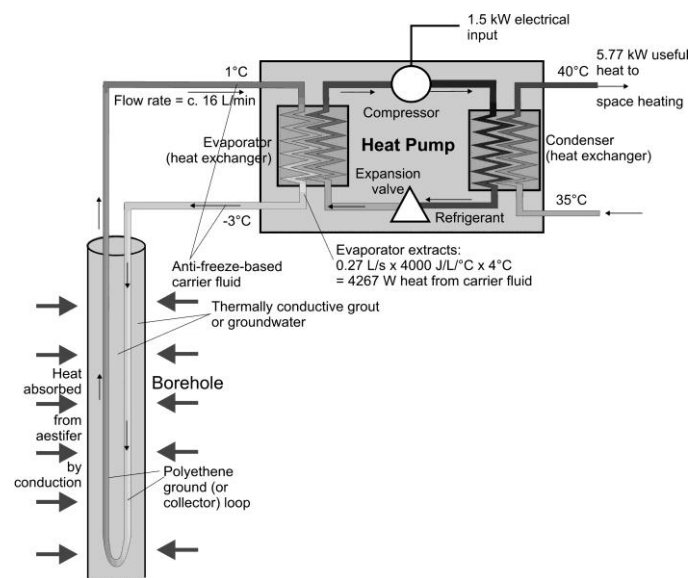
Figure 1.6 - Working principle of a heat pump connected to a BHE (Banks, 2009©)

1.2 Benefits and limitations

Compared to other heating systems (air source heat pumps, electric heaters, oil or natural gas boilers), geothermal heat pumps can provide economical and environmental benefits. Although the installation cost is often higher, they have low operating costs and are highly energy efficient in addition to being sustainable. The operating cost consists in the electrical consumption required for the heat pump and the circulation pump operation. The typical COP is 3-5, which means that the delivered energy (heat) is equal to 3-5 times the consumed energy (electricity). This COP is the highest among the different systems, considering that in some of them (e.g. oil or natural gas boilers) more energy is consumed than produced (COP<1). However, geothermal heat pumps, in particular BHEs, have typically higher installation cost than other heating systems (Figure 1.7). This cost consists in the heat pump

cost and in the borehole drilling and equipment cost, as well as in a permitting study cost in the case of open-loop systems depending on the policies. The drilling and equipment cost can have a share of more than 50% of the total installation cost (Blum et al, 2011; Buckley et al., 2015). Self et al. (2013) studied the overall cost of different heating systems for several countries in Europe. In most of them, geothermal heat pumps are economically advantageous compared to other heating methods, considering a lifespan of 20 years. The economical benefit depends on the prices for electricity in each country compared to the those of fuels, such as natural gas or oil, and it is increased in the case that the existent geothermal heat pump system is used also for cooling. Moreover, geothermal heat pump installations tend to increase the property value of the building and financial support is provided in several countries for individual or collective installations, such as grants or tax reductions (Jaudin et al., 2013).

Average Installation Cost	System Type	Fuel Price (€)	Annual Fuel Cost
€3,500	Oil (Gas Oil - litre)	1.03	€2,297
€3,500	Oil (Kerosene - litre)	1.01	€2,334
€3,500	Natural Gas (Standard Boiler)	0.065	€1,512
€6,000	Natural Gas (Condensing Boiler)	0.065	€1,354
€4,000	LPG (Bulk Tank)	0.93	€3,050
€9,000	Wood pellets (Bulk Delivery - kg)	0.27	€1,223
€9,000	Wood pellets (Bagged - kg)	0.33	€1,495
€18,000	Ground Source Heat Pump	0.20 & 0.08	€697
€8,000	Air Source Heat Pump	0.20 & 0.08	€816

Figure 1.7 - Example of installation and annual running cost for different heating solutions (200 m² house in Ireland, annual heating demand of 100 kWh/m²) (Buckley et al., 2015©)

Concerning the environmental benefits, geothermal heat pumps can contribute to the reduction of greenhouse gas emissions and to the counteract of global warming. Geothermal heat pumps do not emit directly CO_2, since they do not include burning processes. However, electricity is required for the operation of the heat pump. The environmental benefits of geothermal heat pumps will vary in each country, depending on the applied technology for electricity production (Rybach, 2010). In the case that electricity is produced by low CO_2 emitting power plants, the CO_2 emissions related to geothermal heat pumps will be limited. This makes GSHP installations favourable in countries such as Norway, France, Belgium, Sweden, Austria and Switzerland (Bayer et al., 2012). In the case of high CO_2 emitting power plants (e.g. coal-fired power plants), geothermal heat pumps contribution to CO_2 emissions

7

will be increased, but it will still remain lower than other heating systems utilising electricity (Self et al., 2013).

Half of EU's annual energy is consumed for the heating and cooling sector (industry, space heating/cooling, agriculture etc.), which is greater than the required energy for transportation or electricity (Figures 1.8 and 1.9). More than 70% of the required energy for the heating and cooling sector is generated by burning fossil fuels (natural gas, coal, oil), while renewable energy applications contribute at only 18%. The EU's energy target is to increase the share of renewable energy at 20% by 2020 and at 27% by 2030. Viable solutions would allow to reduce the CO_2 emissions, lower the citizens' expenditures for heating and cooling and reduce the energy consumption in industry (European Commission - Fact Sheet, 2016). Despite the applicability and the potential of GSHPs, geothermal energy accounts for less than 1.5% of the energy consumption in the heating and cooling sector, with an uneven distribution among the different countries (Table 1.1). Approximately one third of the European GSHPs in 2008 was based in Sweden, where the highest greenhouse gas emission savings were observed. France and Germany follow, with similar numbers of installed units and growth rates. The greenhouse gas emission savings are much higher in France, where nuclear power plants are dominant, compared to Germany, where coal has the highest share on electricity generation. A relatively significant increasing number of installations is also observed in Switzerland, where more than 2000 km of BHEs were drilled only in 2009. In other countries, despite the increasing number of installations, geothermal heat pumps appear to be still at early stage. This is also the case for Belgium, where the CO_2 emission factor for electricity is relatively small (0.37 kg/kWh) and shows, after France and Switzerland, the highest potential on greenhouse gas savings by a wide application of GSHPs (Bayer et al., 2012).
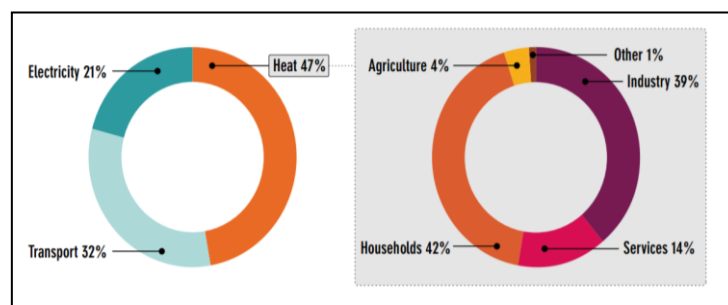
Figure 1.8 - Final energy use in EU-27 by type of energy (left) and for heat by individual sector (right) for 2010 (Sanner et al., 2013©)

8
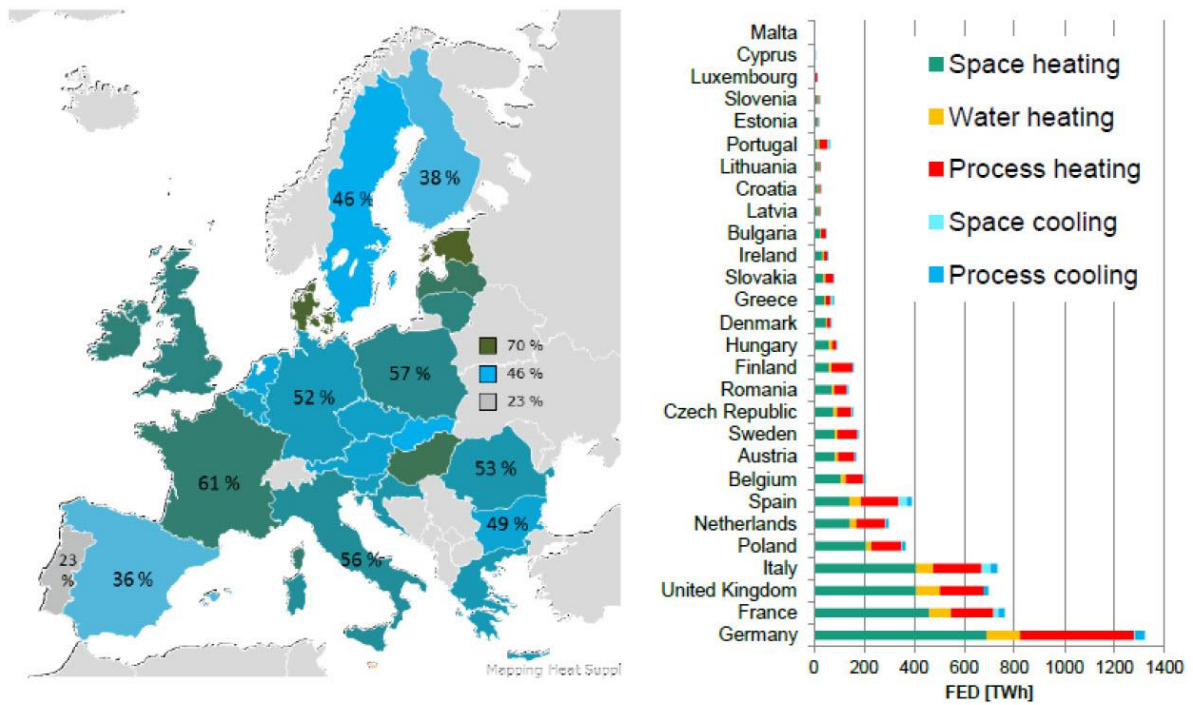
Figure 1.9 - Share of space heating demand of total heating/cooling demand by country (final energy) (European Commission- Fact Sheet, 2016©)

Table 1.1 - Average reported number of GSHPs in European countries (Bayer et al., 2012©)

Country		Year		
		2000	2005	2008
Austria	AUT	19,000	35,810	48,641
Belgium	BEL	n.a.	6000	9500
Czech Republic	CZE	390	3727	9168
Denmark	DNK	250	6000	11,250
Estonia	EST	n.a.	3500	4874
Finland	FIN	10,000	29,106	46,412
France	FRA	4000	63,830	121,900
Germany	DEU	18,000	61,912	148,000
Hungary	HUN	20	230	4000
Ireland	IRL	n.a.	1500	9500
Italy	ITA	100	6000	12,000
Netherlands	NLD	900	1600	14,600
Norway	NOR	500	14,000	26,000
Poland	POL	4000	8100	11,000
Slovenia	SVN	66	300	3440
Spain	ESP	n.a.	n.a.	7000
Sweden	SWE	55,000	230,094	320,687
Switzerland	CHE	21,000	38,128	61,000
United Kingdom	GBR	40	550	10,350
Total		133,266	510,387	879,322

Factors that prohibit the wide application of these systems include the non-standardized design, the regulative framework and the limited information availability. National standards or guidelines exist only in a few countries in Europe (e.g. Germany, Sweden, France, UK, Switzerland), and the regulative framework can often be non-existent or inappropriate (Jaudin et al., 2013). Another major issue is the high capital cost, especially for BHEs, which can result in long payback periods (typically until 20 years). Moreover, although there are systems operating for more than 30 years, the warranted life span of geothermal heat pumps is limited to 20-25 years (Self et al., 2013). Subsurface characteristics are among the critical parameters for the design and the long-term behaviour of BHEs (MIS 3005; VDI 4640; Luo et al., 2016). Though, in practice, they are often not adequately considered (Blum et al., 2011). This can result in increased capital costs, in the case of oversizing, and to malfunctions or short life spans, in the case of undersizing, overwhelming the potential and the applicability of these systems.

1.3 Literature review

Dehkordi and Schincariol (2014) studied the influence of several factors on the thermal performance of a single-U BHE by numerical modelling. Doubling the ground thermal conductivity can result in an increase in the specific heat extraction rate in the order of 50%, in short-term (6 months) as well as in long-term (25 years). Contrary to the thermal conductivity, the volumetric heat capacity of the ground has a negligible effect on the performance of BHEs. The undisturbed ground temperature influence is critical, since a variation in the average ground temperature of 25% modifies the heat extraction rate by approximately 25%. Kurevija et al. (2014) studied the effect of a high geothermal gradient (55 °C/km) on the design of BHEs, for a case study in Zagreb, Croatia. They concluded that estimating the ground temperature by including the influence of the geothermal gradient can result in a decrease of the required pipe loop length, in the order of 4% - 7% for the different investigated borehole array grids. Therefore, an accurate estimation of the in-situ ground thermal conductivity and of the undisturbed ground temperature is crucial in order to optimise the design and to assure the long-term efficiency of BHEs. The variation of ground thermal conductivity with depth is particularly important, since the detection of highly conductive zones will allow an optimization in terms of the required number and length of

BHEs. Moreover, any possible variation of the ground thermal conductivity in space could affect the long-term behaviour of the system, especially in the case of long heating or cooling periods.

1.3.1 Undisturbed ground temperature: in-situ determination and urbanization effect

Concerning the undisturbed ground temperature distribution, three zones can be typically distinguished (Popiel et al., 2001). In the surface zone (until ~1 m depth), ground temperature is strongly affected by the weather conditions. In the shallow zone, varying from 1 m to 20 m depth depending on the local ground type, temperature is mainly influenced by the seasonal weather conditions. At the end of this zone, ground temperature is close to the average annual air temperature. The deep zone follows, where temperature is invariant with time and increases with depth according to the local geothermal gradient (Figure 1.10). Deviations from this distribution can be observed in the case of groundwater flow, varying ground thermal properties and/or anthropogenic effects (e.g. construction, agriculture, industry).
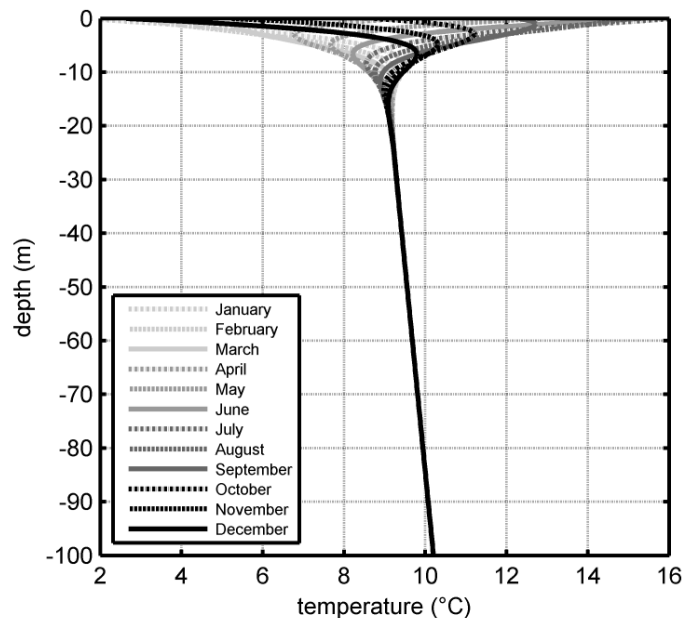
Figure 1.10 - Influence of weather conditions and geothermal gradient on the undisturbed ground temperature in Sart-Tilman (Liege, Belgium) based on analytical solution (Tinti, 2012)

In urban areas, elevated ground temperatures have been observed worldwide (Zhu et al., 2010; Menberg et al., 2013). They are often characterised by a zero or negative temperature gradient extending to depths more than 50 m (Banks et al., 2009). Several researchers relate this phenomenon to urbanization and other anthropogenic activities (Figure 1.11). For example, Yamano et al. (2009) detected a significant increase of the ground temperature (by up to 1 °C) above a depth of 75 m, based on borehole temperature measurements conducted 3 years before and 6 years after the construction of a museum building in Japan. They related their observation to the ground coverage around the borehole due to the museum building, and/or to the disposal of artificial sediments (6.7 m thick) that modified the ground surface level, sometime between 2 and 11 years before the first measurement. In terms of spatial impact, Liebel et al. (2011) presented temperature profiles of four boreholes which are located in different distances from a school building in Norway. They observed that the ground thermal disturbance decreases proportionally to the increasing distance to the school building. Ferguson and Woodbury (2007) conducted a spatiotemporal survey with repeated temperature measurements in a period of 7 years, in wells in the area of Winnipeg, Canada. In one well, 3 m away from a building reoccupied in the last 20 years, they observed a warming trend in the subsurface. In another well, located in an area covered with grass, a cooling trend was observed, mainly attributed to the demolition of buildings in the area during this period.

Figure 1.11 - Potential anthropogenic and natural heat sources in urban areas (Menberg et al., 2013©)

In these studies, elevated temperatures and negative temperature gradients are attributed to the urbanisation effect mainly based on observations of buildings presence and occupation close to the measurement locations. However, to the author's knowledge, this has not bee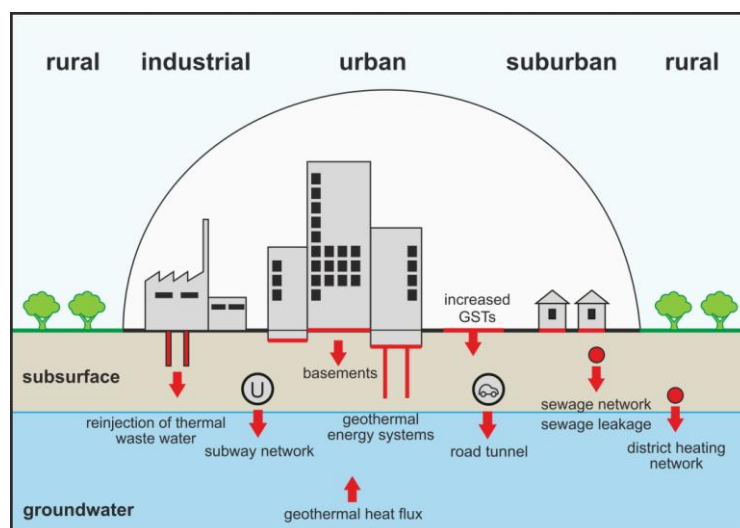n further validated, for example with numerical modelling. This would also allow to provide an indication of the temperature field evolution with time in the surrounding ground and to study its effect on the design of BHEs (section 1.4).

The undisturbed ground temperature is determined in-situ by mainly two methods (Spitler and Gehlin, 2015). The first method consists in temperature logging along the borehole, usually by lowering down a temperature probe inside the U-pipe and measuring the temperature at several depth intervals. The second method consists in circulating the fluid inside the pipe loops without heat injection and recording the temperature at the pipe inlet and outlet. Both methods assume that a thermal equilibrium has been reached between the fluid inside the pipes and the ground and they estimate the mean ground temperature over the depth of the BHE by averaging the measured data. The accuracy of the first method (borehole logging) depends on the accuracy of the measurement equipment and on the chosen depth interval. It is recommended to lower down the temperature sensor slowly, to prevent as possible any disturbance of the water, and to apply sufficiently small depth intervals, in order to capture the possible variations of the ground temperature with depth. The latter could allow to detect any deviations from the typical undisturbed ground temperature distribution. The ground temperature profile can also be obtained by installing temperature sensors or fiber optic cables along the borehole. The second method (during fluid circulation) is widely applied, since it consists in the preliminary phase of a Thermal Response Test (TRT), as described later in this section, and has a typical duration of 2 h - 12 h (Loveridge et al., 2013). Though, apart from the measurement equipment accuracy, the estimated mean ground temperature by this method can be affected by the heat added to the circulating fluid due to friction and the pump work, as well as by the possible thermal interaction between the circulating fluid and the ambient air.

Gehlin and Nordell (2003) compared the two above methods in a single-U BHE of 58 m long, filled with groundwater in a hard crystalline rock in Sweden. First, they lowered down a temperature sensor inside the borehole and measured the temperature at intervals (every 1 m for the first 10 m and every 2 m for the rest). Then, they circulated a water/glycol mixture

inside the pipe loop for 77 min. For the first few minutes of circulation, the recorded temperature was in good agreement with the one of the borehole logging (within 0.1 °C). After about 15 minutes of circulation, a constantly increasing temperature was recorded, resulting in an overestimation of the ground temperature (of 0.4 °C after 30 min and of 2 °C after 60 min). They attributed it, for their case study, to the heat added to the system by the pump work itself. Moreover they suggested that taking the minimum recorded temperature for the estimation of the initial ground temperature (Kavanaugh et al., 2001) could lead in strongly underestimated temperature in case of low ambient temperatures during the test. Loveridge et al. (2013) measured the undisturbed ground temperature in a 150 m deep BHE in London Basin. They obtained the ground temperature profile by fourteen thermistors attached along the U-loop and by lowering a thermistor string at 5 m intervals into the pipe loop. Both data sets showed the same trend, with a greater scatter in the installed thermistors measurements. They also estimated the mean ground temperature by fluid circulation in the pipe loops for 15 h. The mean temperature by the thermistor string (13.4 °C) was in between the range of the recorded fluid temperature during circulation (13.3 °C - 13.5 °C). Acuña et al. (2009) presented measurements in a BHE in Sweden, of about 260 m long, where a fiber optic cable was located inside the U-pipe. They determined the undisturbed temperature from the optical fiber measurements, with a measurement length interval of 10 m, before and after 24 hours of fluid circulation. They observed an increase of the average temperature of 0.09 °C during the fluid circulation and they mainly attributed it to the circulation pump work.

These studies mainly focus on the effect of the pump work on the accuracy of the undisturbed ground temperature estimation. Another important factor is the insufficient equipment insulation, since it can result in oscillations in the recorded temperature evolution, as it is widely illustrated in the heating phase temperature measurements. It would therefore be interesting to investigate if the thermal interaction between the circulating fluid and the ambient air can result in a significant error on the undisturbed ground temperature estimation that has an important effect on the design (section 1.4).

1.3.2 Thermal Response Test and interpretation by the Infinite Line Source model

The in-situ ground thermal conductivity, as well as borehole thermal resistance, are usually obtained by conducting a Thermal Response Test (TRT). Spitler and Gehlin (2015) presented a review on the development of the test equipment, the test procedure and the different interpretation analyses. The typical equipment for a TRT (Gehlin, 2002) consists of a pump (to circulate the fluid inside the pipes), an electric resistance heater (to inject constant heat), temperature sensors (to measure the temperature) and a data logger (to record the measurements during the test). The equipment is connected to the BHE pipes and insulation layers are attached around the pipes to minimize the heat transfer between the circulating fluid and the air (Figure 1.12). Before starting the test, water is circulated at high flow rate to purge air from the system. After purging the air, the first phase of the test starts. During this phase, water is circulated inside the pipe loop to achieve equilibrium between the water and the surrounding ground and to obtain the undisturbed ground temperature. The second phase consists of a continuous water circulation with usually constant heat input. After the heating period, the system is left to recover. During the test, temperature is recorded at the pipe inlet and outlet. Based on the measured data, the mean thermal conductivity of the surrounding ground and the mean borehole thermal resistance can be calculated.
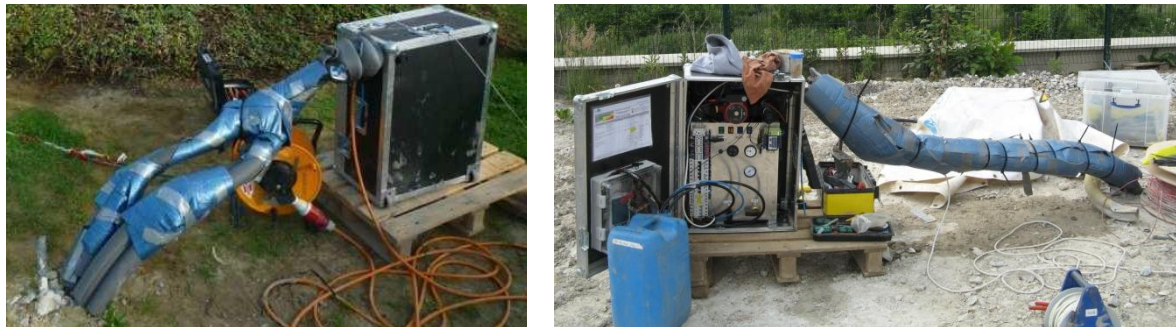
Figure 1.12 - Pipe insulation procedure and TRT equipment

The measured data are widely analysed by applying the simple, analytical solution of the Infinite Line Source (ILS) model. This model describes the heat propagation in an infinite homogeneous medium subjected to a infinite line source embedded along the vertical axis. The line source injects constant heat continuously since time zero and heat flows by conduction in the surrounding medium in the radial direction. Carslaw and Jaeger (1959)

gave a simplified form of the line source solution for the temperature at time t and at distance r from the line source (Figure 1.13):

$$T(r,t) = \frac{q}{4\pi\lambda}\left[\ln(\frac{4at}{r^2}) - \gamma\right] + T_0,$$

where q: the heat flux per unit length produced by the infinite line source *(W/m)*,

λ: the thermal conductivity of the medium *(W/mK)*,

α: the thermal diffusivity of the medium *(m²/s)*,

$\gamma \approx 0.5772$ is Euler's constant and

T_0: the initial temperature of the medium *(K)*.
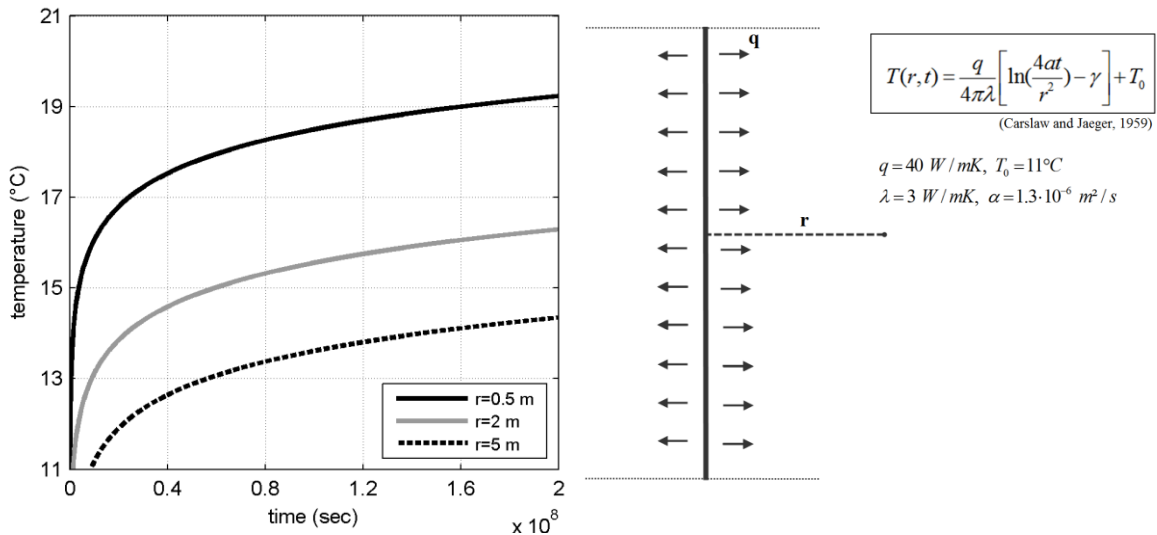
Figure 1.13 - Temperature evolution at certain distances from the line source (simplified ILS solution; Carslaw and Jaeger, 1959)

This simplified expression is valid for steady-state heat transfer conditions within the radius r and results, due to the mathematical simplifications, to a maximum error of 2% for $\alpha t / r^2 \geq 5$ (Hellström, 1991). To apply this solution to BHEs, Mogensen (1983) introduced the borehole thermal resistance, R_b, and considered the mean fluid temperature, T_f, as the mean of the pipe inlet and outlet temperature. By using the simplified line source solution the mean fluid temperature $T_f = (T_{inlet} + T_{outlet})/2$ can be described as (Wagner and Clauser, 2005):

$$T_f = \frac{q}{4\pi\lambda}\ln(t) + \left[qR_b + \frac{q}{4\pi\lambda}\left(\ln\frac{4\alpha}{r_b^2} - \gamma \right) \right] + T_0,$$

where r_b: the borehole radius *(m)*.

In this expression, the mean fluid temperature evolution is a line in a semi-log scale, $T_f = a\ln(t) + b$ (Figure 1.14). The mean thermal conductivity and the mean borehole thermal resistance can be calculated from the slope *a* and the constant *b*, respectively. It should be noted that the results from this approach correspond to the mean values of the effective ground thermal conductivity and borehole thermal resistance. The effective ground thermal conductivity includes possible effects of heterogeneity, of groundwater flow and of the initial ground temperature field in combination with the applied mode (heating/cooling). Factors that influence the effective borehole thermal resistance include the borehole diameter, the grouting properties and the pipe loop position at the borehole cross section, as well as the applied flow rate and the pipe legs interaction.

Figure 1.14 - Mean fluid temperature evolution during the heating phase of a TRT

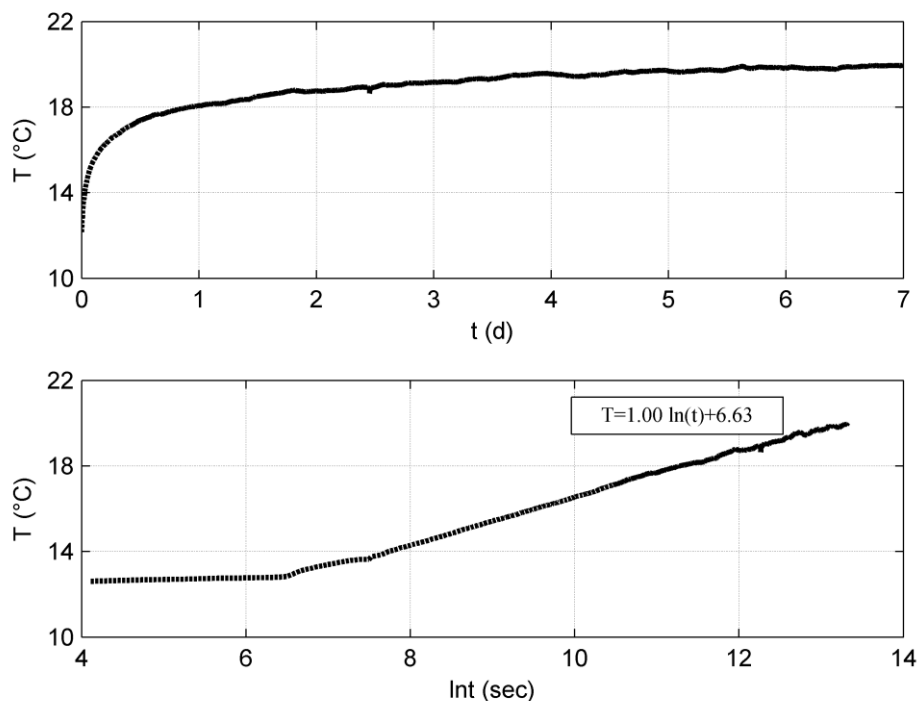The simplified ILS solution is valid for steady-state heat transfer condition inside the borehole, which is generally achieved after 1 h -12 h of operation for normal borehole sizes and ground conditions (Spitler and Gehlin, 2015). Before reaching the steady-state, the fluid temperature evolution is dominated by the borehole filling properties and, therefore, the corresponding data should not be included in the linear interpolation of the TRT data. This solution also requires that sufficient time has elapsed for the mathematical simplifications to be valid. It is proposed for $t/r_b{}^2 \geq 5/\alpha$, indicating that the results are inaccurate for small distances from the borehole center and/or for short time periods. Moreover, the ground is considered as an homogenous and isotropic medium with uniform initial temperature field. Other assumptions of the ILS model are the simulation of the BHE as an infinite long line and that the temperature distribution is radial, which indicate that the thermal effects at the ends of the borehole are negligible. Philippe et al. (2009) compared the ILS model with the Infinite Cylindrical Source (ICS) model, where the heat transfer rate is imposed at the borehole wall instead of its center, and the Finite Line Source (FLS) model, which can include the thermal effects at the ends of the borehole (Figure 1.15). For a typical borehole radius of 0.05 m, they calculated a difference between the ILS and ICS results of less than 10% after 10 h of operation, decreasing to 1% after 2.6 days. The thermal effects at the borehole ends become important after several years of constant heat transfer rate and for short BHEs. For example, the calculated borehole wall temperature by the ILS model was found overestimated of 5% after 6 years for a 50 m long BHE and after 30 years for a 100 m long BHE (α=0.53 10^{-6} m²/s). They concluded that, for typical operational conditions, the maximum error in the borehole wall temperature based on the ILS model is 5% for time limits between 13 h to 18 years. In practice, the typical duration of the TRT is 50 h - 60 h, with proposed values in literature varying from 12 h to 60 h (Singorelli et al., 2007; Rainieri et al., 2011; Spitler and Gehlin, 2015). Considering the typical duration of the TRT and the results presented previously by Phillipe et al. (2009), the error of the ILS model interpretation associated with ends effect and the BHE dimensions will be limited. Singorelli et al. (2007) conducted numerically TRTs and analysed the results by applying the ILS model. They studied, among others, the effects of the test duration and of the ground heterogeneity, by comparing the analytically obtained thermal conductivity with the one assigned to the numerical model. For the investigated heterogeneous cases, the obtained thermal conductivity values were lower than the one of the homogenous case, with small differences for the different operation modes (heating/cooling). Though, all the cases (homogeneous and

heterogeneous) resulted in an error less than 10%, for conduction dominated heat transfer. They proposed that a test duration of 50 h can provide a satisfactory estimation of the ground thermal conductivity, in the case that groundwater effects are not dominant.

Figure 1.15 - Relative difference in borehole wall temperature between the Infinite Cylindrical Source (ICS), the Finite Line Source (FLS) and the Infinite Line Source (ILS) solution for typical operating conditions (Philippe et al., 2009©)

A constant heat input is a critical requirement for the application of the ILS model interpretation. In practise, variations in the applied heat input are attributed to voltage variations in the supplied electricity and/or to insufficient insulation of the test equipment, that allows a thermal interaction between the circulating fluid and the ambient air. This results in oscillations of the recorded fluid temperature profiles, that can affect the accuracy of the ILS results. Singorelli et al. (2007) interpreted the data of an in-situ TRT of a varying heat input. They estimated the ground thermal conductivity numerically, including the variations of the heat input, and observed that there was a correlation between the variations in the estimated thermal conductivity and the ambient air temperature variations. The average estimated thermal conductivity was equal to the one measured at the laboratory. Though, the ILS interpretation, by evaluating 24 h data windows and by assuming the 24 h average power

supply, resulted in varying thermal conductivity with time, with an average value significantly lower (approximately of 15%) than the one estimated numerically. They concluded that there was not a clear definition on the choice of the part of the measured data to be evaluated, that would allow to improve the accuracy of the ILS results. Witte et al. (2002) conducted TRTs by fixing the temperature difference between the pipe inlet and outlet. This allowed to avoid heat input fluctuations due to unstable power supply. They showed that even a small influence of the ambient air on the fluid temperature (variation of ± 0.15 °C) can have an important influence on the estimated thermal conductivity. They proposed that enhancing the insulation of the test equipment and controlling the temperature difference inside the borehole could limit the effect of the air-fluid interaction. Choi and Ooka (2016a) developed a quasi-steady analytical model, which takes into account insulation characteristics and the effect of various weather conditions. To limit the ambient air interaction effect, they recommended an insulation layer of more than 10 mm and retaining the connecting pipes as short as possible. Moreover, they showed that radiation effects can contribute significantly to temperature oscillations and recommended bright, reflecting materials for the insulation and the test equipment. In their study (Choi and Ooka, 2016b), they analysed statistically 36 numerical TRTs influenced by various weather conditions, interpreted by the ILS model. They recommended a minimum test duration of 60 h, to retain the ILS results error lower than 5%. They also proposed that the simplified ILS model interpretation should be avoided, in the case of short TRT duration combined with important radiation effects during the first day of the test.

The importance of the test rig insulation during the heating phase of the TRT is highlighted in these studies, since thermal interaction with the ambient air can result in varying heat input. The duration of the TRT seems to be critical in this case, where temperature oscillations can affect the linear slope sensitivity of the ILS interpretation. Experimental studies in literature are limited to TRTs of a few days and the recommended minimum duration for the TRTs reaches 60 h. The question arises if a longer duration, of several days or even weeks, could significantly improve the accuracy of the results when the ILS model is applied. Moreover, in the case of the typical applied duration (50 h - 60 h), which part of the measured data set should be chosen for the ILS interpretation in order to minimize the influence of the temperature oscillations and to improve the accuracy of the results? Furthermore, the results of the typical duration TRTs might not be representative of the in-situ conditions during the

operation of the system (e.g. for longer heating periods or during the recovery phases, where the heat flow direction is inversed). This is observed in the case that ground water effects are dominant and the TRT interpretation can not provide a unique value for the effective thermal conductivity (Loveridge et al., 2013). It would be interesting to investigate if in the case that groundwater effects are not dominant, the TRT results can be representative of the BHE behaviour for longer heating periods and different modes (heating/recovery) (section 1.4).

1.3.3 Variation of ground thermal properties

At the laboratory scale, several studies include measurement at soil and rock samples, core samples or cuttings to investigate the influence of various factors (e.g. mineral composition, porosity and degree of saturation) on the thermal properties (Clauser and Huenges, 1995; Popov et al., 1999; Pechnig et al., 2010). Moreover, in the case that the rock sample consists of foliations (e.g. shale samples), an anisotropic thermal behaviour is observed depending on the direction of the heat flow with regard to the foliations orientation. The thermal conductivity parallel to the foliations can be up to 2.5 times higher than the one perpendicular to the foliations (Popov et al., 1999; Eppelbaum et al., 2014). These effects are widely studied at the laboratory scale, however, extrapolating laboratory results to in-situ conditions remains challenging (Liebel et al., 2010; Luo et al., 2016). In situ, any possible deviation from the samples characteristics (e.g. degree of saturation, fracturing, porosity), as well as groundwater flow can result in a different effective ground thermal conductivity than the one measured at the laboratory. Moreover, the in-situ ground thermal behaviour will be affected by the in-situ undisturbed temperature field (geothermal gradient effect, urbanisation effect, air variations influence at the top ground meters), an influence that is not included in the laboratory measured thermal conductivity values.

TRTs allow to estimate the effective ground thermal conductivity including the influence of the in-situ conditions. However, the estimated value corresponds to the mean thermal conductivity of the ground surrounding the borehole. The detection of a varying thermal conductivity with depth is particularly important, since the detection of highly conductive zones will allow an optimization in terms of the required number and length of BHEs. Temperature borehole logging during and after a TRT can significantly contribute to this end.

1.3.3.1 Distributed Thermal Response Test

During a Distributed Thermal Response Test (DTRT), temperature is measured not only at the pipe inlet and outlet but also at different depths along the borehole, by temperature sensors or fiber optic cables installed inside the borehole (Figure 1.16). Fujii et al. (2006) instrumented two BHEs of 50 m long, installed at a distance of 5 m from each other, in a heterogeneous deposit in Japan (sand, silt and gravel followed by siltstone and sandstone layers). In the coaxial BHE, a fiber optic cable was fixed at the outer surface of the outer pipe, while in the double-U BHE a cable was fixed at the center of the U-pipes. The distribution of the calculated ground thermal conductivity (interval of 1 m) agreed with the local hydrogeological information and some difference were found between the results for both BHEs at certain zones. Florides et Kalogirou (2008) studied a U-pipe BHE of 50 m long, crossing sandstone and marl layers in Cyprus. They installed 20 thermocouples at various depths in the grout and they detected, based on the recorded temperature profiles, layers with higher heat transfer rate. Acuña et al. (2009) conducted a DTRT in a U-pipe BHE, of about 260 m long, in Sweden. They inserted a fiber optic cable inside the U-pipe and obtained fluid temperature measurements with a length interval of 10 m. They divided the borehole into 12 sections, of 20 m each, and they observed variations in the supplied power during the test with depth and with time. A varying ground thermal conductivity through depth (2.60 W/mK - 3.62 W/mK) was calculated, with almost no deviation between the depth-average value and the one resulting from the conventional TRT procedure. Soldo et al. (2016) presented fiber optic measurements in a 100 m long, double-U BHE in an heterogeneous ground in Croatia (gravel, sand, clay, silt and coal layers). The fiber optic cable was inserted inside one of the U-pipes and the measurement interval was 2 m. They found different thermal conductivity values for the 8 layers, varying from 1.52 W/mK to 2.36 W/mK. Direct thermal measurements (mainly core samples) underestimated the thermal conductivity in most layers (up to 0.78 W/mK), which they mainly attributed to scale and water content problems of the core measurements.
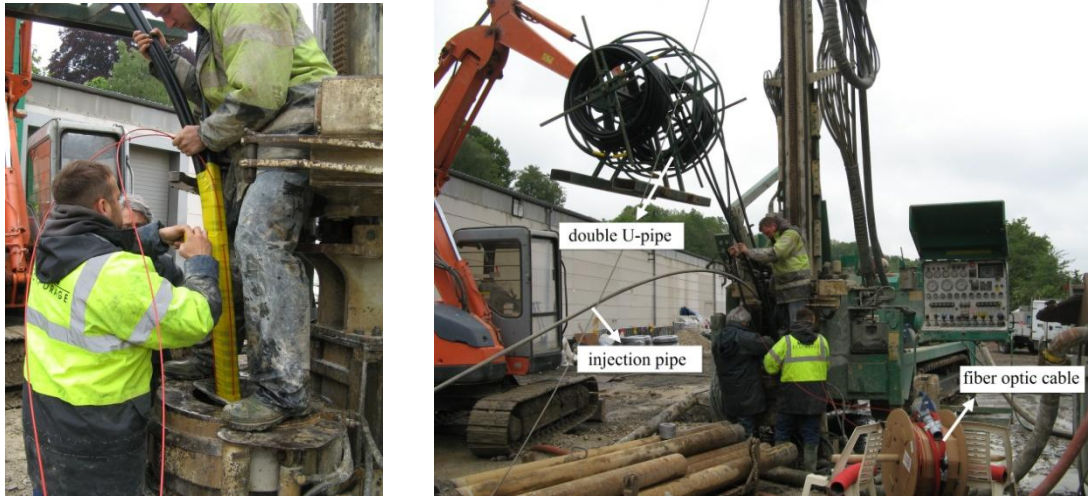
Figure 1.16 - Installation of fiber optic cables at the outer surface of U-pipes (Bassenge, Belgium)

The experimental site of BRGM (Bureau de Recherches Géologiques et Minières, Orléans, France) includes several installed shallow geothermal systems (horizontal, double U-pipe, "basket-type" etc.), in order to compare the different applications and to investigate the influence of several parameters on their behaviour (Philippe, 2010). Concerning the BHE configurations, this site includes two double-U BHEs, of 50 m and 100 m long, and a 5-tube coaxial BHE of 50 m long. The three BHEs and three piezometric boreholes located in between them were equipped with fiber optics (Figure 1.17). Among others, a 100 h-duration TRT was conducted in the double-U pipe of 100 m long and the temperature along its length was measured by the fiber optics (Chalhoub et al., 2014).

Figure 1.17 - Relative position of the BHEs and the piezometric boreholes (left, Chalhoub et al., 2014©) and coaxial pipe equipped with fiber optic cable (right, Philippe, 2010©) in the experimental site of BRGM, Orléans, France

DTRTs allow to investigate any possible variations of the effective ground thermal conductivity with depth by taking into account the in-situ conditions. The experimental studies presented above concern DTRTs of a few days and measu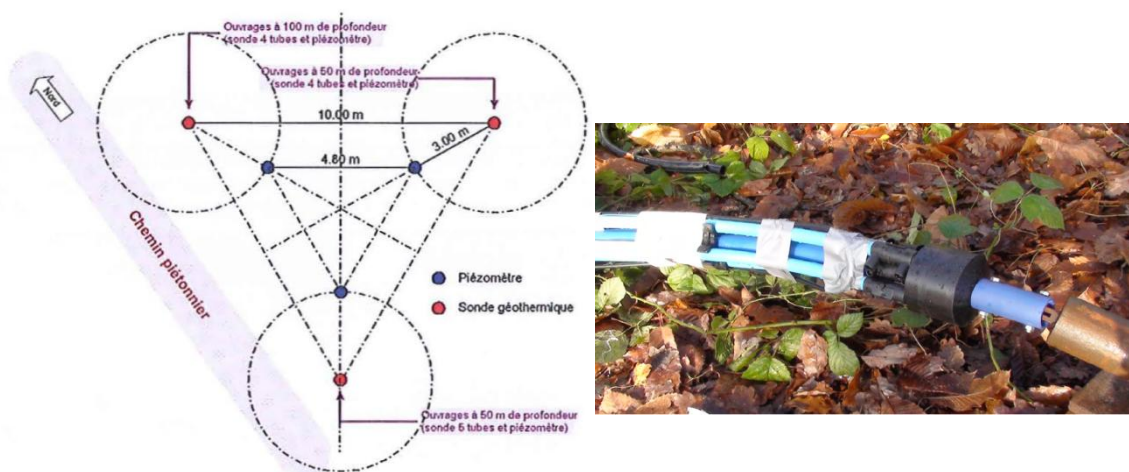rements at the borehole scale. However, due to their limited duration, the BHE behaviour might not be representative of the in-situ conditions during the operation of the system (e.g. for longer heating periods or during the recovery phases, where the heat flow direction is inversed). A long-duration DTRT would allow to detect any possible variation of the effective thermal conductivity while the temperature field evolves in the surrounding ground. In this context, it would be interesting also to monitor the temperature evolution in the surrounding ground that could provide indications on the effect of the subsurface characteristics in the evolving thermal plume (section 1.4).

1.3.3.2 Recovery profiles analysis

The study of recovery profiles can also provide information on the variability of the ground thermal properties. Loveridge et al. (2013) calculated the thermal conductivity during the heating and the recovery phase based on temperature measurements by thermistors, attached along the U-loop in the 150 m deep BHE in London Basin. The results were consistent with the Chalk aquifer characteristics, where major fractures dominate the groundwater flow. Fujii et al. (2009) used optical fiber sensors to record vertical temperature profiles in two bedrock case-studies in Japan and related these results with local geological and groundwater information, to verify the validity of the test and interpretation method. In the first case a permeable granite zone of 10 m thick was related to higher calculated thermal conductivity and quicker temperature recovery compared to non-permeable granite, as an effect of an active groundwater flow. In the second case lower thermal conductivity was related to weathered tuff, compared to unweathered tuff. Liebel et al. (2011) studied non-grouted wells in Norway and proposed taking temperature measurements four to five hours after the beginning of the recovery phase. They related faster temperature recovery to hydraulically active fractures and upcoming groundwater flow from confined artesian aquifers, as an effect of groundwater flow. They verified the existence of fractures by using flow measurement test data, televiewer imaging and/or drillers reports.

The study of recovery profiles allows the detection of layers of high heat transfer rate and contribute to the optimum design of BHEs. The recovery profiles correlations provided in literature mainly concern distinct thick layers and/or are based on groundwater flow effects. The question arises if recovery profiles can provide information in the case that groundwater effects are not dominant and to which extent thin layers can be detected. Moreover, hardening of the grouting material is an exothermic process, during which heat is generated. The temperature evolution along BHEs during this process has not been monitored in-situ, according to the author's knowledge. It would be interesting to investigate if borehole logging during hardening of the grouting material can contribute to the subsurface heterogeneity characterisation (section 1.4).

1.4 Objectives of the thesis

The EU's energy target is to increase the share of renewable energy at 20% by 2020 and at 30% by 2050. Viable solutions would allow to reduce the CO_2 emissions, lower the citizens' expenditures for heating and cooling and reduce the energy consumption in industry. BHEs can significantly contribute to this end due to their high applicability and their economical and environmental benefits. They can be applied in many hydrogeological contexts, are more efficient than horizontal geothermal systems and have a small footprint at the ground surface. Moreover, they have low operating costs, limited CO_2 emissions related to their operation and are highly energy efficient.

However, geothermal energy applications accounts for less than 1.5% of the energy consumption in the heating and cooling sector in Europe and in most of the countries they appear to be still at early stage. Factors that prohibit the wide application of these systems include the non-standardized design, the regulative framework and the limited information availability, and in particular the high capital cost, especially for BHEs, which can result in long payback periods (typically until 20 years). Moreover, although there are systems operating for more than 30 years, the warranted life span of geothermal heat pumps is limited to 20-25 years. There is therefore the need to optimise the design and assure the long-term behaviour of these systems. A controlling factor is the subsurface characteristics, which in practice are often not adequately considered. This can result in increased capital costs or to malfunctions and short life spans, overwhelming the potential and the applicability of these systems.

This thesis focuses on the influence of the in-situ characteristics on the design and the behaviour of BHEs, at the borehole scale and its surroundings, based on an in-situ case study of an heterogeneous bedrock in a semi-urban environment. In a local scale, this thesis puts in evidence the potential of BHEs in a geological context typical of the Walloon region, Belgium, where these applications are still at early stage and there is a great potential on greenhouse gas savings by their wide application. In this thesis, the following topics are studied:

1. A first objective is to provide an estimation of the temperature field evolution with time in the surrounding ground in semi-urban areas and investigate its influence on the design of BHEs. This is also of interest for the long-term behaviour of BHE systems, given that the heat loss through structures into the subsurface is a continuous phenomenon, that recharges the geothermal reservoir potential (Chapter 4).

2. Given that the undisturbed ground temperature is widely estimated during the first phase of a TRT (fluid circulation in the pipe loops), it is investigated if the thermal interaction between the circulating fluid and the ambient air can result in a significant error that has an important effect on the design (Chapter 4).

3. Another objective is to investigate the effect of heat input oscillations during a TRT on the sensitivity of the ILS interpretation results. In particular, it is studied if a test duration, longer than the typical one (50 h - 60 h), of several days or even weeks could significantly improve the accuracy of the results when the ILS model is applied. Moreover, in the case of the typical applied duration, it is of interest to provide recommendations on which part of the measured data set should be chosen for the ILS interpretation in order to minimize the influence of the temperature oscillations and to improve the accuracy of the results (Chapter 5).

4. Obtaining the recovery temperature profiles can allow the detection of layers of high heat transfer rate and contribute to the optimum design of BHEs. The objective is to investigate ifrecovery profiles can provide information in the case that groundwater effects are not dominant and to which extent thin layers can be detected (Chapters 5 and 6). Moreover, it is

of interest to study the contribution of temperature borehole logging during hardening of the grouting material to the subsurface heterogeneity characterisation (Chapter 5).

5. The thermal behaviour of the BHE during operation and the thermal plume in the surrounding ground can be predicted based on the TRT data analysis, considering the ground an homogenous, isotropic material. However, this assumption is not always valid and the estimated effective thermal conductivity might not be representative of the in-situ conditions for longer heating periods or during the recovery phases, where the heat flow direction is inversed (e.g. in the case that groundwater effects are dominant). The last objective consists in investigating if the TRT results could be representative of the BHE behaviour for longer heating periods and different modes (heating/recovery), in the case that groundwater effects are not dominant, and in studying the influence of in-situ characteristics (heterogeneity and anisotropic effects, ambient air temperature variation effect, thermal effects at the borehole end) on the temperature field evolution in the surrounding ground (Chapter 6).

1.5 Outline of the thesis

This thesis provides some insight on the above presented topics, based on an in-situ study of four double-U BHEs, of about 100 m long, installed in an heterogeneous bedrock on the campus of the University of Liege (Liege, Belgium). The BHEs were installed over a surface area of 32 m² and equipped with fiber optic cables along the outer surface of the pipe loops. Fiber optics allowed to obtain continuous, high-resolution temperature profiles along the pipe loops. A detailed bedrock characterisation was achieved based on borehole televiewer measurements in the four boreholes, in this geological context typical of the Walloon region (Belgium). Several temperature measurements were conducted in a period of four years: during hardening of the grouting material, at the undisturbed state and during the heating and the recovery phase of DTRTs of a duration of 7 days. Moreover, a long-duration DTRT (heating phase of 7 months) was conducted in one of the BHEs. During this test, temperature was measured by the fiber optics during the heating and the recovery phase in all the four BHEs. These measurements create a unique data set, that allows to investigate the BHE behaviour for longer heating periods and to investigate the effect of various factors on the thermal plume in the heterogeneous bedrock at the in-situ scale. The measurements of the undisturbed temperature revealed the effect of heat loss through structures into the subsurface

in this semi-urban environment. The influence of the insufficient insulation of the test rig equipment was observed in all the in-situ DTRTs. The temperature measurements during the long-duration DTRT allowed to investigated the influence of the test duration on the ILS interpretation and the effect of in-situ characteristics (e.g. heterogeneity, anisotropic thermal behaviour, ambient air temperature variations) on the thermal plume in the rock mass.

The remainder of the thesis is organised as follows:

Chapter 2 describes the site installation procedure and the geological interpretation based on the borehole televiewer measurements and cuttings observation. It also includes the cuttings thermal conductivity measurements at the laboratory and a discussion on their interpolation to the in-situ conditions.

Chapter 3 concerns the fiber optic measurements principle. It focuses on the accuracy of the fiber optic measurements and highlights the importance of a continuous offset calibration.

Chapter 4 focuses on the determination of the undisturbed ground temperature. Different experimental approaches are compared: borehole logging (by fiber optics and by lowering a temperature sensor inside the pipe loop) and during water circulation in the pipe loops. In the latter, the effect of the insufficient test rig insulation is thoroughly studied. This chapter also includes an analytical estimation of the undisturbed ground temperature for the Sart-Tilman area, as well as a 3D numerical model which takes into account the heat loss through existing structures into the subsurface. The numerical results are compared to the in-situ measurements and the effect of urbanization and of the insufficient test rig insulation on the design is discussed.

Chapter 5 presents the temperature measurements during the in-situ DTRTs in the four BHEs, as well as 3D numerical modelling of the in-situ tests. Based on the experimental data, the heat input oscillations effect on the ILS model analysis is studied and the contribution of a long duration TRT is investigated. The fiber optic measurements during the heating phase are studied, in combination with the numerical results, and a correlation of the recovery profiles with the gamma-ray measurements is provided. Moreover, fiber optic measurements during hardening of the grouting material are presented and correlated with fractured zones in the

surrounding bedrock. Propositions are presented, concerning the potential of the temperature borehole logging, as well as the ILS interpretation in the case of recorded temperature oscillations during a typical duration TRT.

Chapter 6 is devoted to the long-duration (heating phase of 7 months) DTRT conducted in-situ. It presents an analysis of the in-situ measurements during the applied modes (heating/recovery), at the borehole scale as well as at the surrounding rock mass. 3D numerical modelling of the test is also included and the influence of the in-situ conditions on the BHE behaviour and on the thermal plume in the surrounding bedrock is discussed.

Chapter 7 summarizes the conclusions and presents recommendations for BHE installations in practise, as well as perspectives for future research.

Chapter 2 - Experimental site: geological interpretation and cuttings thermal conductivity

This chapter presents a description of the experimental site and a laboratory study of the thermal conductivity of cuttings, that were collected during the drilling of the boreholes. The site is located on the campus of the University of Liege (Liege, Belgium) in a geological context typical of the Walloon region. First, the installation procedure of the four BHEs and of the fiber optic cables is presented. A characterisation of the bedrock heterogeneity (including fracture characterisation, rock identification and layer dip angle determination) based on the borehole logging measurements follows. Then, the laboratory measurements of the cuttings thermal conductivity are presented, as well as their correlation to the rock characteristics as indicated by the borehole logging results. Afterwards, the in-situ measurements conducted in a period of 3 years are summarised. Finally, conclusions are presented, as well as a discussion on the extrapolation of the laboratory measurements to the in-situ conditions. A part of the work included in this chapter is also presented in Radioti et al. (2013; 2015a; 2016a).

2.1 Site location and installation procedure

The site is located on the campus of the University of Liege (Liege, Belgium). It consists of four BHEs (namely B1-B4) installed in the summer of 2013 over a surface area of 32 m², close to buildings and to the university heating feeder pipe (Figure 2.1). The building of the General Service of Informatics (SEGI), constructed in 1980, has a minimum distance of 15 m from the boreholes. The feeder pipe, buried in the ground at an average depth of 2.5 m, is operating since 1970 and has a minimum distance of 6.6 m from the boreholes. It consists of 6 pipes, each covered by a mineral wool insulation layer of a thickness of 12 cm, enclosed in a concrete shell of a thickness of 18 cm.

Figure 2.1 - Site location on the campus of the University of Liege (retrieved from Google Earth©) (red line: heating feeder pipe, SEGI: General Service of Informatics, B1 to B4: four BHEs)

The BHEs installation procedure was as follows: First the boreholes, of a diameter of 135 mm, were drilled by using a DTH hammer bit (Down-The-Hole, destructive drilling technique) and a KLEMM 805-2W drilling rig (Figure 2.2). The drilling parameters logs for the four boreholes are presented in Appendix A. Moreover, cuttings were collected in sampling containers during the drilling of the four boreholes. The boreholes were supported with casing at the first top meters (15.5 m for B1, 13.5 m for B2 and 9.5 m for B3 and B4) to keep loose soil from collapsing into the borehole. Then an acoustic borehole imager, borehole televiewer, was lowered into the four boreholes (Figure 2.3). After the televiewer measurements, double-U pipes were lowered into the boreholes, while fiber optic cables were attached along the pipe loops (Figure 2.4). One fiber optic cable was attached along one U-pipe loop in each borehole. The cables were tapped every 50 cm in direct contact with the outside surface of the pipes wall, and together with the U-pipes were lowered until a depth of 86.4 m for B1, 95.0 m for B2, 98.6 m for B3 and 95.2 m for B4. It should be noted that the

31

exact position of the cable at the outer surface of each pipe leg is not well known, since the U-pipes were being rotated about the borehole axis while lowering them down inside the borehole (Figure 2.5). Spacers between the pipe legs were not used due to the relatively small borehole diameter (approximately 135 mm). Additionally to the fiber optic cables and in direct contact with them, two Resistance Temperature Detector (RTD) probes were also attached at certain depths in each borehole. Then the remaining part[1] of the cables, of a total length between 52.8 m to 77.2 m for the four boreholes, was temporally inserted inside the pipes to allow the retrieval of the casing. Finally, the boreholes were backfilled with the following grouting materials: B1 and B3 with a silica sand-based commercial material (Geosolid), B2 with a bentonite-based commercial material (Füllbinder) and B4 with a homemade admixture with graphite. Erol and François (2014) presented a detailed laboratory characterisation of these materials, including the following thermal conductivity values of grout samples: 2.35 W/mK for Geosolid, 0.95 W/mK for Füllbinder and 2.5 W/mK for the homemade admixture with graphite.

Figure 2.2 -Drilling rig (left) and drill pipes (length of 2 m, outer diameter of 13.5 cm) (right)

---

[1] *i.e.,* the part that was not attached and lowered inside the boreholes
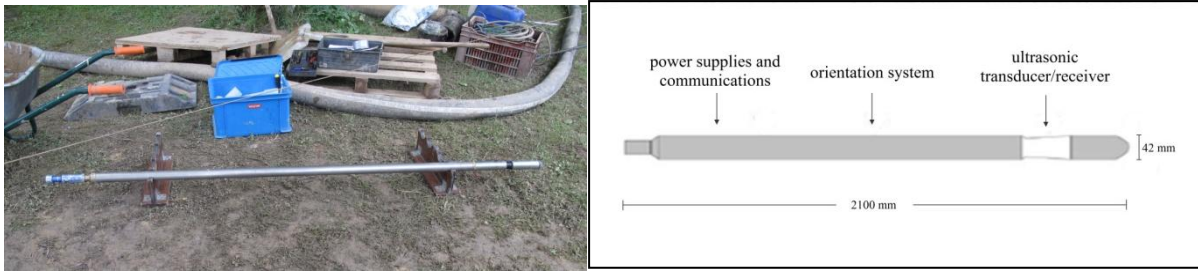
Figure 2.3 -Acoustic borehole imager (length of 2.1 m, diameter of 42 mm) for borehole logging

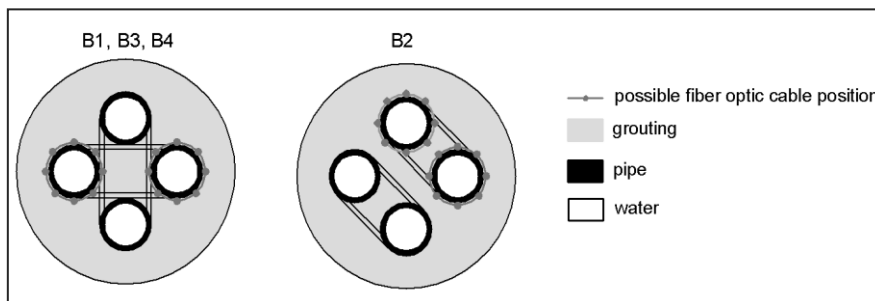Figure 2.4 - Geothermal double U-pipe and fiber optic cable installation

Figure 2.5 - Possible position of the attached fiber optic cable at the outer surface of the pipe legs in each BHEs

During the drilling of B2, B1 has already been drilled but not equipped. The drilling induced water to flow out from B1. This phenomenon was more intense at a drilling depth of about 75 m, where a water column more than 10 m high, in B1, carried away pieces of altered rock. Water flows could be provoked by the high air pressure applied during drilling in combination with the relatively small distance between the two boreholes (4 m at ground surface) and indicate the connection of the two boreholes at depth. The rock surrounding the boreholes is characterised by open fractures, as presented below in section 2.2.2.1, some of which could be connected and significantly contribute to permeable rock zones. Once the boreholes were drilled, the water table was detected to be stable at 10 m below ground surface in all the boreholes.

2.2 Geological interpretation

2.2.1 Preliminary geological investigation

The investigated site is located in the north-east side of the Dinant Synclinorium geological structure. The geological map of Sart-Tilman (Calembert et al., 1964) provides the most recent published geological interpretation of the bedrock for the studied area (Figure 2.6). The site is also located on the North side of a local syncline. The synclinal axis has an E-W orientation. Based on the geological map, the boreholes cross Emsian (Lower Devonian) detrital sedimentary rocks, probably corresponding to Wépion Formation and Burnot Formation. Both formations include alternations of shale, siltstone, sandstone and quartzite. Some of these layers are lenticular. From a general point of view, the Burnot Formation is mainly composed of red sediments while the Wépion Formation is mainly made up of green layers. However, detailed studies show that red layers are not rare into the Wépion Formation and some green beds can be met in the Burnot Formation (Corteel et al., 2004; Bultynck et al., 1991). The lack of easily observable differences between these two Formations makes their distinction very difficult.
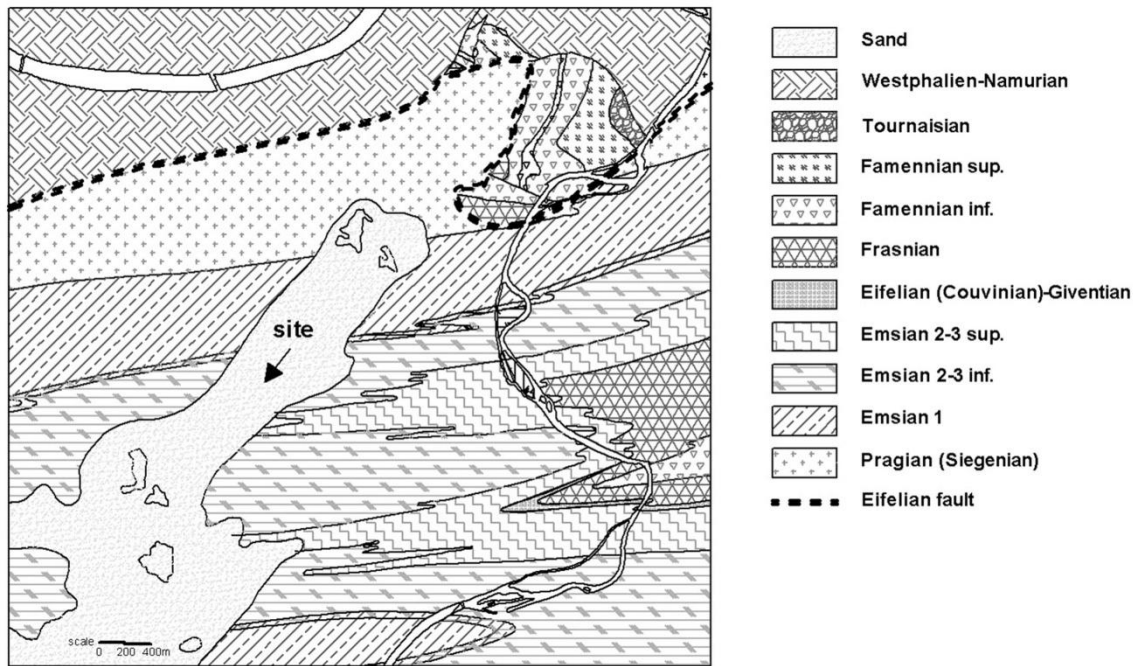
Figure 2.6 - Geological map of the Sart Tilman area (Calembert et al., 1964)

The subsurface sediments are well documented in the geotechnical map of Sart-Tilman (Calembert et al., 1975). This map includes data from two boreholes located in a distance smaller than 200 m from the investigated site. Lithological logs of the two boreholes indicate deposits of silt, sand and gravel until a depth of approximately 7 m. A layer of altered bedrock of a thickness approximately 3 m follows. The non-altered bedrock starts at a depth of approximately 10 m. The information provided by the logs is in good agreement with the observations during the drilling of the four boreholes at the site, where the top approximately 8 m are characterised by sand and gravel layers.

2.2.2 Borehole logging method

A borehole televiewer (Zemanek et al., 1970) was lowered into the four boreholes to obtain high-resolution, continuous images with 360° coverage of the local geology and fracturing. A borehole televiewer is composed of a transducer which is rotated 360° while lowered down inside the borehole. An in-line centralizer allows the tool to be centered during the measurement procedure. The transducer transmits ultrasonic pulses (1.5 MHz), which travel through the drilling mud and undergo partial reflection at the borehole wall, and receives the reflected pulses. The acoustic travel time and amplitude data are recorded. The acoustic travel

35

time depends on the borehole radius and the acoustic amplitude depends on the soil/rock impedance.

In this experiment, azimuth and deviation were constantly measured by magnetometers and inclinometers (Monier-Williams et al., 2009). The inclination of the borehole at each point was calculated based on the moving average of these data over an interval of 10 cm, with an orientation precision of $\pm0.5°$ and $\pm1.0°$ for the inclination and the azimuth respectively. The travel time and amplitude data were oriented with respect to the Magnetic North and converted into colorized, continuous images with 360° coverage of the borehole wall. Moreover natural-gamma radiation emitted by the rocks surrounding the boreholes was measured every 5 cm. Based on the borehole logging data a detailed fracture characterisation (position, opening, orientation, dip angle) can be obtained (Paillet et al., 1990; Williams and Johnson, 2004). Gamma-ray data and observation of the cuttings during drilling may result in rock identification through depth (Keys, 1990). This procedure was applied to the four boreholes in order to investigate the uneven distribution of fractures in the rock mass and to determine the layer dipping.

The televiewer measurements were conducted at depths beneath 15.55 m for B1, 13.50 m for B2, 10 m for B3 and 10.46 m for B4, since the boreholes were supported with casing at the first top meters to keep loose soil from collapsing into the borehole. The bottom depth was 98.67 m for B2, 102 m for B3 and 96.44 m for B4. For B1 the bottom depth was limited to 75.28 m, since collapsed rock pieces had blocked the borehole at that depth. The bedrock characterisation (fracture characterisation, rock identification and layer dip angle determination) presented in the following sections corresponds to above depth intervals.

2.2.2.1 Fracture characterisation

Figure 2.7 shows high-resolution images of the acoustic signal travel time and amplitude for an extended and a slightly fractured zone. Black zones in the travel time column correspond to low travel time values and white zones to high travel time values. Yellow zones in the amplitude column correspond to high amplitude values and indicate the existence of dense soil or rock. Blue zones correspond to low amplitude values and indicate fractures, altered

rock or soft soil. Random blue spots indicate locally broken rock due to the drilling. Shaped curves on the images plot represent planes over a fracture or bedding trace. Based on these data each element is interpreted as an open fracture, a fracture with filling, a stratification/foliation or a lithological contact. It is noted that the distinction between different elements is not always obvious. For example a fracture with filling could be misinterpreted as stratification.
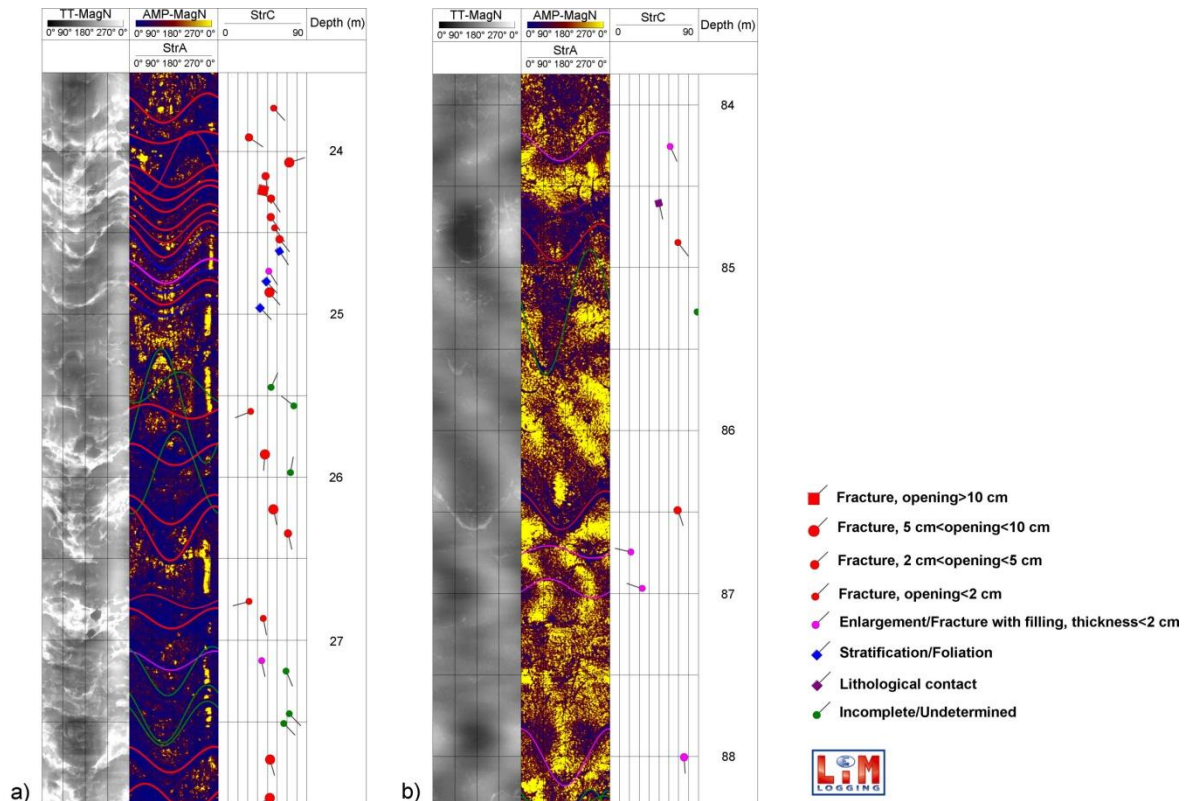

Figure 2.7 - High-resolution images of a) extended fractured zone in B4 and b) slightly fractured zone in B2, from left to right: acoustic travel time column, acoustic amplitude column, structural interpretation of each fracture (opening, orientation, dip angle) and corresponding depth values

The distribution of open fractures more than 5 cm wide for the four boreholes, based on the logging interpretation, is shown in Figure 2.8. Based on these data, fractures significantly vary in number and location in the four boreholes, despite the close distance between them. B4 is more fractured than the other three boreholes, consisting of 12 fractures more than 10 cm wide and 31 fractures of an opening between 5 cm and 10 cm. B3 seems the less fractured, consisting of one fracture more than 10 cm wide and 10 fractures of an opening between 5 cm and 10 cm. Moreover, extended zones (more than one meter thick) of large

fractures (opening greater than 10 cm) are observed in B1 and B4, between 25.6 m and 27.1 m and 29.4 m and 31.3 m depth respectively. B2 is characterised by a smaller fractured zone of 70 cm between 29.2 m and 29.9 m depth. These results indicate also that the extension of some fractures in space is limited.

The depth position where the borehole diameter is larger than 150 mm (equal to hammer bit diameter plus 20 mm) is also shown in Figure 2.8. These measurements could indicate extended fractured zones of more than one meter thick, between approximately 25 m and 27 m for B1, between 24 m and 31 m depth for B2, 29 m and 31 m depth for B3 and between 28 m and 34 m for B4.
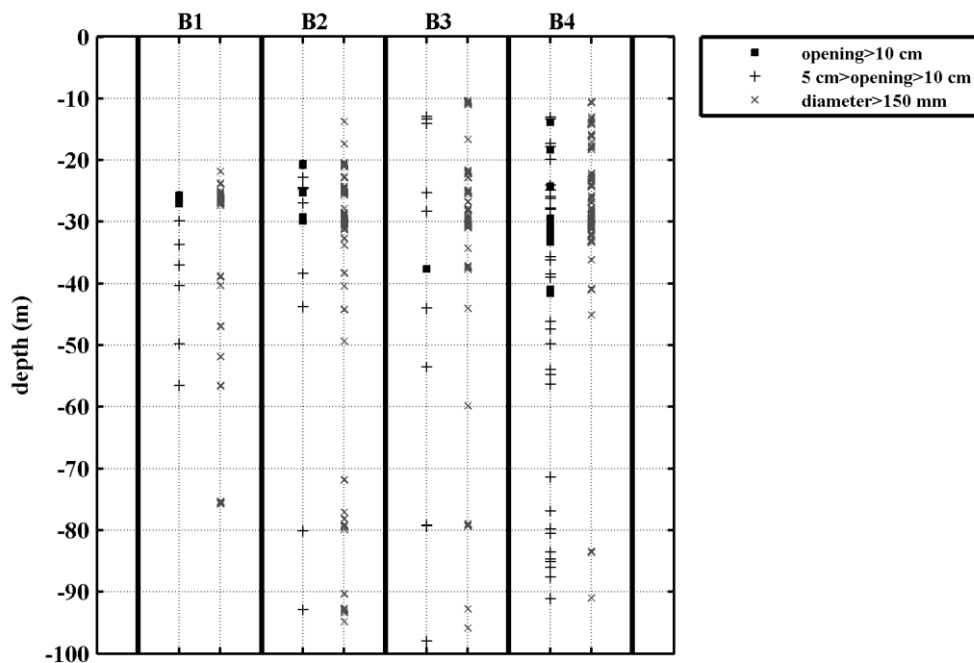

Figure 2.8 - Distribution of open fractures and borehole diameter larger than 150 mm for the four boreholes

Figure 2.9 shows the stereographic projection of the pole of each discontinuity for the four boreholes (Wulff net). The dip angle of most fractures varies between 40° and 70°/horizontal and the orientation varies between N40° and N80° for all the boreholes. The median average dip angle is approximately 52°/horizontal for B1, 54°/horizontal for B2 and 58°/horizontal for

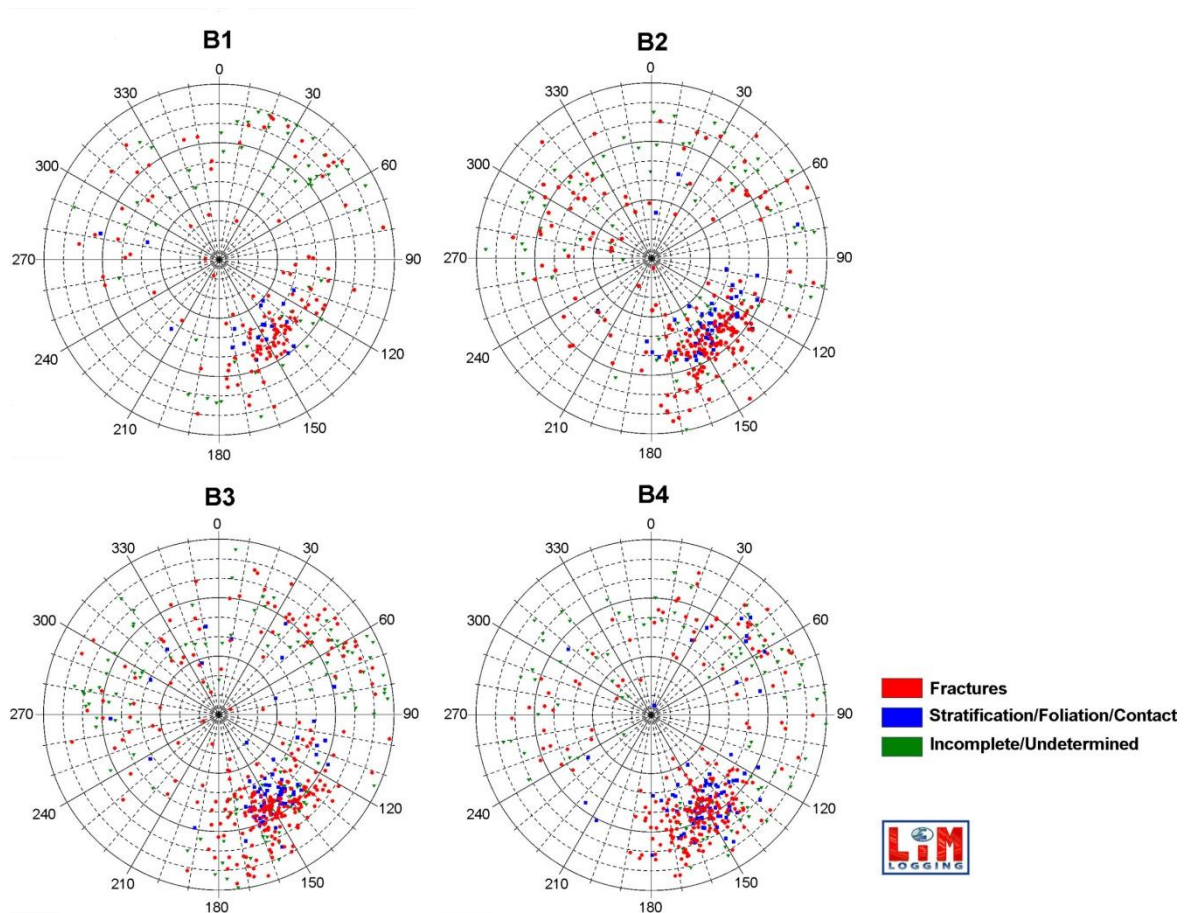B3 and B4. The median average orientation is approximately N57° for B1, N60° for B2 and B3 and N61° for B4.

Figure 2.9 - Structural data projection of the pole of each discontinuity on the upper hemisphere for the four boreholes

2.2.2.2 Rock identification

Natural gamma radiation along the borehole was measured every 5 cm to characterise the clay content of the rock formation. Moreover cuttings were collected during the borehole drilling. The gamma-ray data and observation of the drill cuttings result in a detailed rock identification through depth. The bedrock consists mainly of siltstone and shale interbedded with sandstone layers, ranking between a few centimeters to a few meters (<5 m) thick, for the upper 65 m in B1, 72 m in B2, 75 m in B3 and 80 m in B4. The remaining parts of the boreholes are dominated by sandstone layers more than 5 m thick. Approximately the same lithostartigraphy is observed in the four boreholes, but at different depths. Variations in the

thickness of the layers (in the order of a few meters) are observed based on the analysis of each borehole.

Figure 2.10 shows gamma-ray data and geological information that can be obtained based on the two procedures for the last 60 m of B4. High gamma-ray values in Figure 8 (>80 cps) indicate shale/siltstone layers while low values (<80 cps) indicate sandstone layers. The combination of the two procedures provides information on the rock type and the exact location of even thin rock layers with a resolution of 5 cm.
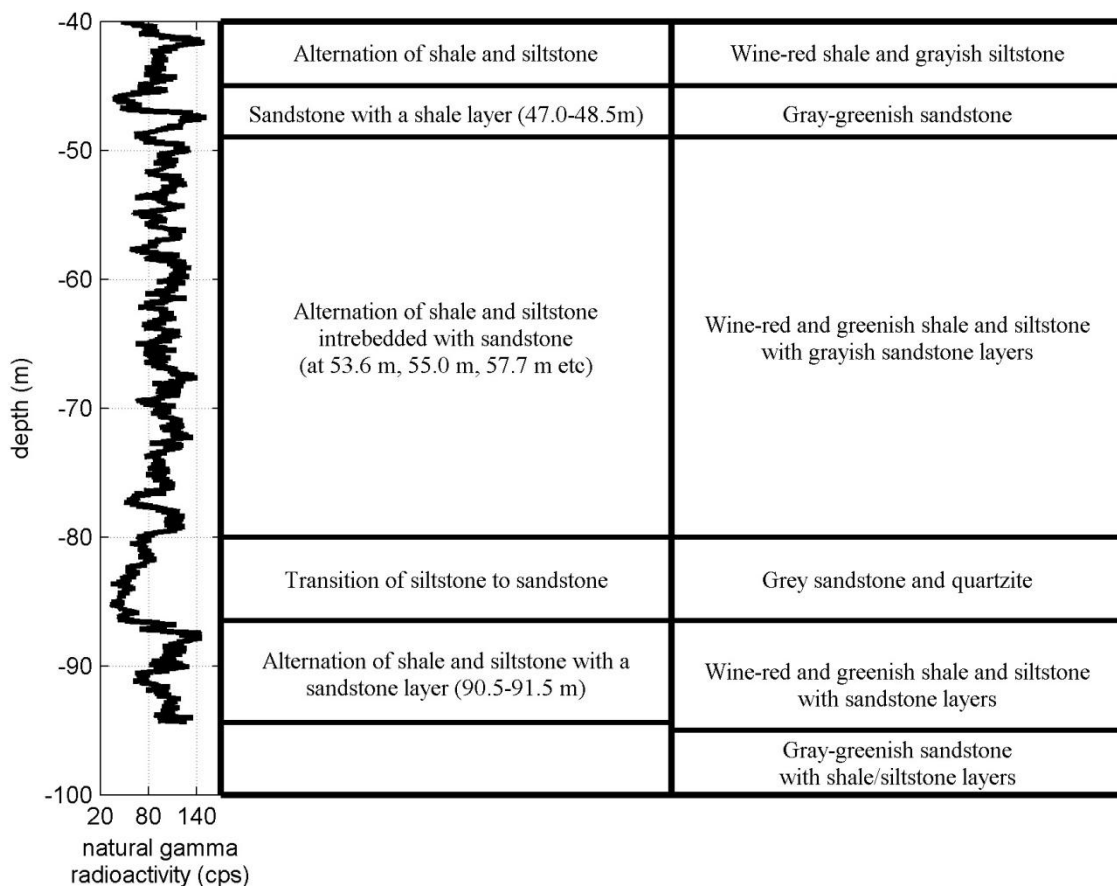

Figure 2.10 - Gamma-ray data (left) and geological interpretation based on gamma-ray data (middle) and cuttings observation (right) for B4

2.2.2.3 Layer dip angle determination

Figure 2.11 shows gamma-ray data for the four boreholes. It is observed that the same local peaks (dots in Figure 2.11) are repeated at different depths in the four boreholes. Based on

these data and the relative distance between the boreholes, the mean layer dip angle can be calculated (Table 2.1). The mean layer dip angle value, approximately 45° SE, is included in the discontinuities dip angle range (40°-70°) as indicated by the stereographic interpretation. Based on this, we may also conclude that the discontinuities presented in the stereographic interpretation are mainly related to stratification discontinuities.

The deviation of the four boreholes is shown in Figure 2.12. The inclination of the boreholes increases progressively through depth (with a value of 6.82° in B1 at 75.8 m, 10.67° in B2 at 98.6 m, 13.69° for B3 at 102.1 m and 12.90° in B4 at 96.4 m).
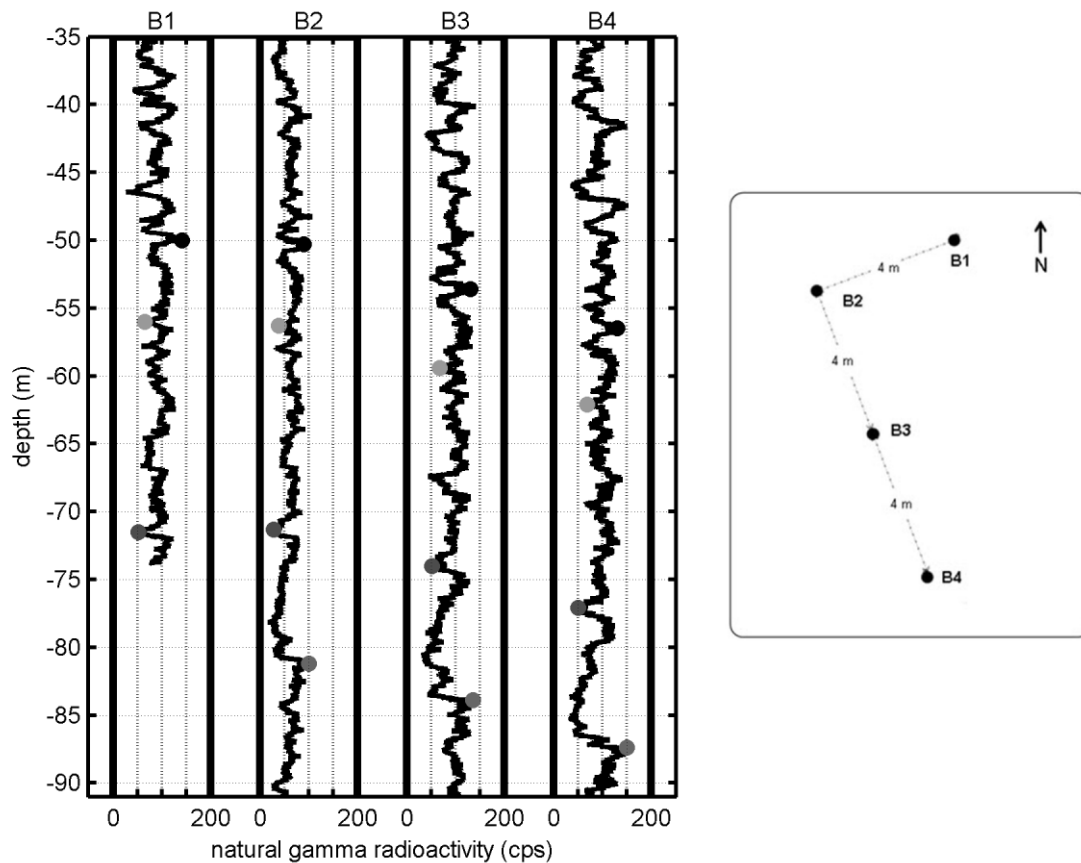

Figure 2.11 - Natural gamma radioactivity data for the four boreholes

Table 2.1 - Layer dip angle calculation based on gamma-ray data

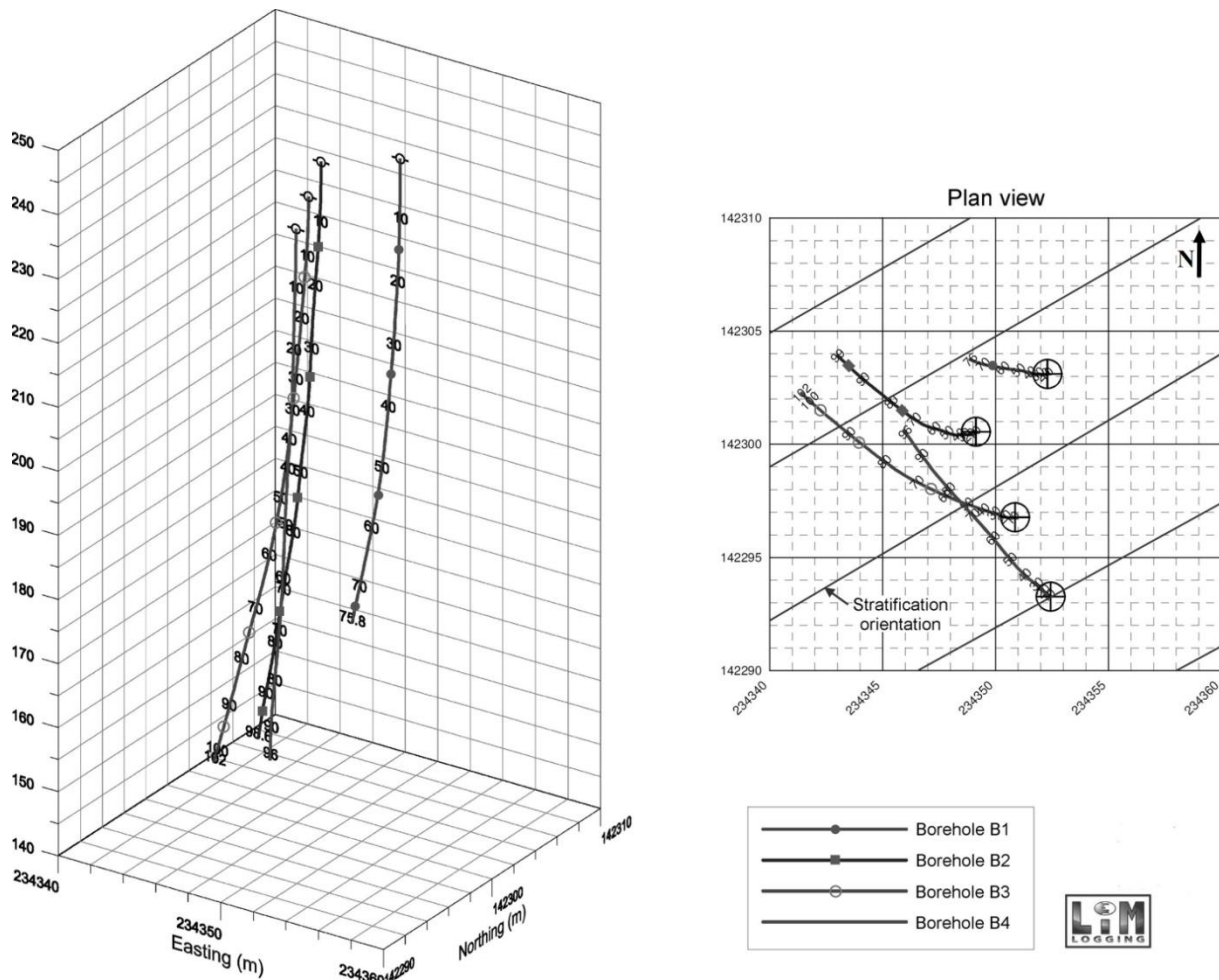| depth at B2 (m)	50.30	56.30	71.30	81.20
	B2B3			
horizontal distance (m)	3.23	3.07	2.75	2.61
elevation difference (m)	3.30	3.10	2.70	2.70
dip angle (°)	45.62	45.32	44.53	45.96
	B3B4			
horizontal distance (m)	2.95	2.85	2.98	3.24
elevation difference (m)	2.90	2.70	3.10	3.50
dip angle (°)	44.54	43.55	46.15	47.18
mean dip angle (°)	45.36			

Figure 2.12 - Deviation of the four boreholes in Belgian Lambert 1972 coordinates

42

2.3 Cuttings thermal conductivity

Sampling containers were used to collect cuttings during the drilling. In each container, cuttings corresponding to a depth interval ranging between 2 to 6 m were gathered. From each container 1 to 5 independent samples were prepared at the laboratory (Figure 2.13, left). The samples were dried in the oven for 48 h and then left to obtain the room temperature. The uncertainty of each sample's corresponding depth[2] depends on the sampling depth interval of each container. All the samples in each container were assigned to the average corresponding depth of the container. The cuttings grain size distribution is presented in Figure 2.13 (right).
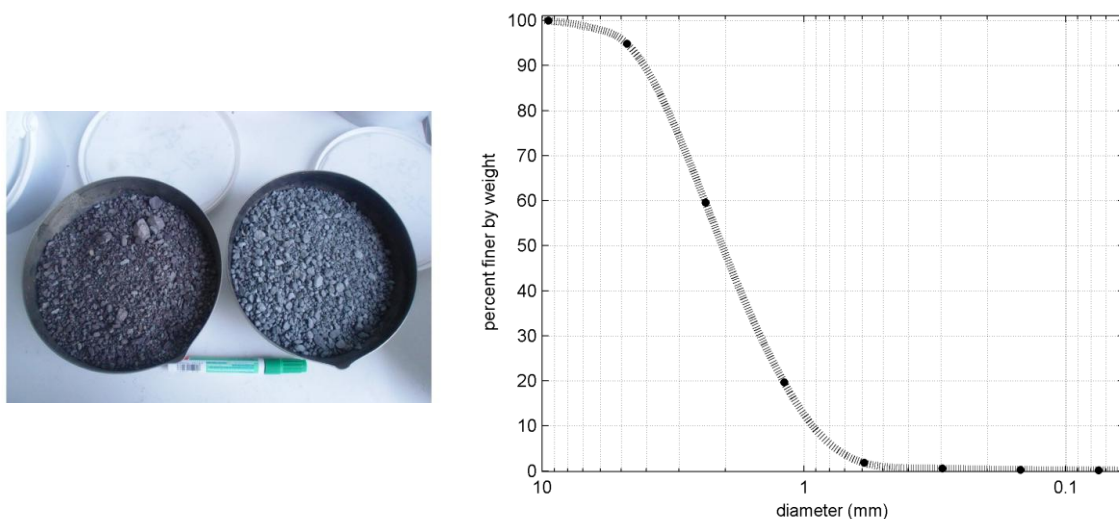

Figure 2.13 - Cuttings corresponding to wine-red shale/siltstone and grey sandstone layers (left) and grain size distribution of cuttings (right)

2.3.1 Thermal needle probe procedure

The thermal conductivity of 21 samples for B3 and 25 samples for B4 was measured at the laboratory by applying the needle probe technique (ASTM D 5334-00, 2000). This method is widely applied for soil and soft rock samples. Theoretically, the temperature rise in an infinite homogeneous medium due to an infinite line source is measured. In practice, the infinite soil mass is replaced by a large cylinder (of a minimum diameter of 51 mm and of a length of

---

[2] *i.e.,* the depth at which the sample was collected.

200±30 mm) and the infinite line source is replaced by a thermal needle probe, a device that consist of a heating wire and a temperature measuring element. The needle is connected to a device that produces a constant current and a device that produces a digital readout of temperature. The needle is inserted in the centre of the sample cylinder and a known constant current is applied to the heater wire for sufficient long time (Figure 2.14, right). During this time the temperature rise is recorded. The temperature evolution with time is then plotted in a semi-log scale, where three portions can be identified: the transient portion (early-time data), the quasi-steady-state portion and the portion dominated by edge and end effects (late-time data) (Figure 2.14, left).
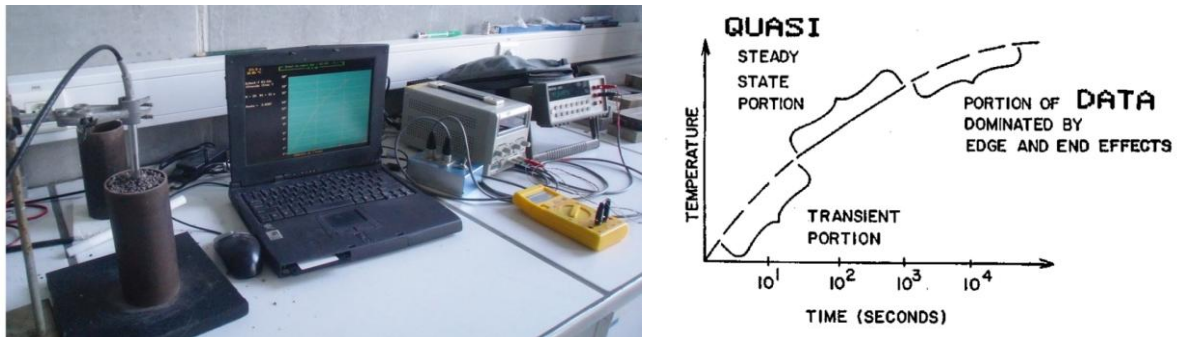

Figure 2.14 - Thermal needle probe equipment (right) and idealized temperature evolution curve plotted in a semi-log scale (left, ASTM D 5334-00©)

The sample's thermal conductivity, λ_{sample} *(W/mK)*, is calculated from the quasi-steady-state portion of the temperature profile as (ASTM D 5334-00) :

$$\lambda_{sample} = \frac{q}{4\pi\Delta T}\Delta \ln t,$$

where *T:* the temperature *(°C)*,

t: the time *(s)* and

q: the heat input *(W/m)*, $q = I^2 R/L$, where *I*: the applied constant current *(A)*, *R*: the total resistance of the heater wire *(Ω)* and *L*: the length of the heater wire *(m)*.

Considering the cuttings sample as a two-phase material consisting of the solid phase (cuttings) and air phase, the cuttings thermal conductivity, λ_{cutt} (W/mK), can be calculated by means of the sample's porosity, *n*, as (Alonso-Sánchez et al., 2012):

$$\lambda_{cutt} = \left(\lambda_{sample} / \lambda_{air}\right)^{1/(1-n)},$$

where λ_{air}: the air thermal conductivity ($\lambda_{air}=0.025 \ W/mK$ at 20 °C).

For an accurate measurement the cuttings grain size should not significantly exceed the needle diameter (Kömle et al., 2010). In this study 33% of the cuttings is finer than the needle diameter (1.5 mm) and 92% finer than 3 times the needle diameter (4.5 mm) (Figure 2.13).

The cuttings samples were prepared in a cylinder of a height of 170 mm and a diameter of 64 mm. The samples thermal conductivity was measured at room temperature and for a heat input of approximately 6 W/m. The TP02 Huksenflux needle probe of a length of 150 mm and of a diameter of 1.5 mm was used (Figure 2.15). This needle probe consists of a heating wire and of two thermocouple junctions. During the test, the cold joint remains in constant temperature, equal to the initial temperature of the medium, while the hot joint is heated. The main signal is the differential signal between the hot and the cold joint. An additional temperature sensor is mounted in the base of the needle, which provides reference temperature measurements for establishing the absolute medium temperature.
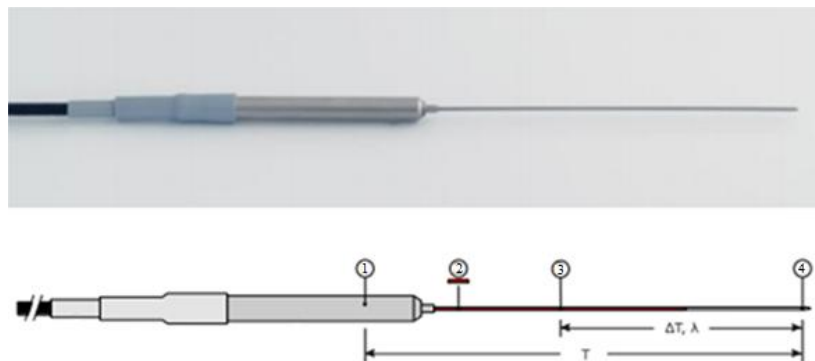
Figure 2.15 - TP02 Huksenflux needle probe (length of 150 mm, diameter of 1.5 mm) consisting of: a reference temperature sensor in the base of the needle (1), a heating wire (2), a hot thermocouple junction (3) and a cold thermocouple junction (4)

Prior to the cuttings thermal conductivity measurements, the thermal sensor of the needle probe was tested in glycerol (calibration verification). Figure 2.16 shows the recorded temperature evolution for a duration of 900 sec. The three portions of the curve are distinct:

transient portion (t<10 sec), quasi-steady-state portion (10 sec<t<200 sec) and portion dominated by edge and end effects (t>200 sec). The thermal conductivity was calculated based on the data of the quasi-steady-state portion of the curve and the calculated value was in good agreement with the corresponding values reported in literature (Table 2.2).
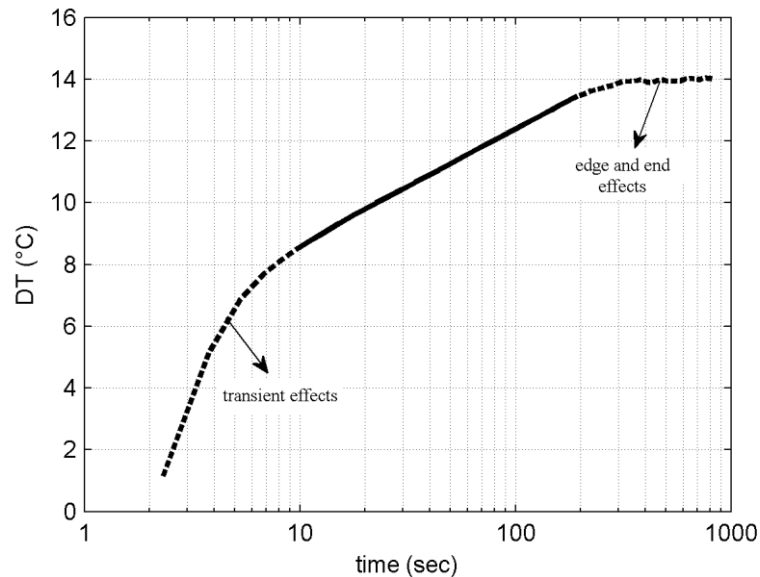

Figure 2.16 - Measured temperature evolution for glycerol by applying the needle probe method (cylinder diameter of 64 mm, heat input of 6.0 W/m)

Table 2.2. Measured and reported values of glycerol thermal conductivity

$\lambda_{measured}$ (W/mK)	$\lambda_{reported}$ (W/mK)	reference
	0.292	Kayode (2010)
0.299	0.293	Hanson et al. (2004)
	0.286	Kaye and Laby (1978)

2.3.2 Thermal conductivity measurements analysis

Figure 2.17 shows the measured thermal conductivity of the cuttings for B3 and B4, where each sample was assigned to the average corresponding depth of the container. It is observed that high thermal conductivity values, indicated with grey colored diamonds, correspond to mainly sandstone/siltstone layers (low gamma-ray values). Low thermal conductivity values, indicated with black colored circles, correspond to mainly shale/siltstone layers (high

46

gamma-ray values). Sandstone is mainly composed of quartz and feldspar while shale and siltstone contain a significant clay fraction. The thermal conductivity of quartz, $\lambda_{quartz} = 7.7 \ W/mK$, is much higher than the one of non-quartz minerals, $\lambda_{non-quartz} = 1.5 - 5.0 \ W/mK$, (Clauser and Huenges, 1995). As a result the sandstone/siltstone thermal conductivity is increased compared to the shale/siltstone thermal conductivity. In this case the transition of one formation to another can be identified by the cuttings thermal conductivity measurements.
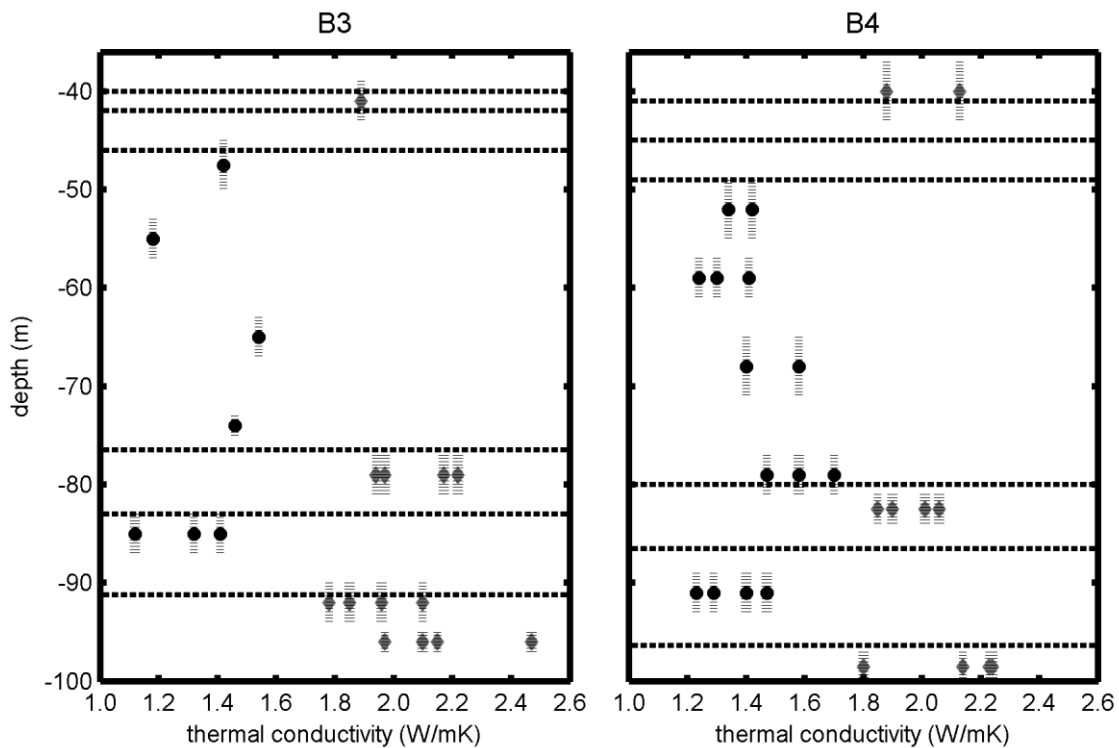
Figure 2.17 - Measured thermal conductivity of cuttings (dry samples) for B3 and B4

Each sample was assigned to a layer according to its corresponding sampling depth interval. Succesive layers with low (or high) thermal conductivity values were merged into one layer. Then, the mean thermal conductivity for each layer was calculated. The results for B3 and B4 are shown in Figure 2.18, where dashed lines indicate the layer dip angle. The mean layer dip angle, approximately 48° SE, can be calculated based on these data and the relative distance between the boreholes (Table 2.3).

Figure 2.18 - Layer dipping indication based on thermal conductivity of cuttings for B3 and B4

Table 2.3 - Layer dip angle calculation based on cuttings thermal conductivity

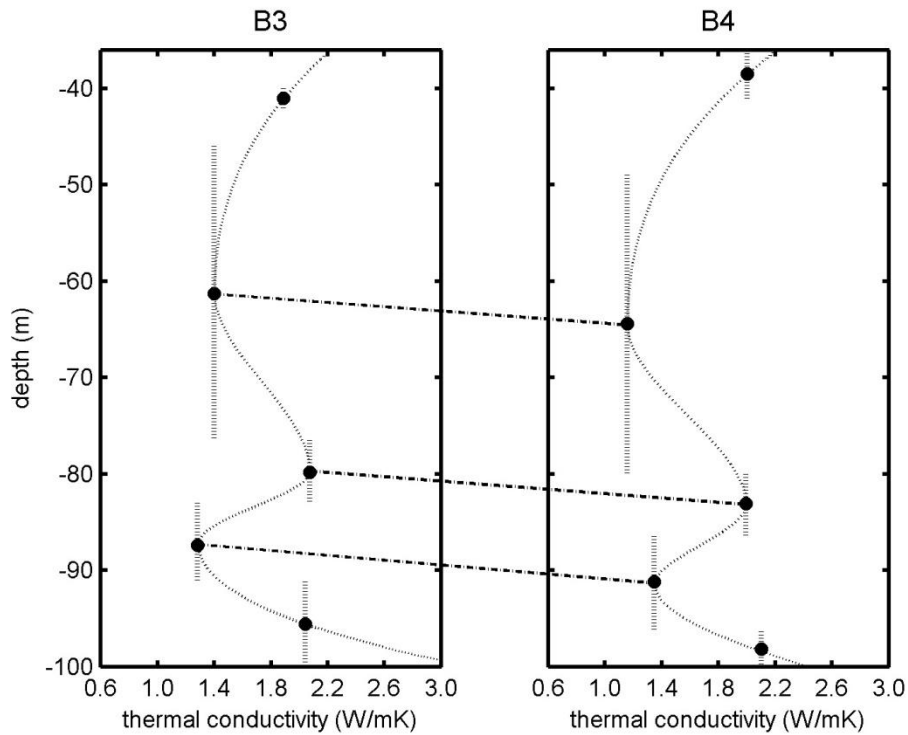| depth at B3 (m)	61.3	79.80	89.4
	B3B4		
horizontal distance (m)	2.93	3.13	3.35
elevation difference (m)	3.10	3.30	3.80
dip angle (°)	47.58	46.53	48.61
mean dip angle (°)	47.57		

The mean measured sandstone/siltstone and shale/siltstone thermal conductivity is equal to 2.0 W/mK and 1.4 W/mK respectively for both boreholes. Given that shale/siltstone layers cover approximately 66% of the boreholes length, while sandstone/siltstone layers only 33%, the mean in-situ thermal conductivity based on the cuttings measurements is equal to 1.6 W/mK (weighted arithmetic mean). This value is 45% lower than the one estimated based on the TRTs conducted in-situ (2.88±0.16 W/mK, Chapter 5). This difference can be attributed to the fact that cuttings contain no information on the rock mass fracturing, the degree of saturation and the thermal interaction between different layers, parameters that influence the effective in-situ thermal conductivity.

However, studying cuttings thermal conductivity measurements qualitatively can provide information on the bedrock heterogeneity and on the possible varying thermal conductivity with depth in-situ. In this study, based on the cuttings thermal conductivity, the transition of one formation to another and the layer dipping is indicated, since in this case their different mineral composition results in a different thermal conductivity. These measurements indicate a possible varying effective thermal conductivity of the rock mass in-situ, due to alternation of different rock layers through depth, with enhanced heat transfer at mainly sandstone layers. This approach is easy to implement but is not applicable if a limited quantity of cuttings is available.

2.4 In-situ temperature measurements and tests

Several fiber optic measurements were conducted in-situ in a period of 3 years: during hardening of the grouting material, at the undisturbed state and during DTRTs in the four boreholes (Figure 2.19). The typical equipment for a TRT (Gehlin, 2002) consists of a pump (to circulate the fluid inside the pipes), an electric resistance heater (to inject constant heat), temperature sensors (to measure the temperature) and a data logger (to record the measurements during the test). The equipment is connected to the BHE pipes and insulation layers are attached around the pipes to minimize the heat transfer between the circulating fluid and the air. Before starting the test, water is circulated at high flow rate to purge air from the system. After purging the air the first phase of the test starts. During this phase water is circulated inside the pipe loop to achieve equilibrium between the water and the surrounding ground. The second phase consists of a continuous water circulation with usually constant heat input. After the heating period, the system recovers to its undisturbed state. During the test, temperature is recorded at the pipe inlet and outlet. During a DTRT temperature is measured not only at the pipe inlet and outlet but also at different depths along the borehole (Fujii et al., 2006; Acuña et al., 2009; Soldo et al., 2016).
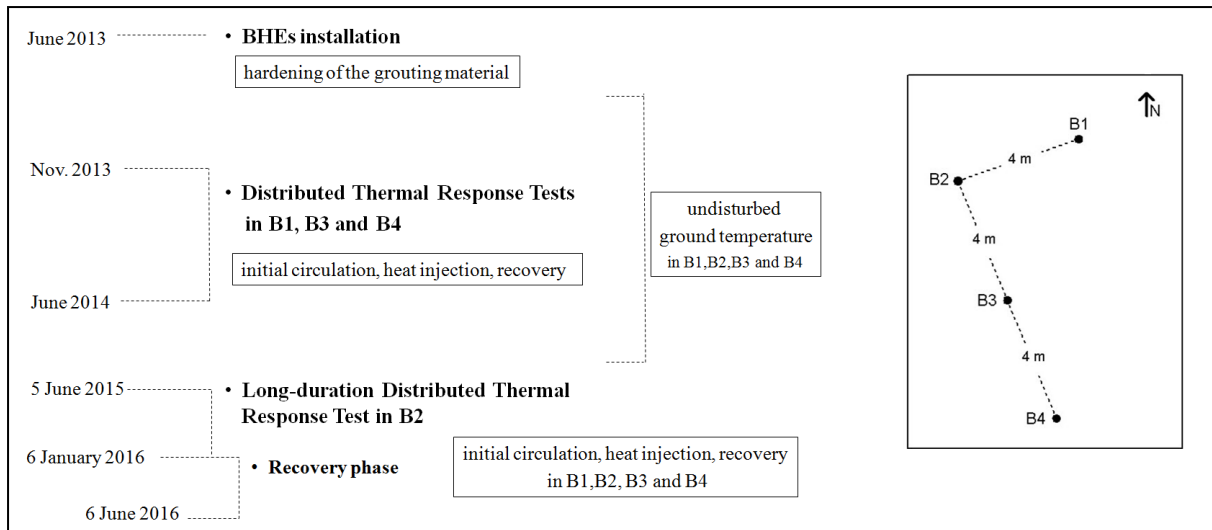
Figure 2.19 - In-situ temperature measurements in the four BHEs (B1-B4) in the period of June 2013 to June 2016

In this experimental site, four temperature sensors were used: two to record the water temperature at the pipe inlet and outlet inside the test rig and two to record the air temperature inside and outside of the test rig (Figure 2.20). Temperature in the four sensors, flow rate and electrical power are recorded at a time interval of one minute. Additionally to theese measurements, temperature was also measured along the pipes by the fiber optics.
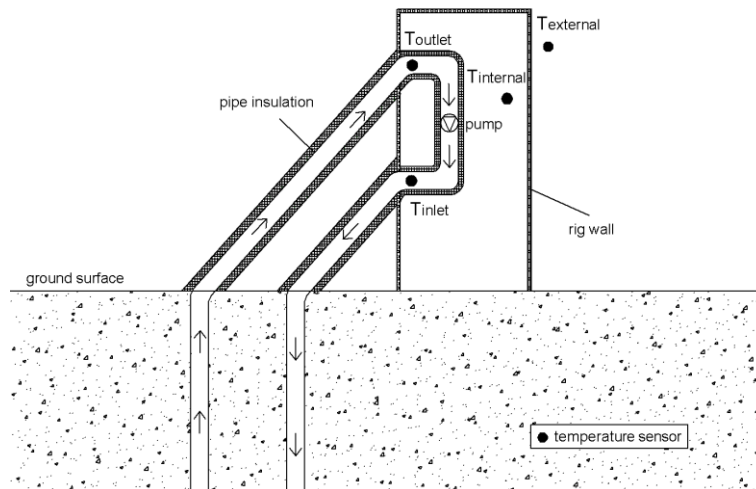

Figure 2.20 - Temperature sensors location during the DTRTs

Table 2.4 presents the duration of the tests conducted in the four BHEs. During the initial water circulation (phase 1) the average ground temperature is obtained. The purpose of the heating phase (phase 2) is to determine the ground thermal conductivity and the borehole

thermal resistance. For the recovery phase (phase 3), where no heat is injected in the pipes, one of the two following procedures was applied: continues water circulation (phase 3a) to confirm the ground thermal conductivity, or no water circulation (phase 3b) to correlate temperature profiles by the fiber optics to the characteristics of the heterogeneous rock mass. In B2 a long-duration test was conducted, during which temperature was measured by the fiber optics in the four BHEs. Theese temperature measurements allowed to investigated the influence of the test duration on the ILS interpretation and the effect of in-situ characteristics (e.g. hetrogeneity, anisotropic thermal behaviour, ambient air temperature variations) on the thermal plume in the rock mass.

Table 2.4 - Duration of conducted DTRTs

BHE			B1	B2	B3		B4		
DTRT			B1	B2	B3.1	B3.2	B4.1	B4.2	
	Water circulation	Heat injection							Typical duration*
Phase 1	√	-	24 h	39 h	16 h	29h	22 h	22 h	2 h - 12 h
Phase 2	√	√	177 h	216 d	10 h	160 h	168 h	91 h	50 h - 60 h
Phase 3a	√	-	-	-	-	35 h	34 h	-	12 h - 24 h
Phase 3b	-	-	302 h	153 d	94 h	240 h	-	127 h	

* Loveridge et al., 2013

2.5 Conclusions

In this chapter, a detailed bedrock characterisation until a depth of approximately 100 m is presented based on borehole logging measurements (natural gamma radioactivity, acoustic amplitude, acoustic travel time, azimuth) and cuttings observation. The site geology is characterised by deposits of sand and gravel until a depth of approximately 8 m. The bedrock follows which consists of siltstone and shale interbedded with sandstone. Fractured zones are detected in the rock mass mainly until a depth of 35 m and the mean layer dip angle is 45° SE.

In the cuttings thermal conductivity measurements the transition of one formation to another and the layer dipping is indicated, since in this case their different mineral composition results in a different thermal conductivity. This approach is easy to implement and can provide information on the bedrock heterogeneity, but is not applicable if a limited quantity of cuttings is available. These measurements indicate a possible varying effective thermal conductivity of the rock mass in-situ, due to alternation of different rock layers through depth, with enhanced heat transfer rate at mainly sandstone layers.

Cuttings measurements should be studied qualitatively for extrapolating them to in-situ conditions. Based on the dry cuttings measurements in this study, the mean bedrock thermal conductivity is equal to 1.6 W/mK, lower of 45% than the one estimated based on the TRTs conducted in-situ (2.88±0.16 W/mK, Chapter 5). This difference can be attributed to the fact that cuttings contain no information on the rock mass fracturing, the degree of saturation and the thermal interaction between different layers, parameters that influence the effective in-situ thermal conductivity.

Chapter 3 - Fiber optic temperature measurements accuracy

3.1 Introduction

DTRTs are conducted in situ to investigate any possible variation of the BHE behaviour with depth and to detect highly conductive zones in the surrounding ground, which contribute to the optimisation of the geothermal system. During a DTRT, temperature is measured not only at the pipe inlet and outlet, but also along the borehole. Temperature borehole logging is achieved by temperature sensors (Florides et Kalogirou, 2008) or fiber optic cables (Fujii et al., 2006; Acuña et al., 2009; Soldo et al., 2016) installed inside the borehole. Fiber optic cables have a great potential, since, contrary to individual temperature sensors, they allow to obtain a continuous high-resolution temperature profile along the borehole length. However, the accuracy of the measured temperature profiles will strongly depend on the calibration accuracy and on the measurement system performance parameters. It is, therefore, crucial an accurate calibration to be achieved and the system performance parameters to be chosen with regard to the desired measurements accuracy. This chapter presents raw and calibrated temperature profiles, obtained by the fiber optics in-situ. It focuses on the importance of a continuous offset calibration during the in-situ measurements and on the effect of the measurement time and the spatial resolution on the fiber optic measurements accuracy.

3.2 Distributed Temperature Sensing technique

Temperature is measured along the fiber optics, by applying the Distributed Temperature Sensing (DTS) technique (Selker et al., 2006; Hermans et al., 2014). This technique is based on Raman optical time domain reflectometry. One (single-ended) or both (dual-ended) fiber ends are connected to the DTS instrument (Figure 3.1, left). A laser pulse is injected into the optical fiber and the light is scattered and reemitted from the observed point. The light is reemited at wavelengths of different frequency than the incident light (Raman scattering). Raman Stokes backscatter signals are characterised by frequencies lower than the one of the incident light, while anti-Stokes signals by frequencies higher than the one of the incident light (Figure 3.1, right). The Raman backscatter signal is temperature sensitive and the temperature along the fiber is determined by the intensity ratio of Raman Stokes and anti-

Stokes signals. The position of the temperature reading is determined by the arrival time of the reemitted light pulse.
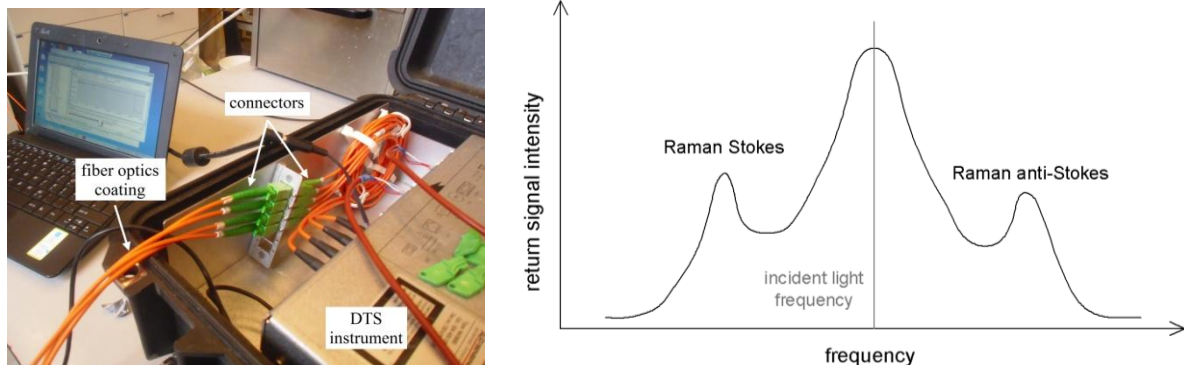

Figure 3.1 - Fiber optics connected to the DTS instrument (left) and sketch of Stokes and anti-Stokes Raman scattering (right; after Hermans et al., 2014)

3.3 Fiber optic profiles calibration

The fiber optics calibration consists in an offset (=constant shift) correction, a gain (=stretch) correction and an attenuation ratio (=tilt) correction (Figure 3.2). The calibration parameters vary with the operating conditions of the DTS instrument and the optical fiber itself (Hausner et al., 2011). A continuous calibration in each optical fiber is necessary for in-situ measurements, where the DTS instrument is exposed to the varying ambient air temperature and the fiber optic cables could be locally bended or strained. Fiber zones of known temperature are used for the calibration procedure. In this experiment two RTD probes were attached at certain depths in the four boreholes, in direct contact with the fiber optic cables. These measurements are invariant to the DTS ambient air temperature and can be used as reference values to calibrate the fiber optic measurements. A temperature sensor was also lowered into the pipes to obtain the reference temperature values, in the case that the pipes were accessible. Figure 3.3 shows raw profiles of the ground temperature for two optical fibers contained in the same cable, obtained before the in-situ TRTs. The RTD measurements are stable at 50 m depth where the ground temperature is not influenced by the air temperature variations (Chapter 4), while the fiber optic profiles show a significant shift. It is observed that a different offset correction should be applied in each optical fiber and for every measurement, to match the corresponding RTD probes measurements.
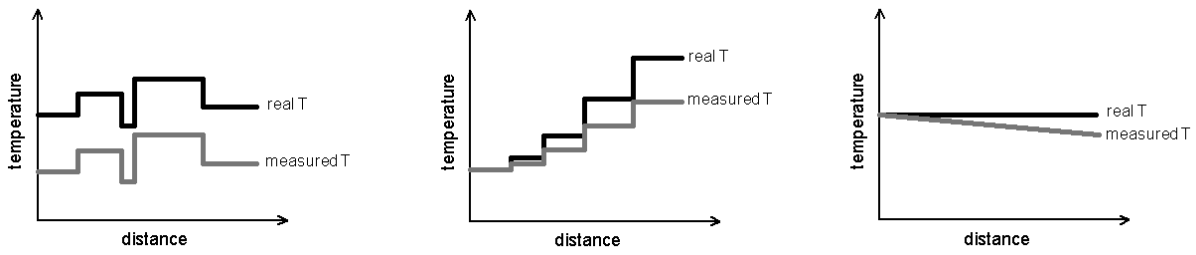
Figure 3.2 - Sketch of offset (left), gain (middle) and attenuation ratio (right) influence on fiber optic temperature profiles
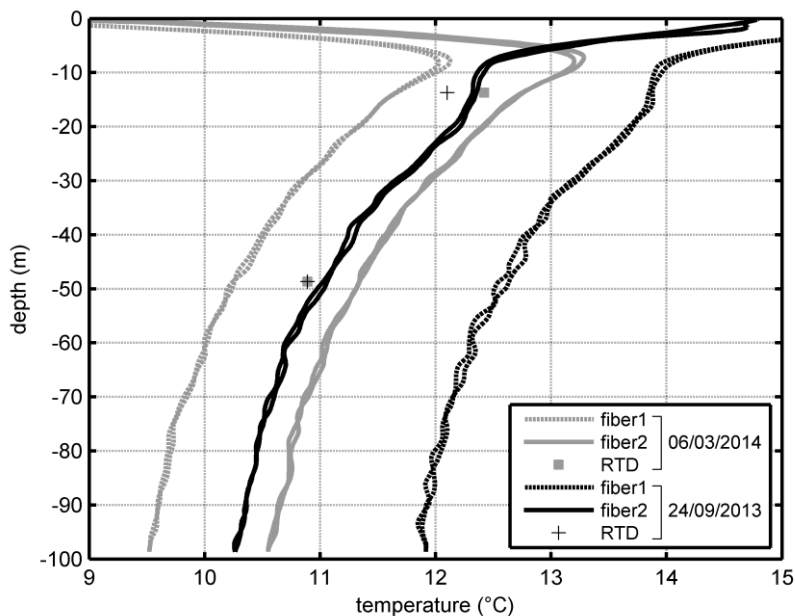

Figure 3.3 - Raw temperature profiles for two optical fibers in the same cable obtained before the in-situ TRTs

Figure 3.4 (left) shows raw temperature profiles measured in single-ended and dual-ended configuration. In the single-ended measurement the attenuation effect is evident, since the attenuation increases with the cable length. Though in dual-ended measurements, where the laser pulses are injected in the optical fiber alternatively from both ends, the attenuation effect is automatically removed and an attenuation ratio calibration is not required in this case. Figure 3.4 (right) shows a corrected single-ended temperature profile, which was calculated from the raw data, T_{meas}, by choosing the appropriate offset factor, c_{off}, and attenuation ratio coefficient, f_{att}, as $T_{corr}=T_{meas}+f_{att} \cdot (fiber\ lenght)+c_{off}$. A gain calibration is

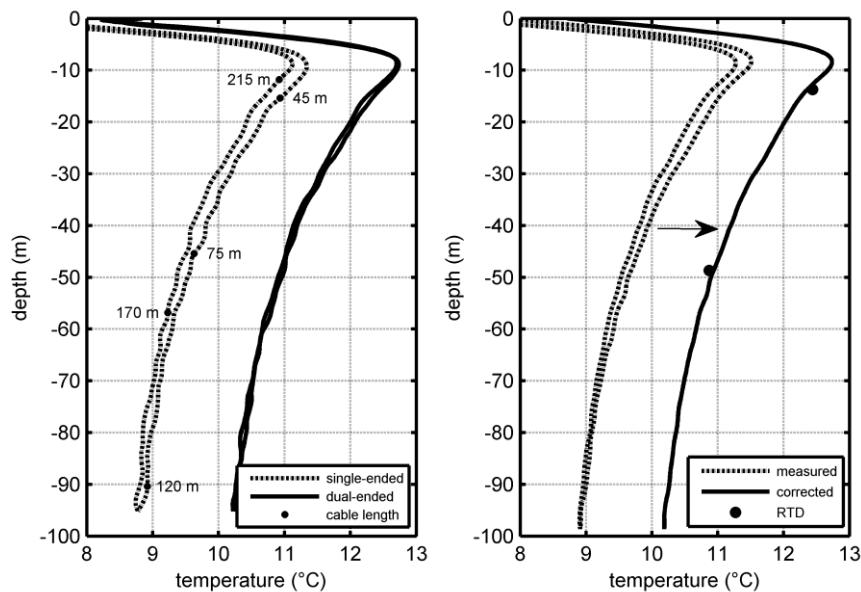not included, since a gain calibration factor equal to one is usually sufficient for most applications.

Figure 3.4 - Raw temperature profiles for single-ended and dual-ended configuration (left) and corrected single-ended profile (offset and attenuation ratio correction) (right)

During the long-duration TRT in B2, the RTD probes attached on the pipes were not operational, probably due to an erosion of the sensor or of the electric wire connecting the sensor to the measurement device. An alternative calibration procedure was attempted based on the recorded temperature of the fiber optic cable part which was not attached at the BHE pipes. After the BHEs installation and grouting, the remaining parts of the cable in each borehole was rolled into loops and inserted in a metallic box (Figure 3.5). The metallic boxes served to protect the measurement equipment (fiber optic connectors, fiber parts not protected by external coating, DTS instrument) from weather conditions and damage. For the calibration, a RTD probe was attached in each cable loop, in direct contact with the fiber optic cable. Then the loops were insulated and inserted back in the box. A third RTD was placed at the center of the loops (Figure 3.6). To investigate if theese measurements can provide an accurate offset calibration, temperature was measured at the undisturbed state. The undisturbed temperature profiles were also obtained by lowering down a RTD probe inside the pipe and measuring the temperature at certain depths. These measurements were used as reference values, to verify the calibration procedure.

Figure 3.5 - Fiber optic cable loops (left) and metallic boxes (100 cm x 60 cm x 40 cm) for protection of the equipment (right)
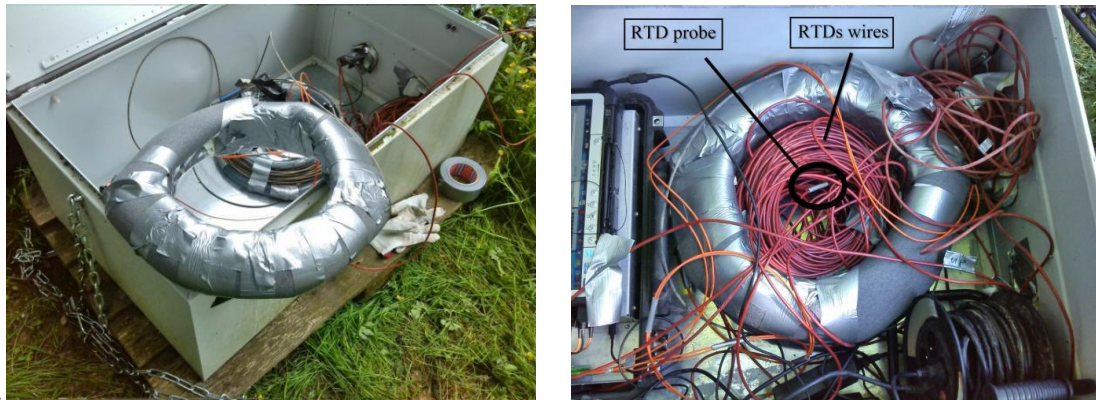

Figure 3.6 - Insulation of fiber optic cable loops (left) and RTD probe at the center of the pipe loops inside the box (right)

Figure 3.7 shows an undisturbed temperature profile given by the two optical fibers of the cable. It is observed that both loops display a different temperature. Moreover, the temperature along each cable loop is not constant, despite the insulation, and differences can be observed in both fibers of each loop. The latter is in particular evident close to the cable ends, where the optical fibers are not protected by the external coating and are not in contact with each other. These measurements indicate that air temperature in the interior of the box varies significantly. The recorded temperature along the cable depends on its location inside the box (e.g. in contact with the box wall, close to the DTS instrument). Given that the exact location of the attached RTD probes on the cable cannot be determined, these measurements are not appropriate for the offset calibration of the fiber optics profiles.

The fiber optic profiles during the long-duration TRT in B2 were calibrated by the RTD probe measurements located at the center of the pipe loops inside the box. For this calibration, the mean temperature of the fiber loops was assumed equal to the recorded air temperature by the RTD probe. Figure 3.8 shows undisturbed profiles calibrated by this approach. The profiles are close to the measurements provided by lowering down a RTD probe inside the pipe, but the offset error can reach the order of ±1 °C. This means that the offset accuracy of the fiber optic profiles during the long-duration TRT in B2 is low.
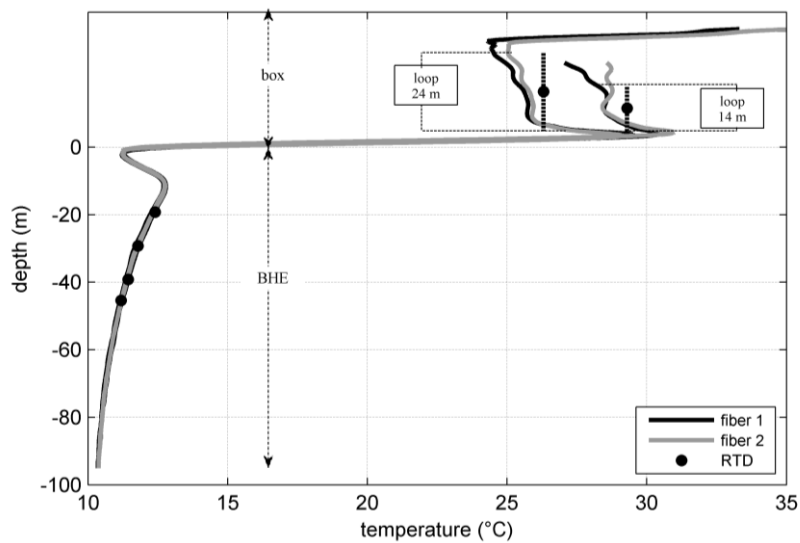

Figure 3.7 - Temperature profiles along the whole length of both optical fibers in B2 and RTD measurements along the BHE and on the cable loops inside the box (June 2015)
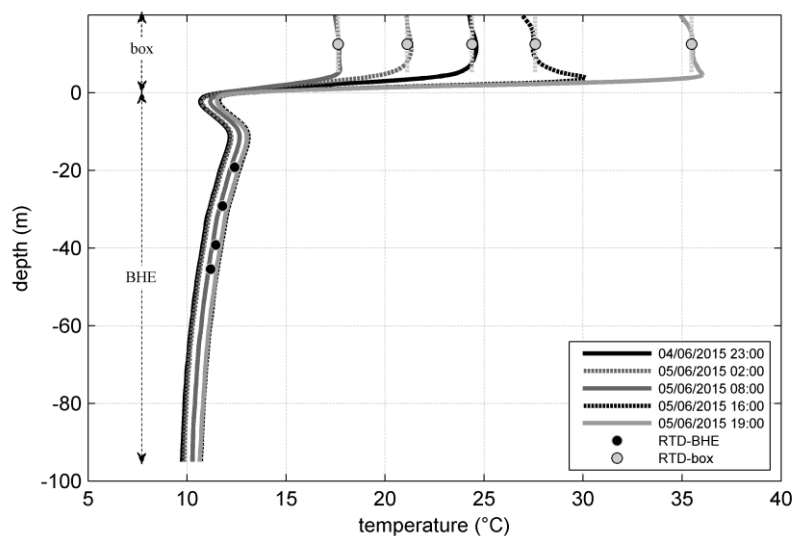

Figure 3.8 - Fiber optics temperature profiles calibrated by RTD measurements at the center of the cable loops inside the box

The measurements presented above show that the air temperature inside the box can vary significantly and this can result in a inaccurate offset calibration of the fiber optic profiles. It is therefore proposed, a sufficiently long cable section to be placed into an environment with known constant temperature, such as a water or ice bath (e.g. Acuña, 2010) (Figure 3.9).
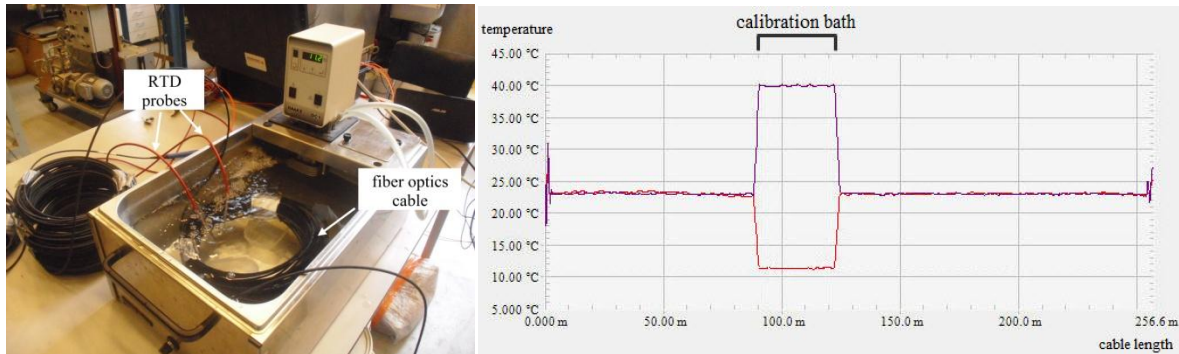

Figure 3.9 - Water calibration bath with two RTD probes (reference water temperature) (left) and temperature traces along the fiber optic cable for 11.0 °C (red line) and 40.3 °C (purple line) water temperature (right)

3.4 Fiber optic profiles accuracy

The accuracy of the fiber optic measurements depends on several factors, including the DTS system performance parameters, such as the measurement time and the spatial resolution. Measurement time is defined as the time for the DTS instrument to acquire measurement data for calculating a temperature trace (acquisition, digitalizing, processing). The instrument conducts independent measurements along the fiber length during the measurement time, and averages the successive readings. Longer measurement time provides more data to average which reduces random noise and improves the precision of the measurement. Figure 3.10 displays this effect on temperature profiles, measured successively in the same fiber, for different measurement time. After a certain number of measurements the temperature profile reaches a convergence point, practically free of noise. Repeating the same measurement with varying measurement time allows to distinguish true temperature variations from random noise.
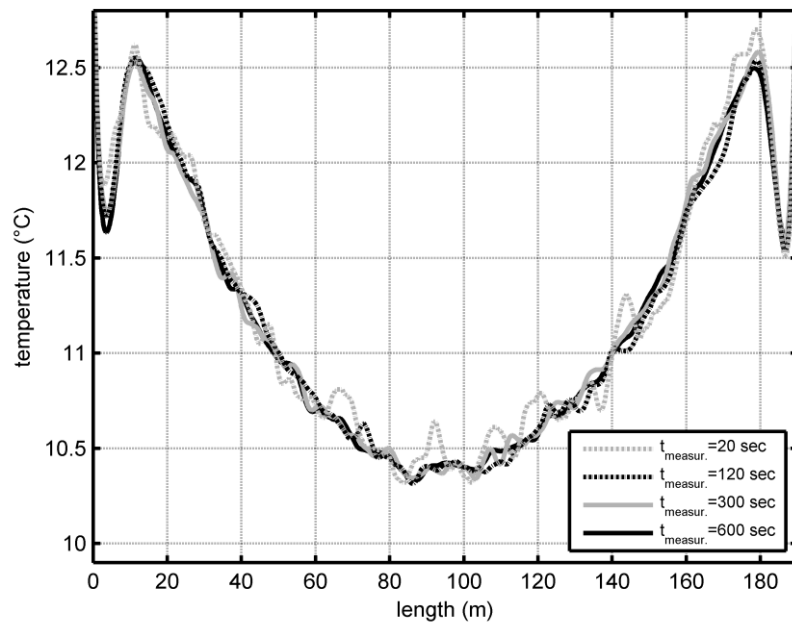
Figure 3.10 - Temperature profiles for varying measurement time (sampling interval of 20 cm, spatial resolution of 2 m)

Spatial resolution determines the slope width of a measured temperature change. As the spatial resolution increases, the pulse width increases and therefore the signal-to-noise ratio increases. Spatial resolution is a critical parameter for the temperature accuracy of local hotspots. Temperature is measured at specific points along the fiber, where the distance between them is defined by the sampling interval. To create a continuous profile along the whole fiber length, temperature at each fiber point is calculated by a spline interpolation of the measured temperature data at an interval equal to the spatial resolution. For instance, a spatial resolution of 4 m indicates that the calculation at a specific position is performed by taking into accounts the measured points 2 m before and after that position. If the width of a hotspot is lower than the spatial resolution, the measured temperature is reduced by approximately the ratio of hotspot width to spatial resolution (Hoffman et al., 2007). Figure 3.11 shows measured temperature profiles during the heating phase of a DTRT for a sufficient long measurement time, 1800 sec, and varying spatial resolution. These profiles highlight the importance of the spatial resolution to the desired measurement accuracy.
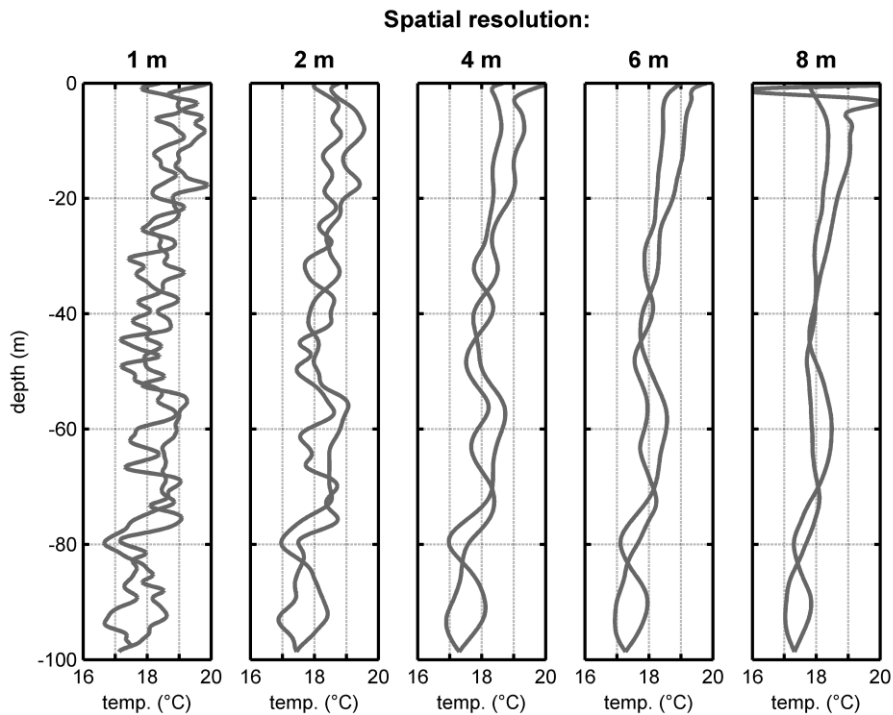
Figure 3.11 - Temperature profiles for varying spatial resolution (sampling interval=20 cm, measurement time=1800 sec)

The temperature resolution (standard deviation) of the DTS instrument used in this study is in the order of 0.05 °C. The offset correction of the temperature profiles was conducted using RTD probes with an accuracy of the order of 0.15 °C (Class A). The fiber optic temperature measurements presented hereafter are obtained for sampling interval of 20 cm, spatial resolution of 2 m and measurement time longer than 1800 sec, if it is not indicated otherwise.

It should be noted that dirty connectors or cable ends should be avoided, since they can significantly reduce the accuracy of the measurements. Moreover, bends and strains on the fiber optic cable can also locally reduce the accuracy of the temperature measurements.

Chapter 4 - Undisturbed ground temperature in a semi-urban environment

4.1 Introduction

The undisturbed ground temperature, i.e. the ground temperature before conducting a TRT, is a critical parameter for the design and the thermal performance of BHEs (Dehkordi and Schincariol, 2014; Kurevija et al., 2014). The undisturbed ground temperature is determined in-situ by mainly two methods: by temperature borehole logging and by circulating the fluid inside the pipe loops and recording the temperature at the pipe inlet and outlet, widely applied before the heating phase of the TRT. The two methods are presented in Chapter 1 (section 1.3.1), together with a literature review on in-situ studies concerning the comparison of both methods. These studies mainly focus on the effect of the pump work on the accuracy of the undisturbed ground temperature estimation. Another important factor is the insufficient equipment insulation, since it can result in oscillations in the recorded temperature evolution, as it is widely illustrated in the heating phase temperature measurements. This chapter investigates if the thermal interaction between the circulating fluid and the ambient air can result in a significant error on the undisturbed ground temperature estimation, that has an important effect on the design of BHEs. Moreover, in urban areas, elevated ground temperatures have been observed worldwide, as presented thoroughly in Chapter 1 (section 1.3.1). The present chapter also focuses on the estimation of the temperature field evolution with time in the surrounding ground in semi-urban areas and on its influence on the design of BHEs. This is also of interest for the long-term behaviour of BHE systems, given that the heat loss through structures into the subsurface is a continuous phenomenon, that recharges the geothermal reservoir potential.

This chapter presents temperature measurements by fiber optics in the four boreholes in a period of two years. The ground temperature profiles, which are in good agreement with those of lowering a temperature sensor inside the pipes, are characterised by elevated temperature and a negative temperature gradient through depth. It is argued that the measured temperature field is the result of the heating of the ground by structures located close to the BHEs. A 3D numerical model is presented to verify this and to investigate the impact on the design of closed-loop systems. Moreover, the depth-average ground temperature was

estimated by measuring the temperature at the pipe inlet and outlet during water circulation in the pipe loops, a typical procedure applied before conducting a TRT. An analysis of the measurements for five tests is presented, which highlights the importance of the rig insulation for the accurate estimation of the ground temperature. The impact of the overestimated ground temperature on the design is investigated for these tests. Fiber optic measurements conducted during the tests are also presented, which provide a more accurate estimation of the ground temperature. Finally, basic conclusions are provided. A part of the work included in this chapter is also presented in Radioti et al. (2015b; 2016a; 2016b).

4.2 Undisturbed ground temperature profiles by borehole logging

4.2.1 In-situ measurements

Figure 4.1 shows undisturbed temperature profiles measured in B2 in a period of two years. The upper 18 m correspond to the thermally unstable zone, where ground temperature is influenced by weather conditions. Below this depth, measured temperatures appear invariant to time in the two-year period. The temperature decreases through depth at a mean rate of approximately 0.25 °C/10 m and the depth-average temperature of this zone is 11.0 °C. Figure 4.2 displays temperature measurements in the four boreholes in December 2013, March 2014 and in June 2015. In each case, the temperature profiles in B2, B3 and B4 coincide with each other and display a higher temperature in the first 20 m compared to B1. Temperature profiles were also obtained by lowering down a RTD probe inside the U-pipe and measuring the temperature at a depth interval of mainly 10 m. The RTD probe measurements can fairly reproduce the corresponding fiber optics profiles (Figure 4.2).
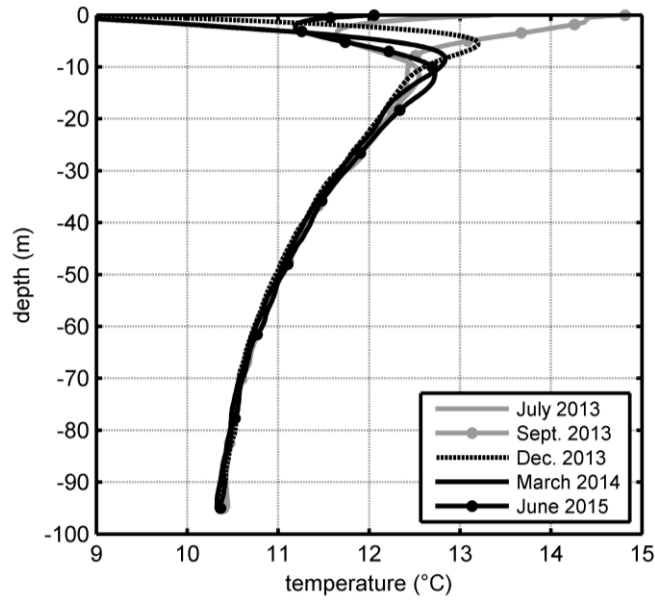
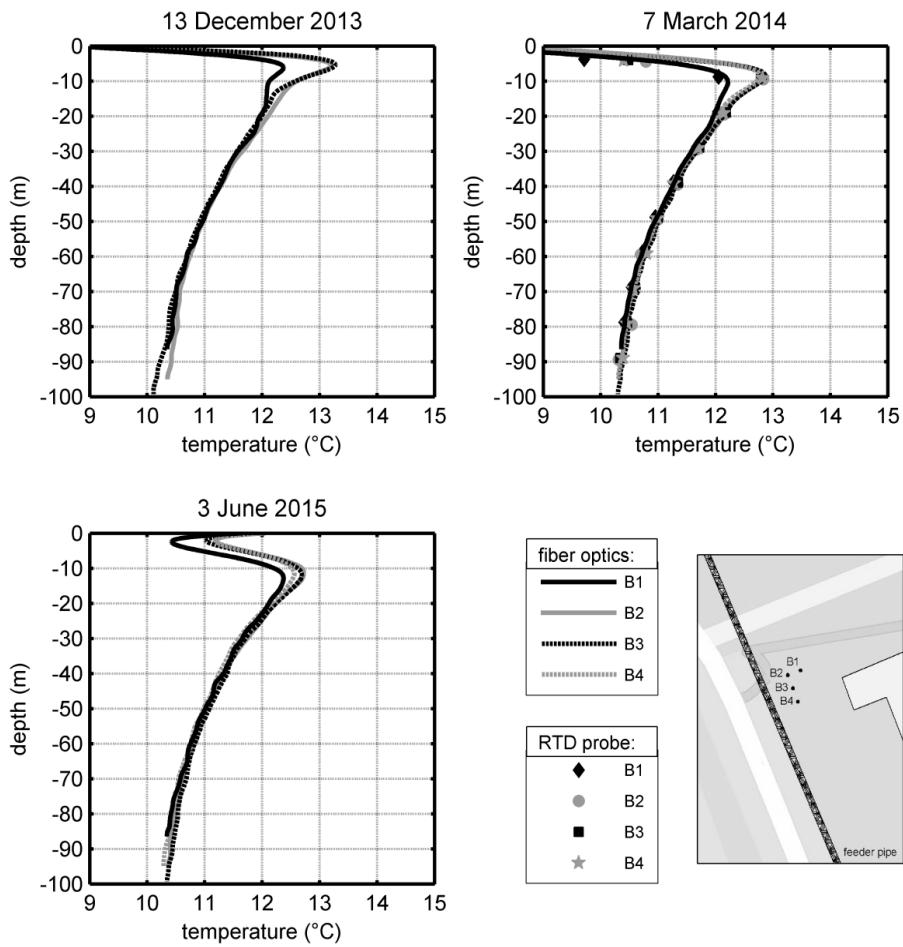Figure 4.1 - Undisturbed ground temperature measured by fiber optics in B2

Figure 4.2 - Undisturbed ground temperature measured by the fiber optics and by lowering a RTD

probe inside the U-pipe in the four boreholes

Temperature was also measured by a RTD probe in a borehole well, which is located 150 m southeast from the site (Figure 4.3). The well is filled with water below 10.6 m. The influence of the air temperature (3.26 °C) is evident in the first meters. Below approximately 14 m, temperature oscillates around a value of 10.1 °C, lower than the corresponding temperature in the four boreholes. Moreover, contrary to what is observed in the four boreholes, the temperature is not decreasing through depth. To further investigate the measured profiles, an analytical solution to estimate the undisturbed temperature is presented in the next section.
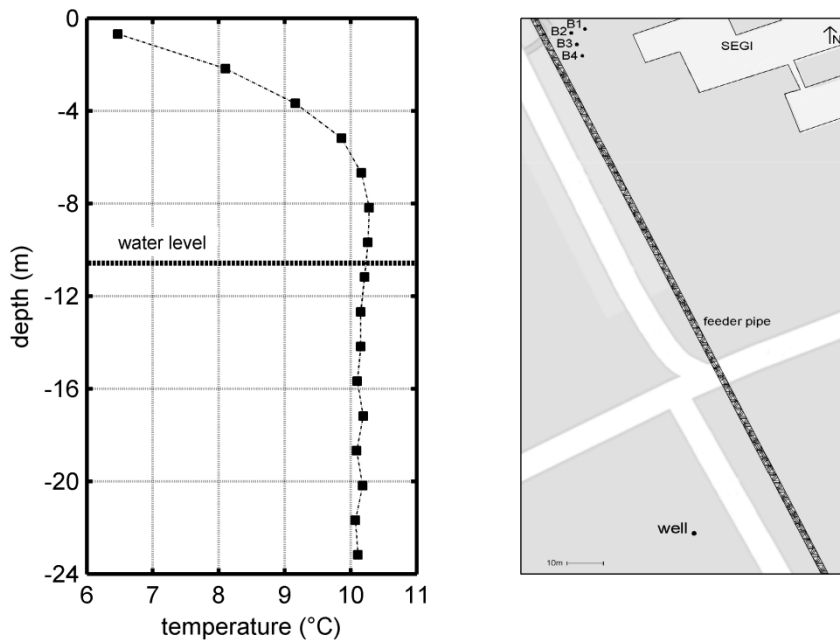
Figure 4.3 - Undisturbed ground temperature measured by lowering a RTD probe inside the borehole well (24 February 2016)

4.2.2 Analytical estimation

The undisturbed ground temperature for the Sart-Tilman area, T_g, was calculated by the heat diffusion analytical equation in a semi-infinite plane due to a temperature sinusoidal stress by including the geothermal gradient effect as (Tinti, 2012):

$$T_g(D,t) = T_m - A\exp\left[-D\sqrt{\frac{\pi}{365\alpha_g}}\right]\cos\left[\frac{2\pi}{365}\left(t - t_{T\min} - \frac{D}{2}\sqrt{\left(\frac{365}{\pi\alpha_g}\right)}\right)\right] + \mathrm{T}_{geo}(D),$$

where D: the depth *(m)*,

t: days from the first day of January,

T_m=8.9 °C, the average annual temperature of the environment,

A=7.2 °C, the annual oscillation amplitude of air temperature,

t_{Tmin}=10, the day number corresponding to the minimum temperature (from 1st January),

α_g=0.1104 m²/d, the equivalent ground daily thermal diffusivity and

Tgeo(D): the product of the geothermal gradient, 0.013 °C/m for the Liege area (Petitclerc and Vanbrabant, 2011), by the testing depth.

The air temperature parameters used in this calculation are based on statistical data for the Sart-Tilman area for a period of 20 years (climate-data.org) and the mean ground thermal conductivity on TRTs conducted in situ in the four BHEs (Chapter 5).

Figure 4.4 presents the ground temperature estimated analytically for the months of the year. The ground temperature in the upper 18 m varies during the year, since it is influenced by the seasonal weather conditions. At the depth of 18 m, the ground temperature reaches 9.1 °C which is close to the average annual air temperature of Sart-Tilman area (8.9 °C). Below this depth temperature increases with depth due to the geothermal gradient effect.
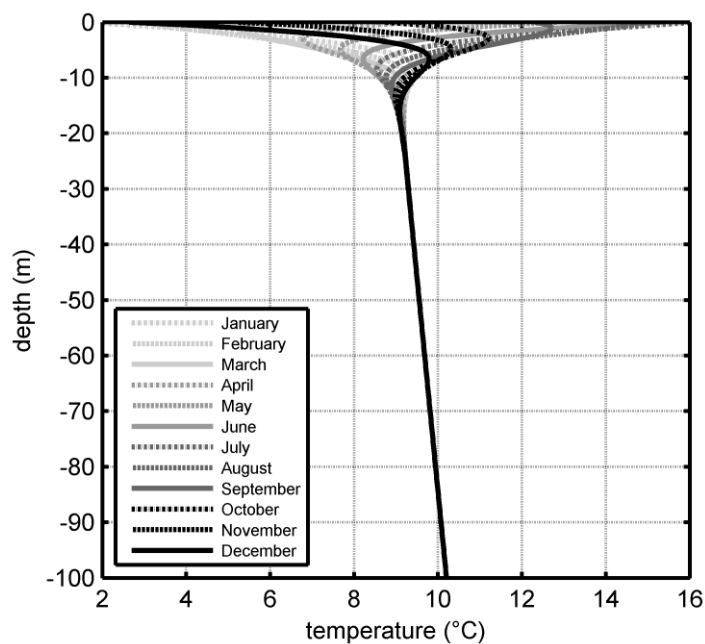

Figure 4.4 - Undisturbed ground temperature estimated analytically for the Sart-Tilman area

Based on the fiber optics measurements, the influence of the air temperature is also limited in the upper 18 m. However, at the depth of 18 m the measured temperature is 3 °C higher in the boreholes and 1 °C higher in the well than the corresponding analytically estimated temperature. Moreover, temperature decreases through depth in the four boreholes, opposite to the geothermal gradient effect. The higher than expected measured temperature and the negative temperature gradient could be attributed to the heating of the ground by structures located close to the BHEs and the well (a university building and a feeder pipe in this case study). This is further investigated by a 3D numerical model, presented in the next section, that takes into account the heat loss through the building basement and through the feeder pipe shell.

4.2.3 Numerical modelling: effect of urbanization

4.2.3.1 Geometry and boundary conditions

The 3D numerical model was developed by using the finite element code LAGAMINE (Charlier et al., 2001; Collin et al., 2002). It includes the influence of the feeder pipe, which is part of the heating network for the ULg campus in Sart-Tilman, and of building of the General Service of Informatics (SEGI). The feeder pipe, which has a minimum distance of 6.6 m from the boreholes and 27 m from the well, was simulated with a surface heating element. The heat loss (150 W/m length) was calculated based on temperature measurements inside the feeder pipes for the year 2011 (Sartor et al., 2014). The SEGI is located close to the boreholes at a minimum distance of 15 m. The heat loss through the foundations of the SEGI building was simulated by imposing a constant temperature through time (17.7 °C) at the whole building surface, as measured by temperature data loggers at the basement of the building.

The ground was simulated with 4-node 3D finite elements until a depth of 220 m, covering a surface area of 0.11 km² (80520 nodes). The applied ground thermal conductivity was estimated based on TRTs conducted in situ in the four BHEs (2.9 W/mK, Chapter 5) and the volumetric heat capacity was taken equal to 2300 kJ/m³K, based on literature values for the in-situ rock types (Smolarczyk, 2003; Nguyen and Lanini, 2012). The initial ground

temperature (before the presence of engineering structures) was estimated analytically, as presented in the previous paragraph, without taking into account the influence of the variation of the air temperature. The temperature at bare ground surface is influenced by several phenomena such us solar radiation, air convection due to wind and long wave radiation. The temperature under an asphalt pavement is also influenced by several factors including the thermal diffusivity and the thickness of the pavement layer, which usually displays a much lower thermal diffusivity than the ground in this case study. In this model, the simplified assumptions were made that at bare ground the temperature is constant through time, equal to the average annual air temperature, and that the ground surface under the pavement can be simulated by a no-heat-flux boundary condition. The computational time was 1.5 h (computer with main memory 16 G RAM, processor Intel I7) for an investigated period of 60 years (1970-2030).

4.2.3.2 Results and impact on the design

Figure 4.5 presents numerical results of the ground surrounding the four boreholes. The initial ground temperature (before the existence of structures, in 1970) is dominated by the geothermal gradient effect. The heating of the ground, through the pipe shell (150 W/m length) and through the SEGI basement (4 W/m² based on the numerical results) modifies the temperature gradient at the location of the boreholes until a depth of 100 m after 20 years (1990). The heating effect becomes progressively evident at greater depth, reaching a depth of 130 m after 45 years (2015). Moreover, the curvature of the temperature profiles is clearly evolving with time, with the increasing amount of heat added to the ground. The depth-average temperature of the ground which is not influenced by the weather conditions (below 18 m) increases at a mean rate of 0.03 °C/year for the first 45 years (1970-2015).
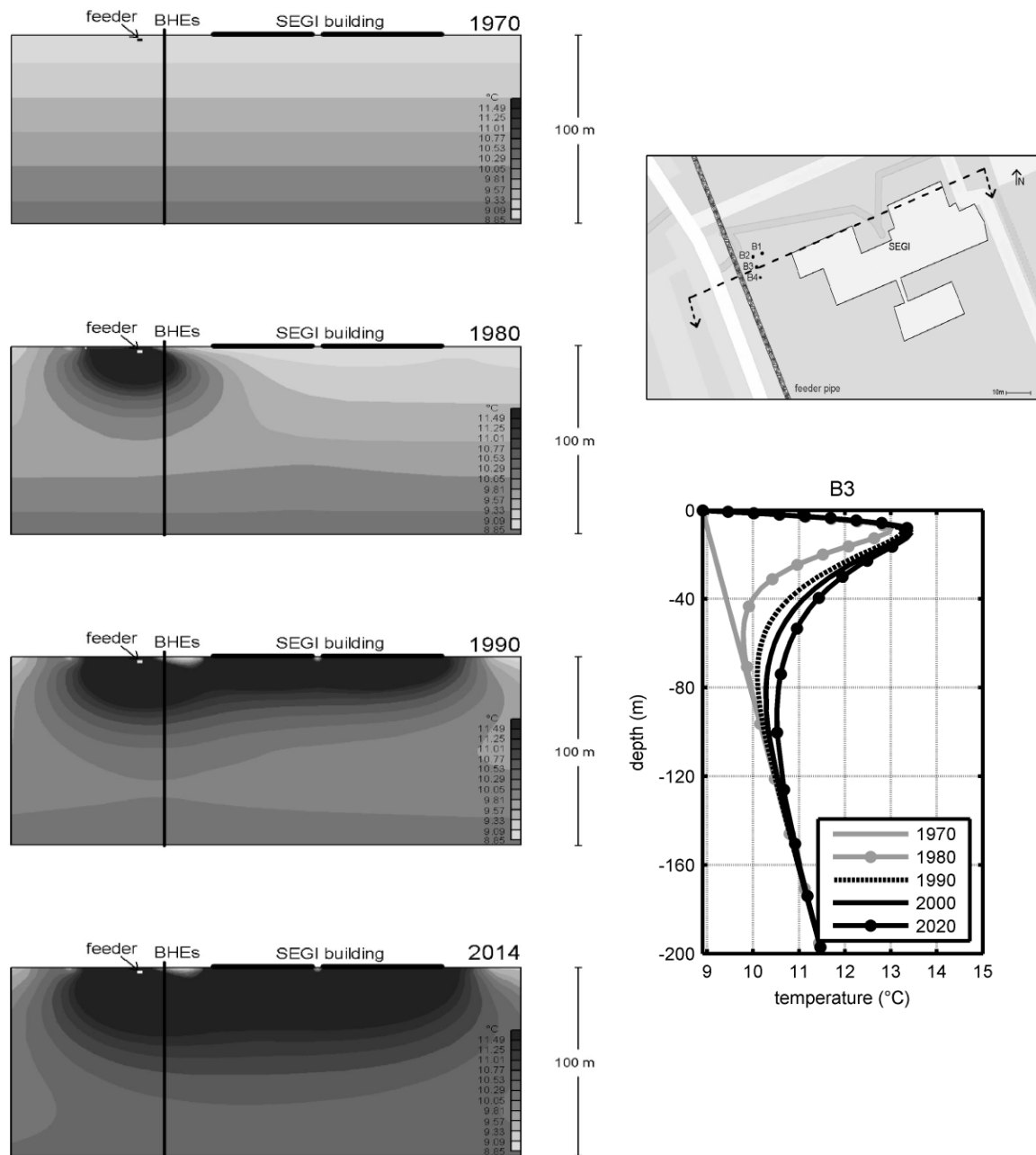
Figure 4.5 - Ground temperature field evolution based on the numerical results

Figure 4.6 shows temperature measurements and numerical results at the location of the four boreholes. Any quantitative comparison between the numerical and the fiber optic measurements is inconsistent for the upper 18 m, since the influence of the air temperature variation is not taken into account in the model and the mean ground thermal conductivity value applied in the model (TRT) may not be representative of the top ground layers (gravel

and sand). Based on a qualitative comparison among the four boreholes for this zone, B1 displays a lower temperature compared to the other three boreholes. This is also observed in the fiber optics measurements, as presented above in Figure 2. The lower temperature could be attributed to the distance of each borehole from the feeder pipe, which is located at an average depth of 2.5 m. Given that B2, B3 and B4 are 4 m closer to the feeder pipe than B1, the heat loss effect from the feeder pipe will be more enhanced in the location of theese three boreholes. Below 18 m, the temperature profile given by the numerical model is in good agreement with the experimental one. The numerical results satisfactory predict the depth-average temperature in the period 2013-2015 (mean overestimation of 0.11 °C). It should be noted that based on the numerical results the ground temperature increases at very low rate of 0.017 °C/year for the two-year measurement period. This low temperature increase is not clearly evident in the fiber optics measurements, given the short measurement period in combination with the accuracy of the fiber optic measurements (Chapter 3).
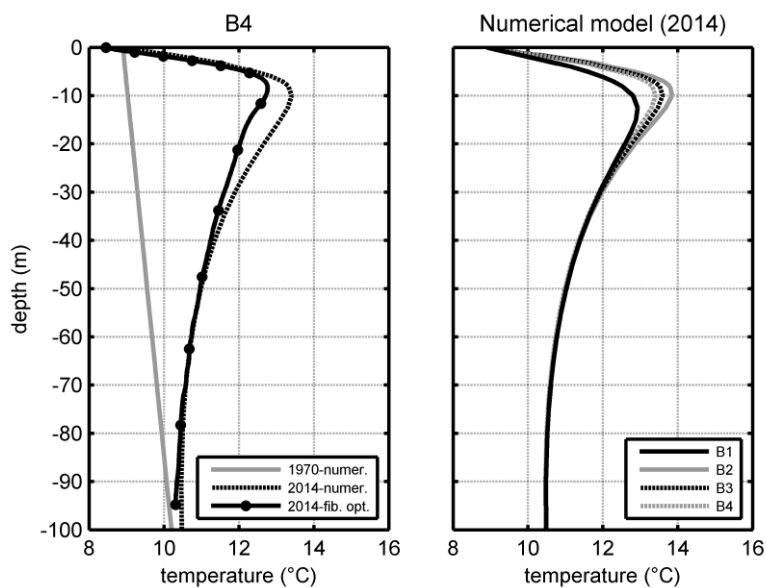
Figure 4.6 - Experimental and numerical results of the ground temperature at the location of the four boreholes

Figure 4.7 presents the numerical results and the temperature measurements in the well. According to the numerical results, the heat loss through the feeder shell modifies the temperature field at the location of the well, despite its great distance to the feeder (27 m). Below 20 m, temperature is almost invariant with depth and reaches a value of 10.1 °C in 2016. This is in good agreement with the measured temperature in the well for this depth.
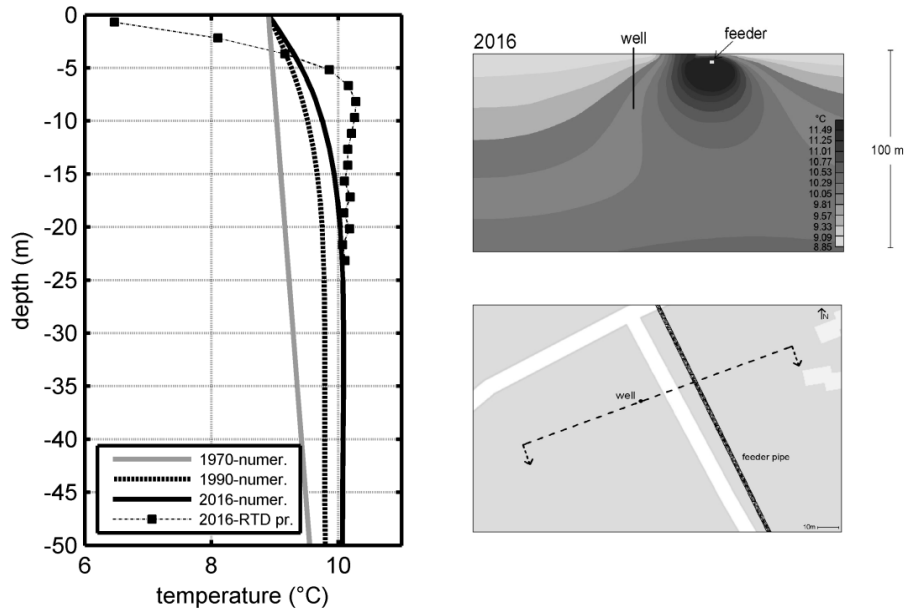
Figure 4.7 - Experimental and numerical results of the ground temperature at the location of the well

Given the good agreement between the temperature measurements and the numerical results, the measured temperature profiles can be attributed to the heat loss through the surrounding structures. According to MIS 3005 (Microgeneration Installation Standard), the extracted power per unit length of the BHE is to be limited by the undisturbed ground temperature. Table 4.1 shows the depth-average temperature at the location of the boreholes during time and the impact on the design. The maximum extracted power (W/m length of the BHE) was estimated based on the MCS 022 (MIS 3005) look-up tables for 1200 annual full load equivalent run hours of heat extraction, borehole thermal resistance of 0.1 mK/W, single U-pipe configuration and borehole spacing of minimum 6 m. The heat pump coefficient of performance (COP) was calculated as:

$$COP = \eta COP_c = \eta \frac{T_H}{T_H - T_C} \ ,$$

where η=0.5: the system efficiency,

COP_C: the theoretical maximum efficiency (-),

T_H=313.15 K: the temperature at the hot reservoir and

T_C: the temperature at the cold reservoir, i.e. ground, (K).

71

The maximum extracted power increases of 9% after 10 years of the feeder operation and 17% after 50 years, for a heating dominated system. The ground temperature increase has also a noticeable effect on the heat pump COP (increase of 6% after 50 years). These results indicate that heat loss through buildings and underground structures can have an important effect on the design of closed-loop systems since they continuously recharge the geothermal reservoir. Moreover, given that a negative temperature gradient is observed in urban areas, short BHEs could be economically advantageous (decreased drilling cost, higher COP) compared to long BHEs, contrary to areas where the undisturbed ground temperature is dominated by the geothermal gradient effect

Table 4.1 - Numerical results of the depth-average temperature evolution at the location of the BHEs, maximum extracted power and coefficient of performance of the heat pump

year	T_{avg} (°C)	Q_{extr}* (W/m)	COP**
1970	9.6	45.3	5.2
1980	10.5	49.3	5.3
1990	10.9	51.0	5.4
2000	11.1	52.0	5.4
2020	11.4	53.1	5.5

* MCS 022 (MIS 3005), 1200 FLEQ run hours
** n=0.5, T_H=40 °C

4.2.3.3 Representativeness of the model

In this model, the average annual heat loss through the feeder shell (150 W/m length) was assumed equal to the one of only one year (2011). The lack of measured data increases the uncertainty of the average annual heat loss for the investigated period of 60 years. Figure 4.8 (left) shows the influence of this parameter to the temperature at the location of the boreholes. The slope of the temperature profile and the depth-average temperature increase clearly with increasing heat loss. The temperature at the surface of the SEGI building was fixed equal to the one measured at the basement of the building during a few weeks in 2015. This could differ from the average annual temperature in the basement. Moreover, this temperature was assumed equal to the one at the interface between the basement's plate and the ground, without taking into account the plate's geometry and thermal properties. However, the

sensitivity analysis presented in Figure 4.8 (right) indicates that a more accurate simulation would not significantly modify the temperature profiles at the location of the boreholes.
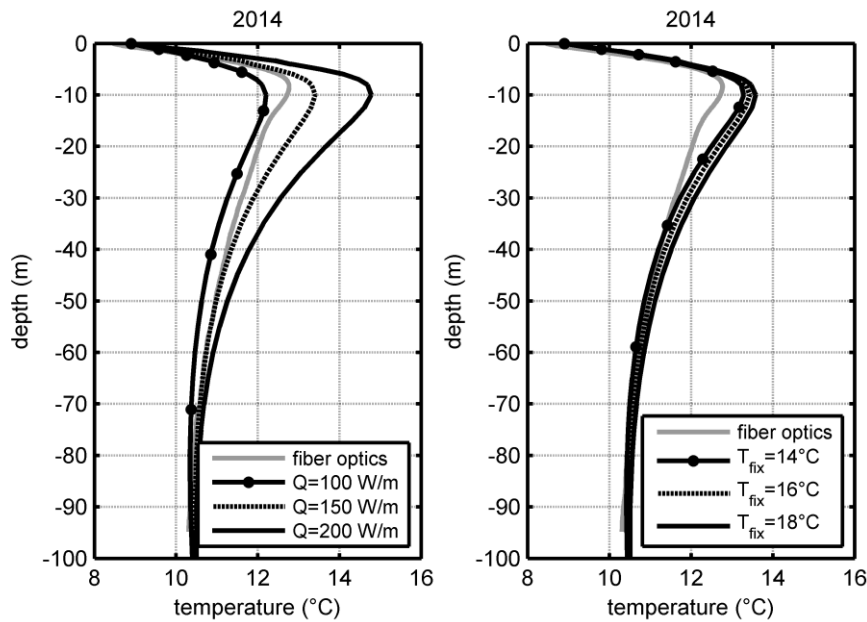

Figure 4.8 - Influence of the applied heat loss through the feeder shell (left) and of the fixed temperature at the SEGI surface (right) on the ground temperature at the location of the boreholes

In this model, the ground was considered homogeneous with an isotropic thermal behaviour. Simulating the different ground layers with varying thermal behaviour could modify the slope of the temperature profiles. Moreover, the boundary conditions applied at the ground surface are simplified without taking in to account wind convection effects, solar radiation effect and the geometry or thermal characteristics of the asphalt layers. The model could be improved by taking into accounts these effects in advanced boundary conditions. The variation of the air temperature through the year could be also included to simulate the temperature in the thermally unstable zone, which would be of high interest for horizontal closed-loop geothermal systems.

4.3 Temperature measurements during water circulation in the pipe loops

Apart from borehole logging, undisturbed temperature was also determined based on measured data during water circulation in the pipe loops. The BHEs pipes were connected to a rig which encloses the typical TRT equipment and insulation layers were attached around the connecting pipes, to minimize air temperature effects. The rig wall consists of a plastic

honeycomb plate and the pipes inside the rig were also insulated. Water was circulated inside the pipe loops, while temperature sensors were recording the water temperature at the entrance (pipe outlet) and at the exit of the rig (pipe inlet), as well as the air temperature inside and outside of the rig (Figure 4.9).
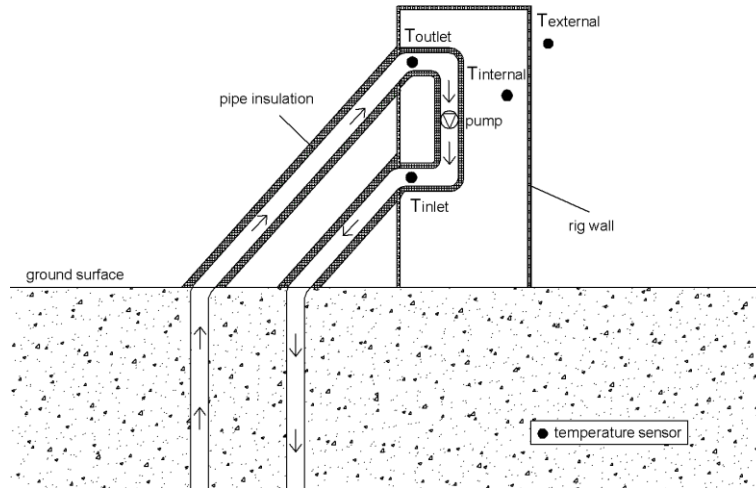

Figure 4.9 - Temperature sensors location during water circulation in the pipe loops

4.3.1 Temperature sensors measurements: impact of rig insulation

Figure 4.10 shows temperature measurements during water circulation inside the pipe loops in B1 and B2, conducted in summer (June 2014 and June 2015 respectively). In a perfect insulated system, the circulating water temperature would be invariant to the outside air temperature variations. The pipe-inlet and outlet water temperature would quickly adapt to the depth-average ground temperature and would remain constant with time, in the case that no significant heat is added to the water due to the pump work. Based on the measured data, the air temperature inside the rig follows the outside air variations and is an evidence for the heat transfer through the rig wall. This correlation is also displayed by the water measurements at the pipe inlet (rig exit), while the pipe-outlet (rig entrance) measurements seem less influenced by the air temperature variations. Moreover the temperature at the pipe inlet is higher than the one at the pipe outlet during the whole test duration, which indicates that heat is added to the water during its circulation inside the rig. The opposite effect is displayed in Figure 4.11, which shows temperature measurements for lower ambient air

74

temperature. In this case, water temperature decreases during its circulation inside the rig, for most of the test duration, which indicates that heat is transferred from the water to the air.
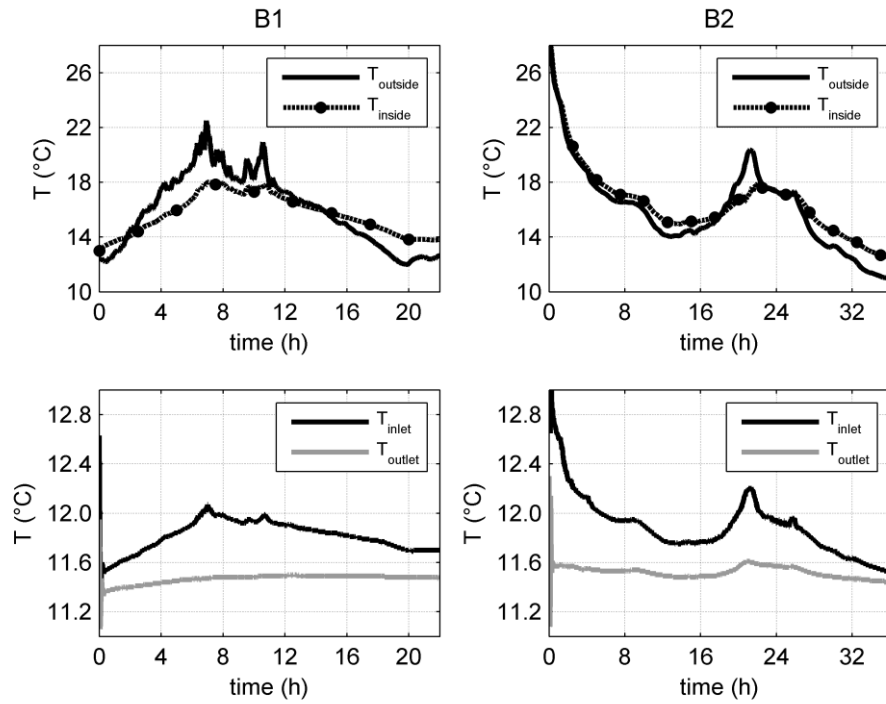

Figure 4.10 - Air (top) and water (bottom) temperature measurements during water circulation in B1(June 2014) and in B2 (June 2015)
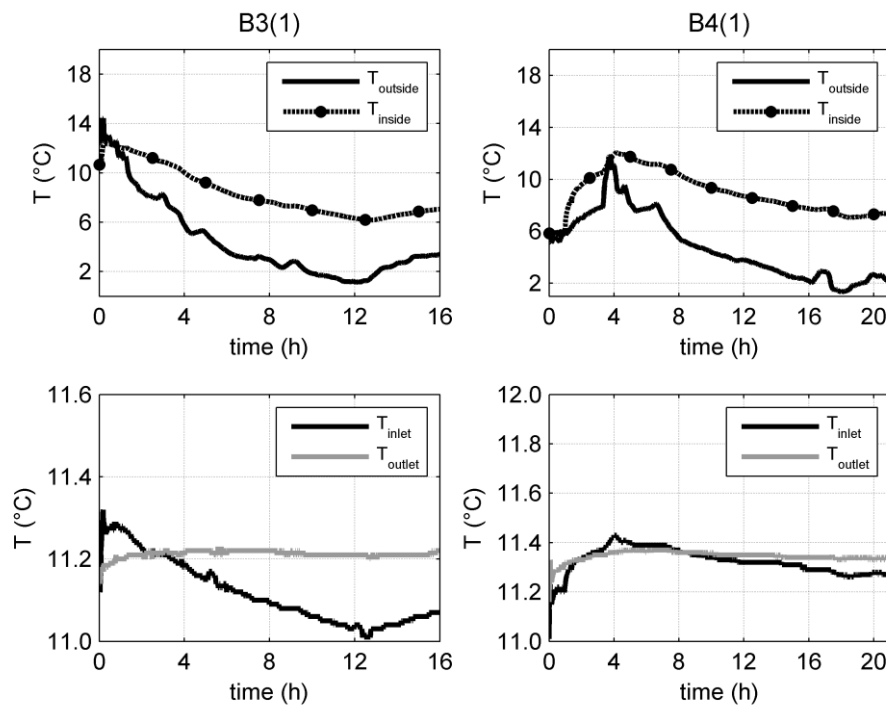

Figure 4.11 - Air (top) and water (bottom) temperature measurements during water circulation in B3 (March 2014) and in B4 (Nov. 2013)

The rate of the heat transfer from/to the water during its circulation inside the rig can be calculated from the convective heat transfer equation as:

$$q = \dot{m}c_p(T_{w,exit} - T_{w,entrance}),$$

where $\dot{m}$: the mass flow rate *(kg/s)*,

c_p=4.19 kJ/kgK: the specific heat capacity of water at 10 °C,

$T_{w,entrance}$: the temperature at the entrance of the rig (pipe outlet) and

$T_{w,exit}$: the temperature at the exit of the rig (pipe inlet).

The calculated heat transfer rate will be the result of the interaction with the air inside the module, as well as of the heat added to the water due to the pump work. Figure 4.12 shows the correlation of the heat transfer rate with the temperature difference $\Delta T = T_{air} - T_{w,entrance}$ for several tests. Figure 4.12 (top) compares data for approximately the same applied flow rate (ranging between 20 l/min to 22 l/min). A linear interpolation can be applied to the data of each test, $q = a\Delta T + b$, with small values of the constants b (-0.02 kW to 0.07 kW). In the case of positive temperature difference, heat is added to the water due to the interaction with the air, as well as due to the pump work. The interpolation lines are in good agreement with each other with a mean value of $q = 0.11\Delta T + 0.06$. Though extrapolation of this line for negative temperature difference is not representative of the measured data. In this case, heat is extracted from the water due to the interaction with the air, while heat is added to it due to the pump work. This could be the reason for the lower inclination of the interpolation line observed in the case of negative temperature difference. Figure 4.12 (bottom) displays the effect of the water flow rate on the heat transfer rate. Higher flow rate induces an enhanced convection, which is illustrated by an increase in the *a* coefficient of the interpolation line.
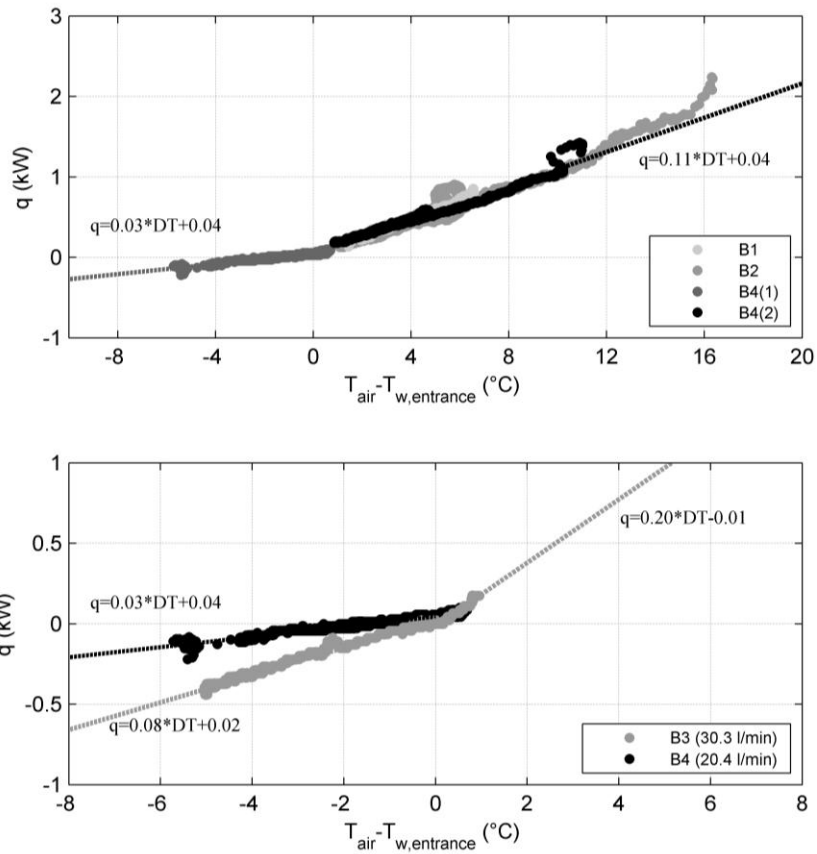
Figure 4.12 - Heat transfer rate during water circulation inside the rig, as a function of the temperature difference between the water entrance temperature and the air temperature inside the rig, for approximately the same applied flow rate (top) and for varying flow rate (bottom)

Despite the pipe insulation, the water measurements can be significantly influenced by the temperature air variations, which can result to an over or underestimation of the ground temperature. This can directly affect the design of BHEs, since the undisturbed temperature controls the maximum power to be extracted per unit length of the BHE (MIS 3005). Table 4.2 shows the maximum overestimation of the ground temperature based on the water measurements and the impact on the design. Reference values correspond to fiber optics measurements conducted at the beginning of the test, since the calibrated fiber optic profiles are not biased by ambient air temperature conditions (Chapter 3). The maximum temperature overestimation (1.7 °C) is observed in the case of B2 and corresponds to air temperature 18 °C higher than the ground temperature. This results in a significant overestimation of the maximum extracted power of 14%. These results indicate that insulating only the pipes is not sufficient for an accurate estimation of the ground temperature and highlight the importance of the test rig insulation to the test procedure.

Table 4.2 - Maximum overestimation of ground temperature during water circulation in the pipe loops and impact on the design

BHE	T_{ref} (°C)	Q_{ref} * (W/m)	T_{water}** (°C)	Q_{water} * (W/m)	$(Q_{water}-Q_{ref})/Q_{ref}$ (%)
B1	11.12	52.0	12.07	56.3	8.3
B2	11.18	52.3	12.91	59.7	14.1
B3 (1)	10.97	51.1	11.32	52.9	3.5
B3 (2)	11.17	52.3	11.90	55.6	6.3
B4 (1)	11.32	52.7	11.44	53.4	1.3

* MCS 022 (MIS 3005), 1200 FLEQ run hours
 **Maximum temperature after the first 5 min of circulation

4.3.2 Fiber optic measurements

Figure 4.13 presents temperature measurements by the fiber optics during water circulation in the pipe loops. A relatively constant temperature is quickly adopted along the whole length with a small negative temperature gradient of 0.005 °C/m, while the air temperature influence is limited at the top approximately 10 m. The negative gradient could be attributed to the ground heating due to the surrounding structures in combination with the low applied volumetric flow rate (~10.1 l/min in each U-pipe) during the test.
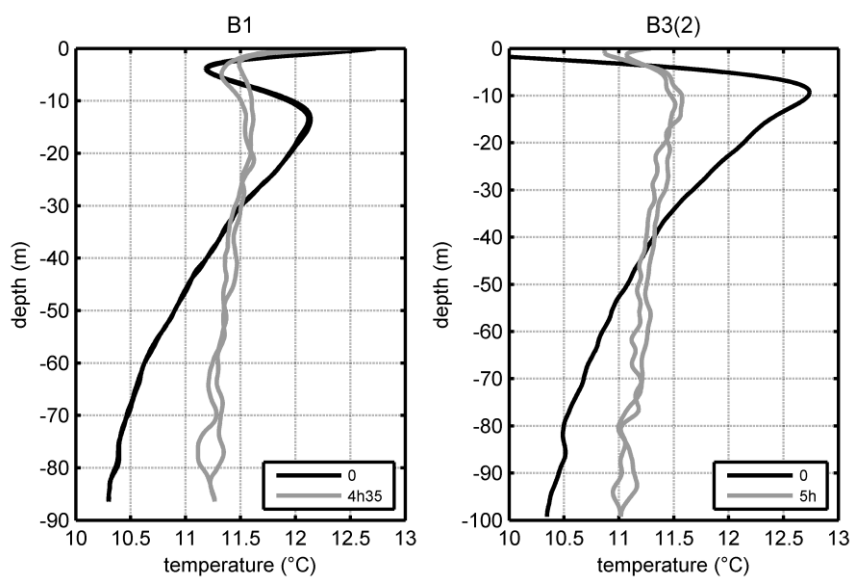

Figure 4.13 - Fiber optics temperature profiles during water circulation in the pipe loops in B1(June 2014) and in B3 (April 2014)

Figure 4.14 presents the depth-average temperature evolution for B3 and B4, considering the whole borehole length. The temperature measurements fluctuate around a mean value of 11.24±0.13 °C for B3 and 11.38±0.06 °C for B4. Calculating the depth-average temperature for a depth greater than 18 m (thermally stable zone) results in a slightly lower mean temperature of 0.03 °C for B3 and of 0.05 °C for B4. The measured profiles during water circulation are highly influenced by the water-ground interaction, minimizing the air temperature effects. These measurements provide a more accurate estimation of the ground temperature (overestimation less than 0.2 °C) than the pipe-inlet/outlet measurements, with no significant effect on the design. Temperature fluctuations are observed during the whole test duration, which might be partially attributed to the pump work and flow rate oscillations.
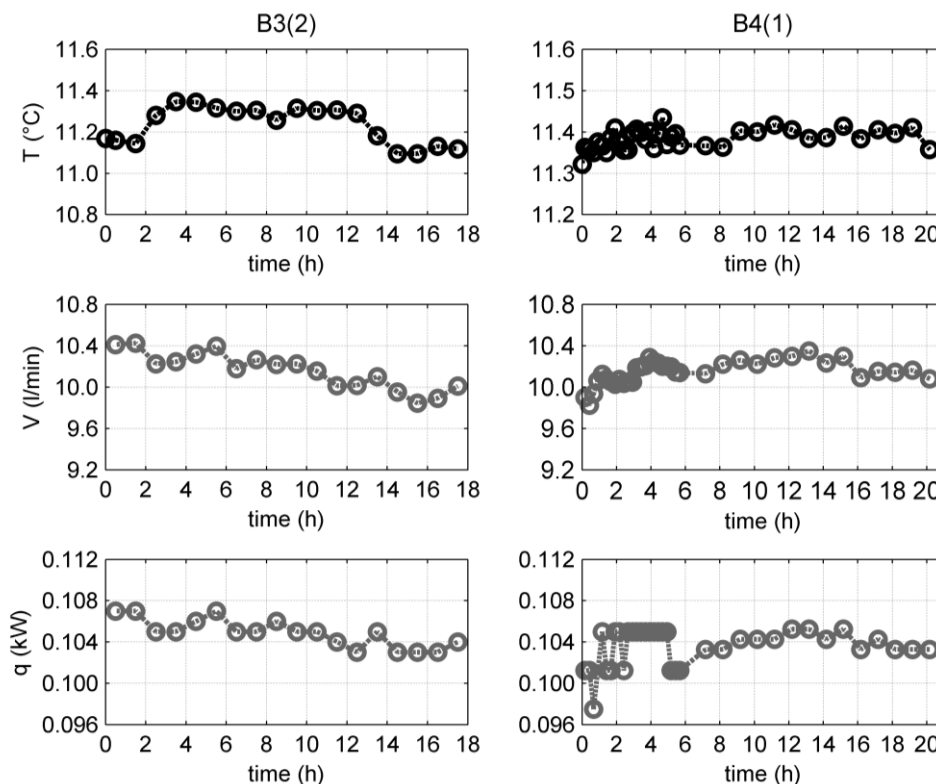

Figure 4.14 - Depth-average ground temperature (fiber optics) (top), average volumetric flow rate (middle) and average pump work (bottom) in B3 and B4

4.4 Conclusions

In this case study, the undisturbed ground temperature profiles are characterised by an elevated temperature and a negative temperature gradient. These profiles can be the result of

the ground heating by structures located close to the boreholes (feeder pipe at a distance of 6.6 m and a building at a distance of 15 m), as verified by the numerical model analysis compared to the analytical predictions. The heat loss into the subsurface, through the feeder pipe shell (150 W/m length) and through the SEGI basement (4 W/m²), has a significant effect on the maximum extracted power of the BHE and on the heat pump COP.

In urban areas, the heat loss through buildings foundations and underground structures (feeder pipes, sewage pipes etc.) recharges the geothermal reservoir. This is a continuous phenomenon which could significantly affect the design and the long-term behaviour of the geothermal systems. Taking this effect into account could contribute to a sustainable geothermal reservoir management in a city scale, as well as to an optimisation of the geothermal systems design. Configurations of short BHEs could be economically advantageous (decreased drilling cost, increased COP), by taking into advantage the negative ground temperature gradient caused by the urbanisation effect. The urbanization effect on the ground temperature could be revealed by temperature monitoring along the borehole length. Apart from fiber optic measurements, the temperature distribution through depth can be fairly obtained by lowering a temperature sensor inside the pipe and measuring the temperature at intervals. This is a cost-effective and easy to implement approach.

In BHEs, water circulation in the pipe loops allows to determine the depth-average ground temperature. The equipment's pipework is usually insulated to minimize air temperature effects. This study highlights the importance of the rig insulation for the accurate estimation of the ground temperature, based on measurements of five tests. Despite the pipe insulation, the measurements analysis indicates a heat transfer between the ambient air and the water during its circulation inside the rig. The maximum ground temperature overestimation is 1.7 °C and corresponds to air temperature 18 °C higher than the ground temperature. This results in an overestimation of the maximum extracted power of the BHE up to 14%.

Given the importance of the undisturbed ground temperature for the design of closed-loop systems, it is recommended to insulate not only the pipes but also the test rig. This allows to avoid a significant overestimation of the extracted power of the BHEs, in the case of high ambient air temperature. An underestimation of the extracted power could be also avoided in the case of low ambient air temperature.

Chapter 5: DTRT measurements analysis: impact of heat input oscillations, in-situ grouting thermal conductivity and bedrock heterogeneity detection

5.1 Introduction

The in-situ ground thermal conductivity, as well as borehole thermal resistance, are usually obtained in-situ by conducting a TRT. The typical equipment for a TRT (Gehlin, 2002) consists of a pump (to circulate the fluid inside the pipes), an electric resistance heater (to inject constant heat), temperature sensors (to measure the temperature) and a data logger (to record the measurements during the test). The equipment is connected to the BHE pipes and insulation layers are attached around the pipes to minimize the heat transfer between the circulating fluid and the air. Before starting the test, water is circulated at high flow rate to purge air from the system. After purging the air the first phase of the test starts. During this phase, water is circulated inside the pipe loop to achieve equilibrium between the water and the surrounding ground and to obtain the undisturbed ground temperature. The second phase consists of a continuous water circulation with usually constant heat input. After the heating period, the system is left to recover. During the test, temperature is recorded at the pipe inlet and outlet. The typical duration of the TRT is 50 h - 60 h, with proposed values in literature varying from 12 h to 60 h (Singorelli et al., 2007; Rainieri et al., 2011; Spitler and Gehlin, 2015).

Based on the measured data during the TRT, the mean thermal conductivity of the surrounding ground and the mean borehole thermal resistance can be calculated. The measured data are widely analysed by applying the simple, analytical solution of the ILS model, which requires a constant applied heat input during the test. In practise, variations in the applied heat input are observed, due to voltage variations in the supplied electricity and/or insufficient insulation of the test equipment, that allows a thermal interaction between the circulating fluid and the ambient air. This results in oscillations of the recorded fluid temperature profiles, that can affect the accuracy of the ILS results.

The importance of the test rig insulation during the heating phase of the TRT is highlighted in many studies in literature (Chapter 1, section 1.3.2). The duration of the TRT seems to be critical in this case. This chapter focuses on the heat input oscillations effect on the ILS model results. In particular, it is investigated if a longer duration, of several days or even weeks, could significantly improve the accuracy of the results when the ILS model is applied. Moreover, it is investigated, in the case of the typical applied duration (50 h - 60 h), which part of the measured data set should be chosen for the ILS interpretation in order to minimize the influence of the temperature oscillations and to improve the accuracy of the results.

TRTs allow to estimate the effective ground thermal conductivity including the influence of the in-situ conditions. However, the estimated value corresponds to the mean thermal conductivity of the ground surrounding the borehole. The detection of a varying thermal conductivity with depth is particularly important, since the detection of highly conductive zones will allow an optimization in terms of the required number and length of BHEs. DTRTs can significantly contribute to this end. During a DTRT, temperature is measured not only at the pipe inlet and outlet but also at different depths along the borehole, by temperature sensors or fiber optic cables installed inside the borehole. Temperature borehole logging during the recovery phase can also provide information on the variability of the ground thermal properties. A literature review on in-situ DTRTs and on borehole logging during the recovery phase in presented in Chapter 1 (sections 1.3.3.1 and 1.3.3.2). The present chapter presents an analysis of the DTRTs measurements, conducted in-situ in the four BHEs. Among others, it is studied if recovery profiles can provide information in the case that groundwater effects are not dominant and to which extent thin layers can be detected. The contribution of temperature borehole logging during hardening of the grouting material to the subsurface heterogeneity characterisation is also investigated.

This chapter is organised as follows. First, the temperature measurements inside the test rig are studied (typical TRT procedure). Oscillations in the applied heat input are correlated to air temperature variations, attributed to the insufficient test rig insulation (see also Chapter 4). A uniform heat input is a basic requirement of the TRT procedure, since the data are usually analysed by applying the simple, analytical solution of the ILS model. The influence of the heat input variation, for this case study, on the ILS model results is investigated, for which the evaluated data time window seems to be a critical factor. Moreover, the in-situ grouting

thermal conductivity is estimated by calibration with regard to the measured water temperature evolution (numerical modelling) and the results are compared to the values proposed by the producers. Then, the fiber optic measurements are studied, as well as the temperature evolution inside the borehole. Numerical results of the transient and steady-state phase are presented. Based on these results, comments on the observed oscillations of the fiber-optic profiles are provided. The required recovery time is estimated numerically as a function of the heating phase duration, for the given BHE geometry. Moreover, an analysis is proposed for detecting the possible ground heterogeneity and determining the layer dip angle, based on temperature profiles during the recovery phase and during hardening of the grouting material. Finally, basic conclusions are provided. A part of the work included in this chapter is also presented in Radioti et al. (2015a; 2015b; 2016a; 2016b).

5.2 Heat input oscillations effect on ILS model results

During the TRTs performed in this study, the connecting pipes were covered with a 2-cm thick insulation layer. The rig wall consists of a plastic honeycomb plate and the pipes inside the rig were also insulated. Temperature sensors were recording the water temperature at the entrance (pipe outlet) and at the exit of the rig (pipe inlet), as well as the air temperature inside and outside of the rig, at a time interval of 1 min.

5.2.1 Impact of test rig insulation

Figure 5.1 shows air and water temperature measurements during the heating phase of TRTs. The air temperature inside the rig follows the outside air variations and is an evidence for the heat transfer through the module wall. Moreover, the inside air temperature fluctuates between the water temperature and the outside air temperature for the whole tests duration. This is an evidence for the thermal interaction between the air inside the rig and the circulating water, which indicates the insufficient insulation of the pipework inside the rig. After the first 20 days of the test in B2, an insulation layer (expanded polystyrene of a few cm thick) was attached around the test rig. For this period, the air temperature inside the rig seems less influenced by the outside air variations than before. Though, this layer only limits

and not eliminates the outside air influence, as indicated by the agreement between the oscillations in the two air temperature profiles.
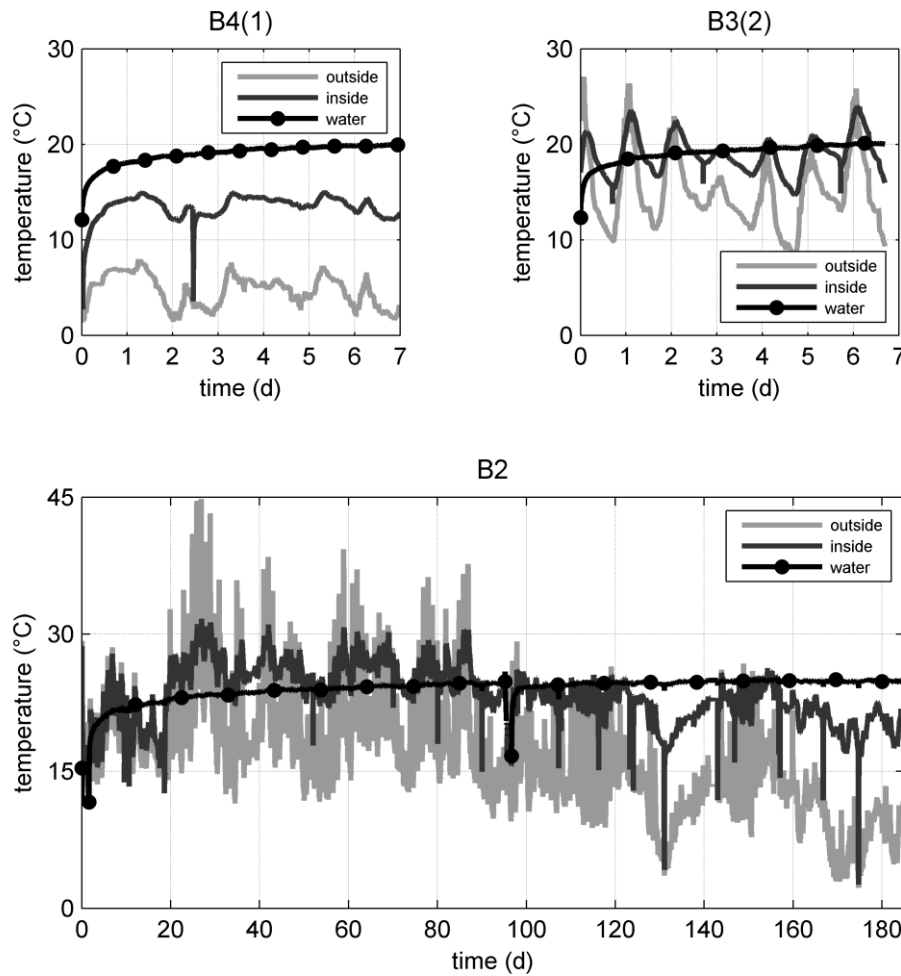

Figure 5.1 - Air and mean water temperature evolution during the heating phase of TRTs in B4 (Nov. 2013), in B3 (April 2014) and in B2 (June-Nov. 2015)

During the heating phase of a TRT, a constant electric power is applied inside the test rig. A part of the applied power is consumed by the pump, to circulate the fluid at constant flow rate (kinetic energy and energy loss due to friction). The remaining part is converted into heating power, via an electric resistance heating element, which is added to the fluid during its circulation inside the rig. Therefore, the nominal heating power is equal to the difference between the electric power and the one consumed by the pump, $q_{nom} = p_{electr} - p_{pump}$, and in a perfectly insulated system is applied as heat input in the BHE.

The actually applied heating power can be calculated from the convective heat transfer equation, as:

$$q_{appl} = \dot{m}c_p(T_{w,inlet} - T_{w,outlet}),$$

where $\dot{m}$: the mass flow rate *(kg/s)*,

c_p=4.19 kJ/kgK: the specific heat capacity of water at 10 °C,

$T_{w,inlet}$: the temperature at the pipe inlet (exit of the rig) *(°C)* and

$T_{w,outlet}$: the temperature at the pipe outlet (entrance of the rig) *(°C)*.

In the case of an insufficiently insulated system, the applied power can differ significantly from the nominal one. If air temperature is higher than the water temperature, heat is added to the water and the applied power is higher than the nominal one. In the opposite case, heat is extracted from the water and the applied power is lower than the nominal one. This results in a varying heat loss/gain during the test, which depends on the air temperature variations. This effect is illustrated in Figure 5.2, which presents power difference data for several tests. Heating power difference variations follow the outside air variations (Figure 5.2, top). The power difference increases with the temperature difference, $T_{air,out} - T_w$, and a linear interpolation can be applied to the data of each test, $q = a\Delta T + b$, with small values of the constants b (0.003 kW to 0.05 kW).
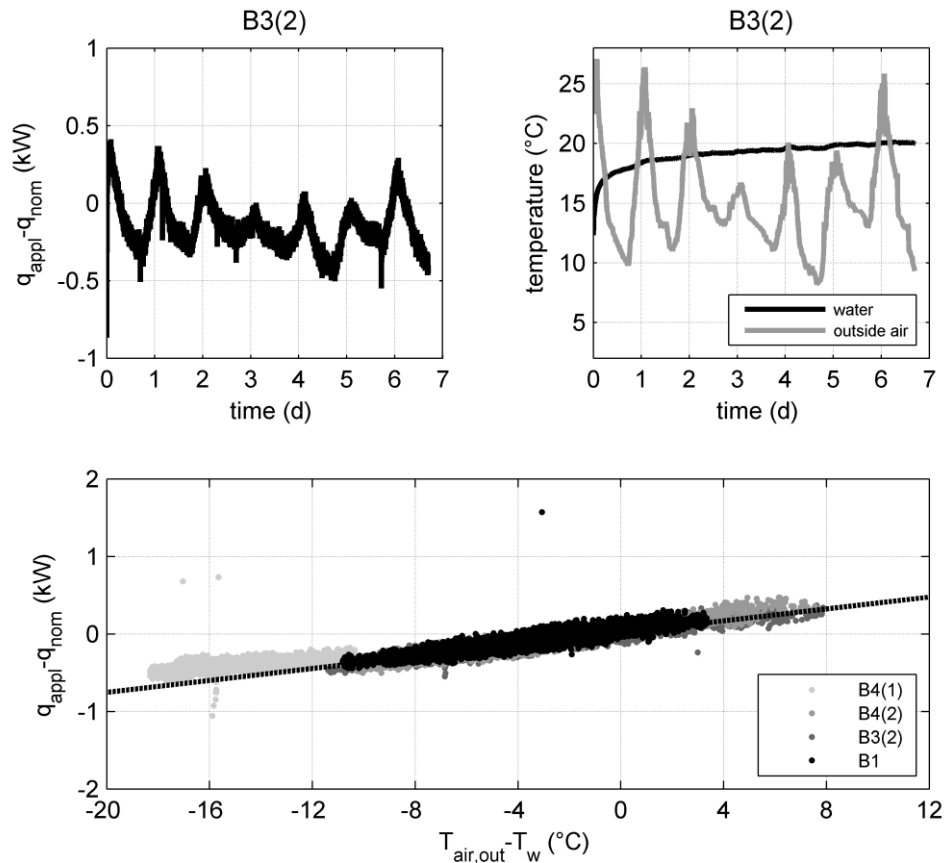
Figure 5.2 - Power difference between the applied and nominal power, as a function of the temperature difference between the mean water temperature and the outside air temperature

Table 5.1 compares the average nominal, $q_{avg,nom}$, and the average applied, $q_{avg,nom}$, heating power for several tests. The maximum power difference is in the order of 10% and corresponds to the lowest ambient air temperature (B4(1)). The coefficient of variation -ratio of standard deviation to the mean value- was calculated for each test. For the nominal power it varies between 1.6% and 2.1% and is attributed to voltage variations during the test. This effect could by minimized by using voltage regulators. Though, the coefficient of variation of the applied power is significantly higher, varying between 3.9% and 6.7%, being the result of air temperature variations in combination with the insifficient equipment insulation. These results highlight the importance of the equipment insulation for a steady heat input, a basic requirement for the TRT procedure.

Table 5.1 - Average nominal and applied heating power for in situ TRTs

TRT	$q_{avg,nom}$ (W/m)	$q_{avg,appl}$ (W/m)	$T_{air,outside}$ (°C)
B1	42.8±0.9	41.3±2.5	16.49±3.16
B2	41.4±0.8	39.5±2.6	15.62±5.62
B3 (2)	37.6±0.6	36.1±1.6	15.09±3.76
B4 (1)	39.0±0.7	34.9±1.4	4.69±1.62
B4 (2)	39.0±0.7	37.3±2.0	14.02±3.90

In B2, the test rig wall was insulated after the first 20 days. To investigate the contribution of this insulation layer, the heat input was calculated for data corresponding to time windows of 50 h (typical TRT duration). Figure 5.3 shows the effect of the wall rig insulation on the heat input variability. For non-insulated rig wall, the heat input variability is in the order of 25% of the air temperature variability, while the insulation layer limits it at 11% of the air temperature variability.
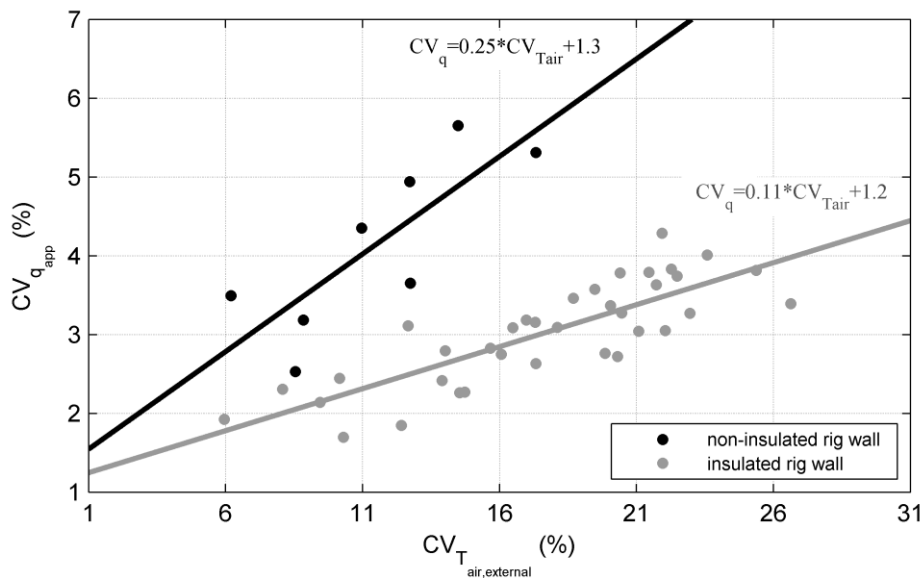
Figure 5.3 -Coefficient of variation (ratio of standard deviation to the mean value) of the applied heat input for insulated and non-insulated rig wall in B2 (data of 50 h time windows)

It should be noted that the BHE heat input is calculated based on water temperature measurements at the rig entrance and exit. This presupposes that the temperature of the water remains constant during its circulation inside the connecting pipes (sufficiently insulated

connecting pipes). During the test in B1, two RTD probes were attached underneath the insulation layer of the outlet connecting pipe: one at the ground level and one at the module entrance. The measurements are displayed together with the outside air temperature and the water temperature in Figure 5.4. The RTD measurements follow the air temperature oscillations. The maximum temperature difference along the outer surface of the pipe is 0.62 °C for air temperature lower than the fluid temperature and -0.78 °C for the opposite case. Though, it is observed that the fluid temperature does not follow the oscillations of the RTD and air temperature profiles, which indicates the significant contribution of the pipe material to the insulation of the system.

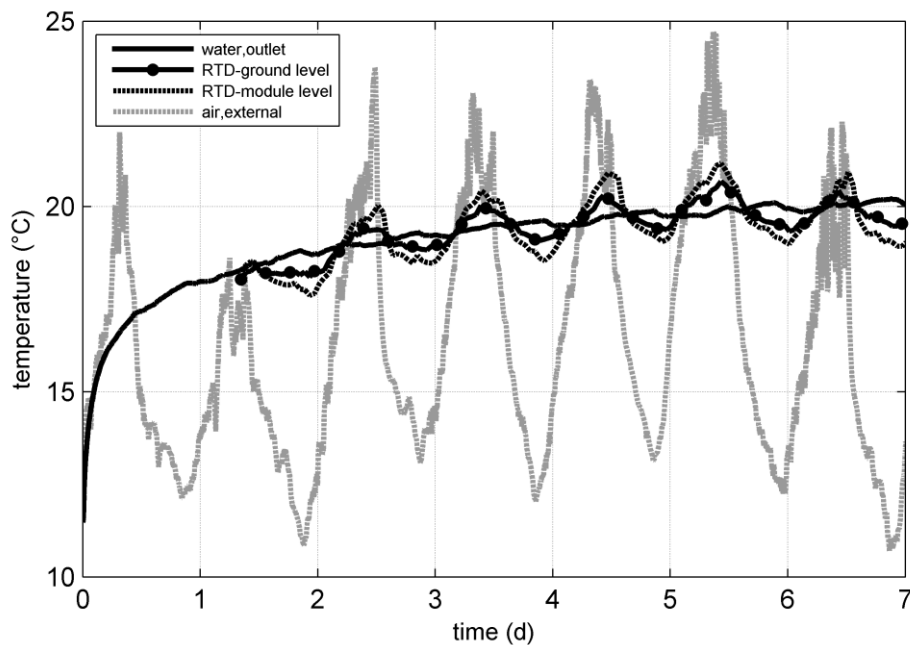Figure 5.4 - Temperature measurements during the TRT in B1: external air, water at pipe outlet, pipe outer surface at the ground level and at the module entrance

5.2.2 ILS model assumptions and limitations

This section focuses on the ILS model with regard to its applicability on the TRT data analysis. It presents the ILS model assumptions and summarises its limitations based on several studies from literature.

The ILS model describes the heat propagation in an infinite homogeneous medium subjected to a infinite line source embedded along the vertical axis. The line source injects constant heat continuously since time zero and heat flows by conduction in the surrounding medium in the radial direction. Carslaw and Jaeger (1959) give a simplified form of the line source solution for the temperature at time t and at distance r from the line source:

$$T(r,t) = \frac{q}{4\pi\lambda}\left[\ln(\frac{4at}{r^2}) - \gamma\right] + T_0 ,$$

where q: the heat flux per unit length produced by the infinite line source *(W/m)*,

λ: the thermal conductivity of the medium *(W/mK)*,

α: the thermal diffusivity of the medium *(m²/s)*,

$\gamma \approx 0.5772$ is Euler's constant and

T_0: the initial temperature of the medium *(K)*.

This simplified expression is valid for steady-state heat transfer conditions within the radius r and results to a maximum error of 2% for $\alpha t / r^2 \geq 5$ (Hellström, 1991). To apply this solution to BHEs, Mogensen (1983) introduces the borehole thermal resistance, R_b, and takes the mean fluid temperature, T_f, as the average of the pipe-inlet and outlet temperatures. By using the simplified line source solution the mean fluid temperature $T_f = (T_{inlet} + T_{outlet})/2$ can be described as (Wagner and Clauser, 2005):

$$T_f = \frac{q}{4\pi\lambda}\ln(t) + \left[qR_b + \frac{q}{4\pi\lambda}\left(\ln\frac{4\alpha}{r_b^2} - \gamma\right)\right] + T_0 ,$$

where r_b: the borehole radius *(m)*.

In this expression, the mean fluid temperature evolution is a line in a semi-log scale, $T_f = a\ln(t) + b$ (Figure 5.5). The mean thermal conductivity and the mean borehole thermal resistance can be calculated from the slope a and the constant b, respectively.
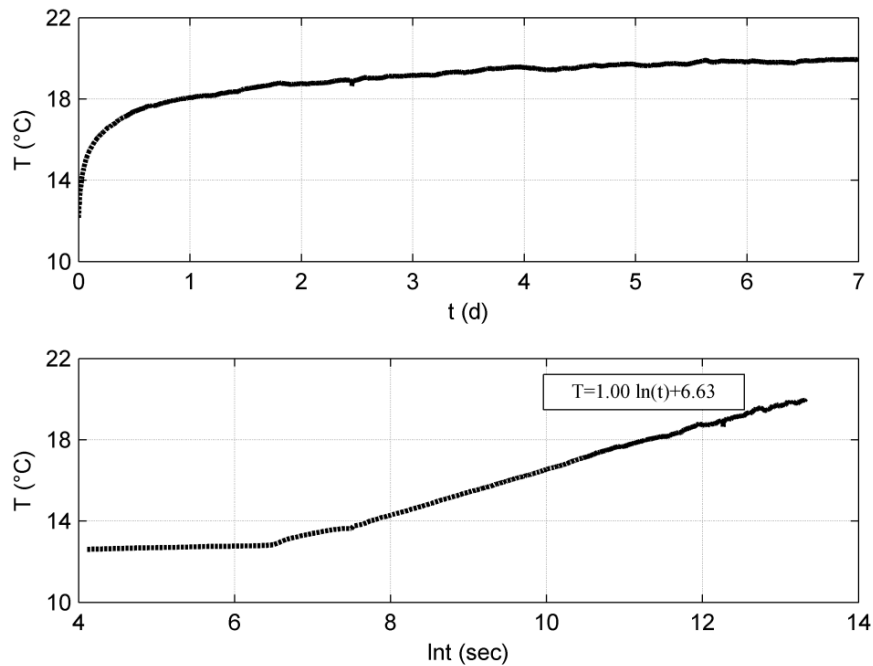
Figure 5.5 - Mean fluid temperature evolution during the heating phase of a TRT

The simplified ILS solution is valid for steady-state conditions inside the borehole, achieved after 1 h - 12 h of operation for normal borehole sizes and ground conditions (Spitler and Gehlin 2015). Before reaching the steady-state, the fluid temperature evolution is dominated by the borehole filling properties and, therefore, the corresponding data should not be included in the linear interpolation of the TRT data. Moreover, this solution is proposed for $t/r_b{}^2 \geq 5/\alpha$, derived from mathematical simplifications, indicating that the results are inaccurate for small distances from the borehole center and/or for short time periods. Other assumptions of the ILS model is the simulation of the BHE as an infinite long line and that the temperature distribution is radial, which indicate that the thermal effects at the ends of the borehole are negligible. Philippe et al. (2009) compared the ILS model with the Infinite Cylindrical Source (ICS) model, where the heat transfer rate is imposed at the borehole wall instead of its center, and the Finite Line Source (FLS) model, which can include the thermal effects at the ends of the borehole (Figure 5.6). For a typical borehole radius of 0.05 m, they calculated a difference between the ILS and ICS results of less than 10% after 10 h of operation, decreasing to 1% after 2.6 days. The thermal effects at the borehole ends become important after several years of constant heat transfer rate and for short BHEs. For example, the calculated borehole wall temperature by the ILS model was found overestimated of 5% after 6 years for a 50 m long BHE and after 30 years for a 100 m long BHE (α=0.53 10^{-6}

m²/s). They concluded that, for typical operational conditions, the maximum error in the borehole wall temperature based on the ILS model is 5% for time limits between 13 h to 18 years. In practice, the typical duration of the TRT is 50 h - 60 h, with proposed values in literature varying from 12 h to 60 h (Singorelli et al., 2007; Rainieri et al., 2011, Spitler and Gehlin, 2015). Considering the typical duration of the TRT and the results presented previously by Phillipe et al. (2009), the error of the ILS model interpretation associated with ends effect and the BHE dimensions will be limited. Singorelli et al. (2007) conducted numerically TRTs and analysed the results by applying the ILS model. They studied, among others, the effects of the test duration and of the ground heterogeneity, by comparing the analytically obtained thermal conductivity with the one assigned to the numerical model. For the investigated heterogeneous cases, the obtained thermal conductivity values were lower than the one of the homogenous case, with small differences for the different operation modes (heating/cooling). Though, all the cases (homogeneous and heterogeneous) resulted in an error less than 10%, for conduction dominated heat transfer. They proposed that a test duration of 50 h can provide a satisfactory estimation of the ground thermal conductivity, in the case that groundwater effects are not dominant.
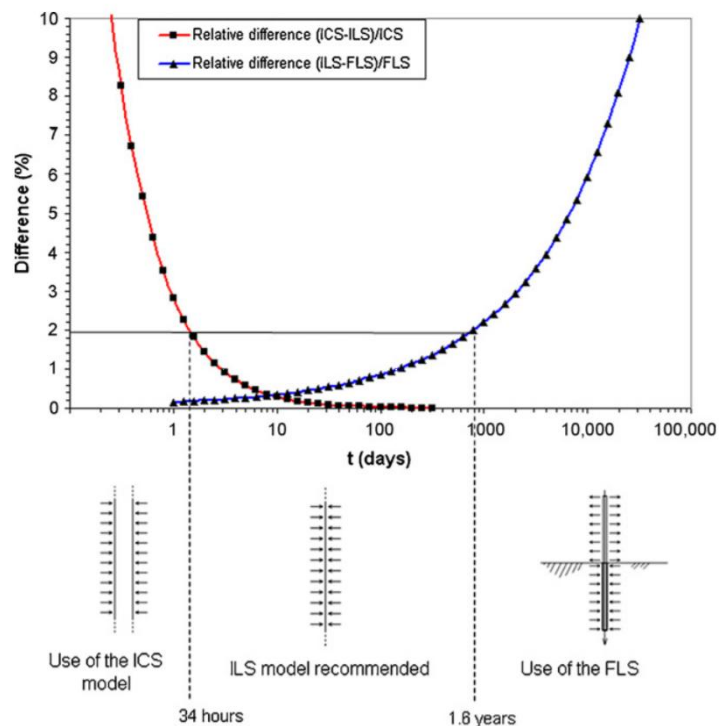

Figure 5.6 - Relative difference in borehole wall temperature between the Infinite Cylindrical Source (ICS), the Finite Line Source (FLS) and the Infinite Line Source (ILS) solution for typical operating conditions (Philippe et al., 2009©)

A constant heat input is a critical requirement for the application of the ILS model interpretation. In practise, variations in the applied heat input are attributed to voltage variations in the supplied electricity and/or to insufficient insulation of the test equipment, that allows a thermal interaction between the circulating fluid and the ambient air. This results in oscillations of the recorded fluid temperature profiles, that can affect the accuracy of the ILS results. Singorelli et al. (2007) interpreted the data of an in-situ TRT of a varying heat input. They estimated the ground thermal conductivity numerically, including the variations of the heat input, and observed that there was a correlation between the variations in the estimated thermal conductivity and the ambient air temperature variations. The average estimated thermal conductivity was equal to the one measured at the laboratory. Though, the ILS interpretation, by evaluating 24 h data windows and by assuming the 24 h average power supply, resulted in varying thermal conductivity with time, with an average value significantly lower (approximately of 15%) than the one estimated numerically. They concluded that there was not a clear definition on the choice of the part of the measured data to be evaluated, that would allow to improve the accuracy of the ILS results. Witte et al. (2002) conducted TRTs by fixing the temperature difference between the pipe inlet and outlet. This allowed to avoid heat input fluctuations due to unstable power supply. They showed that even a small influence of the ambient air on the fluid temperature (variation of ±0.15 °C) can have an important influence on the estimated thermal conductivity. They proposed that enhancing the insulation of the test equipment and controlling the temperature difference inside the borehole could limit the effect of the air-fluid interaction. Choi and Ooka (2016a) developed a quasi-steady analytical model, which takes into account insulation characteristics and the effect of various weather conditions. To limit the ambient air interaction effect, they recommended an insulation layer of more than 10 mm and retaining the connecting pipes as short as possible. Moreover, they showed that radiation effects can contribute significantly to temperature oscillations and recommended bright, reflecting materials for the insulation and the test equipment. In their study (Choi and Ooka, 2016b), they analysed statistically 36 numerical TRTs influenced by various weather conditions, interpreted by the ILS model. They recommended a minimum test duration of 60 h, to retain the ILS results error lower than 5%. They also proposed that the simplified ILS model interpretation should be avoided, in the case of short TRT duration combined with important radiation effects during the first day of the test.

5.2.3 Investigation for different data intervals

Thermal conductivity and borehole thermal resistance were calculated for the long-duration TRT data of B2, by applying the ILS model. The results presented hereafter correspond to the depth-average values of the effective ground thermal conductivity and borehole thermal resistance. A time window of 50 h was chosen for the evaluated data, equal to the typical TRT duration. The power was taken equal to the average power for each window. The results vary significantly with time, including negative values (Figure 5.7). A negative thermal conductivity value results from a negative slope of the interpolation line for the investigated data. This is attributed to temperature oscillations in theses time windows, due to the heat input variability, or to decreasing temperature due to decreasing heat input (Figure 5.8). Increasing heat input can result to stiff interpolation lines, $T_f = a\ln(t) + b$, with negative constants b and negative borehole thermal resistance values. The calculated values by this approach are quite sensitive to the heat input variations, since a basic assumption of the ILS model is a constant heat input. Moreover, the calculated slope sensitivity is increased for late time windows, since the temperature oscillations become more dense, as the x-axis corresponds to the natural logarithm of time. This effect can be limited by increasing the length of the chosen time window. Figure 5.9 presents the results for a significantly increased time window (20 d), where positive reasonable values are obtained for the ground thermal conductivity and the borehole thermal resistance.
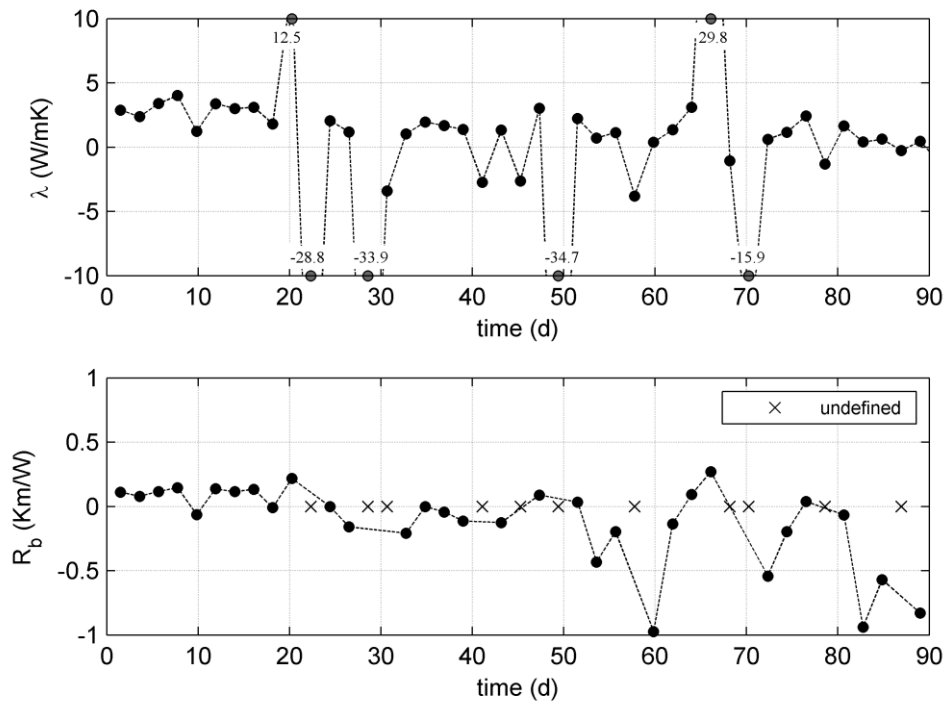
Figure 5.7 - Calculated ground thermal conductivity and borehole thermal resistance for data corresponding to time windows of 50 h in B2
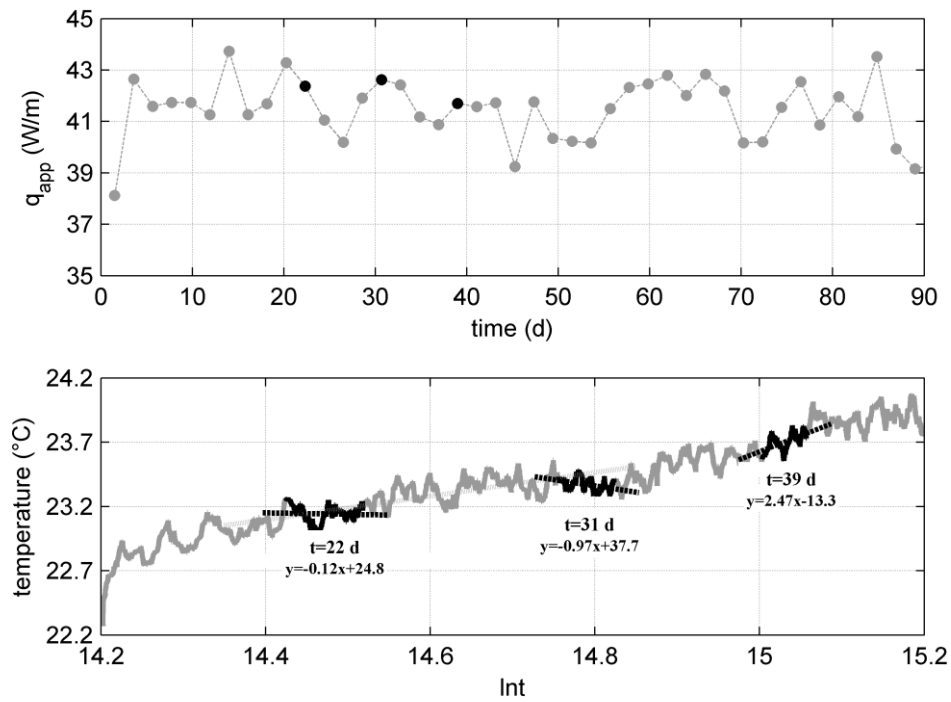

Figure 5.8 - Heat input and interpolation lines for data corresponding to time windows of 50 h in B2
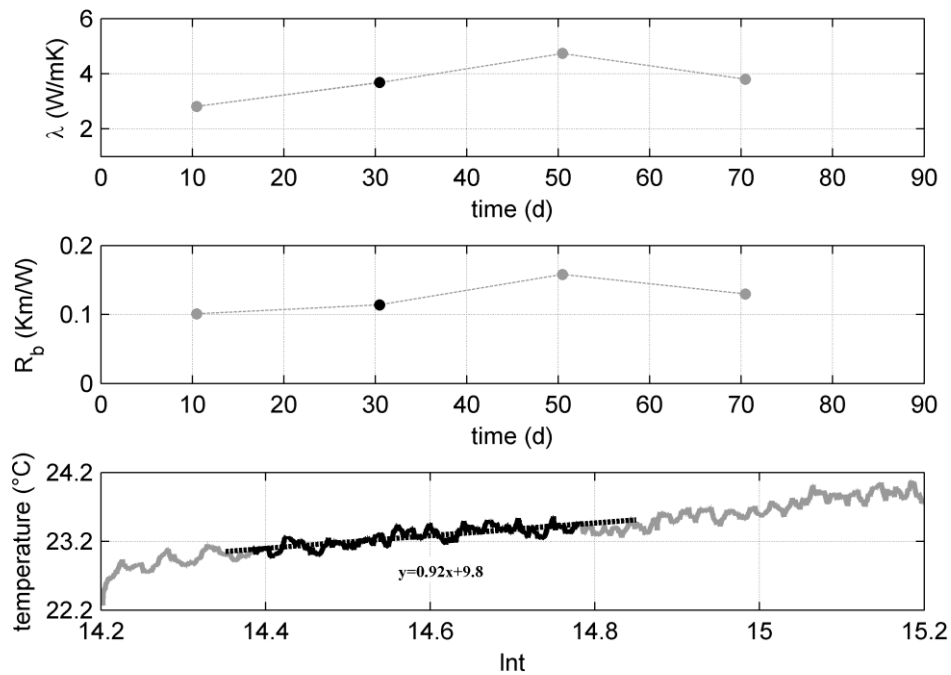
Figure 5.9 - Calculated ground thermal conductivity and borehole thermal resistance for data corresponding to time windows of 20 d in B2

For in-situ TRTs, the effect of the heat input oscillations could be limited by choosing early starting times and by increasing gradually the time window of the evaluated data. The choice of the starting time point is limited by the required time for the heat transfer inside the borehole to reach the steady-state phase. Moreover, it should fulfil the mathematical limitation of the simplified ILS formulation, $t \geq 5r_b^2/\alpha$, where r_b is the borehole radius (m) and α the ground thermal diffusivity (m^2/s). The ending time point increases gradually at a constant interval. The heat input is calculated likewise. The results are time-average values of the corresponding windows. This approach allows to decrease the sensitivity of the calculated slope to temperature oscillations. Figure 5.10 presents the calculated values by this approach for B2, where the x-axis shows the ending time point. The calculated thermal conductivity values vary less than 10% after the first 60 h of the test, and less than 3% after the first 10 d. The calculated borehole thermal resistance oscillates around 0.10 Km/W for the first 17 days, decreases progressively for the next 13 days and converges around a value of 0.085 Km/W for the rest of the time period. It is observed that the decrease of the thermal resistance, starting after 17 days, coincides with the increase of the calculated heat input. This is further investigated in the next section, where the TRT is simulated by a 3D numerical model.
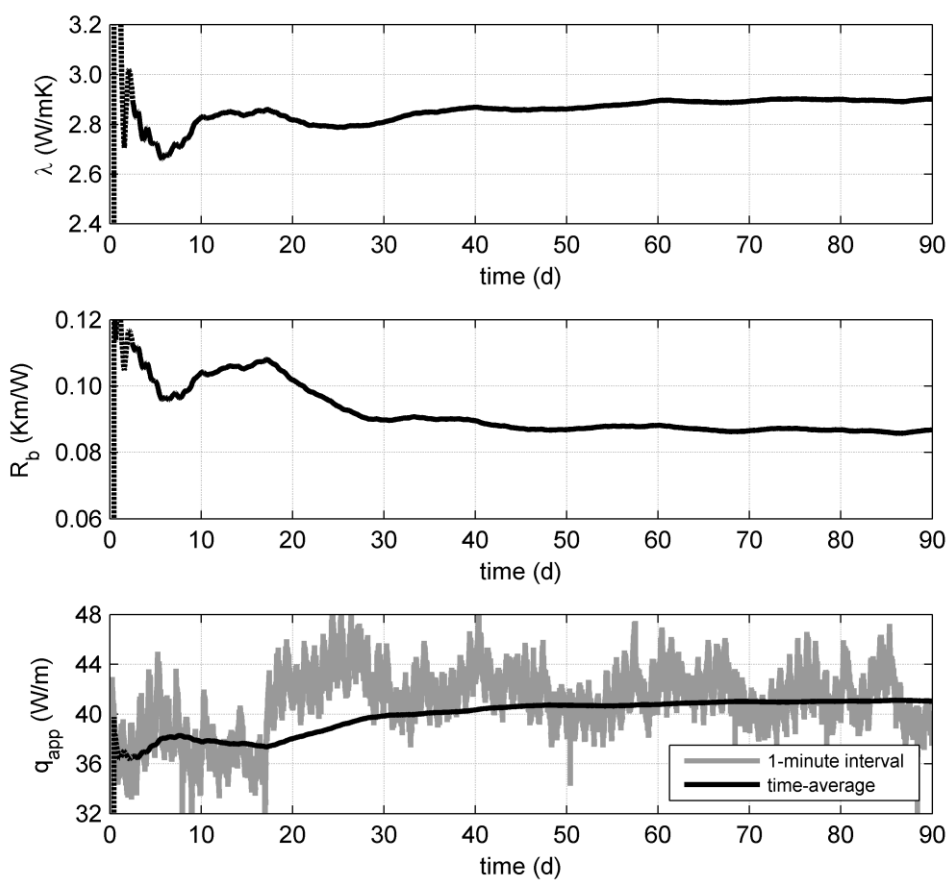
Figure 5.10 - Calculated ground thermal conductivity and borehole thermal resistance for increasing time window length in B2 (starting point at 10 h, ending point varying)

This technique was also applied for the 7-days duration TRTs in the other three BHEs. The results are presented in Figure 5.11, together with those of the first 7 days of the TRT in B2. Thermal conductivity vary less than 10% after the first 60 h for each test. Based on the values at the end of 7 days, the ground thermal conductivity is 2.88±0.16 W/mK. The proposed values were also verified by reproducing the measured temperature slope with numerical modelling, in the next section. Moreover, the convergence of the conductivity curves indicates the absence of a high groundwater flow.

B2 displays a higher thermal resistance compared to the other BHEs. This borehole was backfilled with a bentonite-based grouting material, of a lower thermal conductivity than the other three boreholes (Table 5.2). It should be noted that the proposed thermal conductivity values, presented in Table 5.2, correspond to a specific ratio of water to dry mortar. In-situ,

the admixtures were prepared with a higher water fraction, to decrease sufficiently the viscosity of the admixture and to achieve the flow through the injection pipe (diameter of 26 mm). This, among others, can result in a deviation from the proposed thermal conductivity values of the grouting material. The in-situ grouting thermal conductivity is estimated by calibration with numerical modelling in the next section. A discussion on the proposed and in-situ grouting thermal conductivity is also presented in this section. The presented borehole thermal resistance results correspond to the depth-average values. A local enlargement of the borehole radius, variation in the pipe legs distance or an heterogeneous grouting material can result to a variation of the borehole thermal resistance with depth. Finally, the borehole radius used in the thermal resistance calculation was based on the borehole televiewer measurements. In the case that these measurements are not available, the borehole radius could be assumed equal to the hammer bit radius. This results in a small underestimation of the depth-average borehole radius in the order of 5% and of the thermal resistance in the order of 3%, in this specific case study.
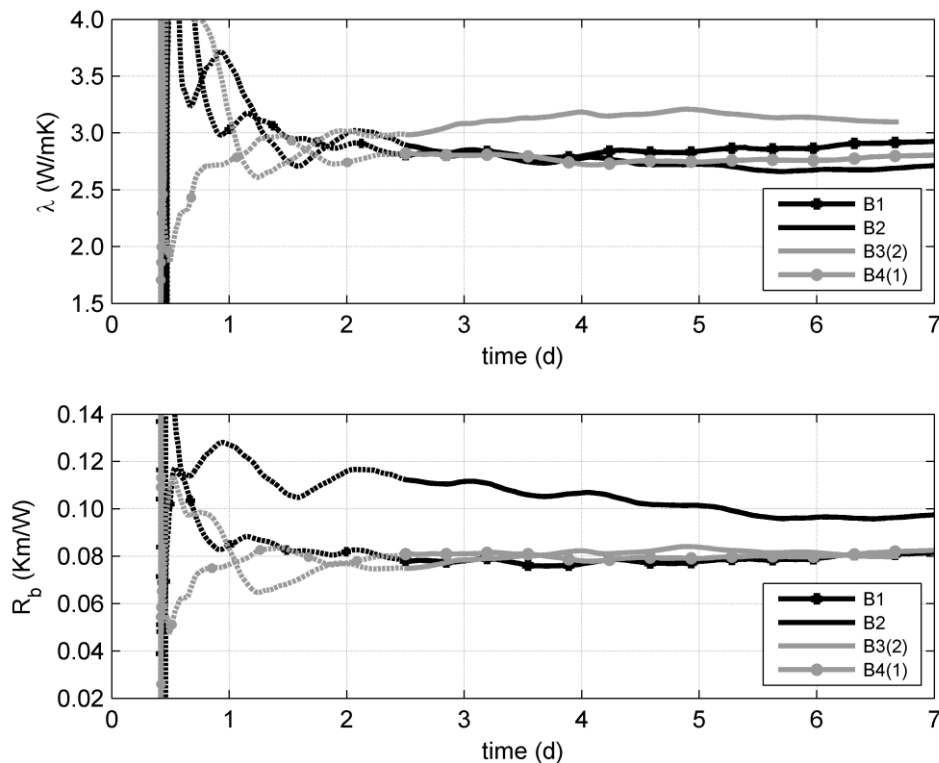

Figure 5.11 - Calculated ground thermal conductivity and borehole thermal resistance for increasing time window length in the four BHEs (starting point at 10 h, ending point varying)

Table 5.2 - Borehole thermal resistance for different grouting materials

BHE	grouting	λ_{grout} (W/mK)	water/mortar (l/kg)	R_b (Km/W)
B1	Geosolid (silica sand-based)	2.35*	0.25*	0.082
B2	Füllbinder (bentonite-based)	0.95*	0.6-1.0*	0.097
B3	Geosolid (silica sand-based)	2.35*	0.25*	0.080
B4	Homemade admixture with graphite	2.5**	0.35**	0.083

* handbooks   ** Erol and François (2014)

5.3 Calibration of in-situ grouting thermal conductivity by numerical modelling

According to the results presented in the previous section, the borehole thermal resistance of B2 starts to decrease after the first 17 d, which coincides with an abrupt increase in the heat input. Moreover, the grouting admixtures were prepared in-situ with a higher water fraction than proposed, which indicates that the estimated borehole thermal resistance of each BHE might not correspond to the proposed thermal conductivity value. The in-situ grouting thermal conductivity is estimated in this section by calibration based on numerical simulations.

5.3.1 Geometry and boundary conditions

To simulate the in-situ TRT, a 3D numerical model was developed by using the finite element code LAGAMINE (Charlier et al., 2001; Collin et al., 2002). The BHEs of approximately 100 m length were modelled with depth discretisation of maximum 5 m. The ground was extended 100 m below the borehole, covering a radial distance of 20 m. The generated mesh consists of 225000 nodes (4-node, 3D finite elements), including an explicit modelling of each BHE component. The flow into each pipe leg is represented by a 1D finite element, following the depth discretisation of the 3D mesh. Each node of this element interacts with a node at the center of the corresponding pipe leg of the 3D mesh (Figure 5.12).
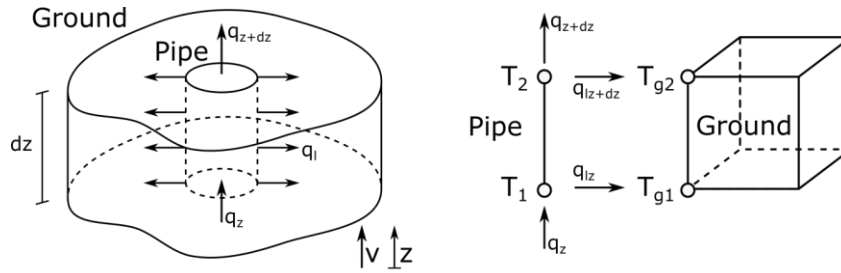
Figure 5.12 - Longitudinal qz and lateral ql heat fluxes between a piece of pipe and the ground (left) and discretisation of the problem with a 1D element (right)

In this model, the water temperature in each pipe cross section is assumed uniform. To insure this, a sufficiently high thermal conductivity and a zero volumetric heat capacity was assigned to the 3D water elements. Moreover, a fluid velocity and a convective heat transfer coefficient was imposed on each node of the 1D finite elements, to simulate the longitudinal and the lateral heat flux respectively. The convective heat transfer coefficient, h, is calculated as:

$$h = Nu \cdot \lambda / D_h \ ,$$

where D_h : the hydraulic diameter of the pipe *(m)*,
λ : the fluid thermal conductivity *(W/mK)* and
Nu: the Nusselt number *(-)*.

The Nusselt number is the ratio of convective to conductive heat transfer across a boundary and for turbulent flow is given as (Gnielinski, 1976):

$$Nu = \frac{(f/8)(\mathrm{Re}-1000)\mathrm{Pr}}{1+12.7(f/8)^{1/2}(\mathrm{Pr}^{2/3}-1)}, \qquad \begin{array}{l} 0.5 < \mathrm{Pr} < 200 \\ 3000 > \mathrm{Re} > 5E6 \end{array}$$

This relationship depends on the Reynolds number, *Re*, the Prandtl number, *Pr*, and the Darcy friction factor, *f*. The Reynolds number is the ratio of inertial forces to viscous forces and classifies the flow as laminar, transient or turbulent. It is described as:

$$\mathrm{Re} = \frac{\rho u D_h}{\mu},$$

where ρ: the fluid density *(kg/m³)*,

u: the mean fluid velocity *(m/s)* and

μ: the fluid dynamic viscosity *(Pa s).*

The Prandtl number is a measure of diffusion with respect to the fluid velocity, defined as:

$$\mathrm{Pr} = c_p \mu / \lambda ,$$

where c_p: the fluid specific heat *(J/kgK).*

The Darcy friction factor is defined, for smooth pipes, as:

$$f = (0.79 \ln(\mathrm{Re}) - 1.64)^{-2} .$$

To represent the continuity of the pipe at the bottom of the pipe legs, the temperature of the upward node at this depth was imposed equal to the calculated one at the downward node. The same condition was also applied at the top of the borehole, to represent the pipe loop formed by the TRT rig equipment. A heat flux was imposed as boundary condition at the inlet surface of the pipe, to simulate the injected heat during the TRT (Figure 5.13). These boundary conditions do not include an explicit modelling of the connecting pipes geometry or of the water thermal interaction with the ambient air during its circulation inside the rig. Though, the latter is taken into account in this model, by imposing the applied, and not the nominal, thermal power at the pipe inlet. For the short-duration tests (in B1,B3 and B4), the applied thermal power was taken constant with time, equal to the time-average thermal power of each test.
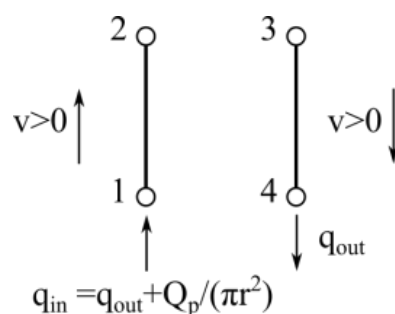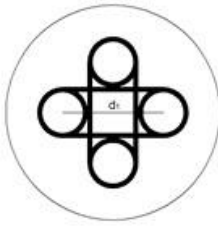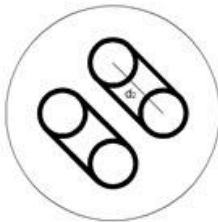

Figure 5.13 - Boundary condition between two vertical finite elements of pipe

The proposed pipe finite element is specially devoted to the modelling of the 1D advection-diffusion problem. The use of Petrov-Galerkin weighting functions reduces instabilities classically encountered. Consequently, higher time steps may be used and the computation time is strongly decreased. For example, for this model of 225000 nodes, the computational time was 1.5 h for a simulation of a 7-days TRT (computer with main memory 16 G RAM, processor Intel I7). Moreover, the 1D finite element formulation models the flow into the pipes without taking into account the grouting effect. This, in combination with its coupling with a 3D mesh, makes it suitable for reproducing temperature gradients inside the borehole for varying BHE configurations, avoiding any hypothesis on the borehole thermal resistance. Finally, imposing the total heating power as boundary condition at the pipe inlet, and not distributed along the pipe length, allows to calculate the possible varying heat transfer rate through depth. This is particularly important in the case of an anisotropic thermal behaviour of the surrounding ground. A detailed description and validation of the 1D finite element formulation can be found in Cerfontaine et al. (2016), presented in Appendix B.

Table 5.3 presents the material thermal properties and the BHE configuration applied in the numerical model. All the materials, including the surrounding bedrock, are assumed homogenous media. The assigned borehole radius (r=0.068 m) is equal to the corresponding depth-average value based on the borehole televiewer measurements. The variation of the borehole radius with depth was not simulated in this model. The relative position of the pipes inside the borehole was taken equal to the one measured in-situ, since spacers were not used during the installation procedure. A uniform initial temperature (11 °C) was assumed for the whole model domain and no-heat flux boundary conditions were applied at the boundaries of the model.

Table 5.3 - BHE geometry and materials properties for the numerical modelling

r_{bor} (m)	0.068
$r_{p,inner}$ (m)	0.0131
$r_{p,outer}$ (m)	0.016
d_1 (m)	0.064
d_2 (m)	0.045

	pipe
λ (W/mK)	0.42*
ρc_p (kJ/m³K)	2083*

*handbooks

	Geosolid	Füllbinder	Hom. admixture with graphite	ground
ρc_p (kJ/m³K)	1600*	2500**	2550***	2300****

*handbooks **Delaleux (2012) ***Erol and François (2014)
****Smolarczyk (2003), Nguyen and Lanini (2012)

5.3.2 Results and comparison with proposed values

The ground thermal conductivity resulting from the ILS model analysis, was assigned to the ground finite elements for each test. These values can fairly reproduce the temperature slope of the experimental data in each test. The grouting thermal conductivity was then estimated by fitting the experimental water temperature curve. This estimation is based on the assumption that the in-situ BHE geometry (borehole radius, relative position of the pipe legs inside the borehole) is fairly reproduced in the numerical model. Figure 5.14 compares the experimental with the numerical results by this approach. Oscillations in the measured temperature profile are attributed to the varying heat input. These oscillations are not reproduced numerically, since a constant heat input was applied for the numerical analyses, equal to the time-average heat input.
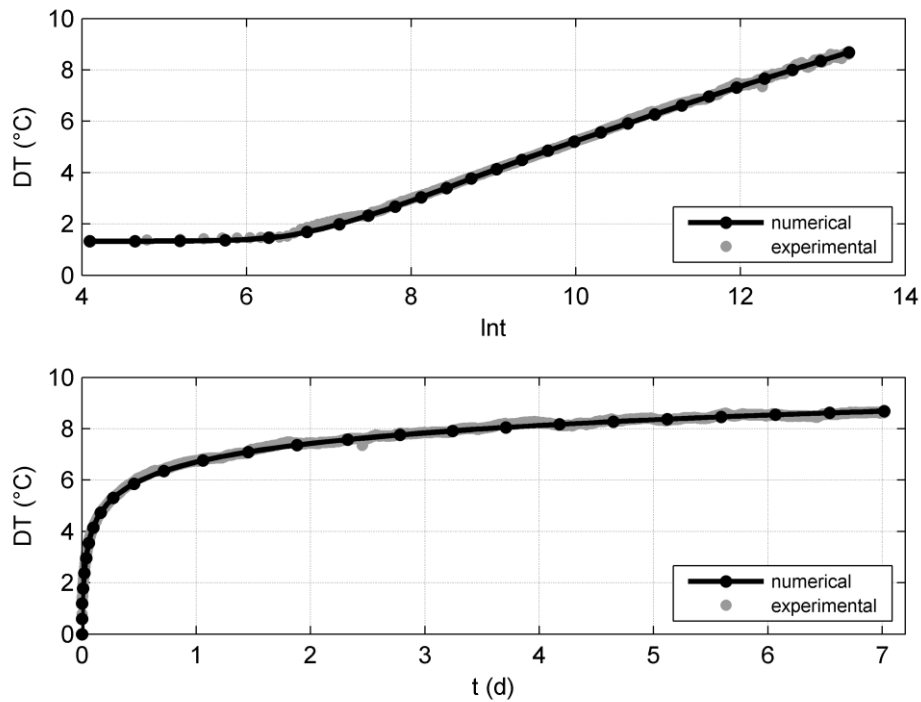
Figure 5.14 - Experimental and numerical water temperature evolution during the heating phase of B4(1) (λ_{ground}=2.8 W/mK, λ_{grout}=1.7 W/mK)

Table 5.4 shows the numerical results of the grouting thermal conductivity together with the proposed values by the producers for 7-days TRTs in the four BHEs. According to the numerical results, thermal conductivity is significantly lower (more than 20%) than the proposed one in B1,B3 and B4. The proposed values are based on cured samples of a given density. In-situ, the admixtures were prepared with a higher water fraction, which can result to a lower density and hence a decreased effective thermal conductivity. Moreover, air bubbles trapped inside the grouting could also contribute to a decrease of the thermal conductivity. The accuracy of the estimated values depends on the representativeness of the model regarding the BHE geometry. Any deviation from the assigned geometry (e.g. borehole radius, relative position of the pipe legs inside the borehole) would affect the borehole thermal resistance and therefore the estimated grouting thermal conductivity by this calibration process.

Table 5.4 - Grouting thermal conductivity proposed by the producers and by calibration with numerical modelling

BHE	grouting	λ_{pr} (W/mK) water/mortar (l/kg)	λ_{num} (W/mK) water/mortar (l/kg)[***]
B1	Geosolid (silica sand-based)	**2.35**[*] 0.25[*]	**1.7** 0.36
B2	Füllbinder (bentonite-based)	**0.95**[*] 0.6-1.0[*]	**1.0** 1.1
B3	Geosolid (silica sand-based)	**2.35**[*] 0.25[*]	**1.8** 0.36
B4	Homemade admixture with graphite	**2.5**[**] 0.35[**]	**1.7** 0.70

[*] handbooks [***] in-situ
[**] Erol and François (2014)

Based on the forward regression analysis for B2, the borehole thermal resistance starts to decrease after 17 days, which coincides with an abrupt increase in the heat input. This was investigated by numerical modelling including the heat input increase. The results are presented in Figure 5.15. The applied heat input is 3.6 kW for the first 17 days and 4.0 kW for the rest, taken as time-average values of the corresponding time periods. First, a grouting thermal conductivity of 1.0 W/mK was applied for the whole test duration. The numerically obtained temperature evolution fits well the experimental data for the first 17 days. At 17 days temperature increases of 1 °C, following the applied heat input increase of 0.4 kW. Though, this is not displayed in the experimental data. To fit the experimental data after 17 days, a grouting thermal conductivity of 1.6 W/mK was applied for this period. Based on the good agreement between the experimental and the numerical results, the sudden change in the grouting thermal conductivity could be associated with the sudden increase of the heat input. This increase occurs in a time window of 10 h at a rate of 140 W/h. A sudden temperature change in the grouting mass could result in a thermally induced cracking and, hence, in a modification of its effective thermal conductivity. Though, in this case study, this seems quite improbable since an increase of 140 W/h results in a relatively low temperature increase rate of 0.25 °C/h, based on numerical results. Moreover, cracks in the grouting mass filled with air (λ_{air}=0.025 W/mK) or water (λ_{water}=0.58 W/mK) would result in a decrease and not an increase of the effective thermal conductivity, in the case that convection effects are not dominant.
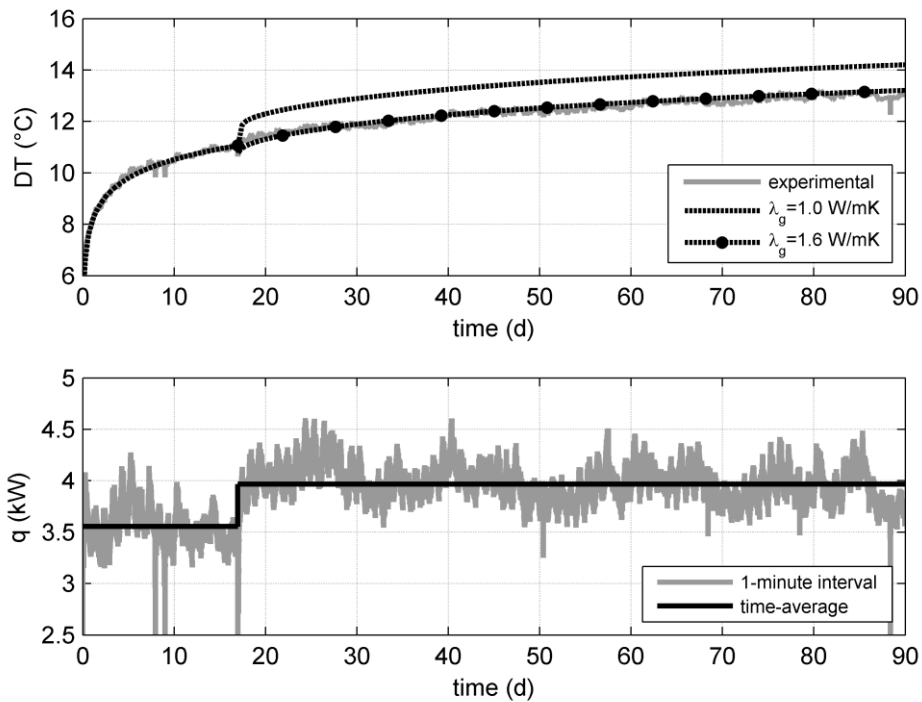
Figure 5.15 - Experimental and numerical mean water temperature evolution for varying grouting thermal conductivity in B2

Figure 5.16 shows numerical results for a varying heat input and a constant grouting thermal conductivity of 1.0 W/mK during the period of the 90 days. The numerically obtained temperature evolution fits the experimental data. Moreover this value of the grouting thermal conductivity allows to reproduce the experimental data during the whole interrupted heating phase and the recovery phase in B2 (total duration of 13 months), as presented in the next chapter. These results indicate that the calculated decrease of the borehole thermal resistance by the ILS model analysis is attributed to the sensitivity of this model to abrupt changes in the heat input and highlights the importance of the heat input variations simulation on the TRT data analysis.
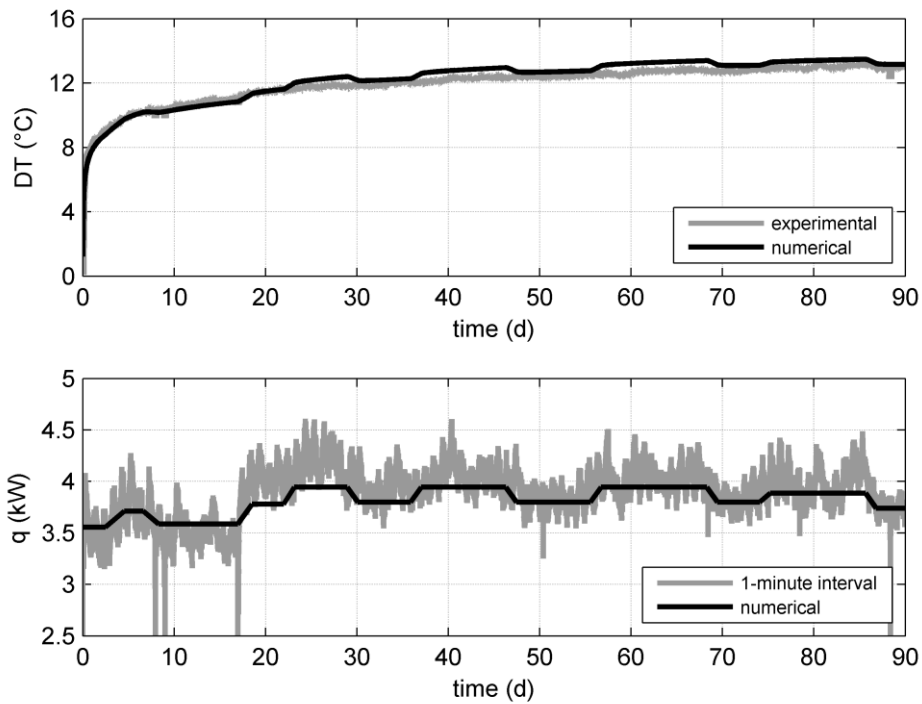
Figure 5.16 - Experimental and numerical mean water temperature evolution for varying heat input and grouting thermal conductivity of 1.0 W/mK in B2

As presented previously in section, the in-situ grouting thermal conductivity can be significantly lower than the one proposed by the producers. Numerical modelling has been used to investigate the influence of the grouting thermal conductivity on the borehole thermal resistance. First, TRTs were simulated for different values of the grouting thermal conductivity. Then, the borehole thermal resistance was calculated by applying the ILS model on the numerically obtained water temperature evolution. The results are presented in Figure 5.17. The borehole thermal resistance varies significantly for grouting thermal conductivity lower than 2 W/mK. For higher values, an increase of 0.1 W/mK in the grouting thermal conductivity results to a decrease of the borehole thermal resistance in the order of only 0.001 Km/W. Therefore, for the given BHE geometry, any significant difference between the in-situ and the proposed grouting thermal conductivity will have an important effect on the borehole thermal resistance for thermal conductivity values lower than 2 W/mK.
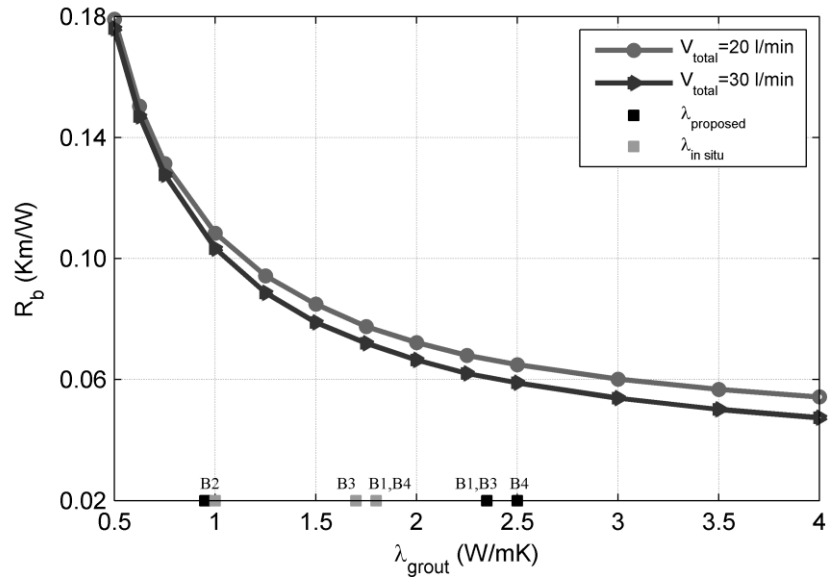
Figure 5.17 - Influence of grouting thermal conductivity on borehole thermal resistance (double-U pipes, r_p=0.016 m, d_{shank}=0.064 m, r_b=0.068 m) ($\lambda_{proposed}$: grouting thermal conductivity proposed by the producers, $\lambda_{in\ situ}$: in-situ grouting thermal conductivity by calibration with numerical modelling for the four BHEs)

5.4 Temperature distribution inside the borehole

5.4.1 Heating phase

Figure 5.18 shows the water temperature distribution along the pipe loop in B4 based on the 3D numerical model results. In this model, the ground was considered homogeneous and isotropic and a constant heat input was applied for the whole test duration. The temperature profile develops gradually, obtaining the characteristic V-shape after approximately 12 min. The duration of this transient phase decreases with increasing flow rate and for shorter BHEs. Once it reaches the steady state, water temperature rises more quickly with time. This transition is also indicated in the experimental water temperature evolution (Figure 15.18, bottom). At steady state, the transferred heat decreases while water progressively advances along the pipe loop, indicated by the non-symmetrical obtained profile. This is attributed to the lesser amount of heat subjected to each water section, starting with the maximum value at the ground level at the pipe inlet, and to the possible thermal interaction between the pipe legs. Approximately 70% of the injected heat is transferred in the downward pipe, while only

30% in the upward pipe, for this BHE geometry and for a flow rate of 9 l/min in each pipe loop. The proportion of heat transferred from the downward pipe was calculated by the convective heat transfer equation (section 5.2.1) based on the water temperature at the pipe-inlet and at the bottom of the pipe loop. The water temperature at the pipe-outlet and at the bottom of the pipe loop was used for the upward pipe heat transfer. The transferred heat per meter of the borehole (sum of downward and upward transferred heat) decreases of only 3.2% with depth, in this study of homogenous ground and uniform initial ground temperature. Greater variation is expected in the case of heterogeneous ground and/or due to an initial temperature gradient.

The steady-state heat transfer at the whole borehole cross section (fully developed temperature profile at the borehole wall) is achieved after 10 h. This is included in the proposed range (1 h - 12 h) for normal borehole sizes and ground conditions, according to Spitler and Gehlin (2015). Before reaching the steady state, the temperature evolution inside the borehole is dominated by the borehole filling heat capacity. The ILS model assumptions are not valid for transient heat transfer inside the borehole, and therefore data of this phase should not be included in the ILS model analysis.

During the pipes installation, fiber optic cables were attached at the outer surface of the pipe loop. The fiber optics profiles were calibrated by two RTD probes, attached on the pipes at certain depths (Chapter 3). Figure 5.19 (top) shows the depth-average temperature evolution, as measured by the fiber optics. The temperature is lower than the mean water temperature of approximately 1 °C. Oscillations in the fiber optics profile coincide with the water temperature oscillations, which are attributed to the varying heat input. Figure 5.19 (bottom) shows the temperature profiles through depth, obtained with measurement time of 60 min. This means that the first measurement is the time-average profile of the first hour. As a result, the profile development (transient phase) is not clearly displayed in these measurements. Temperature oscillations are observed along the whole pipe length including overlapping of the downward and upward measured temperature. Similar profiles are obtained during the heating phase of all the tests that conducted in-situ. It should be noted that the exact position of the cable at the outer surface of the pipes is not well known, since it was observed that the U-pipes were being rotated about the vertical axis while lowering them down inside the borehole.
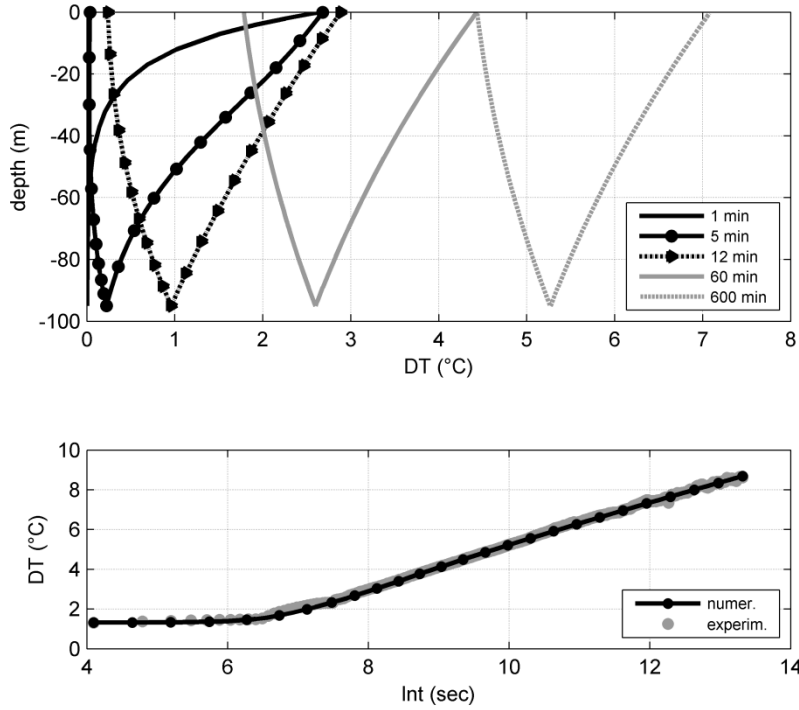
Figure 5.18 - Development of water temperature profile (top) and mean of pipe inlet and outlet water temperature evolution (bottom) for B4(1)
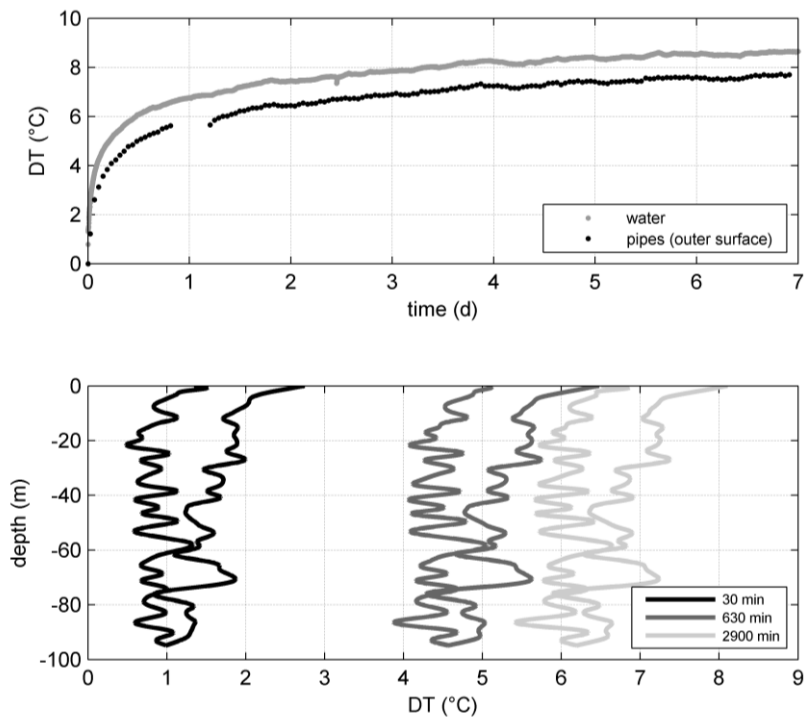

Figure 5.19 - Measured water temperature evolution (mean of pipe-inlet and outlet) and pipe temperature evolution (depth-average) (top) and temperature distribution at the outer surface of the pipes (bottom) for B4(1)

To better understand the measured profiles, the temperature distribution in the borehole cross section, based on the numerical results, is presented in Figure 5.20. The distribution is not uniform at the borehole cross section, controlled by the relative position of the pipe legs and the thermal conductivity of the different materials. Temperature can also vary significantly (in the order of 1 °C) along the outer surface of the each pipe leg, depending on the exact location of the measurement point. Higher temperatures are observed between the pipe legs and lower temperatures close to the borehole wall.
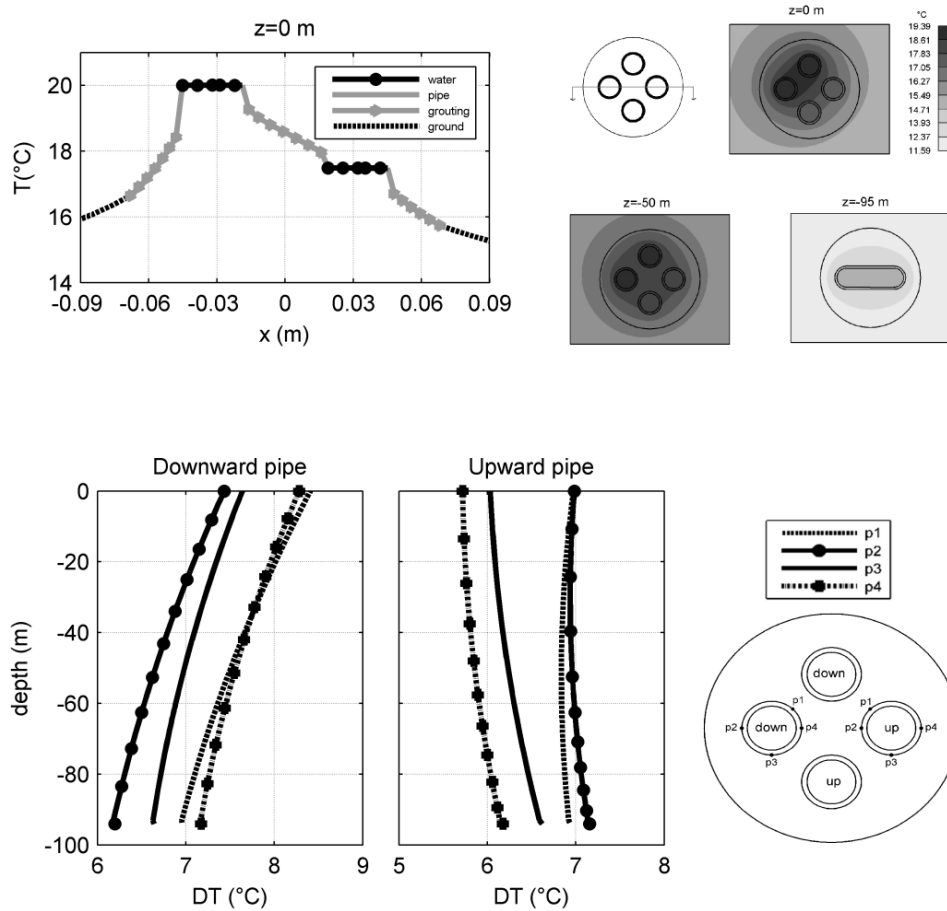

Figure 5.20 - Numerical temperature distribution at the borehole cross section after 3 d of heat injection for B4(1)

The temperature envelope for each pipe leg is presented in Figure 5.21, together with the fiber optic measurements. The measured temperature is in the range proposed by the numerical results, justifying the observed oscillations. Other reasons that could partially

contribute to the fiber optic oscillations are the accuracy of the fiber optic measurements, the possible detachment of the fiber optic cable and the varying heat transfer rate with depth due to the bedrock heterogeneity. However, the latter could not explain the overlapping of the upward and downward profiles or the locally increasing temperature along the direction of the water flow, since it would indicate that heat is transferred from the ground to the circulating water during the heating.
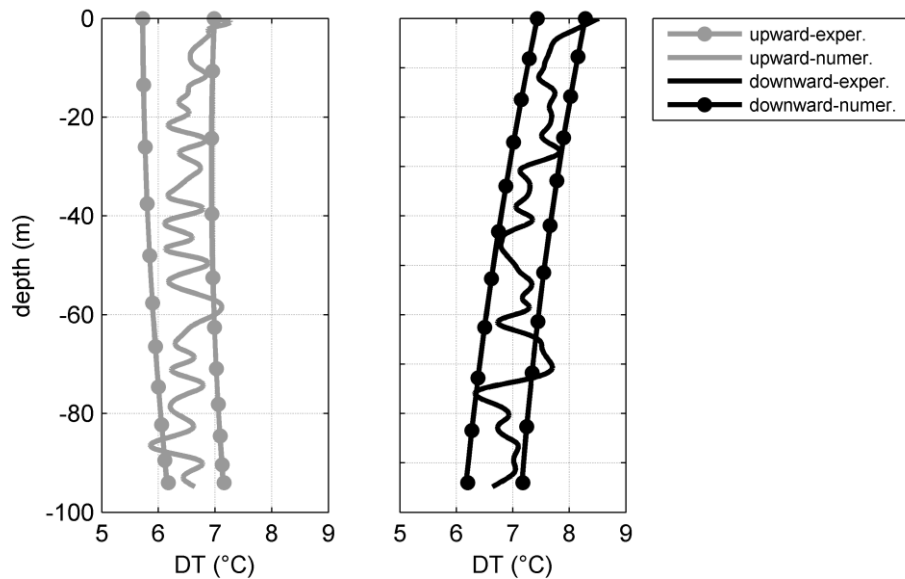
Figure 5.21 - Experimental and numerical temperature profiles at the pipes outer surface after 3 d of heat injection for B4 (1)

5.4.2 Recovery phase

Figure 5.22 shows the temperature evolution during the heating and the recovery phase in B1. Experimental data for the heating phase correspond to the water temperature at the pipe-inlet and outlet and for the recovery phase to the depth-average fiber optic temperature. To simulate the recovery phase, a zero velocity was imposed on each node of the 1D finite elements and the water thermal properties (λ=0.58 W/mK, ρc_ρ=4184 kJ/m³K) were assigned to the 3D water elements. The temperature at the borehole cross section varies less than 2 °C after 1 h of recovery and becomes almost uniform (DT<0.1 °C) after 20 h. Water temperature decreases at a high rate of 0.55 °C/h during the first 12 h, but of only 0.04 °C/h

for the next 36 h. After a period of 177 h (equal to the heating phase duration), temperature reaches 11.8 °C, recovering the temperature rise at the end of the heating phase of 92%.
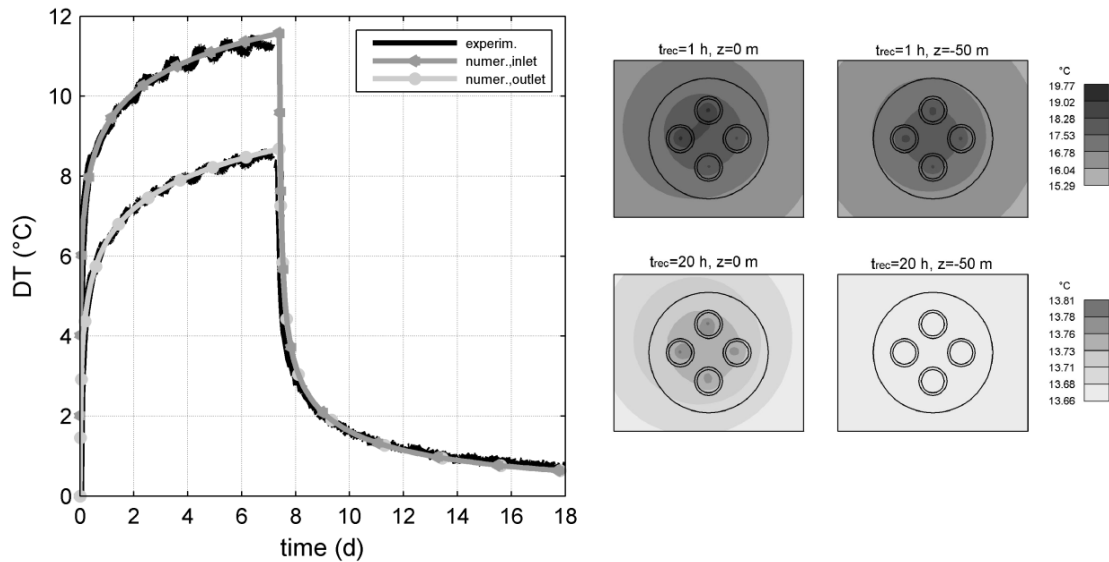

Figure 5.22 - Experimental and numerical temperature evolution during the heating and the recovery phase in B1

The required time for the recovery of different percentages of the temperature rise (ΔT) was investigated numerically, for the BHE geometry presented in Table 5.3 and for the following parameters: V_{total}=30 l/min, λ_{grout}= 1.5 W/mK, λ_{ground}= 3W/mK and q_{extr}=40 W/m. The results are presented in Figure 5.23 (left), as a function of the heating phase duration. To achieve a 75% of ΔT (°C) recovery, the required recovery time is less than 50% of the heating time. For more than 90% recovery, a recovery time greater than the heating time is required. For example, after 12 h of heating, only 3.5 h are required for a 75% recovery and 15 h for 90% recovery. Though, to achieve a 95% recovery, the required time is significantly increased (>30 h). Moreover, the ratio of the recovery time to the heating time decreases slightly with increasing heating time, for the investigated range. This is attributed to the higher difference between the water and ground temperature at the end of the heating phase, which provokes a quicker recovery. The same behaviour is observed in the case of extracting heat from the ground.

The water temperature evolution for two daily operation schemes is presented in Figure 5.23 (right). At the end of the first day, temperature decrease has recovered of 93% for the first

operation scheme (8 h/16 h) and 79% for the second one (16 h/8 h). These percentages decrease as the thermal cyclic loading continues. A fully recovery is not achieved at the end of each day, which results to a progressive cooling of the ground that could affect the long-term sustainability of the system.
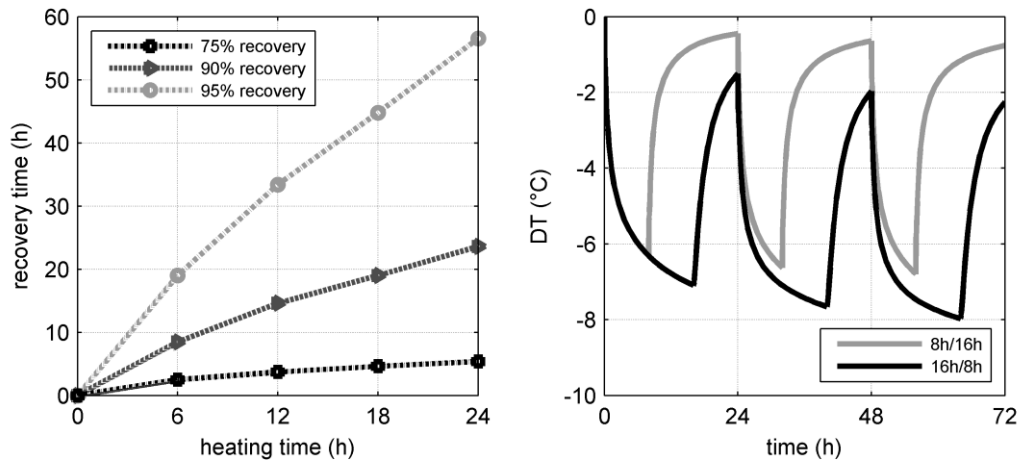

Figure 5.23 - Required recovery time for different heating phase durations (left) and temperature evolution for two daily operation schemes (operation time/recovery time) (right)

5.5 Detection of bedrock heterogeneity and layer dip angle determination

5.5.1 Temperature profiles during hardening of the grouting material

Temperature was measured by the fiber optics after injecting the grouting material. Heat is generated during the first hours of hardening of the grouting material, which results in a temperature increase along the borehole length. In the following days temperature retrieves its initial undisturbed profile. Figures 5.24 and 5.25 show temperature profiles a few days after injecting the grouting material in B1 (Geosolid, silica sand-based admixture) and in B4 (homemade admixture with graphite) respectively. The upper 18 m correspond to the thermally unstable zone, where ground temperature is influenced by weather conditions. In B1, the temperature profile during hardening of the grouting material (3 days after grouting) is characterised by a local maxima, of a significantly increased temperature value, at 26 m. This is also observed during the temperature recovery (9 days after grouting). In B4, the temperature profile during hardening of the grouting material is characterised by a local

maxima at a depth of 29 m. Theese depth locations correspond to extended fractured zones more than one meter based on the borehole logging analysis. The local maxima of the temperature curves are probably due to a local larger quantity of grouting material and/or local lower thermal diffusivity due to gathering of fractures. The lower thermal diffusivity of these zones is also indicated in the recovery temperature profiles, presented in the next section.

Close to the local maxima of the temperature profile in 5.24, temperature is increased between 22 m and 29 m deep. This depth difference, equal to 7 m, corresponds to the maximum and not to the exact thickness of the fractured zone. Assuming that the thickness of the fractured zone is 2 m and is located between 25 m and 27 m deep (as indicated by the borehole logging analysis), a larger quantity of grouting material, and hence an increased heat generation, is limited between 25 m and 27 m deep. The increased temperature observed at the non-fractured zone in this case (22-25 m and 27-29 m deep) could be explained as the result of the heat transfer to the surrounding ground. Hence, the maximum thickness of the extended fractured zone is estimated to 7 m (in between 22 m and 29 m depth) for B1 and 8 m (in between 26 m and 34 m depth) for B4.
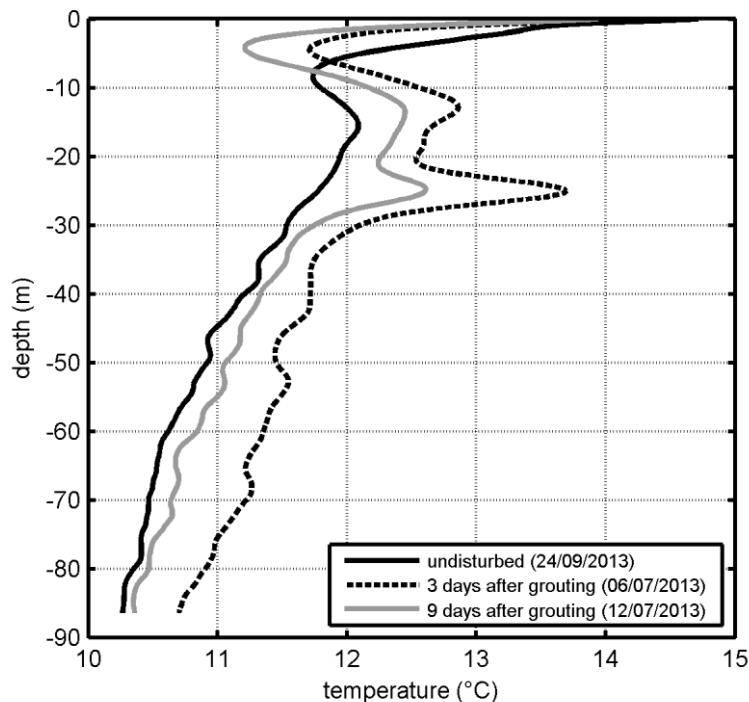

Figure 5.24 - Temperature profiles after injecting the grouting material in B1
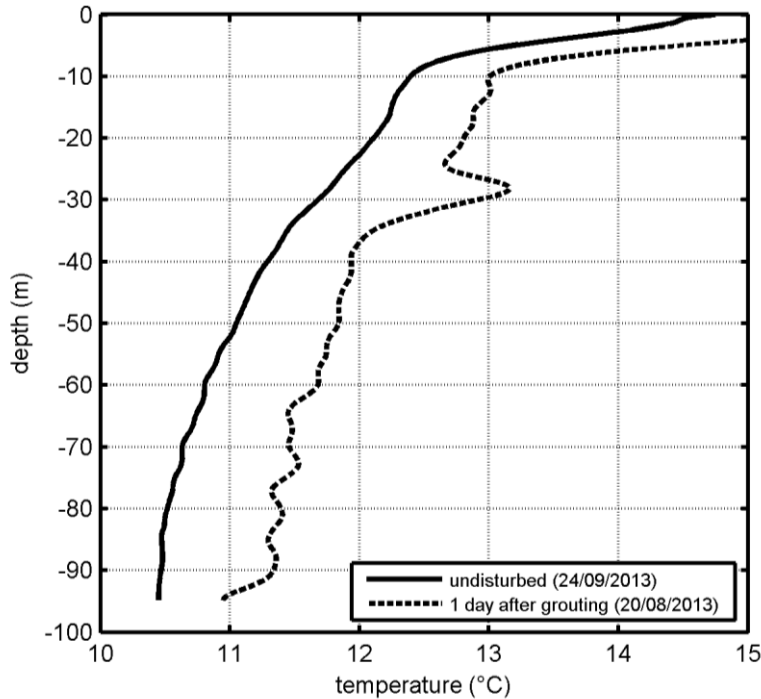
Figure 5.25 - Temperature profiles after injecting the grouting material in B4

Figure 5.26 compares the fractured zones identification by the temperature profiles analysis and by the borehole logging analysis (acoustic signal travel time and amplitude analysis). For B1, the middle of the fractured zone is located at a depth of 26 m for both approaches. The thickness of this fractured zone is 2 m based on the borehole logging analysis and between 1 m and 7 m based on the temperature profile analysis. For B4, two extended zones are located close to each other (between 28.0 m and 31.4 m and between 32.1 m and 33.4 m depth) based on the logging analysis. The fiber optic temperature analysis indicates one fractured zone, coinciding with the two fractured zones of the logging analysis. Its middle is located at 29 m and its thickness is between 1 m and 8 m. The results of both analyses are in good agreement with each other. However, random large fractures (more than 10 cm wide) or smaller fractures (of an opening between 5 and 10 cm) cannot be identified by the temperature profiles analysis. This can be attributed to the to the width of hotspots corresponding to random fractures with regard to the DTS performance parameters. In this case study, the width of hotspots corresponding to random fractures is quite lower than the spatial resolution of the measurements (2 m) and the sampling interval (20 cm). Even if these hotspots were included in the measurement points, the measured temperature could be significantly reduced, and hence become undetectable in the temperature profiles (Chapter 3, section 3.3).
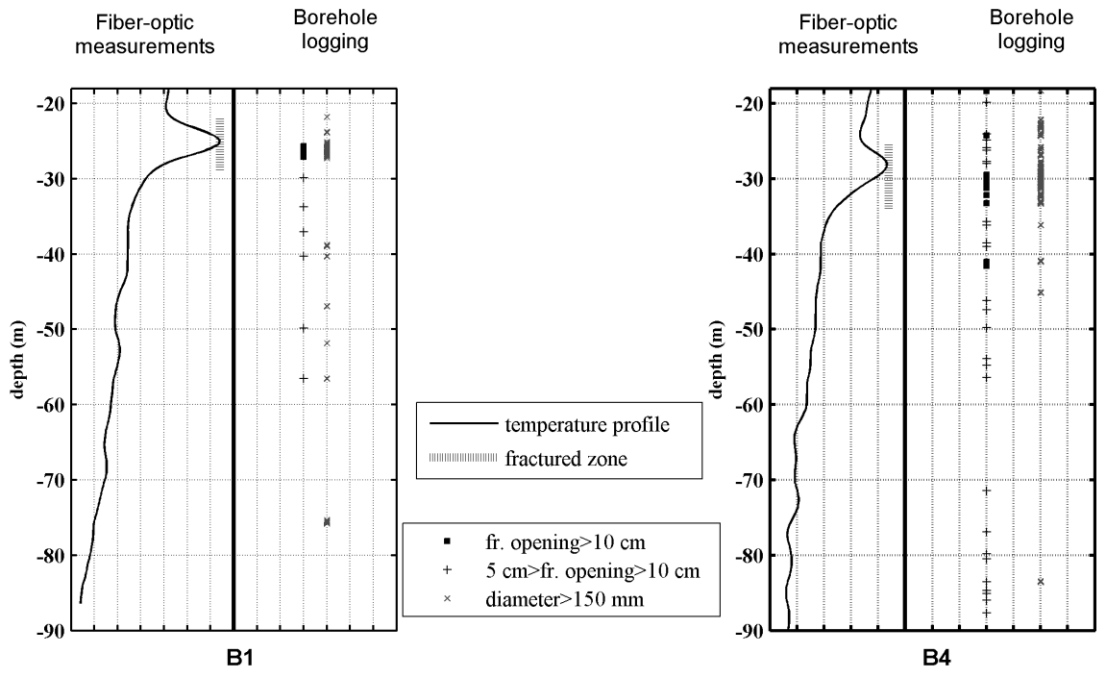
Figure 5.26 - Fractured zones identification by the temperature profiles analysis and by the borehole logging analysis for B1 and B4

5.5.2 Temperature profiles during the recovery phase

Figure 5.27 shows fiber optics temperature profiles obtained during the recovery phase in B3, where t=0 corresponds to the start of recovery. The temperature difference between the initial (t=0) and the undisturbed temperature increases through depth, due to the negative gradient of the undisturbed temperature profile (Chapter 4). Thus, considering homogeneous geological conditions, the heat transfer rate would increase with depth during the first hours of recovery. In order to remove this effect from the measurements, the temperature difference between each recovery profile and the undisturbed temperature was calculated (Figure 5.28). Local peaks in these profiles indicate an uneven heat transfer rate through depth.

Figure 5.27 - Recovery temperature profiles after 10 h of constant heat injection in B3

Figure 5.28 - Temperature difference between the recovery and the undisturbed temperature profile in B3

In order to investigate the possible correlation of these profiles to rock characteristics, a temperature difference profile after 4 h of recovery is presented in Figure 5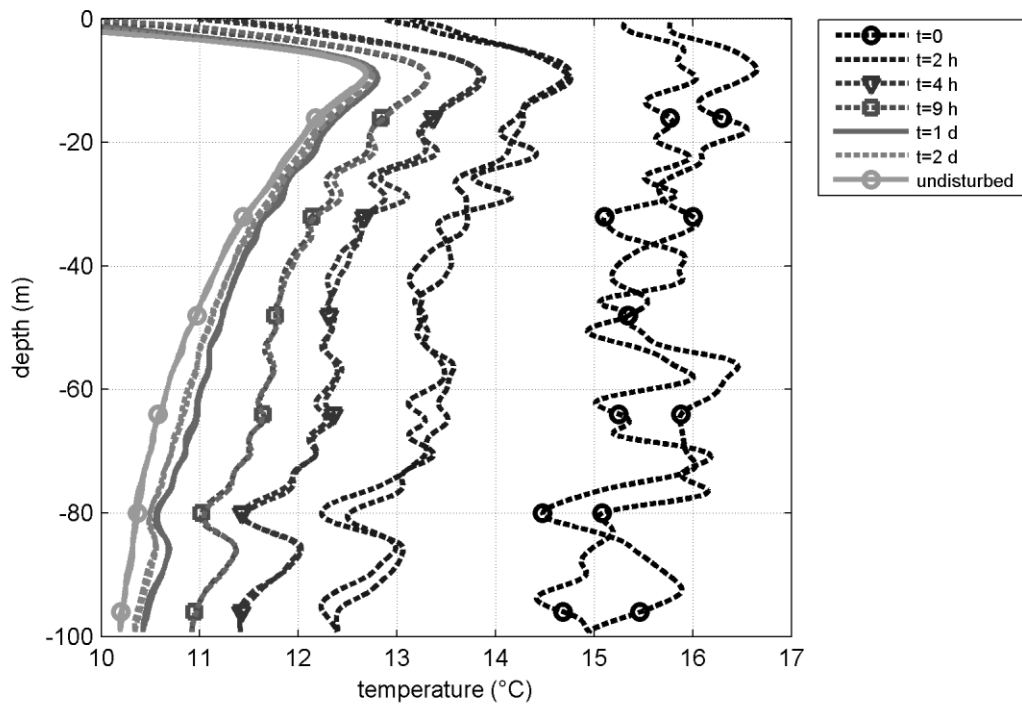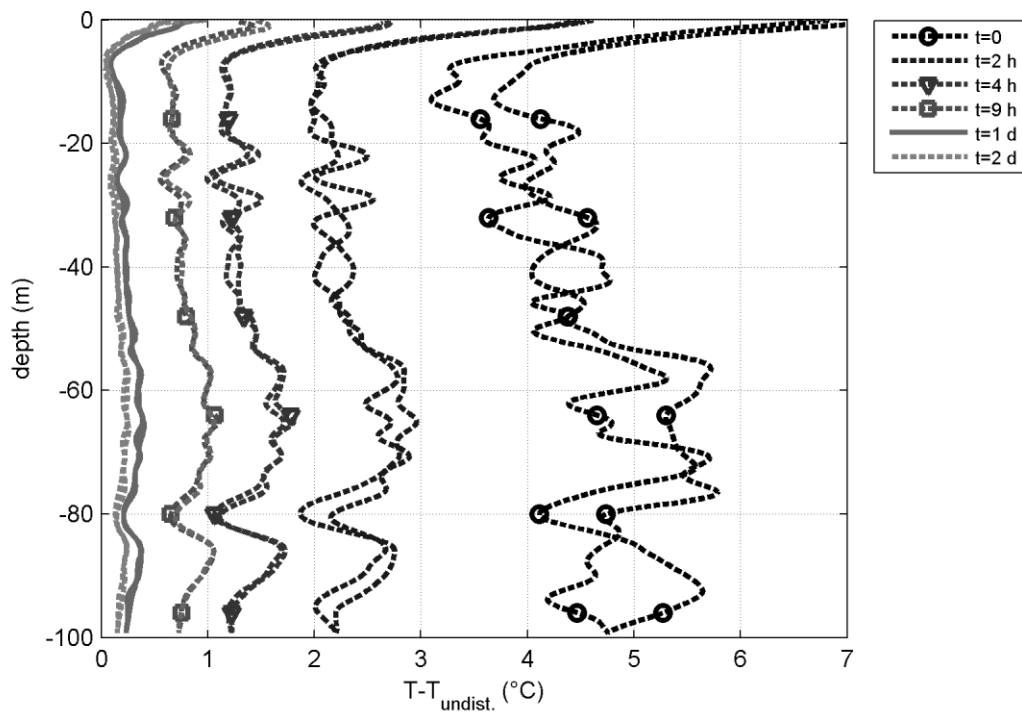.29 and compared to gamma-ray data (moving average of 2 m) and the fractures distribution through depth. The first 18 m are not included in this graph since they correspond to the thermally unstable zone and any correlation would be inconsistent. It is observed that temperature local minima correspond to gamma-ray local minima, indicating sandstone/siltstone layers, while temperature local maxima to gamma-ray local maxima, indicating shale/siltstone layers. The higher thermal diffusivity of sandstone/siltstone is evident in the in-situ measurements despite the relatively small thickness of these layers. The results are in good agreement with those of the gamma-ray data analysis and the cuttings thermal conductivity analysis, presented in Chapter 2. B3 is characterised of a few large open fractures (opening>5 cm) - and not by extended fractured zones - and hence any correlation between the fracturing and the temperature measurements is not evident in this case.

Figure 5.29 - Open fractures distribution, temperature difference after 4h of recovery and natural gamma radioactivity data for B3

The same procedure is applied for B4, which is quite more fractured than B3. Figure 5.30 shows the temperature difference profile after 4 h of recovery compared to gamma-ray data (moving average of 2 m) and fractures distribution through depth for B4. Temperature local peaks coincide to gamma-ray local peaks, as in B3, for depth greater than 35 m. Though this

118

correlation is not persistent for the upper part of the borehole where an extended fractured zone exists, at 30 m depth, probably filled with grouting material. The quite fractured rock at this position could be characterised by a lower thermal diffusivity, due to air or grouting material (λ=1.7 W/mK, Table 5.4) filling the fractures, compared to the surrounding less/non fractured rock (λ=2.88 W/mK, Figure 5.11). Thus a local maxima is observed in the temperature profile at the depth corresponding to the fractured zone.
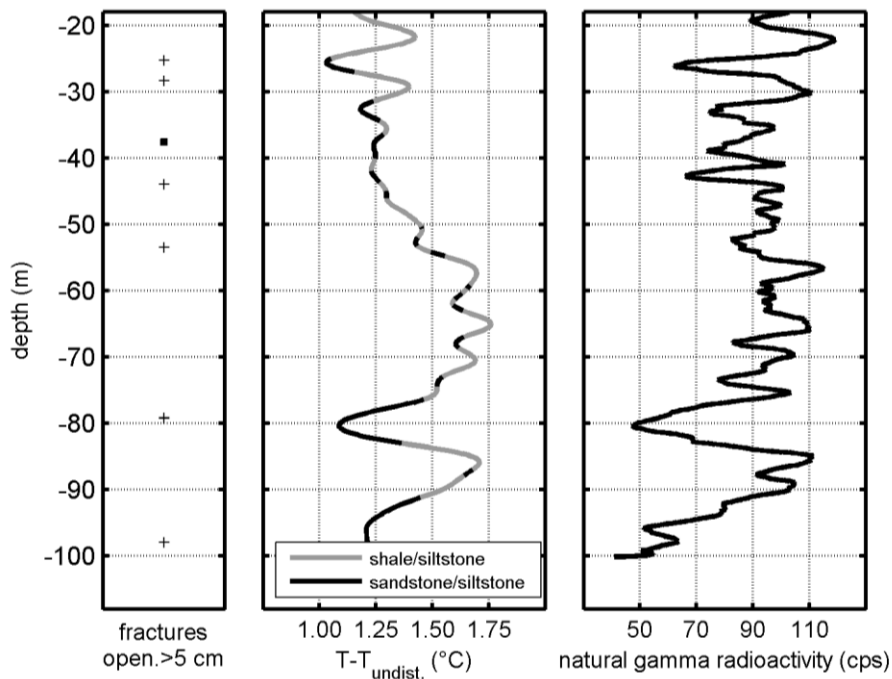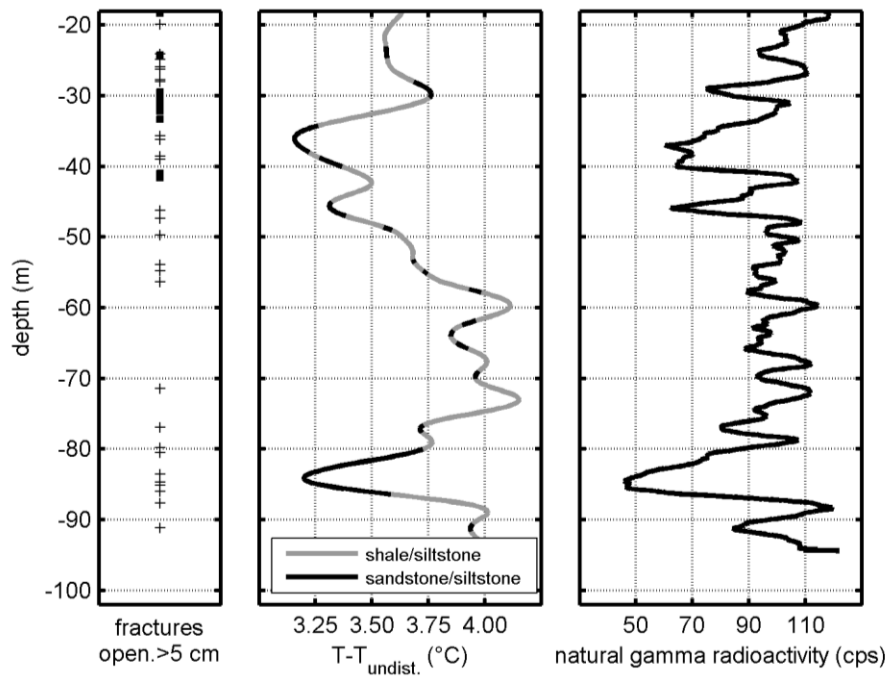

Figure 5.30 - Open fractures distribution, temperature difference after 4h of recovery and natural gamma radioactivity data for B4

In both profiles, B3 and B4, sandstone/siltstone layers more than 1.2 m thick can be identified as local minima in the temperature profiles, while thinner layers are not always detectable. As mentioned in the case of the temperature profiles during hardening of the grouting material, local temperature changes of width smaller than the spatial resolution (equal to 2 m in this case) could be undetectable in the measured temperature profiles. Moreover groundwater effects are not considered in this analysis since TRTs measurements analysis indicate the absence of high groundwater flow, as presented previously in this chapter.

A local maxima is also observed at the fractured zone in B1, which is located at the transition from a sandstone to a shale layer. In B2, the fractured zone is located at a shale/siltstone layer and therefore, the possible detection is not evident. Figure 5.31 presents the recovery profiles

for the four BHEs. The layer dip angle can be calculated based on theese profiles and the relative distance between them. The depth location of local peaks in B1 and B2 coincide with each other, as also observed in the gamma-ray profiles (Chapter 2). The mean layer dip angle proposed by this analysis is approximately 45° SE (Table 5.5) and is in good agreement with those proposed by the gamma-ray data analysis and by the cuttings thermal conductivity analysis (Chapter 2).
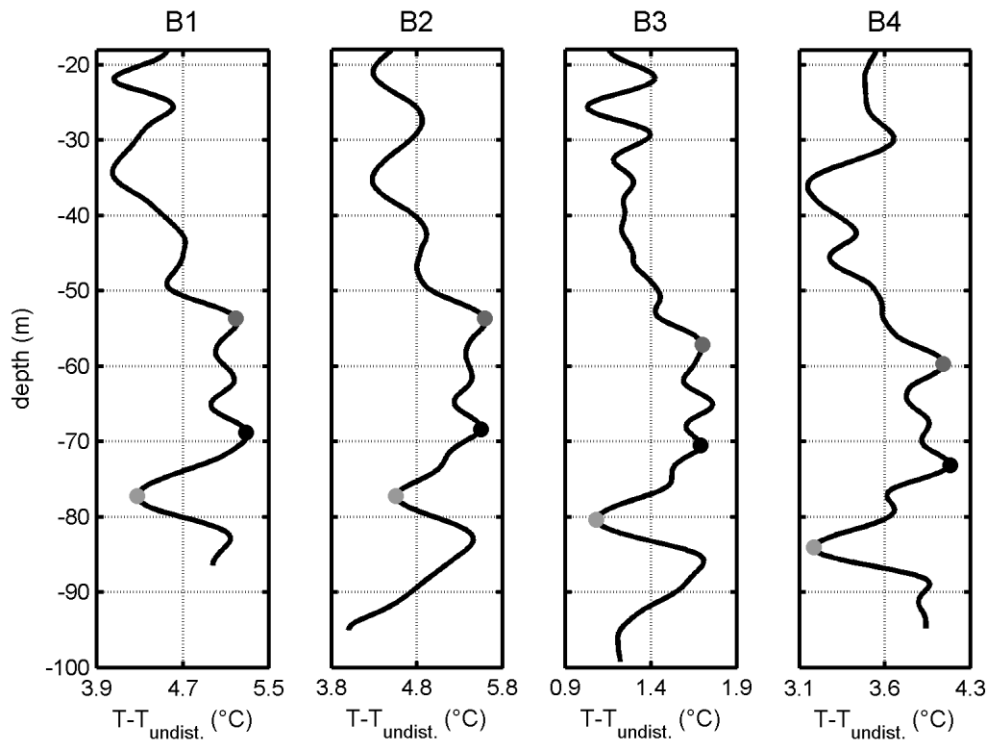
Figure 5.31 - Layer dipping indication based on B3 and B4 temperature measurements

Table 5.5 - Layer dip angle calculation based on fiber optics temperature profiles

depth at B2 (m)	54.0	68.0	77.4
	B2B3		
horizontal distance (m)	3.20	2.80	2.69
elevation difference (m)	3.10	2.50	3.00
dip angle (°)	44.09	41.76	48.12
	B3B4		
horizontal distance (m)	2.87	2.91	3.15
elevation difference (m)	2.70	2.80	3.50
dip angle (°)	43.25	43.93	48.01
mean dip angle (°)	44.86		

5.6 Conclusions

In this case study, the importance of a sufficiently insulated TRT equipment for a steady heat input is highlighted. The ILS model results are quite sensitive to the heat input oscillations. This sensitivity increases for late starting times and for short data time windows. It could be, therefore, proposed to evaluate the data of the in-situ TRTs by avoiding late starting times and by increasing gradually the length of the time window. This approach was applied to the in-situ TRT measurements and the proposed results were verified by numerical simulations of the in-situ TRTs, for this specific case study. Though, the results of this study also indicate that there is not a unique proposition for the TRT duration for a given accuracy of the results, since it will depend in each case on the extend of the heat input oscillations, and that the typically proposed duration (50 h) might not give accurate results in the case of insufficiently insulated TRT equipment.

The in-situ grouting thermal conductivity was estimated lower than the one proposed by the producers. This could be mainly attributed to the water fraction applied in-situ for the preparation of the admixtures, which was higher than the one proposed by the producers. For the given BHE geometry, this could have an important effect on the borehole thermal resistance for grouting thermal conductivity values lower than 2 W/mK.

The fiber optic profiles of the heating phase are characterised by temperature oscillations along the whole pipe length including overlapping of the downward and upward measured temperature. This could be mainly attributed to the exact position of the cable at the outer surface of the pipes, which varies through depth in this case study, in combination with the non-uniform temperature distribution inside the borehole.

Based on fiber optics temperature profiles of the recovery phase, we can detect layers with different mineral content that display a different thermal behaviour. Layers thinner than 1.2 m cannot be identified by this procedure. The resolution of the applied procedure is limited by the measurement parameters, spatial resolution and sampling interval. Lower spatial resolution and sampling interval could improve the resolution of the results. Moreover, comparison of the boreholes temperature profiles can result in determination of the layer dipping.

Temperature profiles during hardening of the grouting material allow to locate extended fracture zones, more than one meter in this case study. The results are in good agreement with those of the borehole logging analysis. These temperature measurements could contribute to the bedrock heterogeneity investigation. Fractures filled with grout would locally influence the effective thermal properties of the rock mass. Moreover, they would locally affect the fracture transmissivity and hence the rock mass permeability. The grouting could locally reinforce the rock mass and modify its mechanical characteristics. These parameters are important for the hydro-thermo-mechanical behaviour of the bedrock.

The profiles during hardening of the grouting material were obtained at different time period after grouting in B1 and B4. Hence, a behaviour comparison between the two types of the grouting cannot be deduced by these measurements. More measurements or a continuous monitoring could provide information on the behaviour of different grouting materials during hardening, as well as on the required time for the temperature to retrieve its initial profile after the BHE installation. The latter is crucial for the reliability of the TRT results, which control the design of closed-loop systems. Moreover, a study of the thermal response during hardening of the grouting material which is an exothermic process could provide information on the possible bedrock heterogeneity and the varying heat transfer rate with depth.

It is also possible to conclude that it would be of interest in any BHE to measure the temperature along the borehole before conducting the TRT (undisturbed ground temperature), during hardening of the grouting material and after 4h of recovery. Alternatively to fiber optic cables, a temperature sensor (e.g. thermocouple element, resistance temperature detector) can simply be lowered down into the pipe to obtain the temperature profiles. This approach is cost-effective and easy to implement and would give valuable information about the rock nature and stratification, as well as about the rock geothermal reservoir potential.

Chapter 6: Long-duration DTRT and thermal plume in the surrounding bedrock

6.1 Introduction

At the laboratory scale, several studies include measurement at rock samples, core samples or cuttings to investigate the influence of various factors (e.g. mineral composition, porosity and degree of saturation) on the thermal properties (Clauser and Huenges, 1995; Popov et al., 1999; Pechnig et al., 2010). In the case that the rock sample consists of foliations (e.g. shale samples), an anisotropic thermal behaviour is observed depending on the direction of the heat flow with regard to the foliations orientation. The thermal conductivity parallel to the foliations can be up to 2.5 times higher than the one perpendicular to the foliations (Popov et al., 1999; Eppelbaum et al., 2014). These effects are widely studied at the laboratory scale, however, extrapolating laboratory results to in-situ conditions remains challenging (Liebel et al., 2010; Luo et al., 2016). In-situ, any possible deviation from the rock samples characteristics (e.g. degree of saturation, fracturing, porosity), as well as groundwater flow can result in a different effective thermal conductivity of the rock mass than the one measured at the laboratory. Moreover, the thermal behaviour of the bedrock will be affected by the in-situ undisturbed temperature field (geothermal gradient effect, urbanisation effect, air variations influence at the top ground meters), an influence that is not included in the laboratory measured thermal conductivity values.

TRTs allow to estimate the effective ground thermal conductivity including the influence of the in-situ conditions. The estimated thermal conductivity corresponds to a depth-average value and the typical duration of a TRT is a few days, which indicates that the results are representative of the ground mass surrounding the borehole at a radius of a few meters. The thermal behaviour of the BHE during its operation and the thermal plume in the surrounding ground can be then predicted based on the TRT data analysis, considering the ground a homogenous, isotropic material. However, this assumption is not always valid and the estimated effective thermal conductivity might not be representative of the in-situ conditions for longer heating periods or during the recovery phases, where the heat flow direction is inversed. This is critical in the case that ground water effects are dominant and the TRT

interpretation can not provide a unique value for the effective thermal conductivity, which depends on the characteristics of the aquifer and the heat flow direction (Loveridge et al., 2013). Moreover, the air temperature influence can affect the ground temperature at the top even 20 m of the ground (Popiel et al., 2001) and the borehole wall temperature distribution at the bottom of the borehole is affected by its finite length (Philippe et al., 2009).

Thus, the following questions arise:

- Could the typical-duration TRT results be representative of the BHE behaviour for longer heating periods and different modes (heating/recovery), in the case that groundwater effects are not dominant?

- Are heterogeneity and anisotropic effects a controlling factor for the thermal plume in-situ, in the presence of the thermal interaction between the different rock layers?

- Is the influence of the thermal effects at the borehole end negligible on the rock mass temperature distribution?

- Does the ambient air temperature variation have an important effect on the BHE behaviour?

This chapter investigates these questions based on experimental measurements of a long-duration DTRT (heating period of 7 months), conducted in-situ in a heterogeneous bedrock, where convection effects in the rock mass are not dominant. During the heating and the recovery phase of the test, temperature was measured by the fiber optics in the heated BHE (B2), as well as in the surrounding boreholes (B1,B3 and B4) covering a surface area of 32 m². These measurements create a unique data set, that allows to investigate the behaviour of the BHE for longer heating periods and to investigate the effect of various factors on the thermal plume in the heterogeneous bedrock at the in-situ scale. The heating phase, characterised by a varying heat input, was interrupted twice to investigate the influence of a short recovery on the temperature evolution at the borehole scale, as well as in the surrounding ground. The test was simulated by numerical modelling, without including heterogeneity or anisotropic effects in the rock mass. A constant ground thermal conductivity was applied, equal to the one estimated by the ILS interpretation of the first days of the TRT. The numerical results allow to investigate the effects of the varying heat input, of the distance to the heating source and of the thermal effects at the bottom end of the borehole on the temperature field, at the borehole scale as well as at the surrounding bedrock. The comparison with the in-situ measurements allows to investigate any possible variation of the

effective thermal conductivity with time and with depth during long heating and recovery periods and to study the possible effect of heterogeneity and anisotropic thermal behaviour of the bedrock on the temperature field evolution.

First, a description of the test procedure and the fiber optic calibration is presented. Then the temperature evolution at the heated BHE is investigated. The fiber optic profiles during the heating and the recovery phase are analysed to investigate the possible variations of the effective rock thermal conductivity with depth and with time. The 3D numerical modelling of the in-situ test follows and the results are compared with the in-situ measurements. The effect of the heat input interruptions is studied based on the numerical and experimental results. Afterwards, the temperature evolution in the rock mass is presented. The influence of heat transfer effects close to the borehole bottom end and of the heat input interruptions on the temperature field are studied by numerical modelling, with regard to a varying distance to the heating source. The measured temperature profiles in the rock mass in this case study are the result of a combination of different factors: bedrock heterogeneity, air temperature variations, borehole end thermal effects, varying heat input and varying distance to the heating source. The effect of each factor is identified in the in-situ measurements. Moreover, the effect of the anisotropic thermal behaviour of shale, which displays a varying effective thermal conductivity depending on the foliations orientation with regard to the heat flow direction, is investigated based on the in-situ measurements. Finally, conclusions are provided and the influence of the various factors is discussed. A part of the work included in this chapter is also presented in Radioti et al. (2016b).

6.2 Applied phases and fiber optic measurements calibration

A long-duration DTRT was conducted in B2 (June 2015- January 2016). The relative position of the boreholes (B1-B4) was chosen as presented in Figure 6.1 in order to investigate any possible anisotropic thermal behaviour of the bedrock along two perpendicular planes: the first along the axis crossing B1 and B2 and the second along the axis crossing B2, B3 and B4. The bedrock consists of siltstone and shale layers interbedded with sandstone layers (Chapter 2). Due to the layer dip angle orientation, B1 and B2 are characterised by roughly the same lithostratigraphy, which is observed at different depths in B3 and B4.

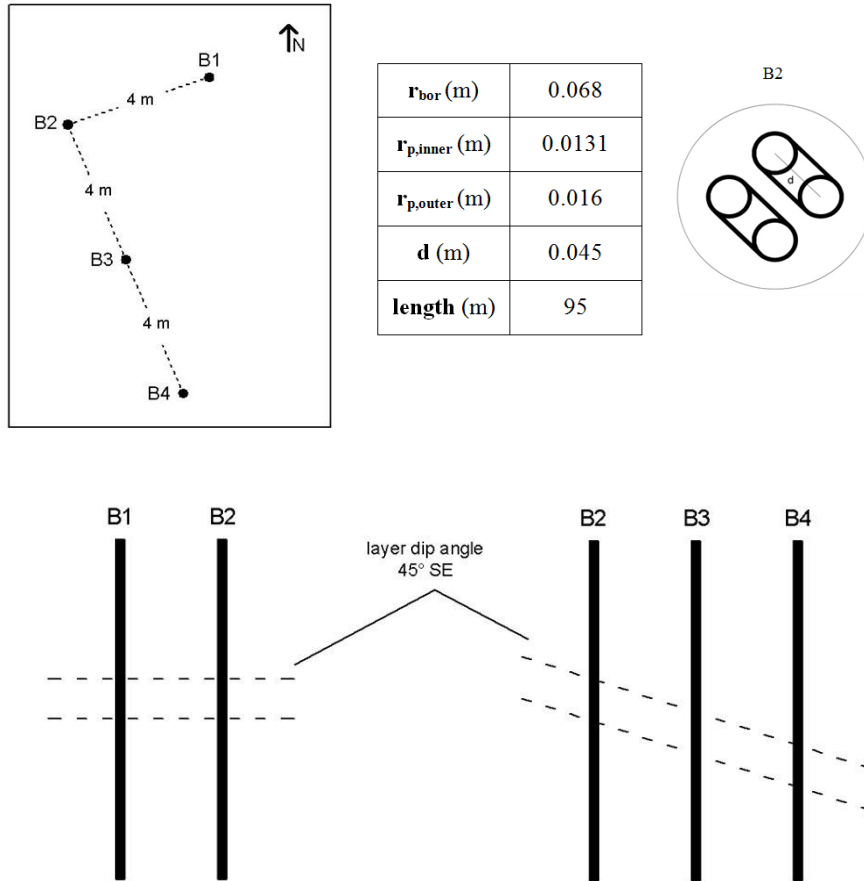|			
r_{bor} (m)	0.068		
$r_{p,inner}$ (m)	0.0131		
$r_{p,outer}$ (m)	0.016		
d (m)	0.045		
length (m)	95		

Figure 6.1 - Geometry of the heated BHE (B2) and relative position between the four BHEs

Figure 6.2 shows the different phases applied during the test. Before starting the test, water was circulated at high flow rate to purge air from the system. Then, water has been circulating in the U-pipe loops for 39 h, to achieve equilibrium between the water and the surrounding ground and to obtain the undisturbed ground temperature. Afterwards, the heating phase started. A constant heat input was applied to the double-U pipe for a duration of about 3 months. The heat input (42 W/m length) is in the order of the specific heat extraction proposition during the operation of the system for the geological context of the site, according to the VDI 4640 guidelines (50 W/m length for 2400 h, normal rocky underground and water saturated sediment with 1.5 W/mK<λ<3.0 W/mK). Then, the test was interrupted for 1.5 d, to study the influence of a short recovery on the thermal response of the system. A constant heat injection followed for about another 3 months. The test was stopped for the following 1 day and the TRT equipment was connected to only the one U-pipe. A heating phase followed, of a duration of 22 d. During the heating phases of both configurations (double-U and single-U), the same nominal power was applied in each U-pipe

loop. This means that, after the single-U heating phase started, the total nominal power applied in the BHE decreased in half. This allowed to investigate the effect of a varying heat input on the water temperature evolution, as well as on the surrounding rock mass.

In a perfect insulated system, there is no thermal interaction between the circulating fluid and the ambient air. A part of the nominal power is consumed by the pump, to circulate the fluid at constant flow rate (kinetic energy and energy loss due to friction), equal to approximately 0.1 kW in this case study based on data of the water circulation phase. The remaining part is converted into heating power, via an electric resistance heating element, which is added to the fluid during its circulation inside the rig. Oscillations in the nominal heating power profile in Figure 6.2 are attributed to voltage variations during the test. This effect is also displayed in the flow rate profile and could by minimized by using voltage regulators.

The actually applied heating power can be calculated from the convective heat transfer equation, as:

$$q_{appl} = \dot{m}c_p(T_{w,inlet} - T_{w,outlet}) \, ,$$

where $\dot{m}$: the mass flow rate *(kg/s)*,
c_p=4.19 kJ/kgK: the specific heat capacity of water at 10 °C,
$T_{w,inlet}$: the temperature at the pipe inlet (exit of the rig) *(°C)* and
$T_{w,outlet}$: the temperature at the pipe outlet (entrance of the rig) *(°C)*.

Figure 6.3 presents the calculated applied heating power and the air temperature measurements inside and outside of the test rig. The applied power oscillations follow the air temperature oscillations for the whole test duration, indicating the thermal interaction between the ambient air and the circulating water. During the TRT in this study, the connecting pipes were covered with a 2-cm thick insulation layer. The rig wall consists of a plastic honeycomb plate and the pipes inside the rig were also insulated. After the first 20 days of the test, an insulation layer (expanded polystyrene of a few cm thick) was attached around the test rig. For this period, the air temperature inside the rig seems less influenced by the outside air variations than before. Though, this layer only limits and not eliminates the outside air influence, as indicated by the agreement between the oscillations in the two air

temperature profiles. As thoroughly presented in section 5.1.1, the applied heating power variation during the test, which is greater than the nominal one, is the result of the ambient air temperature variations in combination with the insifficient equipment insulation.
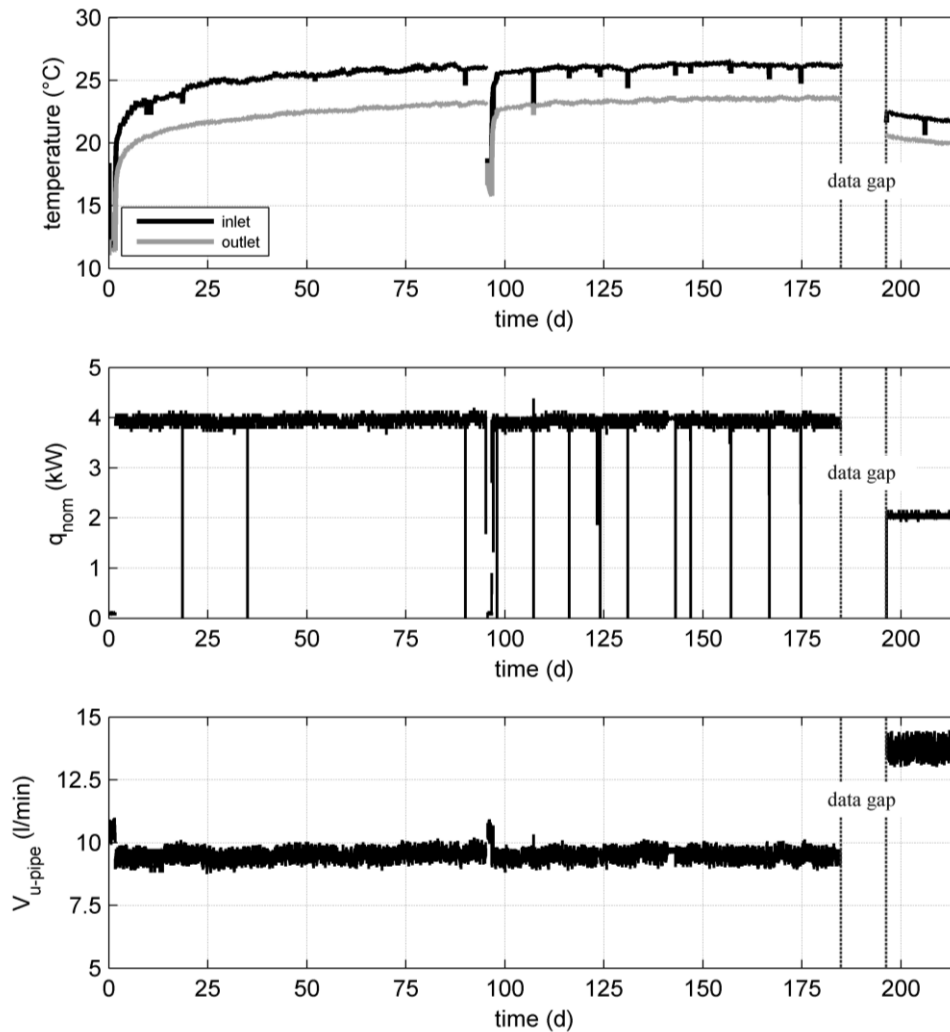
days	water circulation	heat injection	configuration
0-1.63	√	-	double-U
1.63-95.18	√	√	double-U
95.18-95.61	-	-	-
95.61-96.67	√	-	double-U
96.67-191.7	√	√	double-U
191.7-192.6	-	-	-
192.6-214.7	√	√	single-U

Figure 6.2 - Water temperature measurements, nominal heating power and flow rate per single U-pipe during the long-duration TRT in B2 (June 2015- January 2016)
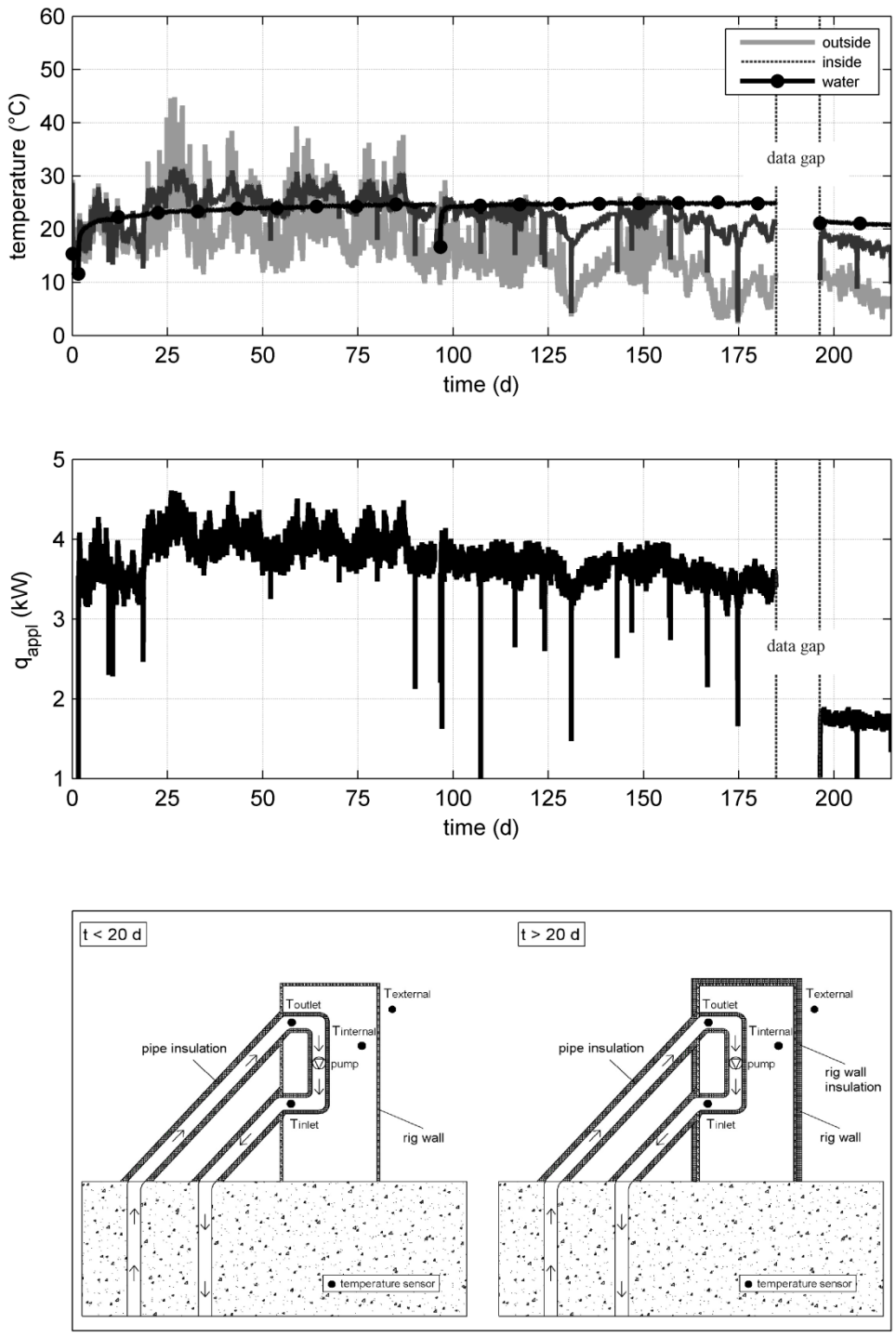
Figure 6.3 - Mean water temperature, air temperature and applied heating power during the long-duration TRT in B2 (June 2015- January 2016)

During the installation of the BHEs, fiber optic cables were attached at the outer surface of the U-pipes wall. Each cable contains two oprical fibers. Two RTD probes (Class A, T±0.15 °C) were also attached at certain depths in each borehole, in direct contact with the fiber optic cable, which would allow the offset calibration of the recorded fiber optic profiles (Chapter 3). At the undisturbed state temperature was also measured by lowering down a RTD probe inside the pipes, since the pipes were accessible. The calibration of the fiber optic profiles based on these measurements was in good agreement with the one based on the attached RTD probes, indicating the accurate estimation of the depth position of the attached RTD probes in each borehole. After the BHEs installation and grouting, the remaining parts of the cable in each borehole was rolled into loops and inserted in a metallic box (Figure 6.4), which served to protect the measurement equipment from weather conditions and damage.

Figure 6.4 - Fiber optic cable loops (left) and protection metallic box (100 cm x 60 cm x 40 cm) (right)

During the long-duration DTRT in B2, the RTD probes were not operational, probably due to an erosion of the sensor or of the electric wire connecting the sensor to the measurement device. The fiber optic profiles during the heating phase were calibrated based on the measurements of a RTD probe, located at the center of the pipe loop inside the box. The mean temperature of the fiber loops was assumed equal to the recorded air temperature by the RTD probe. As presented in Chapter 3, this approach was investigated based on fiber optic measurements at the undisturbed state and it can result in a significant error (in the order of ±1 °C), since air temperature inside the box varies significantly (Figure 6.5).
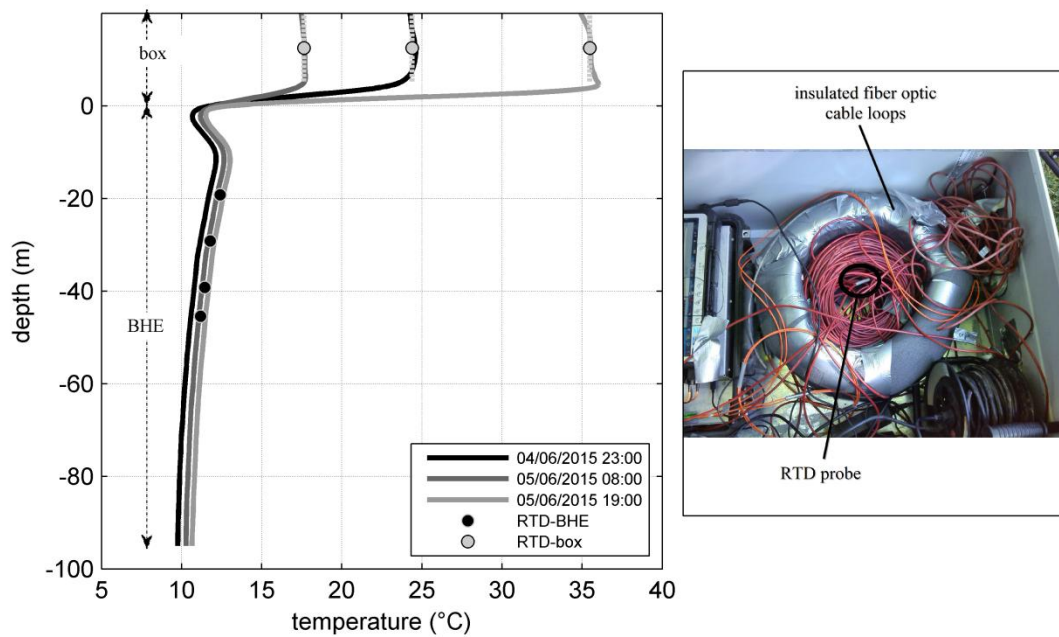
Figure 6.5 - Fiber optics temperature profiles calibrated by RTD measurements at the center of the cable loops inside the box

Figure 6.6 (top) shows the depth-average temperature by the fiber optics, calibrated based on this procedure. Oscillations are observed during the whole heating period and the fiber optic temperature becomes equal or even greater than the water temperature for certain periods. The fiber optic oscillations were expected to follow the water profile oscillations, associated with the varying heat input due to the insufficient test rig insulation. Moreover, given that the fiber optic cables are attached at the outer surface of the U-pipes, the recorded temperature was expected to be lower than the one of the water, due to the pipe resistance. These characteristics were observed in the fiber optic measurements of the DTRTs in the other three BHEs (Figure 6.6 bottom), where the profiles were calibrated by the RTDs attached along the U-pipes, as presented and verified by numerical modelling in Chapter 5. Therefore, the temperature evolution by the fiber optics during the heating phase in B2 is probably not representative of the actual temperature evolution at the outer surface of the pipes, since it can be overwhelmed by significant offset errors. The recovery profiles after the end of the heating phase (t=214.7 d), as well as the profiles in the other BHE during the whole test, were calibrated by lowering a RTD probe inside the U-pipe, since the pipes were accessible during this phase. Theese profiles can be considered representative of the temperature evolution.
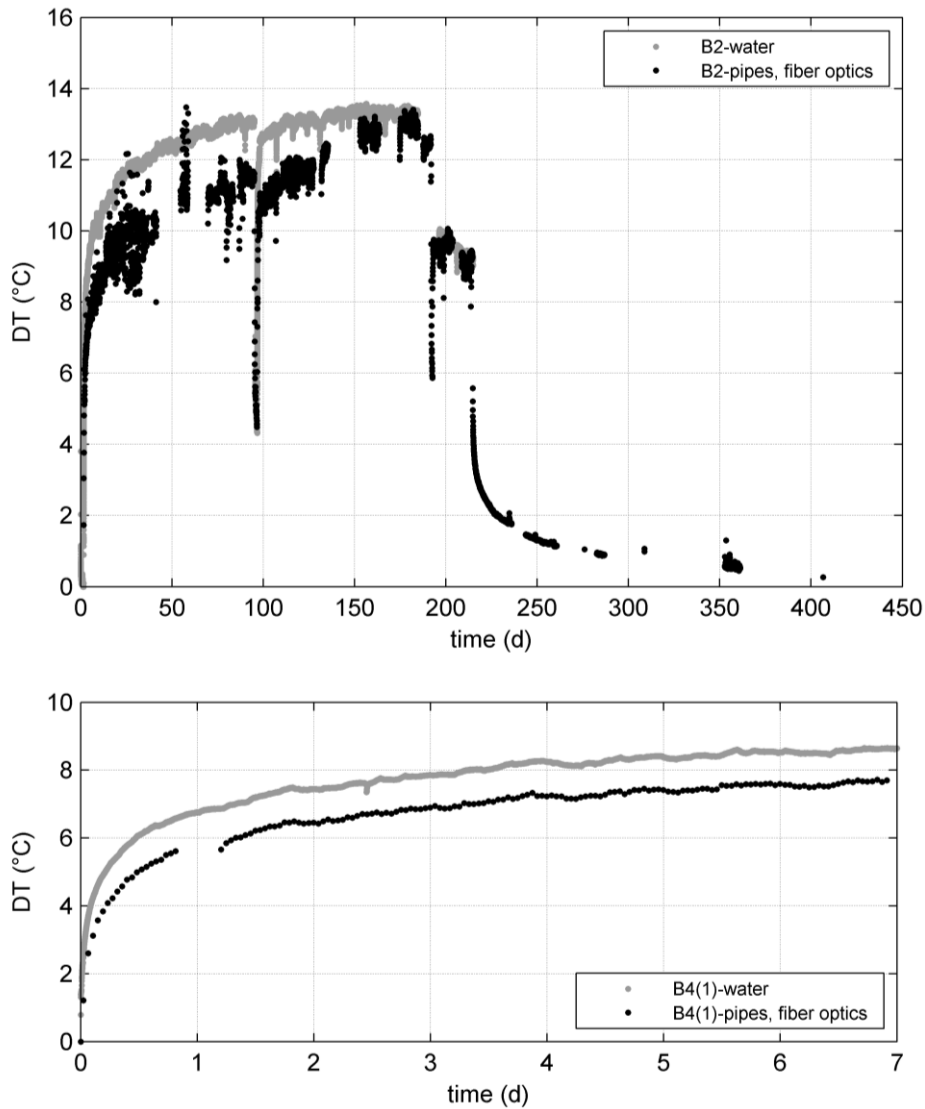
Figure 6.6 - Measured water temperature evolution (mean of pipe-inlet and outlet) and pipe temperature evolution measured by the fiber optics (depth-average) during the DTRT in B2(top) and in B4(bottom)

6.3 Bedrock thermal behaviour investigation: fiber optic profiles of the heated BHE

6.3.1 During the heating phase

Figure 6.7 shows temperature profiles during heating of the double-U pipe, obtained with measurement time of 60 min, spatial resolution of 2 m and sampling interval of 20 cm. Close to the ground surface (1 m - 2 m depth), temperature varies with time which can be attributed

to the influence of the air temperature variations. At greater depth, temperature increases with time. However, the relative temperature distribution along the pipe loop remains constant with time (identical shape of temperature profiles), during both heating periods (t<95.2 d and t>95.6 d). Oscillations are observed along the whole pipe length including overlapping of the downward and upward measured temperature. Figures 6.8 and 6.9 show the temperature evolution measured by the fiber optics at different depths for the upward and the downward pipe respectively. The oscillations observed in these profiles are the result of the insufficient calibration. The temperature evolution profiles corresponding at different depths are parallel with each other for the whole heating period in both pipe legs.

These measurements indicate that the heat transfer in the surrounding bedrock, and hence the effective thermal conductivity of each layer, does not vary significantly with time. A significant variation of the effective thermal conductivity in a layer (eg. due to convection effects) would have resulted in a variation of the water temperature distribution along the pipe loop and consequently to a modification of the temperature distribution along the pipes outer surface. It is possible, however, that small variations of the effective thermal conductivity occur (e.g. spatial variation of mineral composition or density along a layer), that result in temperature variations lower than the accuracy of the fiber optic measurements and are not captured in the recorded profiles.

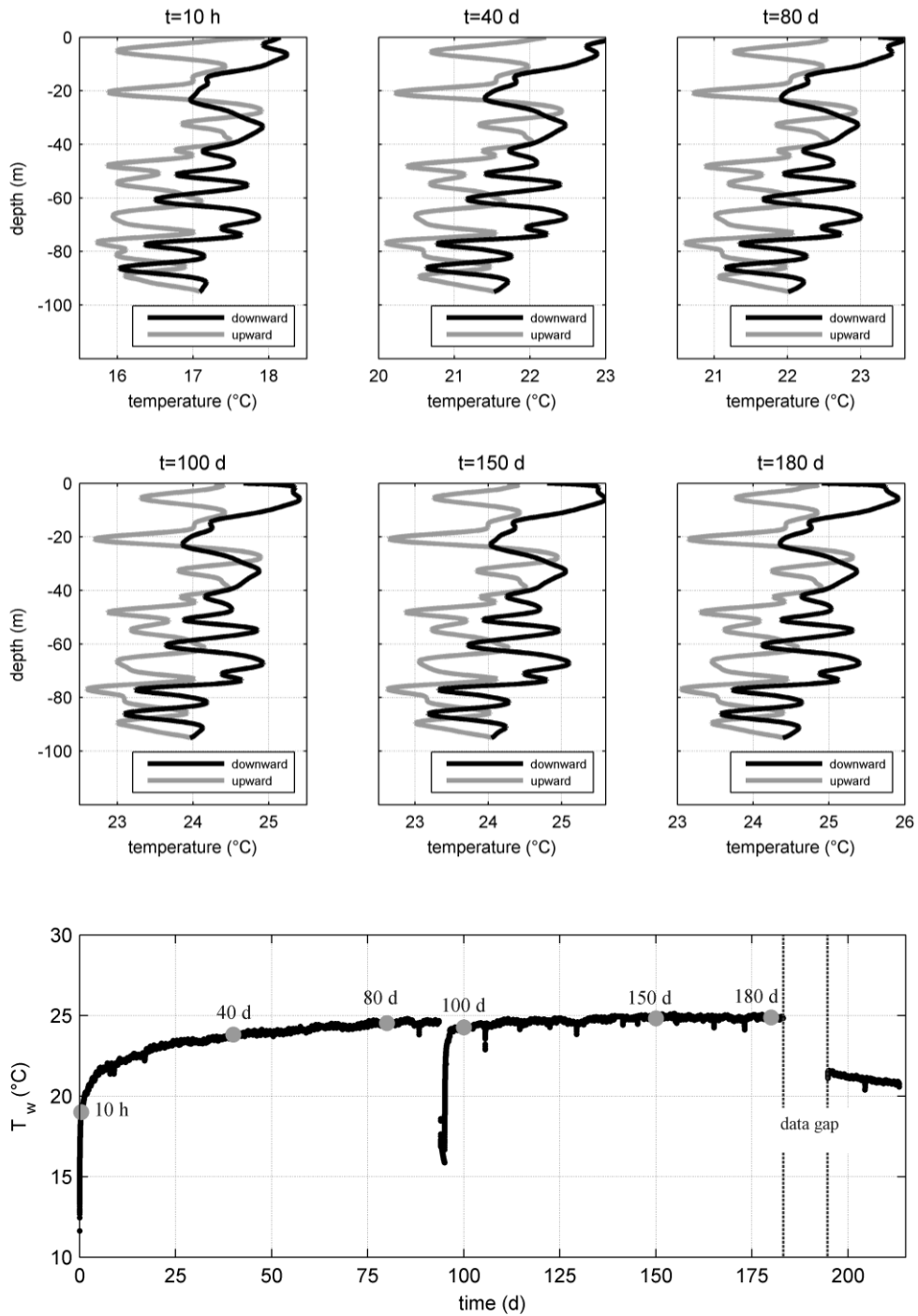Figure 6.7 - Temperature distribution at the outer surface of the pipes measured by the fiber optics (top, middle) and mean of pipe inlet and outlet water temperature evolution (bottom) during the heating phase in B2 (double-U configuration)
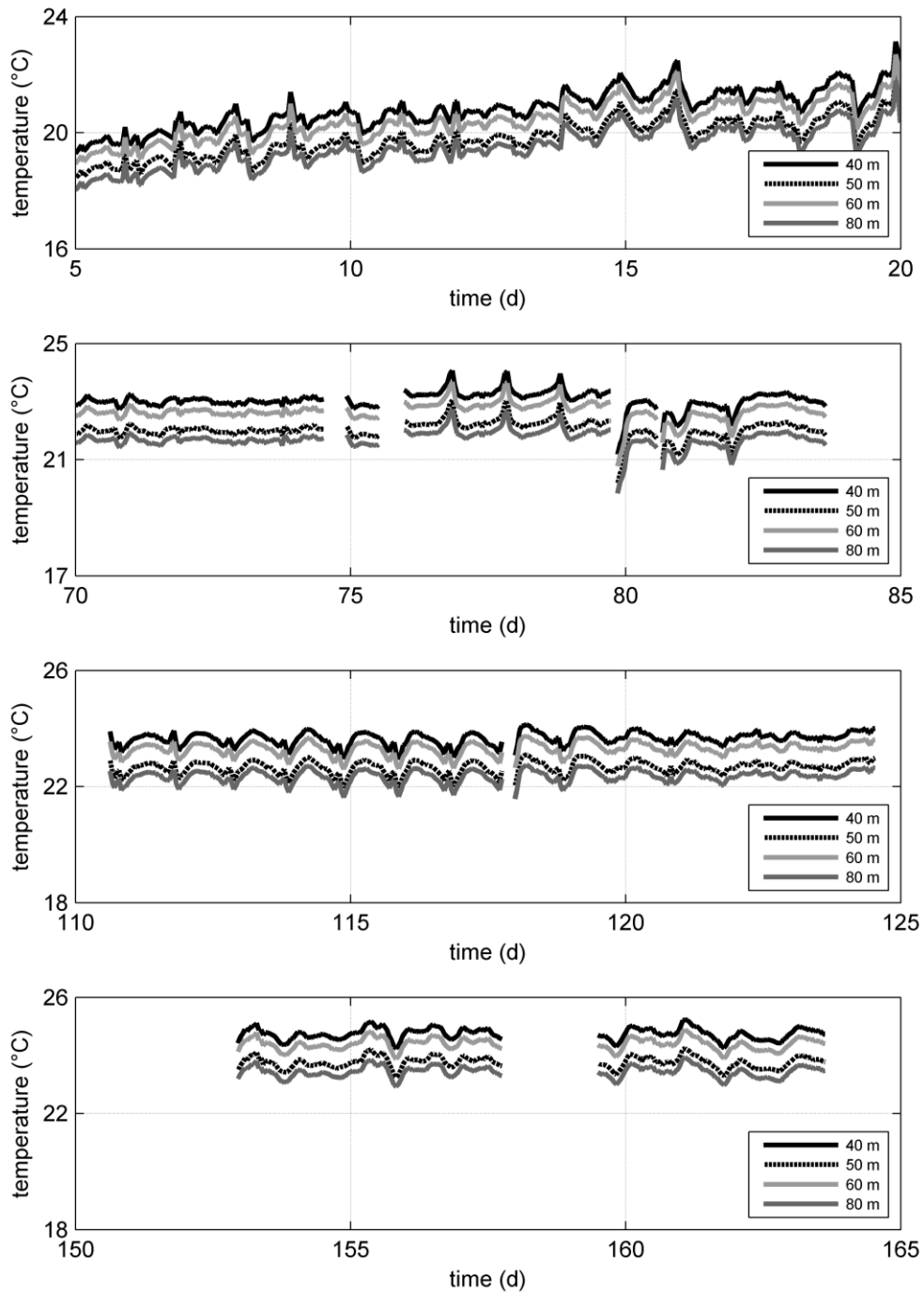
Figure 6.8 - Temperature evolution at different depths for the upward pipe measured by the fiber optics during the heating phase in B2 (double-U configuration)
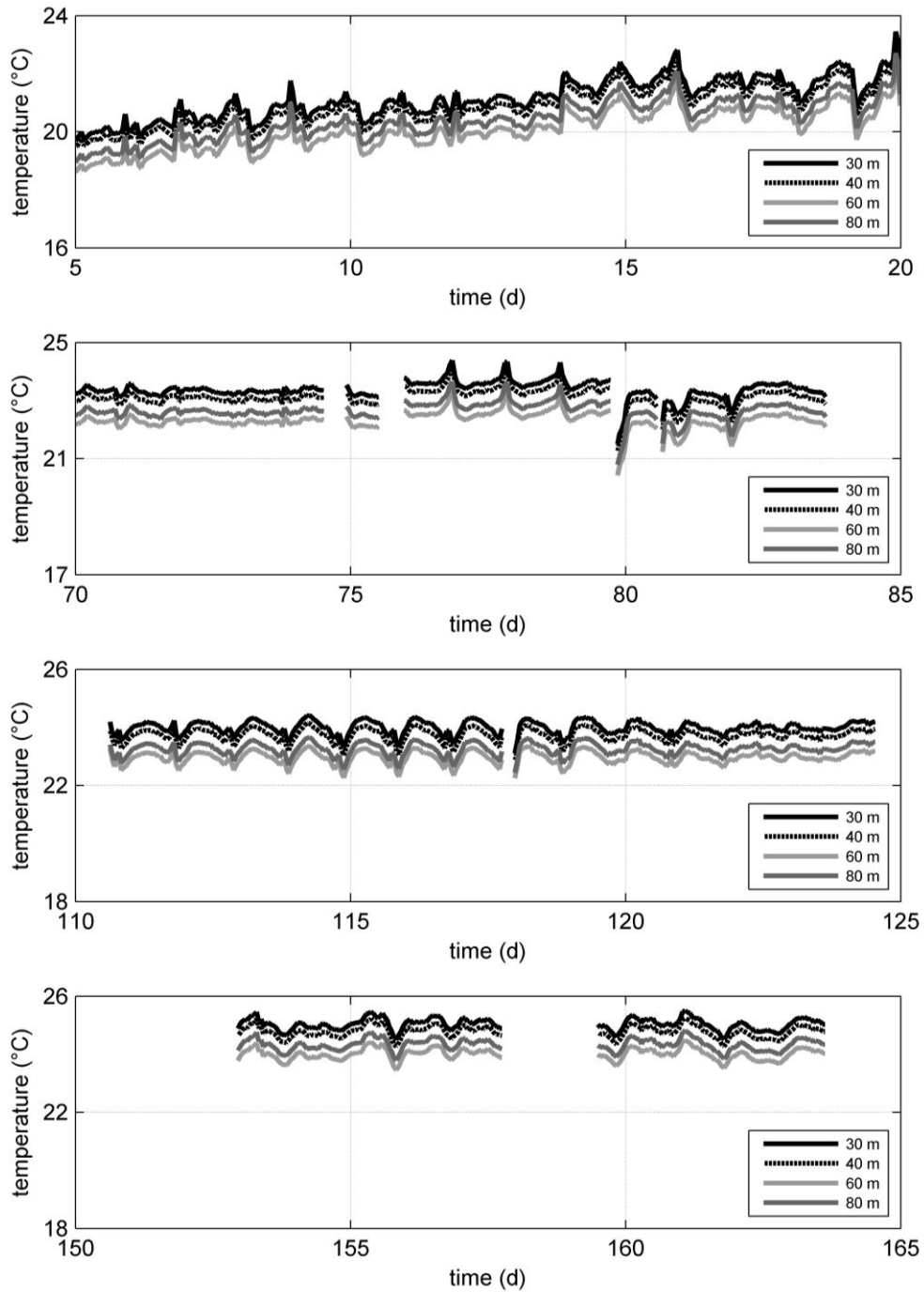
Figure 6.9 - Temperature evolution at different depths for the downward pipe measured by the fiber optics during the heating phase in B2 (double-U configuration)

Figure 6.10 show fiber optic temperature measurements during heat injection in the one U-pipe (t>192.6 d). As observed during the heating of the double-U pipe, the temperature distribution along the pipes does not vary with time (identical shape of temperature profiles), indicating the constant heat transfer along the different layers. The recorded profiles are not

identical with those of the double-U pipe heating. The applied heat input at the single-U pipe is equal to the one applied at each U-pipe during the double-U heating. Though, the applied flow rate in the single-U pipe configuration (13.8 l/min) is higher than the one in the double-U pipe configuration (9.5 l/min). Moreover, the temperature distribution at the borehole cross section is not dominated by the interaction of the two U-pipes during the single-U heating. This could explain the different shape of the recorded profiles.

Both profiles (double-U and single-U configuration), are characterised by temperature oscillations along the whole pipe length, including overlapping of the downward and upward measured temperature. The flow rate direction was inversed during the single-U heating. This means that the downward pipe leg of the double-U configuration coincides with the upward pipe leg of the single-U configuration (pipe leg 1). Respectively, the upward pipe leg of the double-U configuration coincides with the downward pipe leg of the single-U configuration (pipe leg 2). Figure 6.11 compares the profiles that correspond to the two pipe legs. The temperature oscillations in each pipe leg are observed at the same depth locations for both configurations. The exact position of the cable at the outer surface of the pipes is not well known, since the U-pipes were being rotated about the borehole axis while lowering them down inside the borehole. The recorded oscillations could be attributed to the varying position of the cable at the outer surface of the pipes in combination with the varying temperature at the surface of the U-pipes wall. This is further investigated in the next section by numerical modelling. Similar profiles were also obtained during the 7-days DTRTs conducted in the other three BHEs, for which the exact position of the cable at the outer surface of the pipes seemed to be a critical factor (Chapter 5).

Figure 6.10 - Temperature distribution at the outer surface of the pipes measured by the fiber optics during the heating phase in B2 (single-U configuration)
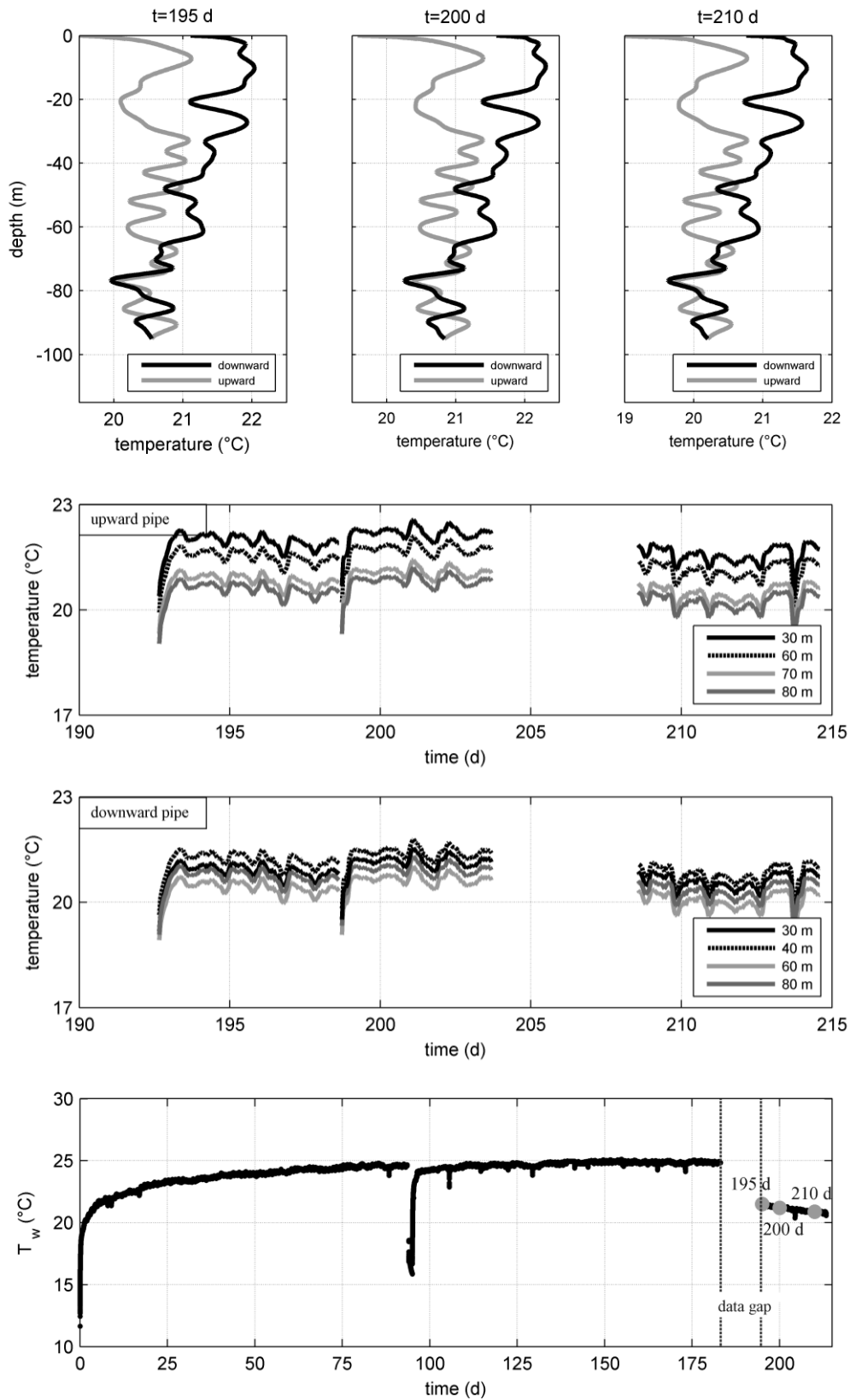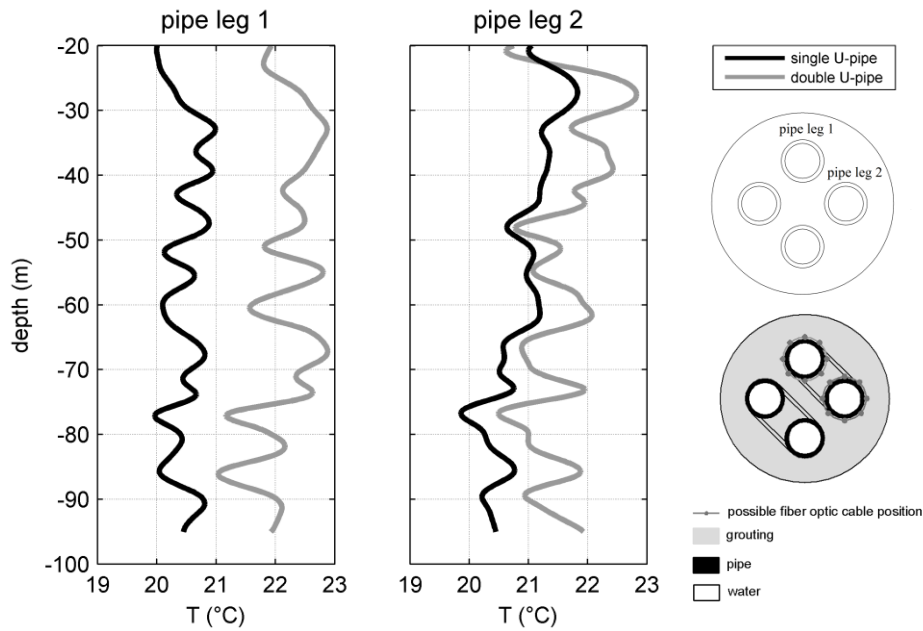
Figure 6.11 - Fiber optic temperature profiles at the outer surface of the pipe legs for both applied configurations (single U-pipe, t=195 d, and double-U pipe, t=80 d)

6.3.2 During the recovery phase

Figure 6.12 shows recovery profiles during the recovery phase (t>214.7 d) in B2. The temperature distribution with depth gradually reaches the undisturbed one, i.e. the temperature before heating, with the upward and downward pipe temperature profiles becoming identical after approximately 4 h of recovery. The temperature difference between the initial (t=0, end of heating phase) and the undisturbed temperature increases through depth, due to the negative gradient of the undisturbed temperature profile. Thus, considering homogeneous geological conditions, the heat transfer rate would increase with depth during the first hours of recovery. In order to remove this effect from the measurements, the temperature difference between each recovery profile and the undisturbed temperature was calculated and presented in Figure 6.13. Local peaks are observed during the first days of recovery. These local peaks indicate an uneven heat transfer rate through depth.
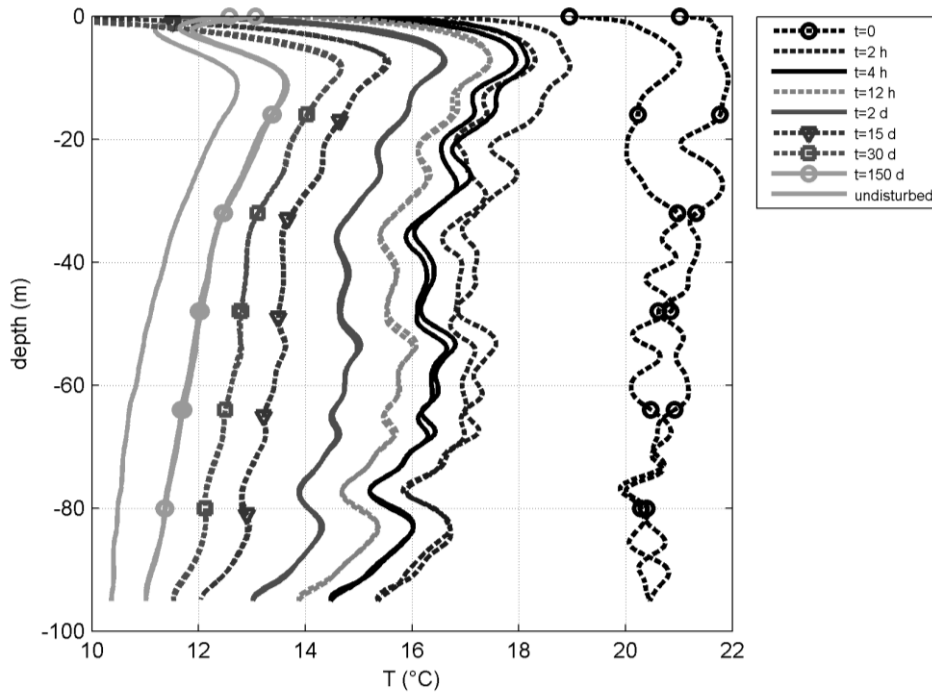
Figure 6.12 - Recovery temperature profiles measured by the fiber optics after 7 months of heating in B2
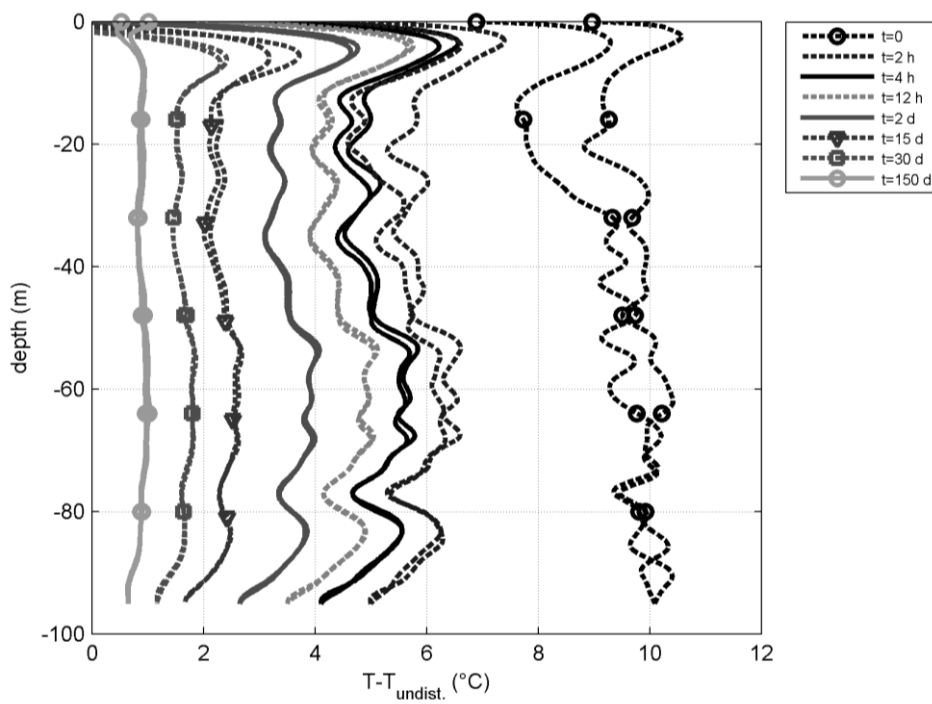

Figure 6.13 - Temperature difference between the recovery and the undisturbed temperature profile in B2

In order to investigate the possible correlation of these profiles to rock characteristics, a temperature difference profile after 4 h of recovery is presented in Figure 6.14 and compared to gamma-ray data (moving average of 2 m) and the fractures distribution through depth. The first 18 m are not included in this graph since they correspond to the thermally unstable zone, where ground temperature is influenced by air temperature variations, and any correlation would be inconsistent. It is observed that temperature local minima correspond to gamma-ray local minima, indicating sandstone/siltstone layers, while temperature local maxima to gamma-ray local maxima, indicating shale/siltstone layers. The higher thermal diffusivity of sandstone/siltstone is evident in the in-situ measurements despite the relatively small thickness of these layers. Sandstone/siltstone layers more than 1.2 m thick can be identified as local minima in the temperature profiles, while thinner layers are not always detectable. Local temperature changes of width smaller than the spatial resolution of the fiber optic measurements (equal to 2 m in this case) could be undetectable in the measured temperature profiles. B2 is characterised by a fractured zone between 20 m and 30 m depth, probably filled with the bentonite-based grouting material. The thermal diffusivity of this grouting material ($\alpha = \lambda / \rho c_\rho \approx 1.0 / 2.5 \cdot 10^6 = 4.0 \cdot 10^{-7}\ m^2 / s$) is lower than the one of the surrounding non-fractured bedrock ($\alpha = \lambda / \rho c_\rho \approx 2.9 / 2.3 \cdot 10^6 = 1.3 \cdot 10^{-6}\ m^2 / s$). The fractured zone is located at a shale/siltstone layer and therefore, the possible detection of this zone is not evident.
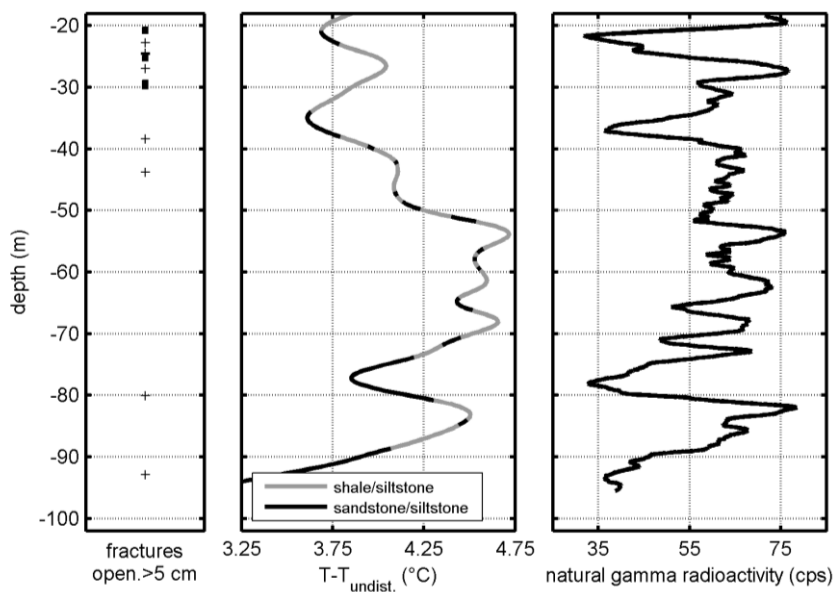

Figure 6.14 - Open fractures distribution, temperature difference after 4h of recovery and natural gamma radioactivity data for B2

Figure 6.15 shows recovery profiles obtained 4 h after each heat input interruptions in B2. The profiles are similar to the one obtained after the end of the heating phase (Figure 6.15 right), displaying the heat transfer rate variation with depth. The recovery profiles of the 7-days duration DTRTs in the other three BHEs were studied in Chapter 5. In B4, a fractured zone located at a sandstone/siltstone layer was detected as a local maximum in the temperature profile. The correlation of the temperature profiles after 4 h of recovery with the gamma-ray data was also consistent for all the three BHEs (B1, B3 and B4), providing the same resolution in the detection of layers with higher thermal diffusivity (layer thickness more than 1.2 m). Based on theese observations, it is possible to conclude that obtaining the temperature profile after 4 h of recovery can allow to detect layers with high heat transfer rate, which contributes to the optimal design of BHEs. Based on the measurements of this case study, this seems to be invariant to the duration of the heating phase (investigated range of 7 d to 7 months), the grouting thermal conductivity (investigated range of 1.0 W/mK - to 1.8 W/mK) or the U-pipe configuration (single-U or double-U). The resolution of the applied procedure is limited by the measurement parameters, spatial resolution and sampling interval. The fiber optic recovery profiles in this study were obtained for sampling interval of 20 cm and spatial resolution of 2 m. Lower spatial resolution and sampling interval could improve the resolution of the results. Though this is not the case for a longer heating duration of the test.

Figure 6.15 - Temperature difference profiles 4 h after the first heat input interruption (t=95.3 d), the second heat input interruption (t=191.9 d) and the end of the heating phase (t=214.9 d) in B2

6.4 Numerical modelling

This section presents the numerical simulation of the long-duration DTRT in B2. The aim of this modelling is to investigate if the ground thermal conductivity estimated by the ILS model analysis of a typical-duration TRT can fairly reproduce the water temperature evolution for longer heating periods and different modes (heating/recovery). It also allows to study the temperature distribution at the borehole cross section and to further investigate the fiber optics profiles measured at the outer surface of the pipes at the heated BHE. Moreover, the comparison between the numerical and the measured temperature profiles in the surrounding

143

bedrock will allow to detect the effect of various factors on the temperature field evolution in the rock mass.

6.4.1 Geometry and boundary conditions

To simulate the in-situ TRT, a 3D numerical model was developed by using the finite element code LAGAMINE (Charlier et al., 2001; Collin et al., 2002). The BHE of 95 m length was modelled with depth discretisation of maximum 5 m. The ground was extended 100 m below the borehole, covering a radial distance of 20 m, including only conductive heat transfer. The generated mesh consists of 225000 nodes (4-node, 3D finite elements), including an explicit modelling of each BHE component. The flow into each pipe leg is represented by a 1D finite element, following the depth discretisation of the 3D mesh. Each node of this element interacts with a node at the center of the corresponding pipe leg of the 3D mesh (Figure 6.16).
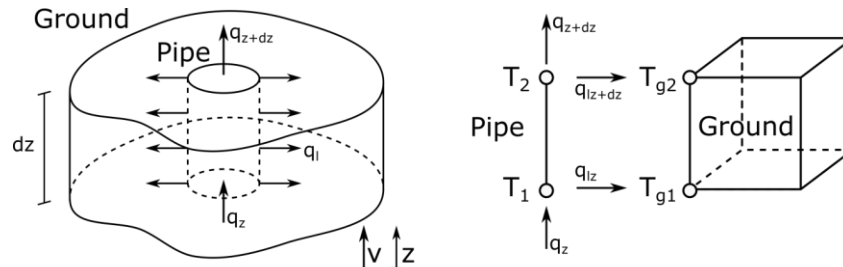
Figure 6.16 - Longitudinal qz and lateral ql heat fluxes between a piece of pipe and the ground (left) and discretisation of the problem with a 1D element (right)

A fluid velocity and a convective heat transfer coefficient was imposed on each node of the 1D finite elements, to simulate the longitudinal and the lateral heat flux respectively. The convective heat transfer coefficient, h, is calculated as:

$$h = Nu \cdot \lambda / D_h ,$$

where D_h : the hydraulic diameter of the pipe *(m)*,

λ : the fluid thermal conductivity *(W/mK)* and

Nu: the Nusselt number *(-)*.

The Nusselt number is the ratio of convective to conductive heat transfer across a boundary and for turbulent flow is given as (Gnielinski, 1976):

$$Nu = \frac{(f/8)(\text{Re}-1000)\,\text{Pr}}{1+12.7(f/8)^{1/2}(\text{Pr}^{2/3}-1)}, \qquad \begin{array}{l} 0.5 < \text{Pr} < 200 \\ 3000 > \text{Re} > 5E6 \end{array}$$

This relationship depends on the Reynolds number, *Re*, the Prandtl number, *Pr*, and the Darcy friction factor, *f*. The Reynolds number is the ratio of inertial forces to viscous forces and classifies the flow as laminar, transient or turbulent. It is described as:

$$\text{Re} = \frac{\rho u D_h}{\mu},$$

where ρ: the fluid density *(kg/m³)*,

u: the mean fluid velocity *(m/s)* and

μ: the fluid dynamic viscosity *(Pa s)*.

The Prandtl number is a measure of diffusion with respect to the fluid velocity, defined as:

$$\text{Pr} = c_p \mu / \lambda$$

where c_p: the fluid specific heat (J/kgK).

The Darcy friction factor is defined, for smooth pipes, as:

$$f = (0.79\ln(\text{Re}) - 1.64)^{-2}.$$

To represent the continuity of the pipe at the bottom of the pipe legs, the temperature of the upward node at this depth was imposed equal to the calculated one at the downward node. The same condition was also applied at the top of the borehole, to represent the pipe loop formed by the TRT rig equipment. A heat flux was imposed as boundary condition at the

145

inlet surface of the pipe, to simulate the injected heat during the TRT (Figure 6.17). These boundary conditions do not include an explicit modelling of the connecting pipes geometry or of the water thermal interaction with the ambient air during its circulation inside the rig. Though, the latter is taken into account in this model, by imposing the applied, and not the nominal, thermal power at the pipe inlet.
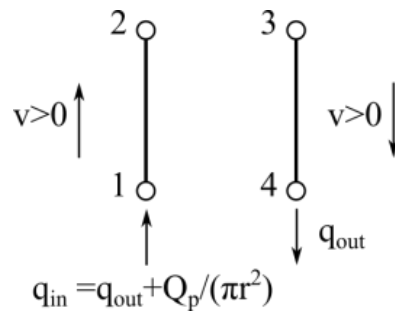

Figure 6.17 - Boundary condition between two vertical finite elements of pipe

The proposed pipe finite element is specially devoted to the modelling of the 1D advection-diffusion problem. The use of Petrov-Galerkin weighting functions reduces instabilities classically encountered. Consequently, higher time steps may be used and the computation time is strongly decreased. For example, for a model of 225000 nodes and a simulation of a 7-days TRT, the computational time was 1.5 h (computer with main memory 16 G RAM, processor Intel I7). Moreover, the 1D finite element formulation models the flow into the pipes without taking into account the grouting effect. This, in combination with its coupling with a 3D mesh, makes it suitable for reproducing temperature gradients inside the borehole for varying BHE configurations, avoiding any hypothesis on the borehole thermal resistance. Finally, imposing the total heating power as boundary condition at the pipe inlet, and not distributed along the pipe length, allows to calculate the possible varying heat transfer rate through depth. This is particularly important in the case of an anisotropic thermal behaviour of the surrounding ground. A detailed description and validation of the 1D finite element formulation can be found in Cerfontaine et al. (2016), presented in Appendix B.

Table 6.1 presents the thermal properties applied in the numerical model for the different phases of the test. All the materials, including the surrounding bedrock, are assumed homogenous media and a uniform initial temperature (11 °C) was assumed for the whole model domain. No-heat flux boundary conditions were applied at the boundaries of the model. In this model, the water temperature in each pipe cross section is assumed uniform

during the heating phases. To insure this, a sufficiently high thermal conductivity and a zero volumetric heat capacity was assigned to the 3D water elements. To simulate the single-U heating phase, a zero velocity and heat input was imposed on the nodes of the 1D finite elements corresponding to the one U-pipe. The water circulation phase without heat injection was simulated by applying a zero heat input at the inlet surface of the pipes and by imposing the corresponding h coefficient and velocity values on the 1D finite elements nodes. To simulate the recovery phases, the water thermal properties were assigned to the water elements of the 3D mesh ($\lambda=0.58$ W/mK, $\rho c_\rho=4.184{\cdot}10^3$ kJ/m^3K) and a zero velocity and heat input was imposed on each node of the 1D finite elements. The high h coefficient values applied during the recovery phase and at the non-heated U-pipe (single U-pipe heating) allow numerically to transfer the water temperature of the 3D mesh nodes at the center of the pipes to the 1D elements nodes.

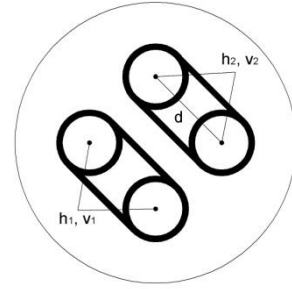The bedrock thermal conductivity was assumed constant with depth and time (2.9 W/mK), equal to the one resulting from the ILS model analysis of the TRT data, presented in Chapter 5 (section 5.2). A constant grouting thermal conductivity (1.0 W/mK) was applied for the whole test duration. An investigation of the grouting thermal conductivity value in B2 was also presented in Chapter 5 (section 5.3).

Table 6.1 - BHE geometry and materials properties for the numerical modelling in B2

r_{bor} (m)	0.068	λ_{pipe} (W/mK)	0.42[*]
$r_{p,inner}$ (m)	0.0131	$\rho c_{\rho,pipe}$ (kJ/m³K)	2083[*]
$r_{p,outer}$ (m)	0.016	λ_{grout} (W/mK)	1.0
d (m)	0.045	$\rho c_{\rho,grout}$ (kJ/m³K)	2500[**]
length (m)	95		

[*] handbooks
[**] handbooks, Delaleux et al. (2012)

double U-pipe heating		single U-pipe heating		water circulation		recovery	
h_1 (W/m²K)	1385	h_1 (W/m²K)	5000	h_1 (W/m²K)	1519	h_1 (W/m²K)	5000
v_1 (m/s)	0.294	v_1 (m/s)	0	v_1 (m/s)	0.323	v_1 (m/s)	0
h_2 (W/m²K)	1385	h_2 (W/m²K)	1957	h_2 (W/m²K)	1519	h_2 (W/m²K)	5000
v_2 (m/s)	0.294	v_2 (m/s)	0.425	v_2 (m/s)	0.323	v_2 (m/s)	0

6.4.2 Results

Figures 6.18 and 6.19 compare the measured and the numerically obtained temperature evolution during the heating phase and the recovery phase respectively. Given that a uniform initial temperature (T_0=11 °C) was assumed for the whole model domain and the initial measured temperature gradient was not simulated in the numerical model, the comparison is presented in terms of temperature increase for both numerical and experimental data (DT=T-T_0). Experimental data for the heating phase correspond to the water temperature at the pipe-inlet and outlet and for the recovery phase to the depth-average fiber optic temperature. Numerical results for both phases correspond to the pipe inlet and outlet water temperature. A varying heat input was applied, that follows the variations of the one calculated based on the pipe inlet and outlet temperature measurements (section 6.2). The numerical results can fairly reproduce the measured temperature evolution during the heating as well as the recovery phase. In this model, a uniform, constant bedrock thermal conductivity was applied during both phases, equal to the one estimated by the ILS model analysis of the TRT data after the first 60 h of the test (Chapter 5). Based on the good agreement between the experimental and numerical data, we can conclude that the mean effective ground thermal conductivity does not vary significantly during both applied modes (heating and recovery) and that groundwater

effects in the rock mass are not dominant. This is consistent with the analysis of the fiber optic profiles during the heating phase (section 6.3.1).
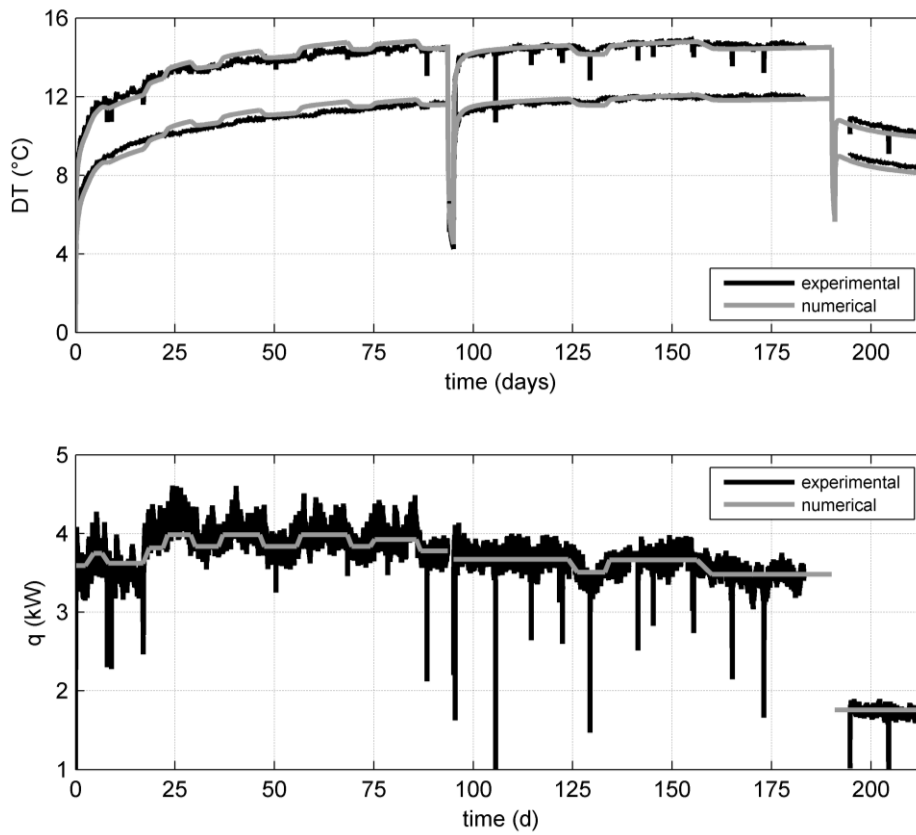

Figure 6.18 - Experimental and numerical water temperature evolution (top) and applied heating power (bottom) during the heating phase in B2
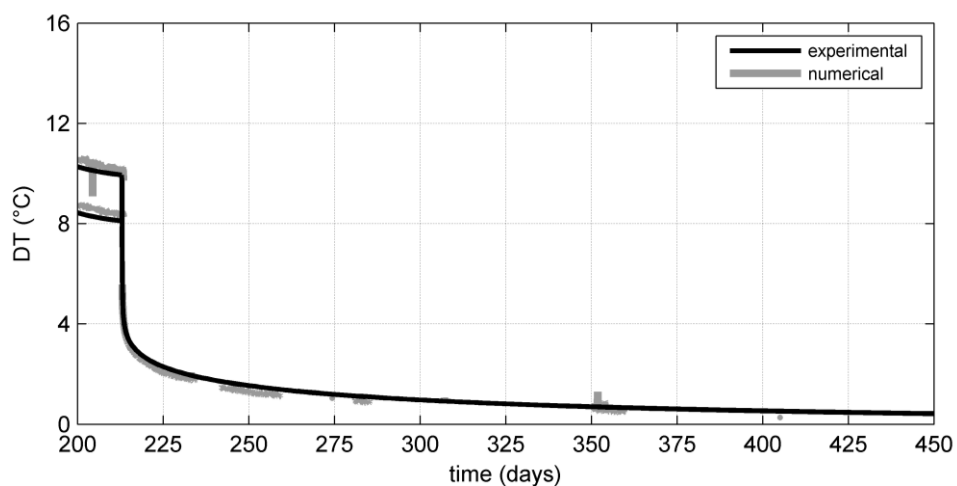

Figure 6.19 - Experimental and numerical temperature evolution during the recovery phase in B2 (numerical data: pipe inlet and outlet water temperature, experimental data: depth-average fiber optic temperature)

6.4.2.1 Water temperature evolution: effect of heat input interruptions

Figure 6.20 shows the water temperature distribution along the pipe loop during the first hours of the first heating phase (t_0=1.63 d) and of the second heating phase (i.e. after the first heat input interruption, t_0= 95.61 d). Both phases correspond to heating of the double-U pipe loop with the same applied flow rate. For both phases, the temperature profile develops gradually, obtaining the characteristic V-shape after approximately 12 min. Once it reaches the steady state, water temperature rises more quickly with time. This transition is also indicated in the water temperature evolution displayed in a semilog scale (Figure 6.20 bottom). At steady state, the transferred heat decreases while water progressively advances along the pipe loop, indicated by the non-symmetrical obtained profiles. This is attributed to the lesser amount of heat subjected to each water section, starting with the maximum value at the ground level at the pipe inlet, and to the thermal interaction between the pipe legs. Approximately 65% of the injected heat is transferred in the downward pipe, while only 35% in the upward pipe, for this BHE geometry and for a flow rate of 9.5 l/min in each pipe loop. Greater variations are expected in the case of heterogeneous ground and/or due to an initial temperature gradient.

The steady-state heat transfer at the whole borehole cross section is achieved after approximately 10 h for both heating phases. At the beginning of the first heating phase, a uniform temperature (11 °C) was assigned to the whole model domain. Before starting the second heating phase, water was circulating in the pipe loops for 25.4 h. This, in combination with the preassigned recovery phase, resulted in an almost uniform temperature at the whole borehole cross section with depth (DT<0.025 °C), based on the numerical results (Figure 6.21). This small temperature variation does not seem to have a critical influence on the required time for the heat transfer to reach the steady state at the whole borehole cross section.

Before reaching the steady state, the temperature evolution inside the borehole is dominated by the borehole filling heat capacity. In B2, the assigned grouting heat capacity and thermal conductivity are 2550 kJ/m³K and 1.0 W/mK respectively. In B4, which is characterised by the same geometry and the corresponding values are 2500 kJ/m³K and 1.7 W/mK respectively, the same required time was observed based on numerical results. This is

included in the proposed range (1 h -12 h) for normal borehole sizes and ground conditions, according to Spitler and Gehlin (2015). The required time will be increased for larger boreholes.
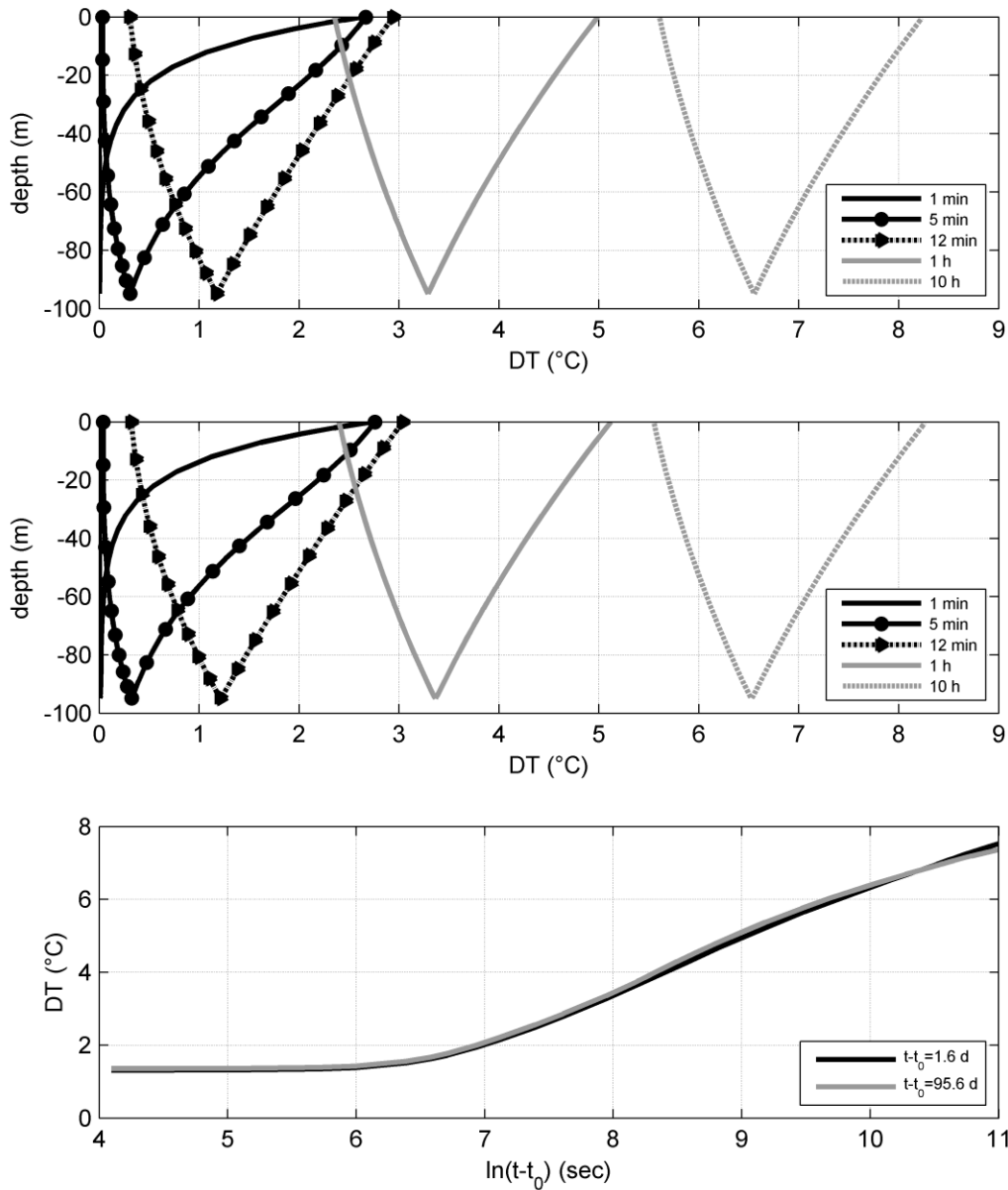

Figure 6.20 - Numerical water temperature profiles during the first heating phase (t_0=1.63 d, T_0=11 °C) (top), after the first heat input interruption (t_0= 95.61 d, T_0=15.5 °C) (middle) and mean of pipe inlet and outlet water temperature evolution for both heating phases (bottom) in B2

Figure 6.21 - Numerical temperature distribution at the borehole cross section at the beginning of the second heating phase (t=95.61 d)

Figure 6.22 shows the water profile development during the third heating phase (i.e. after the second heat input interruption, t_0= 192.6 d). This phase corresponds to the heating of the one U-pipe. The temperature profile obtains the characteristic V-shape after approximately 8 min, and the transferred heat in the downward and upward pipe is 62% and 38% respectively. In this case of the single-U configuration, a higher flow rate (13.8 l/min) than in the double-U configuration (9.5 l/min in each U-pipe) was applied. Moreover, the duration of the preassigned recovery phase was 20 h and water has not been circulated in the pipe loop before starting the heating phase. This resulted in a varying temperature at the borehole cross section along the borehole length of more than 0.2 °C (Figure 6.23).

Figure 6.22 - Numerical water temperature profiles (top) and mean of pipe inlet and outlet water temperature evolution (bottom) during the third heating phase (t_0=192.6 d, single-U configuration) in B2
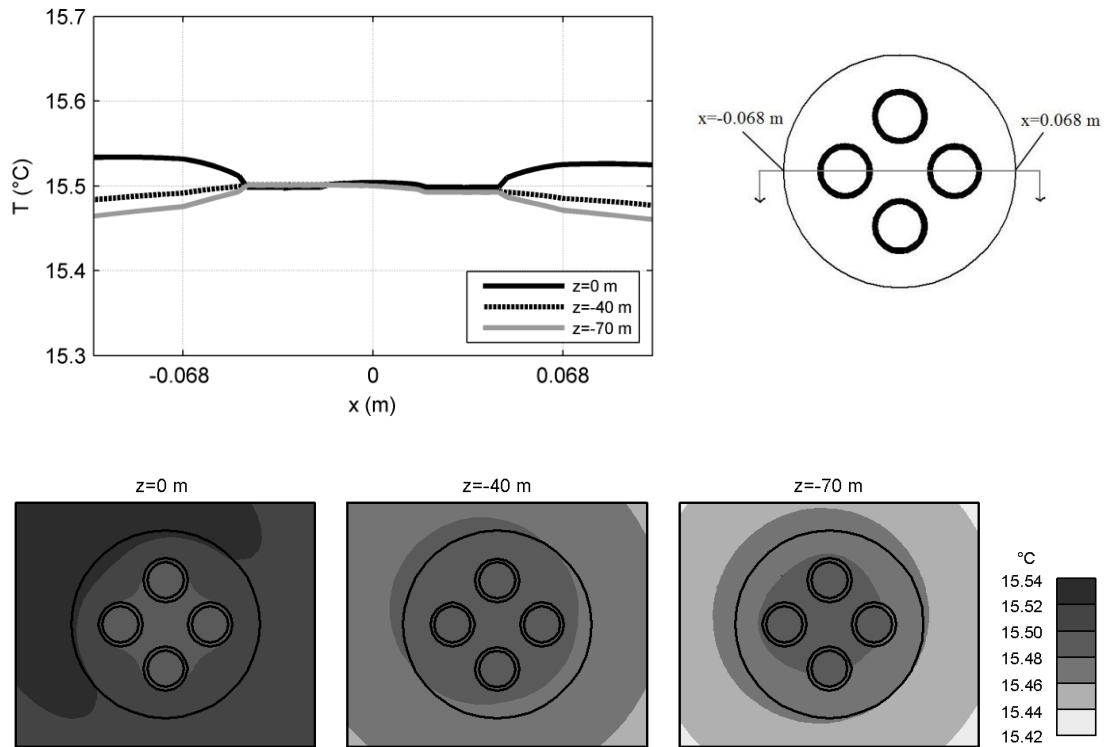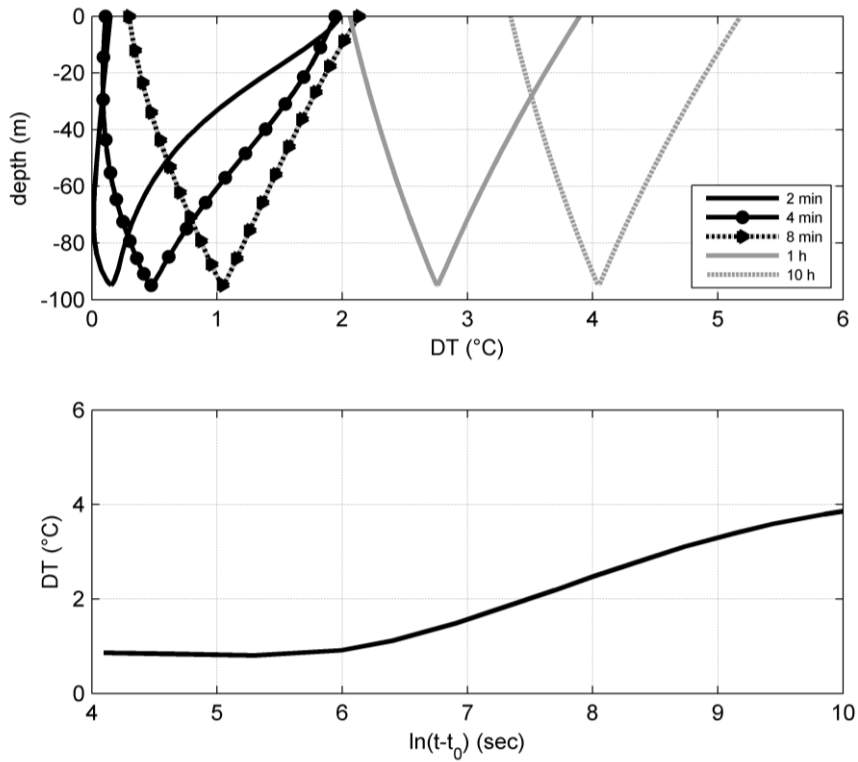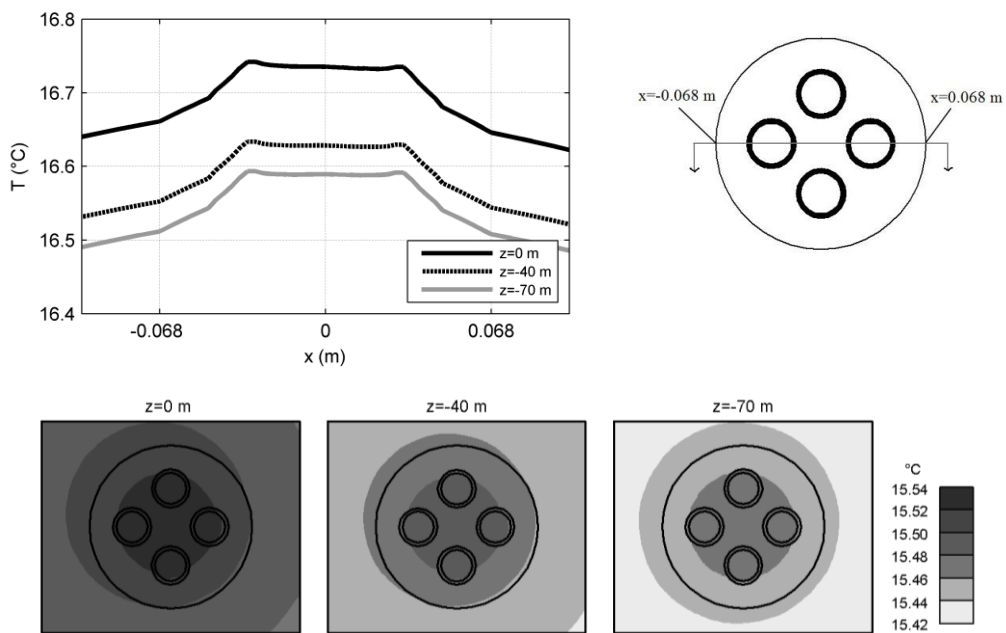

Figure 6.23 - Numerical temperature distribution at the borehole cross section at the beginning of the third heating phase (t=192.6 d) in B2

Figure 6.24 shows the temperature evolution at the surrounding ground before and after the first heat input interruption. The heat input was interrupted for 36 h (recovery). At the end of this recovery phase (t=96.7 d), temperature in the surrounding ground has decreased in a distance smaller than 1.5 m from the borehole center. Then the second heating phase started. Water temperature increases at a high rate for the first 36 h (96.7 d<t<98.2 d), equal to the duration of the recovery phase. However, after 36 h of heating, water and ground temperature is lower than the one reached before the interruption. For the rest of the heating phase, heat is progressively transferred to the surrounding ground, while the water temperature remains lower than the expected one, obtained by interpolating the temperature evolution of the first heating phase. Despite that the same nominal heating power was applied during both phases, the mean applied power of the second heating phase (3.60 kW) is lower than the one of the first heating phase (3.88 kW), due to the thermal interaction with the ambient air. This could explain the lower than expected measured water temperature during the second heating phase.

Figure 6.24 - Experimental water temperature (mean of pipe inlet and outlet) evolution (top) and numerical temperature evolution at the ground surface (middle, bottom) before and after the first heat input interruption

Figure 6.25 shows the temperature evolution at the surrounding ground before and after the second heat input interruption. In this case, the heat input was interrupted for 20 h (recovery). Then the single-U pipe heating started with the total heat input in the BHE decreasing in half. As also observed in the first heat input interaction, water temperature increases at a high rate for the first 20 h (192.6 d<t<193.5 d), equal to the duration of the recovery phase. While heating continues, water temperature is not only lower than before the interruption, but also decreases with time. This is also observed in the numerical results, where a constant heat

input was applied during this period. The decreasing water temperature is attributed to the non-uniform temperature field, developed by a higher applied heat input before the interruption. These results highlight the sensitivity of the water temperature evolution on a variable heating loading.
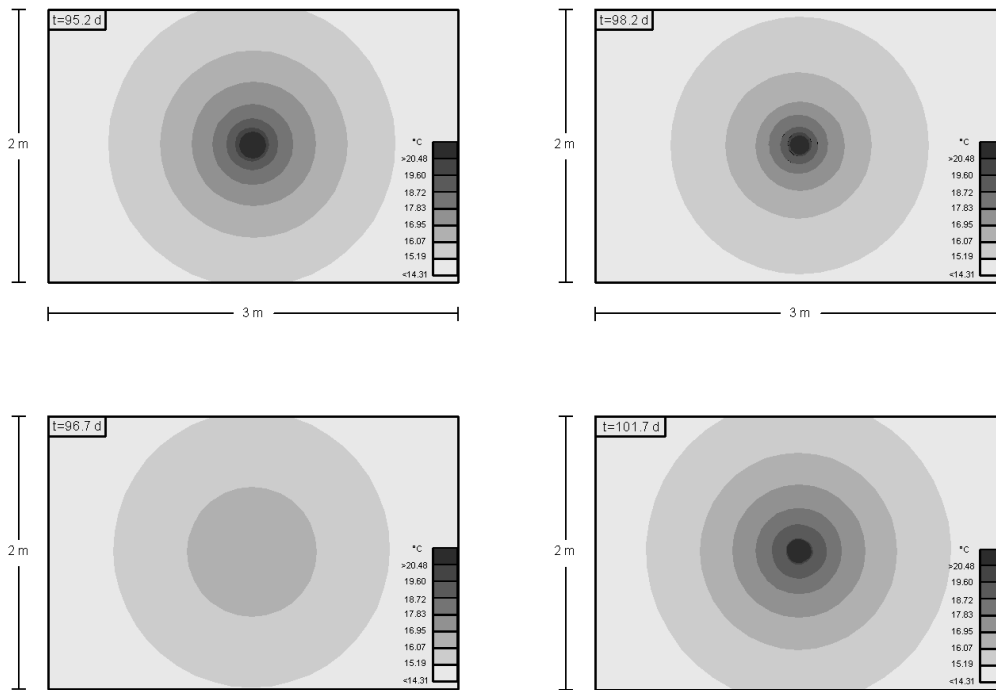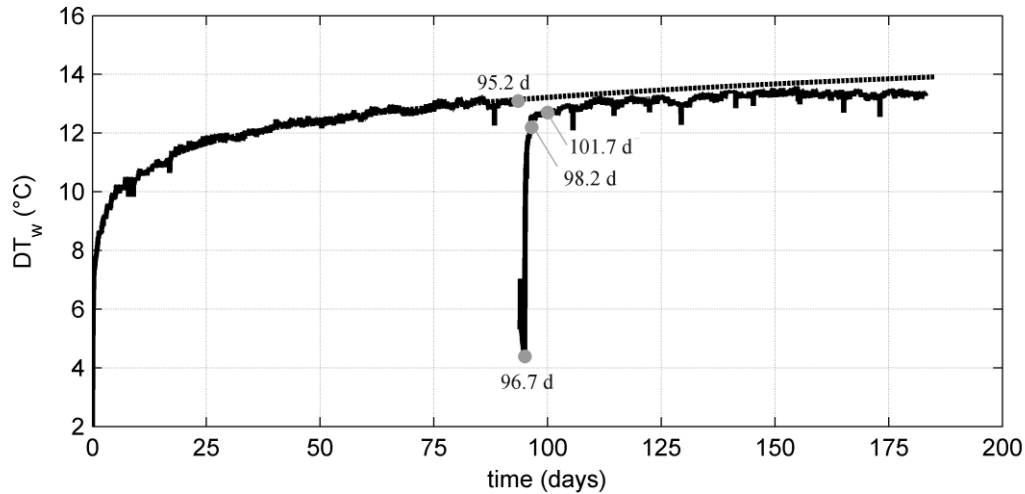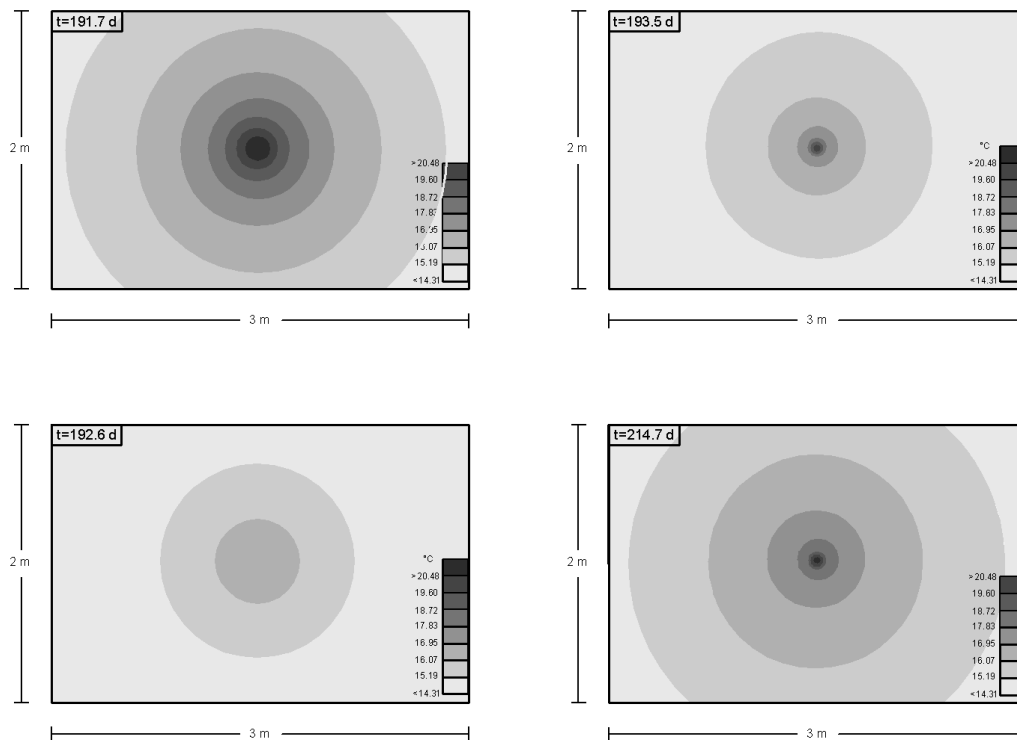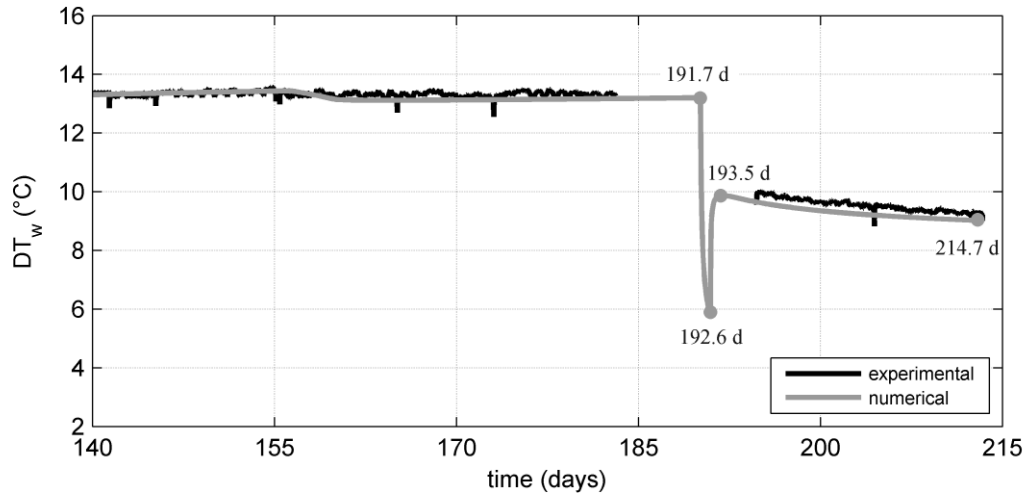

Figure 6.25 - Experimental water temperature (mean of pipe inlet and outlet) evolution (top) and numerical temperature evolution at the ground surface (middle, bottom) before and after the second heat input interruption

Figure 6.26 shows the numerically obtained temperature evolution at the borehole cross section during the first hours of recovery. The temperature field is not symmetrical since the recovery phase followed the heating of the one U-pipe loop, located at the upper right part of the borehole cross section. The temperature inside the borehole varies less than 1 °C after 2 h of recovery and becomes almost uniform (DT<0.1°C) after 24 h. During the first 24 h, water temperature decreases at a high rate of 0.22 °C/h (Figure 6.27), provoked by the non-uniform temperature field inside the borehole. After approximatelly 7 months of recovery (equal to the heating phase duration), water temperature has not fully recovered to its undisturbed value (DT=0.6 °C). The temperature difference between the water and the unbdisturbed ground reaches the order of 0.1 °C after 14 months of recovery.
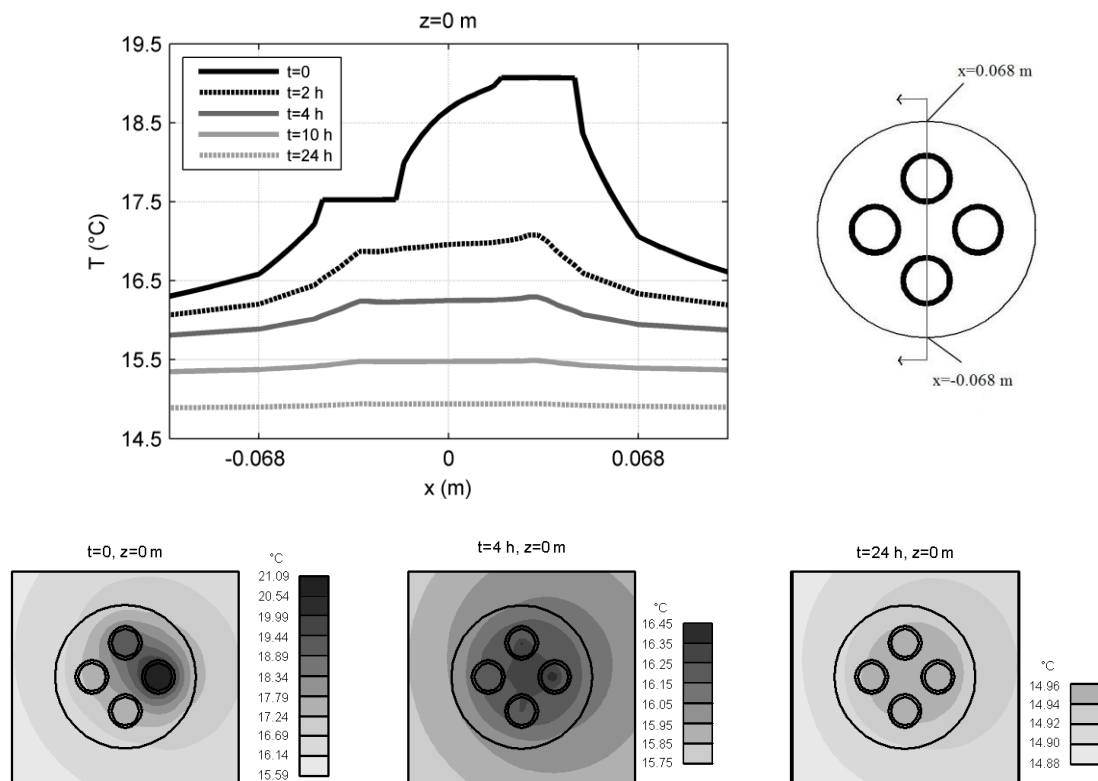
Figure 6.26 - Numerical temperature distribution at the borehole cross section during the first hours of recovery in B2
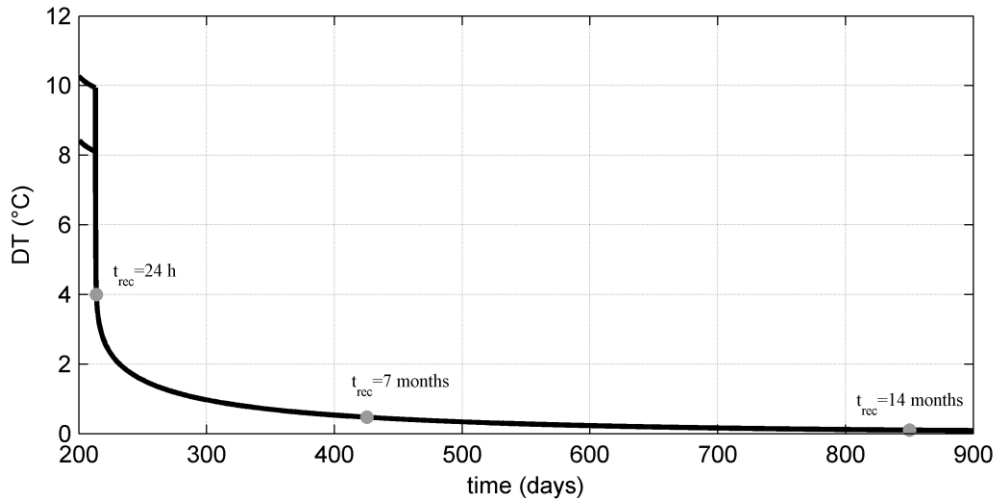
Figure 6.27 - Numerical water temperature evolution during the recovery phase in B2

6.4.2.2 Comparison with fiber optic profiles

The fiber optic profiles during the heating phase are characterised by spatial oscillations along the whole pipe length, including overlapping of the downward and upward measured temperature (section 6.3.1). Given that the exact position of the cable at the outer surface of the pipes is not well known, this section investigates based on the numerical simulation if the recorded oscillations could be attributed to the varying position of the cable at the outer surface of the pipes.

The temperature distribution at the borehole cross section, based on the numerical results, is presented in Figures 6.28 and 6.29, for the double-U and the single-U heating phase respectively. The distribution is not uniform at the borehole cross section, controlled by the relative position of the pipe legs and the thermal conductivity of the different materials, for both configurations. Temperature vary in the order of 1 °C along the outer surface of the each pipe leg of the double-U configuration, depending on the exact location of the measurement point. Higher temperatures are observed between the pipe legs and lower temperatures close to the borehole wall. The temperature field distribution is symmetrical in this case, since both U-pipes are heated. A varying temperature is also observed in the case of the single-U configuration, in the order of 0.5 °C, with higher temperatures between the heated pipe legs. The temperature field distribution is not symmetrical in this case, given that the heated U-pipe is placed at the upper right part of the borehole section.

158
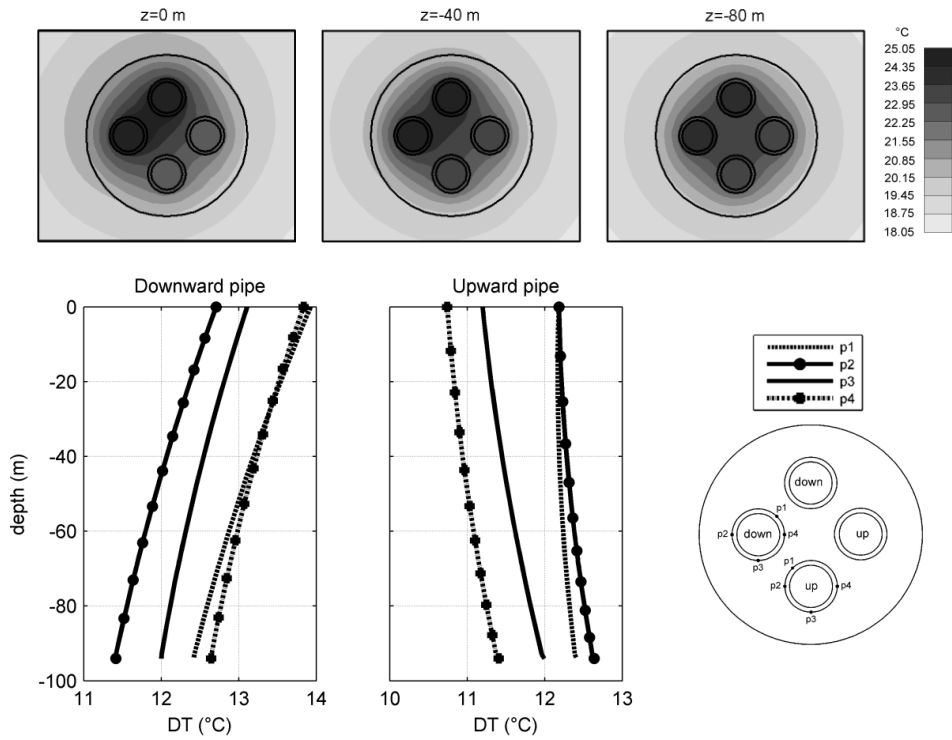
Figure 6.28 - Numerical temperature distribution at the borehole cross section at steady-state heat transfer condition in the double-U configuration in B2 (t=95 d)
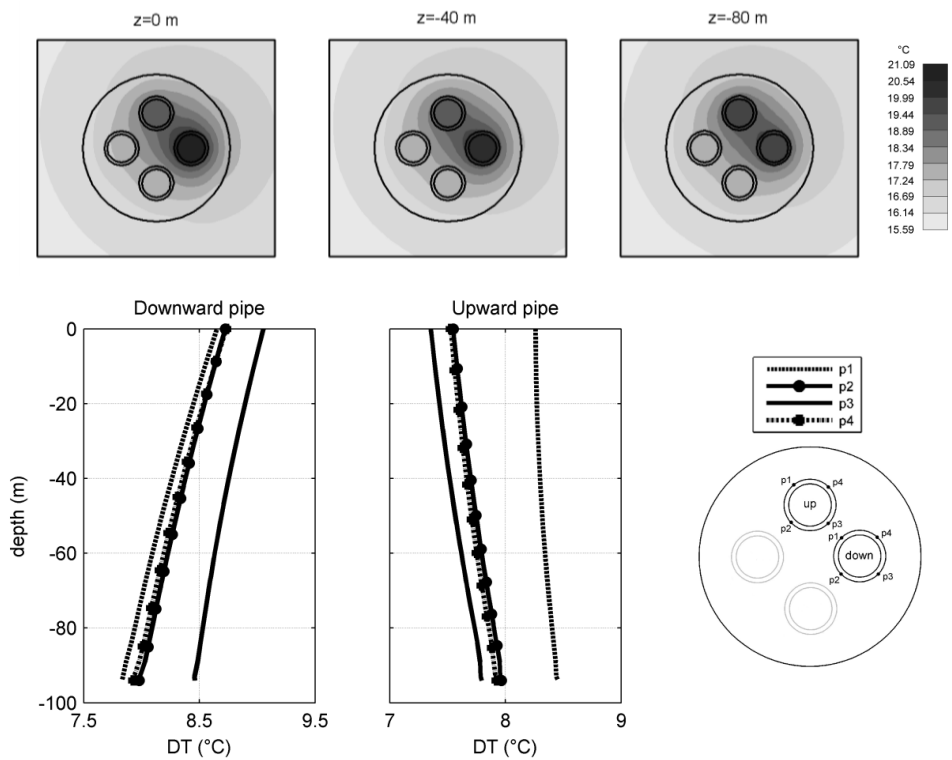
Figure 6.29 - Numerical temperature distribution at the borehole cross section at steady-state heat transfer condition in the single-U configuration in B2 (t=214 d)

The temperature envelopes for both pipe legs of each configuration are presented in Figures 6.30 and 6.31, together with the fiber optic measurements. The measured temperature is in the range proposed by the numerical results for most of the borehole length, justifying the observed oscillations. The flow rate direction was inversed during the single-U heating. This means that the downward pipe of the double-U configuration coincides with the upward pipe of the single-U configuration (pipe leg 1) and vice versa. The oscillations exceeding the numerical temperature envelopes are mainly located at the same depth for both pipe legs. Moreover, measured temperature is significantly lower (in the order of 1 °C) than the numerical one between 20 m to 25 m depth in pipe leg 2. This is extended until a depth of 30 m for pipe leg1. At this depth (20 m to 30 m), the bedrock is characterised by fractures that could be filled with grouting material and modify locally the effective rock thermal conductivity. This effect is not simulated in the numerical analysis and might contribute to the observed difference. Other reasons that could partially contribute to the fiber optic oscillations are the accuracy of the fiber optic measurements, the possible detachment of the fiber optic cable and the varying heat transfer rate with depth due to the bedrock heterogeneity. However, the latter could not explain the overlapping of the upward and downward profiles or the locally increasing temperature along the direction of the water flow, since it would indicate that heat is transferred from the ground to the circulating water during the heating.
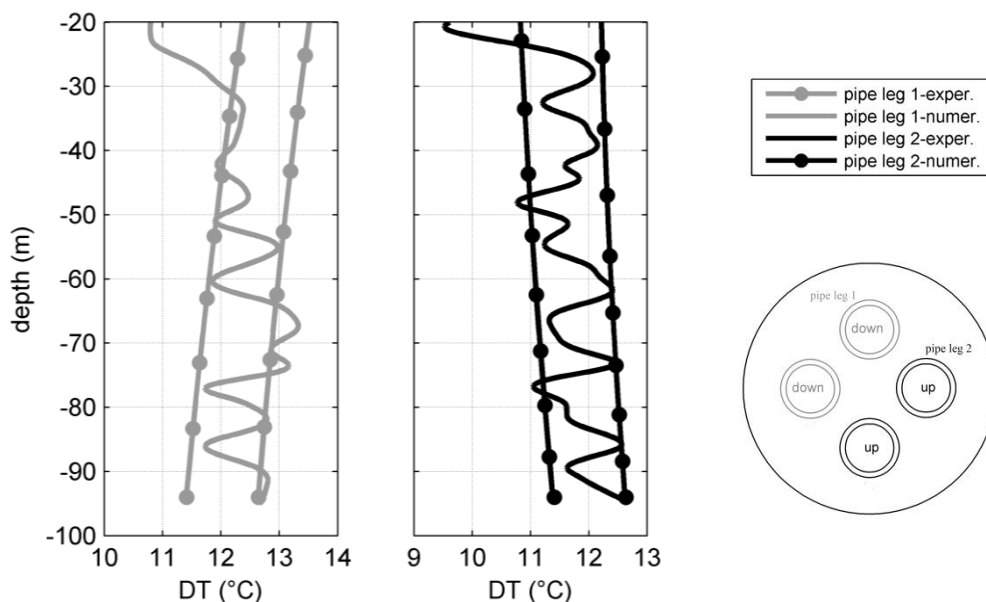
Figure 6.30 - Experimental and numerical temperature profiles at the pipes outer surface for the double U-pipe heating in B2
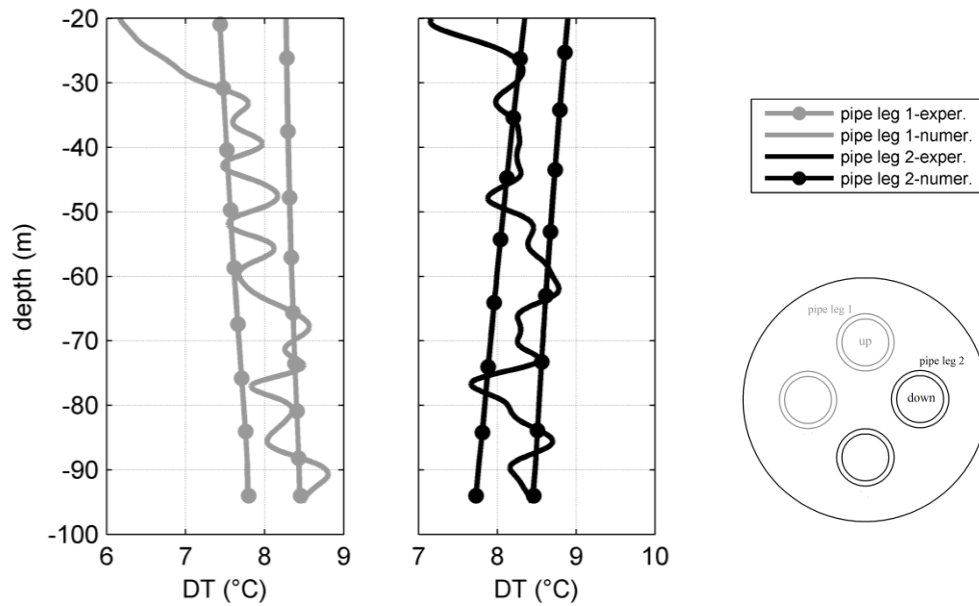
Figure 6.31 - Experimental and numerical temperature profiles at the pipes outer surface for the single U-pipe heating in B2

6.5 Thermal plume in the surrounding heterogeneous bedrock

This section presents the temperature evolution in the rock mass simulated by the numerical analysis and measured by the fiber optics at the location of the B1, B3 and B4, during the long-duration TRT in B2. In the numerical analysis, a uniform initial temperature (11 °C) was assumed for the whole model domain and the surrounding bedrock was considered a homogeneous, isotropic medium. The numerical results allow to study the influence of the distance to the heating source and the end effect in the ground surrounding the bottom of B2.

The fiber optic measurements presented in this section were calibrated by lowering a RTD probe (T±0.15 °C, Class A) inside the pipes after each measurement and measuring the temperature at two different depths. The relative position of the boreholes (B1-B4) was chosen as presented in Figure 6.32 (top) in order to investigate any possible anisotropic thermal behaviour of the bedrock along two perpendicular directions: the first along the axis crossing B1 and B2 and the second along the axis crossing B2, B3 and B4. After drilling the boreholes, a borehole televiewer was lowered down inside the four boreholes and natural-gamma radiation emitted by the surrounding bedrock was measured every 5 cm. The different

rock layers crossing the boreholes were identified and the layer dip angle was determined based on the gamma-ray data (Chapter 2). The layer dip angle was also determined based on cuttings thermal conductivity measurements (Chapter 2) and based on the fiber optic measurements during the recovery phase of the in-situ DTRTs (Chapter 5). All the three procedures result in a mean layer dip angle of approximately 45° SE. Due to the layer dip angle orientation, B1 and B2 are characterised by roughly the same lithostratigraphy, which is observed at different depths in B3 and B4 (Figure 6.32 bottom). Moreover, azimuth and deviation were measured by magnetometers and inclinometers in the four boreholes. The inclination of the borehole at each point was calculated based on the moving average of these data over an interval of 10 cm, with an orientation precision of ±0.5° and ±1.0° for the inclination and the azimuth respectively. The horizontal distance between B2 and the other three boreholes was also calculated based on theese data, as presented in Figure 6.33. The distance between B2 and B1 oscillates around 4.1 m. The distance between B2 and B3 decreases through depth, becoming almost the half at the bottom of the boreholes. This is also the case for the distance between B2 and B4.
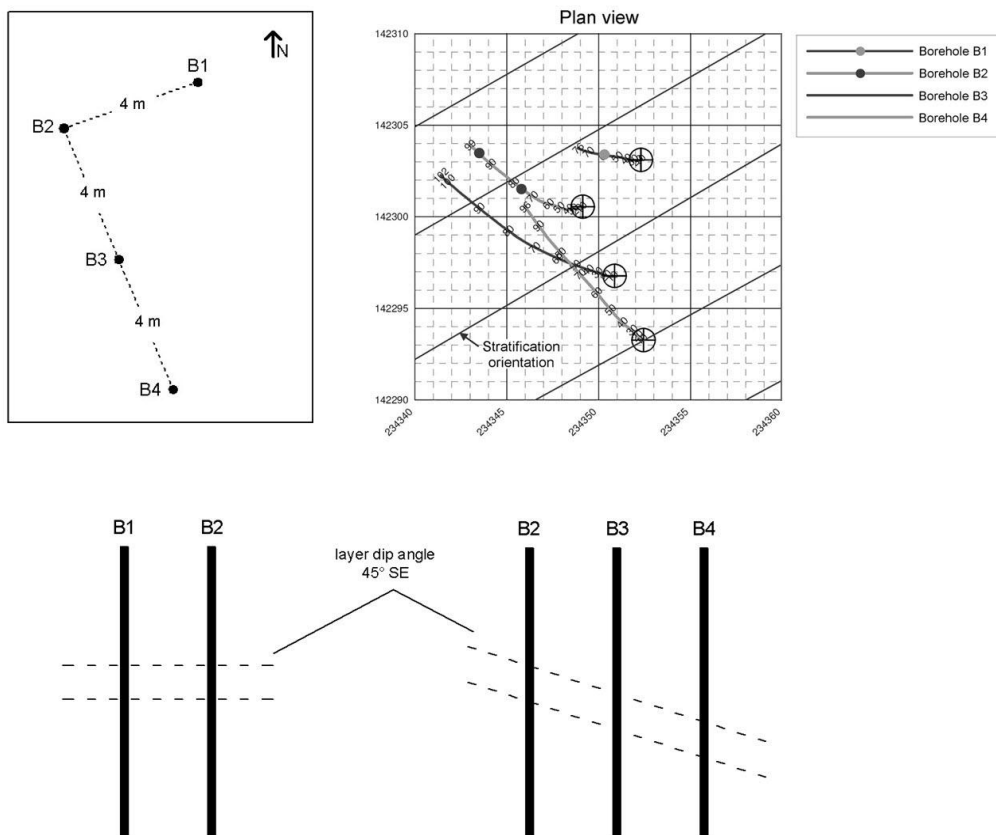
Figure 6.32 - Relative position between the four BHEs
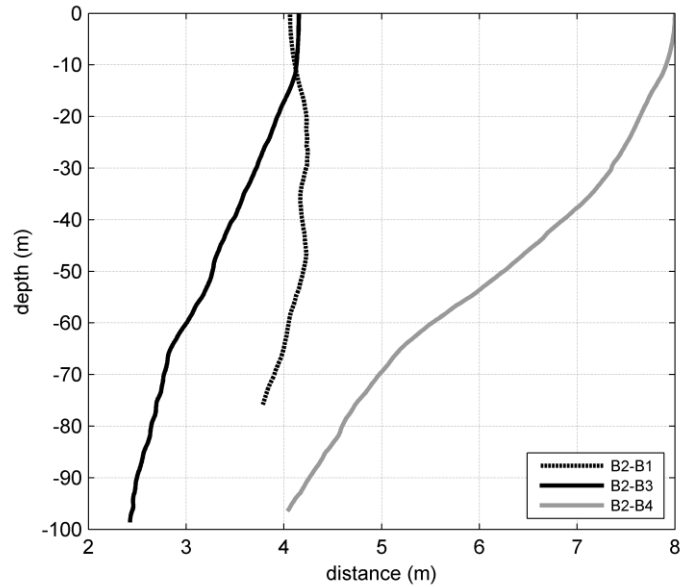
Figure 6.33 - Horizontal distance between B2 and the other three BHEs

6.5.1 Numerical investigation

Figure 6.34 shows the simulated temperature profiles with depth around the borehole in B2, which has a length of 95 m. Temperature evolves symmetrically around the borehole, since the numerical analysis was conducted for a uniform initial temperature and the surrounding ground was considered a homogeneous, isotropic medium. During the heating phase (t<214.7 d), heat flows at the radial direction in the first approximately 90 m. The transferred heat per meter of the borehole decreases in the order of 3% with depth. This has no effect in the temperature distribution at great distance (r=5 m). Close to the borehole (r=0.2 m), this effect is insignificant, since it results to a low temperature gradient of 0.001 °C/m at the first 90 m. The direction of the flow is modified in the next 5 m (bottom end thermal effects), illustrated by the decreasing temperature with depth, and heat flows at the axial direction below the center of the borehole bottom. The bottom end effects are the result of the finite length of the borehole. During the recovery phase (t>214.7 d), heat diffusion results progressively to a temperature gradient extending to the depth that corresponds to the last 10 m of the borehole length (end of the recovery phase, t=450 d).

Several studies highlight the effect of the bottom end at the borehole wall temperature distribution (e.g. Philippe et al., 2009). The results of the present study indicate that these

163

effects are non-negligible also at the rock mass temperature distribution and that the assumption of the BHE as an infinite heating source is not valid in the ground surrounding the bottom of the borehole. The influence of the end effects are observed not only close to the borehole (e.g. r=0.2 m), but also at greater distance (e.g. r=5 m) and becomes more important with increasing heating time.
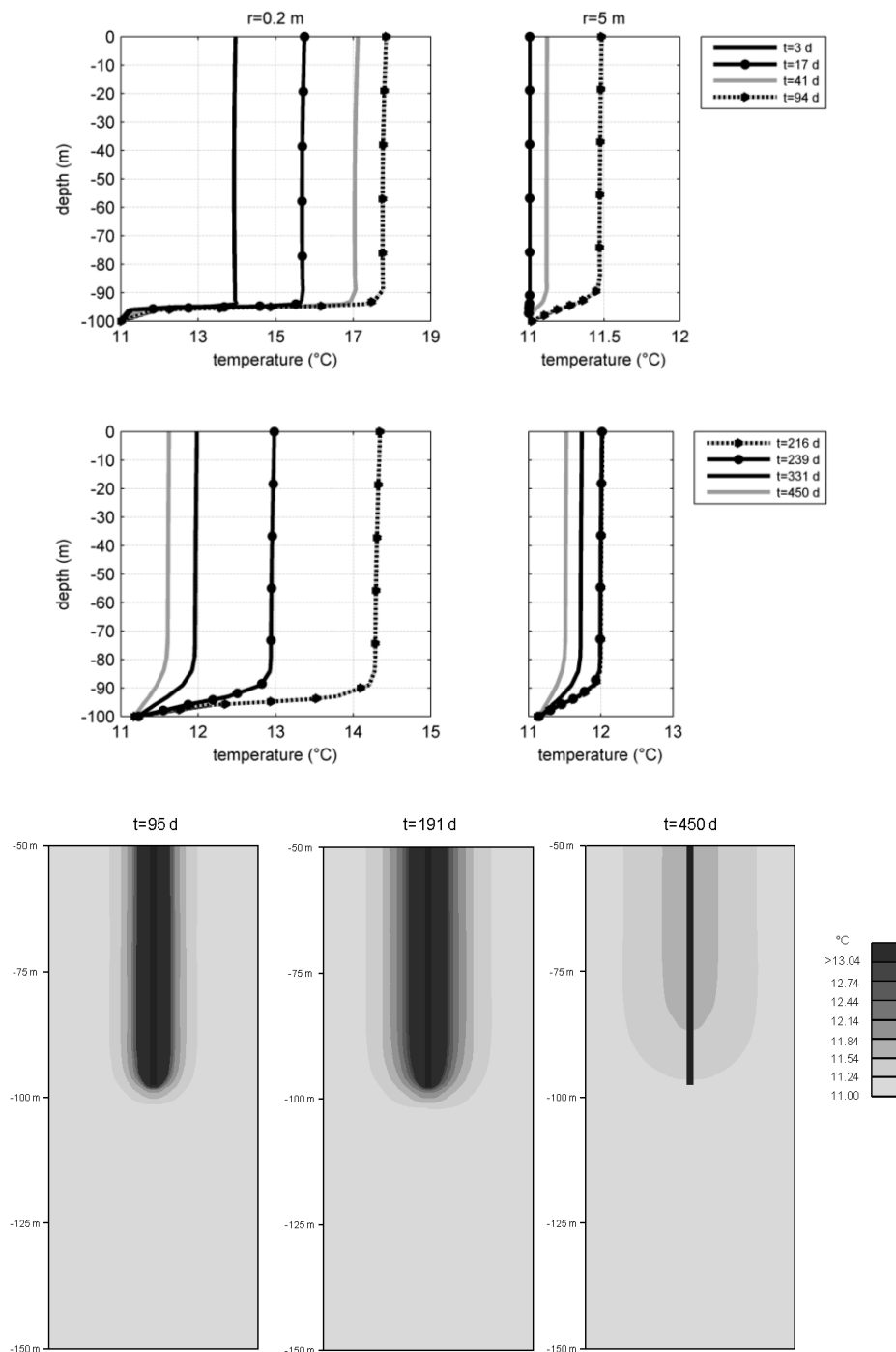
Figure 6.34 - Numerical results of the thermal effects at the bottom end during the heating and the recovery phase of the DTRT in B2 (borehole length of 95 m)

Figure 6.35 shows numerical temperature results at various distances from the borehole center at a depth of 50 m, compared with experimental results (for the water temperature). These results correspond to a uniform bedrock thermal conductivity of 2.9 W/mK and thermal diffusivity of $1.3 \cdot 10^{-6}$ m²/sec. The heat input variations applied during the heating of the double-U pipe (t<191.7 d) are illustrated in the temperature profiles of a distance lower than 1 m. The two heat input interruptions, of a duration of 36 h and 20 h respectively, and the heating of the single-U pipe, during which the total applied power in the BHE has decreased in half, result in a temperature decrease in a radius of approximately 3 m from the borehole center. The first 5 d of heating (typical TRT duration) modify the temperature at a distance lower than 2.5 m (DT>0.01 °C). This indicates that the effective ground thermal conductivity estimated based on the typical TRT procedure is representative of the ground mass expanding in a few meters around the BHE. The thermal plume reaches a distance of 5 m and 8 m after 18 d and 46 d of heating respectively (DT=0.01 °C).

During the whole recovery period, temperature decreases close to the borehole (Figure 6.36). The heat input interruption results in a modification of the temperature field followed by an inversion of the heat flow direction. Though, this is observed after several days at great distances (>5 m). In this case, the temperature field during the first days of recovery has not yet been affected by the temperature modification close to the borehole and is insufficient for the flow direction inversion. The duration of this effect increases with increasing distance from the borehole. After approximatelly 7 months of recovery (equal to the heating phase duration), temperature in the whole rock mass varies less than 0.6 °C.
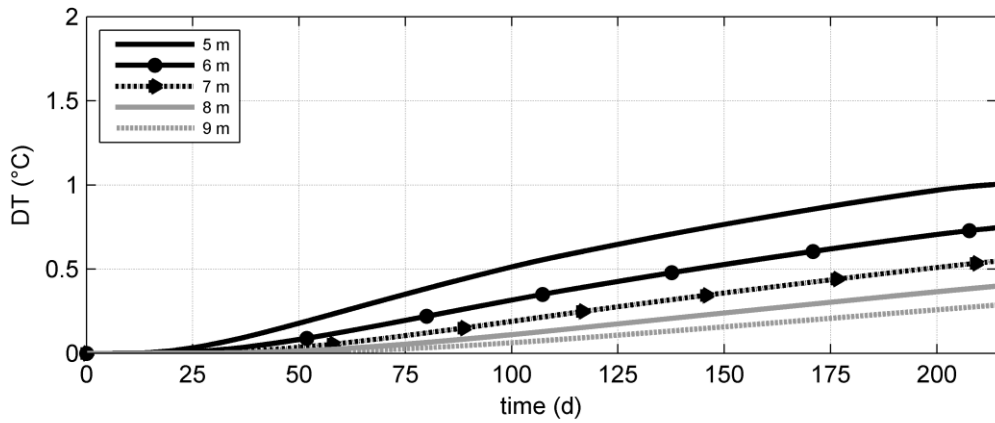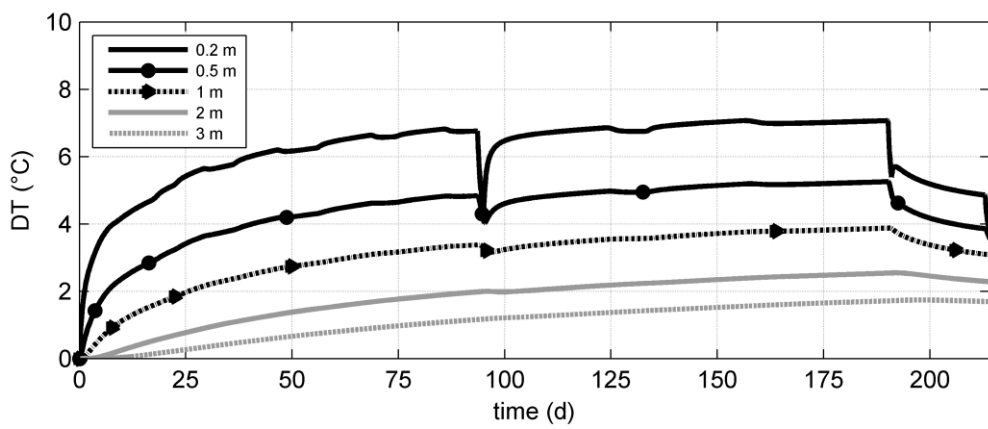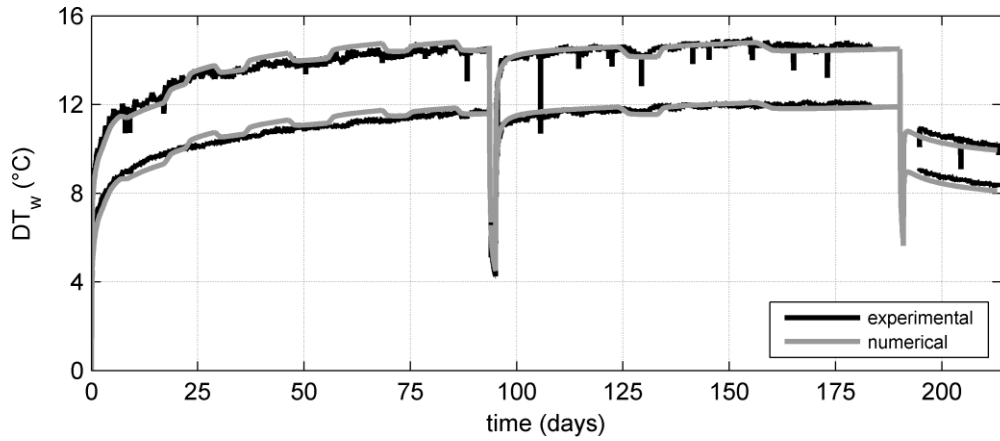
Figure 6.35 - Numerical and experimental water temperature evolution (top) and numerical temperature evolution in the rock mass (middle, bottom) during the heating phase of the DTRT in B2 (z=-50 m)
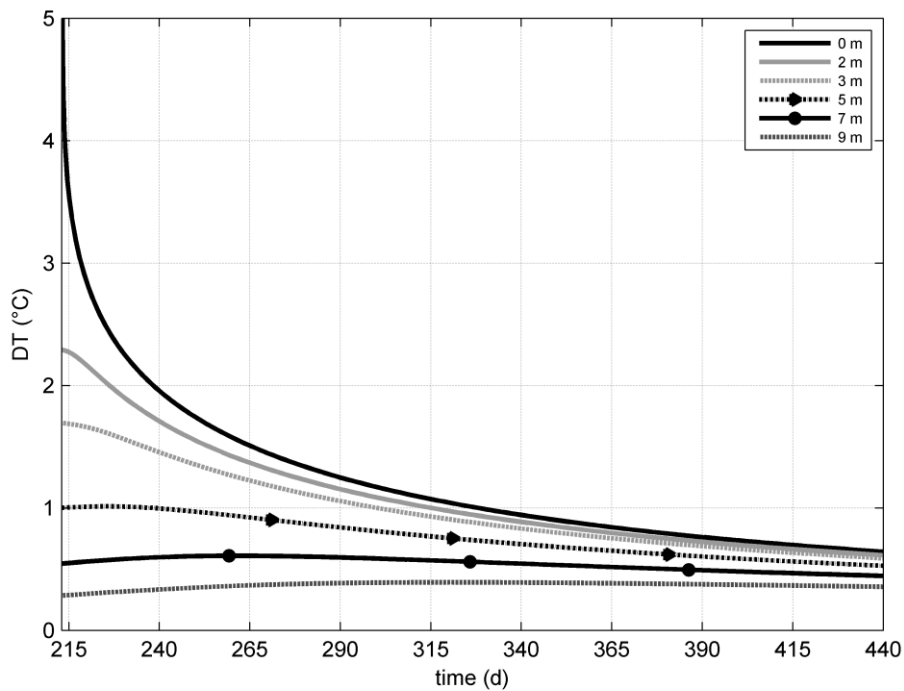
Figure 6.36 - Numerical temperature evolution in the rock mass during the recovery phase of the DTRT in B2 (z=-50 m)

6.5.2 Measured temperature evolution

This section presents the fiber optic temperature profiles in the three boreholes (B1,B3 and B4). The temperature evolution along the boreholes length is affected by several factors: varying distance from the heating source (B2), bedrock heterogeneity, layer dip angle orientation, ambient air temperature variations and end effects. The influence of theese factors are identified in the in-situ measurements, by taking into account the numerical analysis observations presented above, the geological interpretation (Chapter 2) and the analysis of temperature profiles at the undisturbed state (Chapter 4) and during the recovery of the short-duration DTRTs (Chapter 5) in the three investigated boreholes.

Figure 6.37 and 38 show the temperature evolution along B3 (length of 100 m) during the heating phase of the DTRT in B2 (length of 95 m). Based on the gamma-ray data and the recovery profiles analyses of the short-duration DTRT, B3 is characterised by two thick (> 6 m) sandstone/siltstone layers at the lower part of the borehole (between 76 and 100 m depth)

of high thermal diffusivity. In between them, shale/siltstone layers were detected of lower thermal diffusivity.

In the first approximately 18 m, ground temperature varies significantly, influenced by the ambient air temperature variations (thermally unstable zone). Temperature starts to increase at the location of the sandstone layers in the lower part of the borehole, since this part is closer to B2 than the upper part and these layers are characterised by a higher thermal diffusivity compared to the shale/siltstone layers. Temperature increases progressively at higher depths, where the distance to B2 increases, while heating continues. The two thick sandstone layers at the bottom of the borehole are clearly detected as local maxima in the temperature profiles, indicating the higher heat transfer rate along them. This is in good agreement with the geological context of the site and with the observations of the recovery profiles of the short-duration DTRT conducted in B3. These results indicate that heterogeneity effects could be also important for the study of the thermal interaction between BHEs.

During the heating of the single-U pipe, the total applied power in the BHE has decreased in half. Based on the numerical results, this resulted in a temperature decrease until a distance of approximately 3 m from the borehole center. This is also observed in the fiber optic measurements (Figure 6.38), where temperature decreases at a depth lower than 60 m (distance to B2 lower than 3 m). In the recorded profiles during the heating phase, temperature decreases at high rate in the last 10 m (90 m -100 m depth), despite that a sandstone layer is located at this depth. This is attributed to the length of the heating BHE (B2, 95 m) and to the thermal effects at the borehole end that influence the temperature field at depths close to the bottom of the borehole. In the numerical results, where bedrock heterogeneity was not taken into account, this effect was also extended to a depth lower than 90 m.

During the recovery phase (t>214.7), heat diffusion driven by the varying temperature in the rock mass progressively modifies the temperature profile, that tends to obtain the shape of the undisturbed profile (Figure 6.39, left). Figure 6.39 (right) shows temperature profiles with time at certain depths locations, during the recovery phase. Temperature decreases since the

beginning of the recovery phase along the whole borehole length. This is in good agreement with the numerical results for distances lower than 5 m.
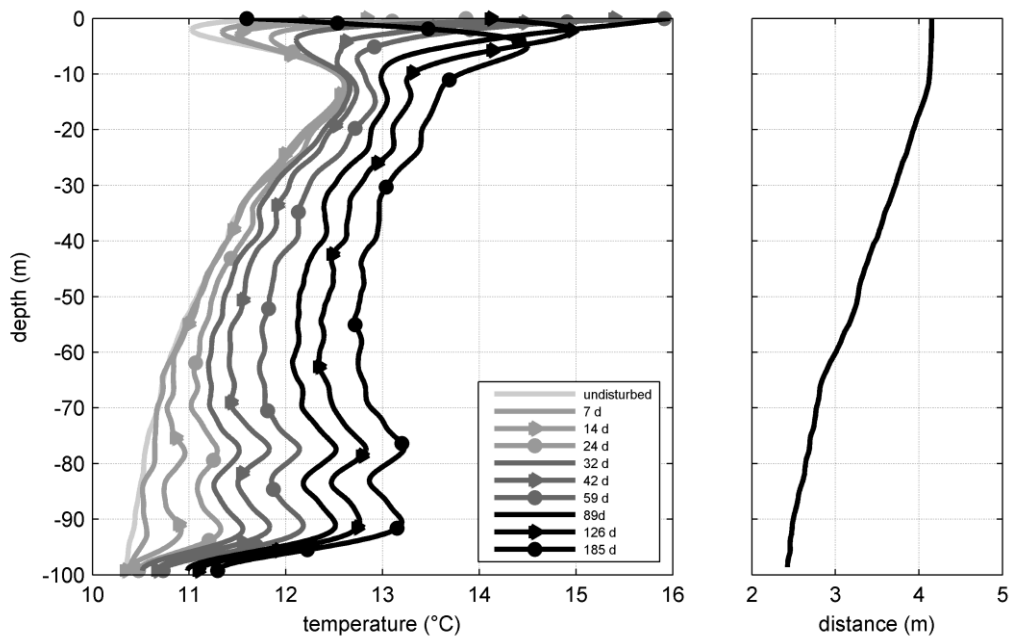
Figure 6.37 - Fiber optic temperature profiles in B3 during the heating of the double-U pipe in B2 (1.63 d<t<191.7 d)
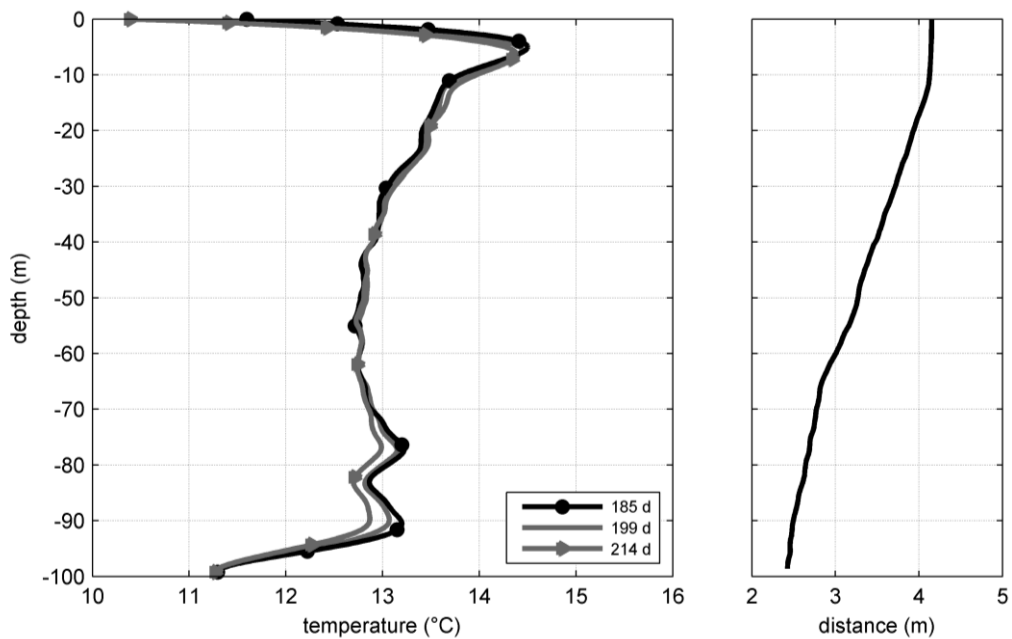
Figure 6.38 - Fiber optic temperature profiles in B3 during the heating of the single-U pipe in B2 (192.6 d<t<214.7 d)
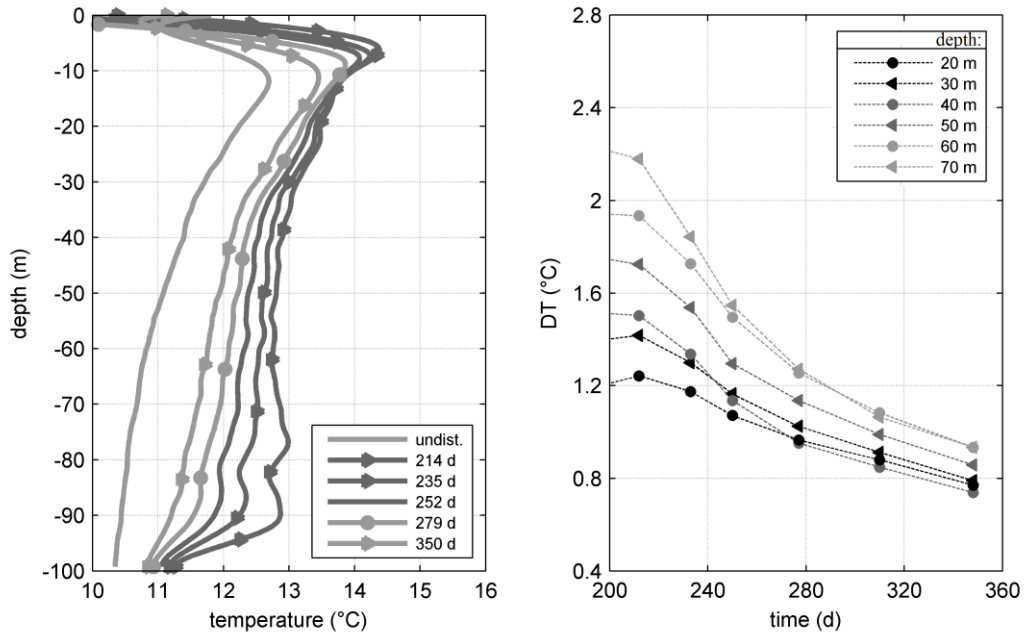
Figure 6.39 - Fiber optic temperature profiles in B3 during the recovery phase (t>214.7 d)

Figure 6.40 show fiber optic temperature profiles in B4 (length of 95 m). In this borehole, the thick sandstone layers at the bottom of the borehole are located approximately 3.5 m deeper than in B3 due to the layer dip angle orientation. Temperature start to increases later than in B3 and remains lower during the heating phase, since this borehole has a greater distance from B2 than B3. As also observed in B3, temperature starts to increase at the lower part of the borehole at the location of the sandstone layers and increases progressively at higher depths while heating continues. Close to the ground surface, the air temperature effect is also displayed in these measurements. The temperature decrease in the last 5 m (90 m -95 m depth) could be attributed to the end effects influence. However, this is not evident in this case, since a shale/siltstone layer is located at the bottom of the borehole (91.6 m - 95 m depth) which could also contribute in the observed temperature decrease.

Figure 6.41 shows the measurements during the recovery phase in B4 (t>214.7 d). Below a depth of 70 m, the distance to B2 is lower than 5 m, and temperature decreases since the beginning of the applied recovery phase. At depths corresponding to a distance between 5 m and 6 m, temperature starts to decrease approximately 38 d after the heat interruption. At greater distance (d>6 m), temperature increases during the first 65 d of the recovery phase. These observations are in good agreement with the recovery behaviour of the rock mass based on the numerical analysis.

170
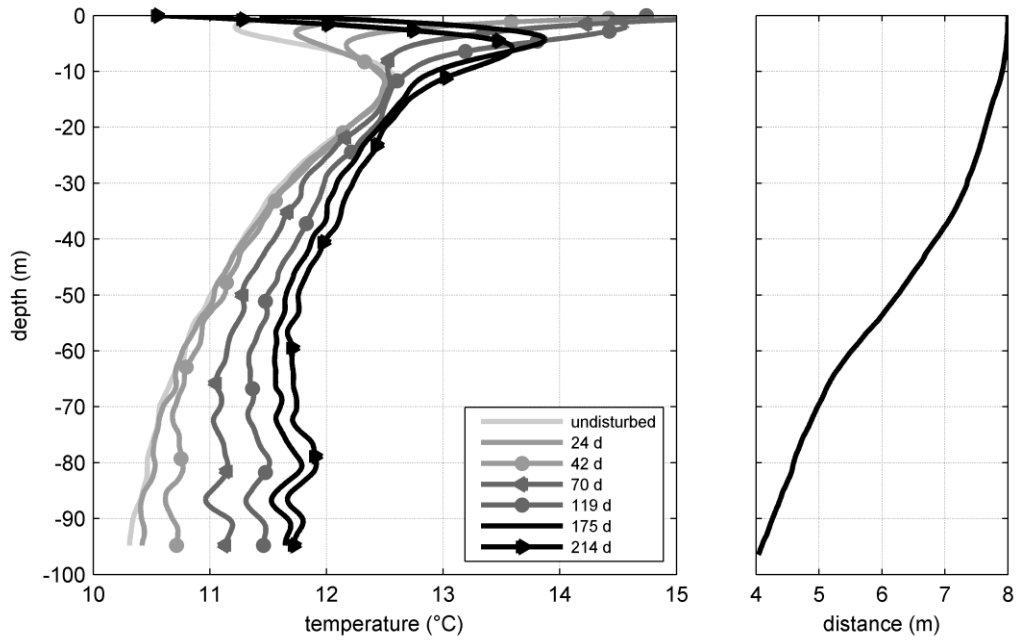
Figure 6.40 - Fiber optic temperature profiles in B4 during the heating phase (1.63 d<t<214.7 d) (left)
and horizontal distance between B4 and B2 (right)
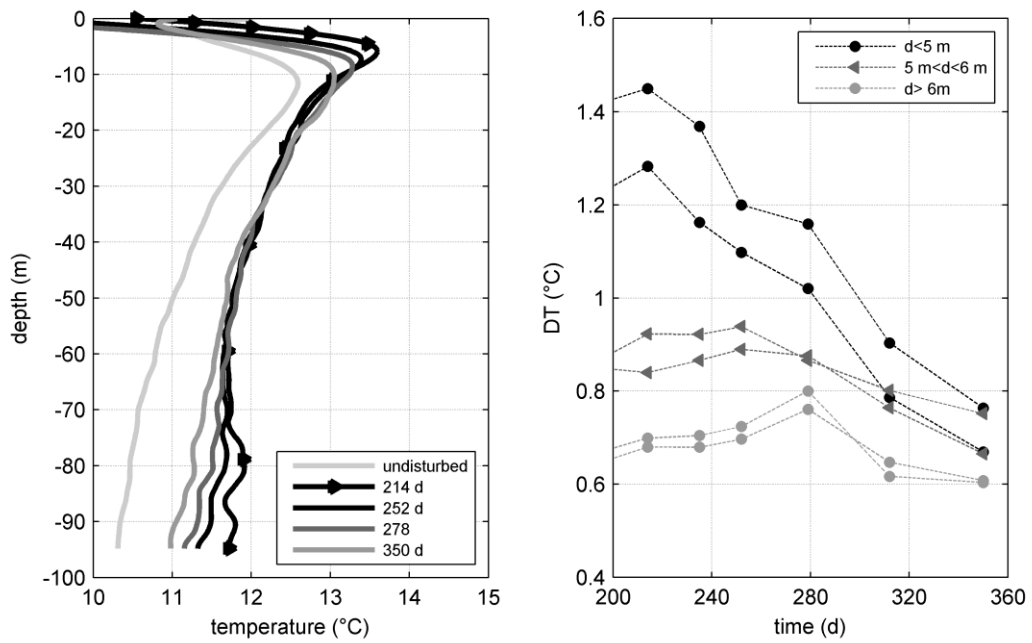
Figure 6.41 - Fiber optic temperature measurements in B4 during the recovery phase (t>214.7 d)

The temperature evolution in B1 is displayed in Figures 6.42 and 6.43. In this case, the distance to the heating BHE is almost constant along the borehole length. It is observed that the measured profiles are parallel to the undisturbed profile, during the heating and the recovery phase. Local maxima at the profiles during the heating phase correspond to the locations of sandstone layers thicker than 1.2 m (at 22 m, 34 m, 49 m and 77 m depth). The air temperature influence is also observed at the top meters. The influence of the end effects can not be identified in this case, since B4 is 10 m shorter than B2.
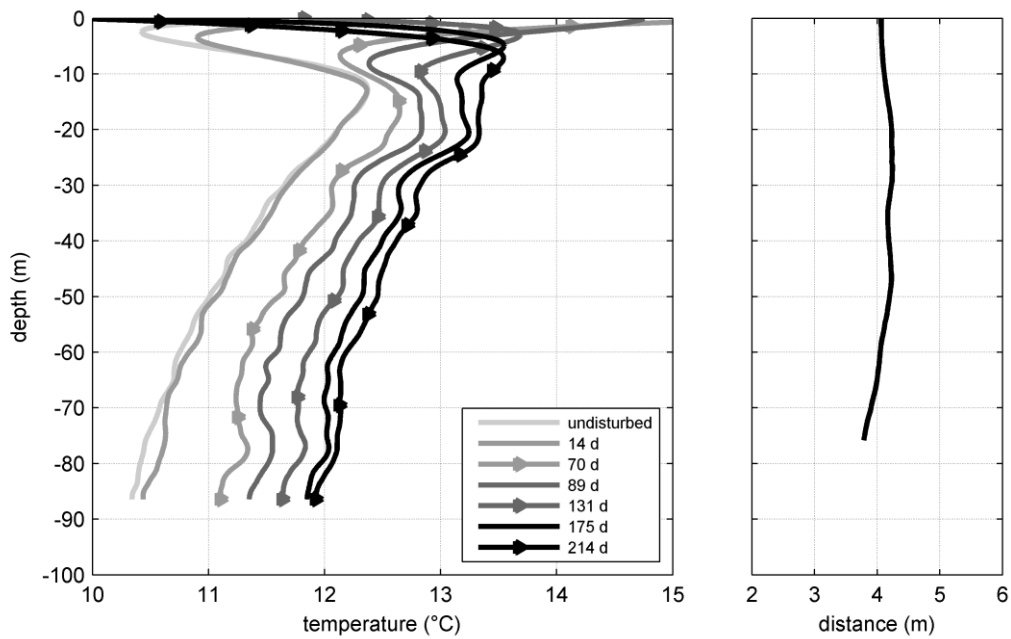
Figure 6.42 - Fiber optic temperature profiles in B1 during the heating phase (1.63 d<t<214.7 d) and horizontal distance between B1 and B2 (right)
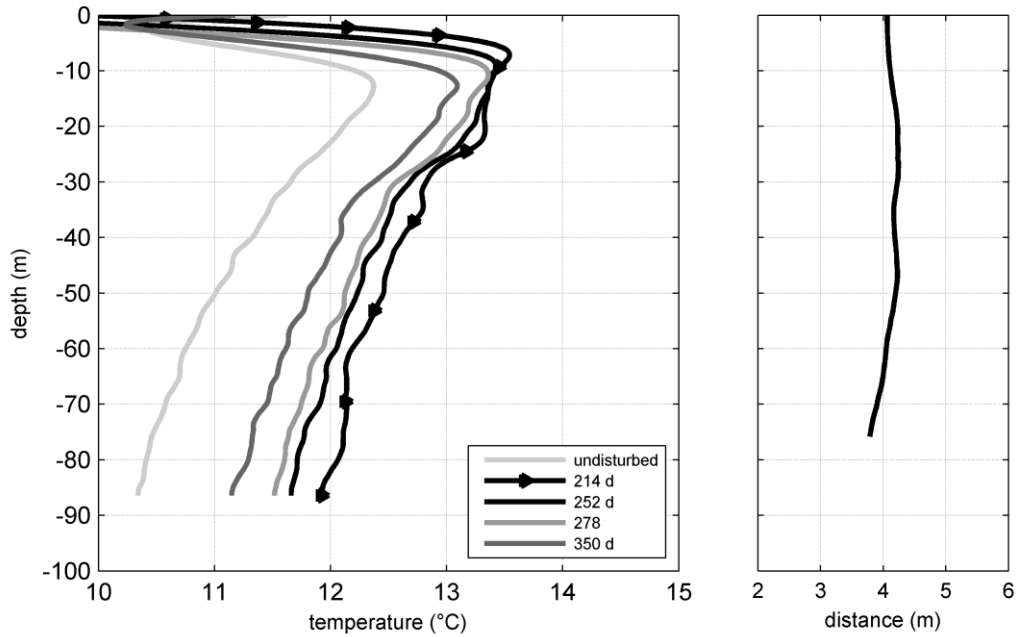
Figure 6.43 - Fiber optic temperature profiles in B1 during the recovery phase (t>214.7 d) and horizontal distance between B1 and B2 (right)

The presented temperature evolution along the boreholes length is dominated by the varying distance to the heated BHE, the air temperature variations at the top of the borehole and end effect at the bottom of the boreholes. The enhanced heat transfer rate at the sandstone/siltstone layers is indicated as local maxima in the temperature profiles. In the next section, the influence of the bedrock heterogeneity and anisotropic thermal behaviour is further investigated.

6.5.2.1 Bedrock heterogeneity and anisotropic thermal behaviour

The measured temperature that corresponds in the top 18 m and in depth greater than 85 m is not included in the following, since temperature is highly influenced by the air temperature and by bottom end effects. Moreover, given that the distance to the heated BHE is a controlling factor, the measured temperature along the different layers in the three boreholes is investigated using as reference values the numerical results for a uniform ground thermal conductivity equal to 2.9 W/mK. The numerical results include the influence of the distance to the heating source, but not heterogeneity or anisotropic effects, and would allow by

comparing them to the experimental results to detect the effect of the bedrock heterogeneity and its possible anisotropic thermal behaviour.

Figure 6.44 compares the depth-average (18 m - 85 m depth) measured temperature evolution with the numerical one for B1. The numerical results correspond to the mean distance to B2 (4.1 m). The mean measured temperature is higher of 0.15 °C than the numerical one. This small difference can be attributed to the accuracy of the offset calibration procedure and/or to an underestimation of the mean thermal conductivity and of the heat input, applied in the numerical analysis. These results indicate that heterogeneity or anisotropy do not have an important effect on the depth-average temperature evolution in the rock mass, in this case study.
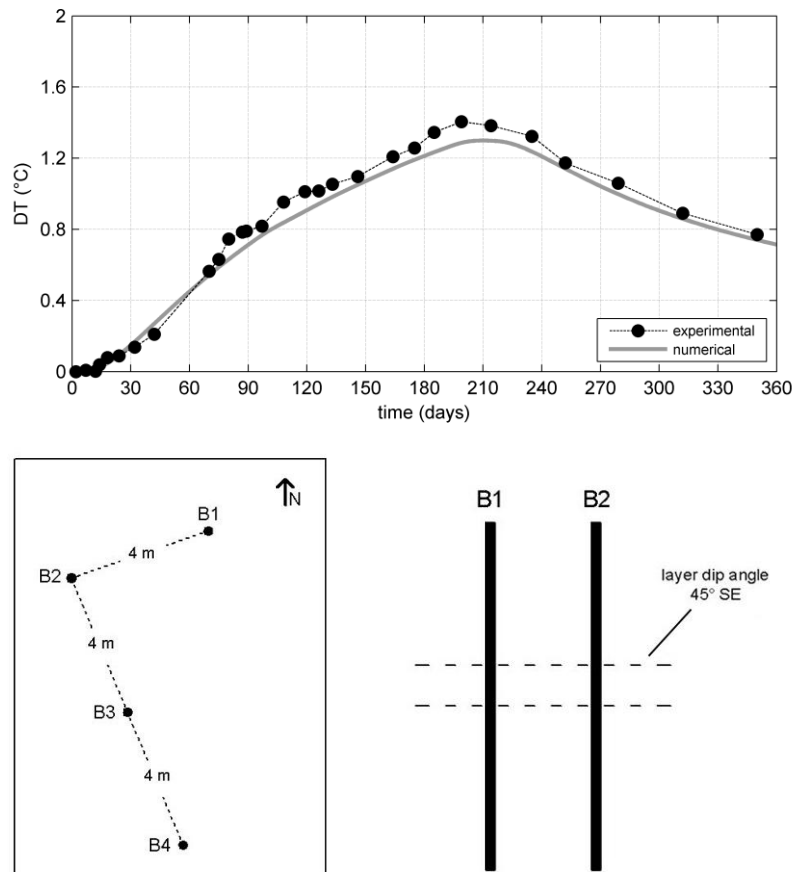
Figure 6.44 - Depth-average temperature increase evolution in B1 during the DTRT in B2

Figure 6.45 shows the temperature evolution at the location of two successive layers, that have approximately the same distance to B2: a sandstone/siltstone layer (thickness of 6.5 m) and a shale/siltstone layer (thickness of 4.4 m). The higher heat transfer rate during the

heating phase at the sandstone/siltstone layer is indicated by the higher temperature rise. During the recovery phase (t>214.7 d), temperature becomes progressively uniform along the two layers. Figure 6.46 shows numerical and experimental temperature results at the center of thick (>3 m) layers in B1. The mean measured temperature for the sandstone/siltstone layer is higher of 0.23 °C than the numerical one. In the shale/siltstone layers, this difference ranges between 0.12 °C and 0.16 °C. The differences observed at the shale/siltstone layers are closer to the corresponding depth-average temperature difference (DT=0.15 °C), since shale/siltstone layers cover approximately 66% of the boreholes length. By assuming the same volumetric heat capacity for both layers (ρc_ρ=2300 kJ/m³K), the energy stored ($E_{stor}=\rho c_\rho*DT$) in the sandstone/siltstone layer is in the order of 500 kJ/m³ higher than the one stored in the shale/siltstone layers.
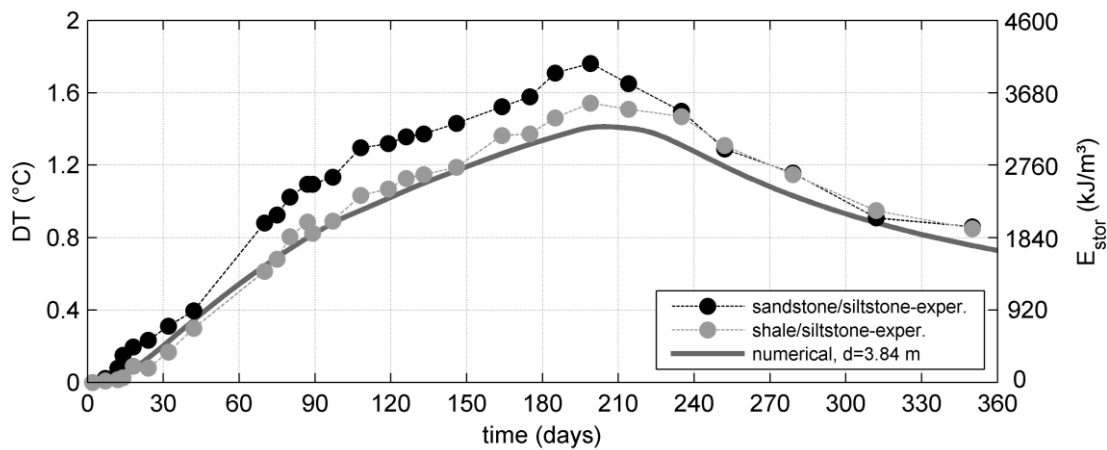
Figure 6.45 - Temperature increase evolution and energy stored ($E_{stor}=\rho c_\rho*DT=2300*DT$) at a sandstone/siltstone layer (z=-77.3 m, d=3.76 m) and at a shale/siltstone layer (z=-68.4 m, d=3.93 m) in B1 during the DTRT in B2
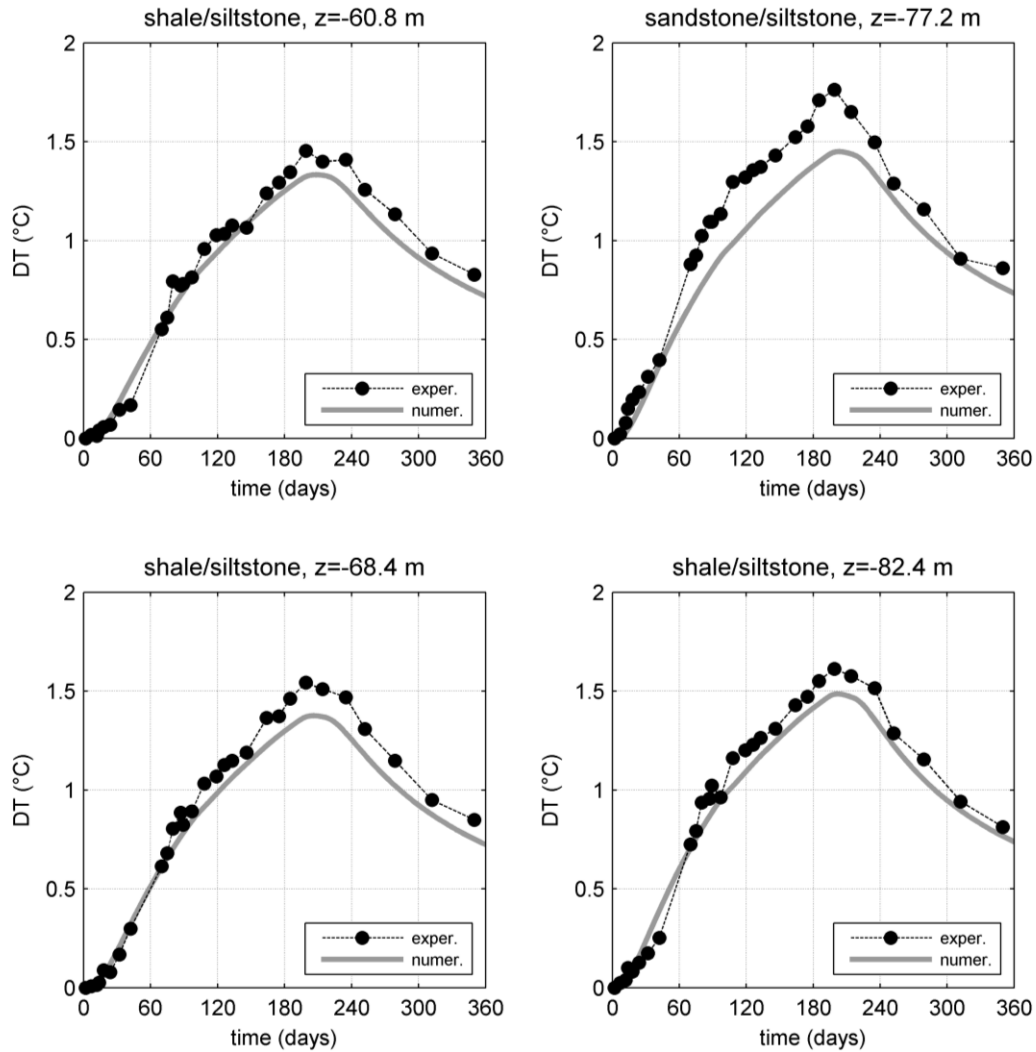
Figure 6.46 - Numerical and experimental temperature increase evolution at the center of thick layers (thickness>3 m) in B1

Shale, and in a small extend siltstone, consists of foliations and displays an anisotropic thermal behaviour depending on the direction of the heat flow with regard to the foliations orientation. The thermal conductivity parallel to the foliations is up to 2.5 times higher than the one perpendicular to the foliations (Popov et al. 1999; Eppelbaum et al. 2014). By assuming that the foliations are oriented parallel to the bedding planes, heat is transferred parallel to the foliations along the B1-B2 plane. Along the B2-B3-B4 plane, heat flows at an angle of approximately 45° with regard to the bedding planes. Figure 6.47 shows the depth-average measured and numerical temperature evolution in B3 and B4. The mean measured temperature is higher than the numerical one of 0.13 °C and 0.10 °C for B3 and B4 respectively. The differences are in the same order as in B1 (0.15 °C). Figure 6.48 shows the

temperature evolution in the three boreholes along the same layers. In all the layers, the highest temperature is observed in B3, which is closer to the heated BHE (B2), and the lowest temperature in B4, which has the greatest distance to the heated BHE. The temperature difference among the three numerical profiles at each layer is representative of the different distance to the heating source, since in the numerical model the bedrock is considered an homogenous and isotropic medium. The corresponding difference among the experimental profiles will include the distance effect as well as the potential anisotropy effect. The higher thermal diffusivity parallel to the foliations in the shale layers would be indicated by a greater difference in the experimental results between B1 and B3 (or B4) than in the numerical results. Table 6.2 summarizes the calculated experimental and numerical differences for thick layers. The differences between the experimental and the numerical profiles are the same along the sandstone/siltstone layer, where anisotropic effects are not expected to be dominant. Along the shale/siltstone layers, smaller differences are observed in the experimental data between B1 and the other two boreholes, which might be attributed to the lower effective shale thermal conductivity along the B2-B3-B4 plane. However, the difference between the numerical and experimental profiles at these layers is lower than 0.1 °C, which can be attributed to the accuracy of the fiber optic measurements and the offset calibration procedure.

These results indicate that, in this case study, the shale anisotropic thermal behaviour does not have a significant effect on the effective thermal behaviour of the bedrock and that the measured temperature differences among the three boreholes are controlled by the varying distance to the heating source. The anisotropy effect would be more important in the case of greater difference between the effective shale thermal conductivity along two directions (e.g. parallel and perpendicular to the foliations) and of higher ratio of shale to sandstone layers.
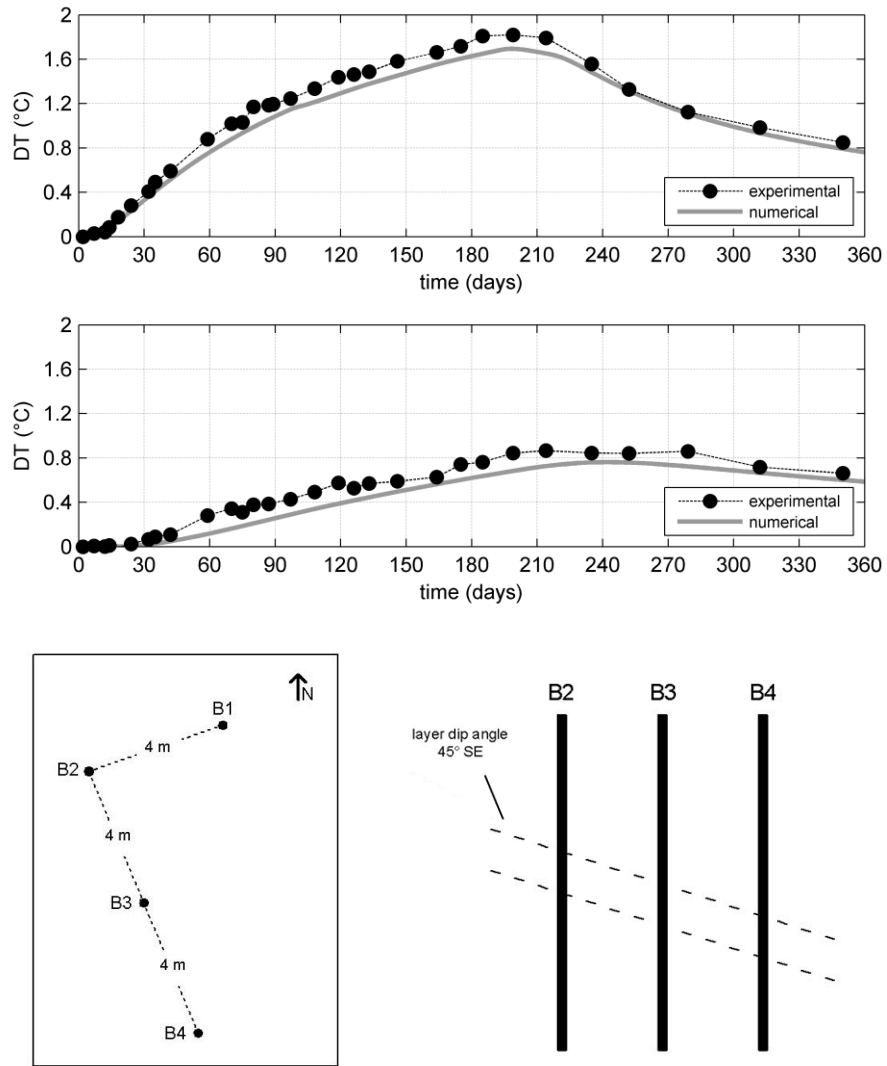
Figure 6.47 - Depth-average temperature increase evolution in B3 (top) and B4 (middle) during the DTRT in B2
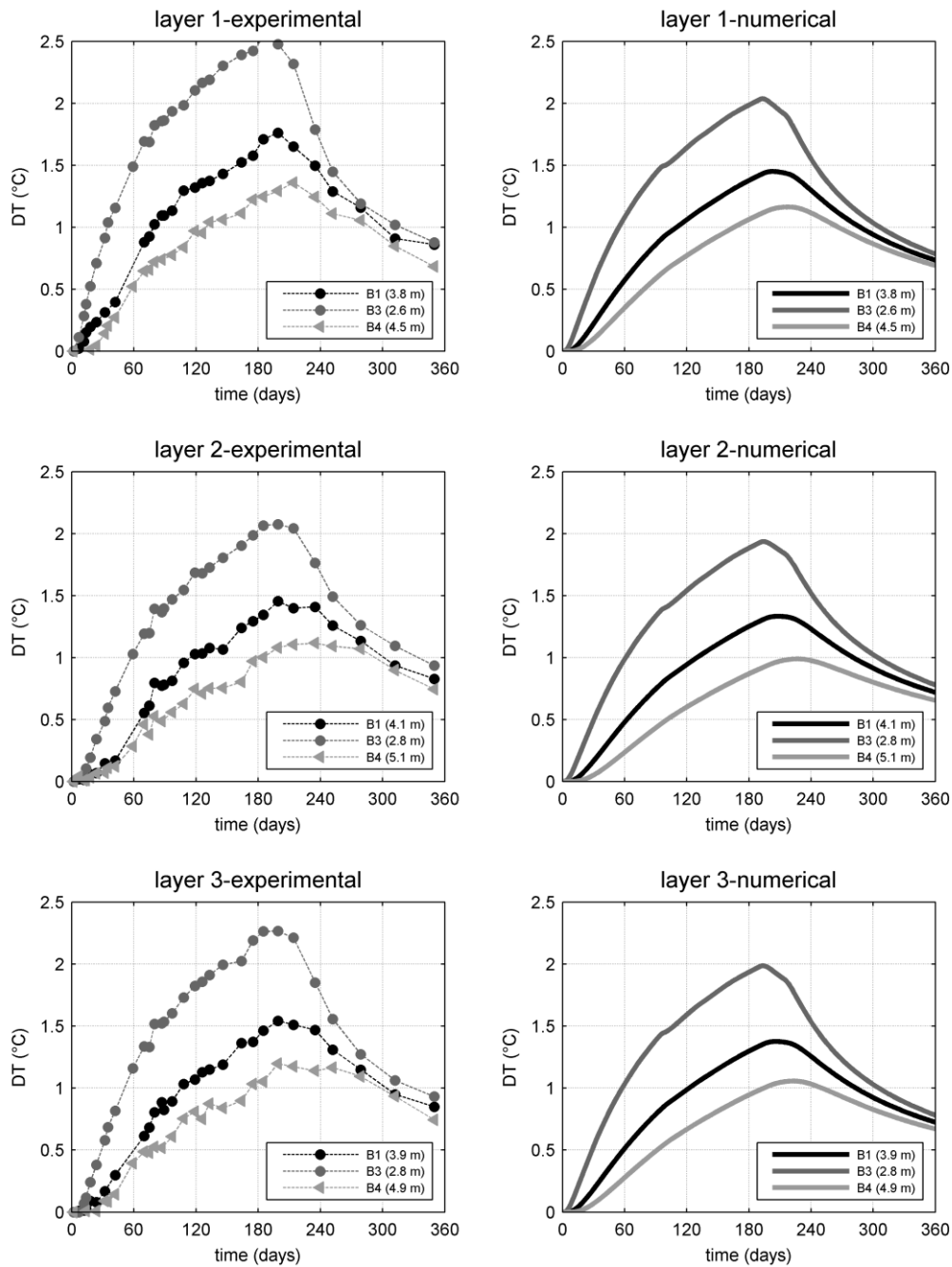
Figure 6.48 - Numerical and experimental temperature increase evolution along the same layer in B1,B3 and B4 during the DTRT in B2 (layer 1: sandstone/siltstone of 6.5 m thick at z=-77.4 m in B1, layer 2: shale/siltstone of 4.6 m thick at z=-60.8 m in B1, layer 3: shale/siltstone of 4.4 m thick at z=-68.4 m in B1)

Table 6.2 - Time-average temperature difference between the numerical and experimental profiles of the three boreholes (B1,B3,B4) along the same layers during the DTRT in B2

layer 1: sandstone/siltstone of 6.5 m thick (-77.4 m depth in B1)		
	numerical	experimental
$DT_{B3}-DT_{B1}$	0.50	0.50
$DT_{B1}-DT_{B4}$	0.24	0.24
layer 2: shale/siltstone of 4.6 m thick (-60.8 m depth in B1)		
	numerical	experimental
$DT_{B3}-DT_{B1}$	0.48	0.41
$DT_{B1}-DT_{B4}$	0.27	0.20
layer 3: shale/siltstone of 4.4 m thick (-68.4 m depth in B1)		
	numerical	experimental
$DT_{B3}-DT_{B1}$	0.49	0.46
$DT_{B1}-DT_{B4}$	0.25	0.20

6.6 Conclusions

This chapter presents temperature measurements during a long-duration DTRT in a heterogeneous bedrock, where groundwater effects are not dominant, as also shown by the typical duration TRTs conducted in situ (Chapter 5). The test was simulated by numerical modelling, considering the surrounding ground a homogenous, isotropic material. The applied ground thermal conductivity was taken equal to the one estimated by the ILS interpretation of the TRT.

The numerical results are in good agreement with the measured water temperature evolution and with the measured depth-average ground temperature evolution in the rock mass (DT<0.15 °C) for the heating and the recovery phase. Moreover, the measured temperature distribution along the pipes of the heated BHE (B2) remains constant with time during the heating phase. These results indicate that, in this case study, the heat transfer in the surrounding bedrock does not vary significantly with time and that variations of the effective thermal conductivity along a layer (e.g. due to variation of the mineral composition or the

density) do not have a dominant effect on the BHE behaviour. Moreover, groundwater effects are not dominant, since they would have resulted to a varying effective ground thermal conductivity during the test.

The effect of the distance to the heating source is a controlling factor for the temperature evolution in the surrounding bedrock, as indicted by the numerical results and verified in the fiber optic measurements of the three boreholes (B1, B3 and B4). This is also the case for the temperature distribution at the borehole cross-section of the heated BHE (B2) during the heating phase. The temperature at the borehole cross section can vary in order of 5 °C (steady-state heat transfer) based on the numerical results and the non-uniform temperature distribution can explain the measured temperature oscillations along the pipe loops.

The effect of the ambient air temperature variations during the heating phase is limited to the top 2 m as far as the pipe temperature evolution of the heated BHE is concerned. However, this effect dominated the temperature distribution in the first 18 m in the measurements at the surrounding boreholes. This is also the case during the recovery period at the borehole and the rock mass scale. This influence has been also observed until a depth of 18 m during the measurements at the undisturbed state in all the boreholes (Chapter 4). Given the good agreement between the measured and the numerical water temperature evolution, where the air temperature variations are not simulated, this effect does not seem to have an important influence on the BHE behaviour during the whole test duration. This effect could be more important for shorter BHE and especially for the operation of horizontal systems.

The influence of the thermal effects at the bottom end on the borehole wall temperature distribution have been highlighted in several studies (e.g. Philippe et al., 2009). The results of the present study indicate that these effects are non-negligible also at the rock mass temperature distribution and that the assumption of the BHE as an infinite heating source is not valid in the ground surrounding the bottom of the borehole. The influence of the end effects are observed not only close to the borehole (e.g. r=0.2 m), but also at greater distance (e.g. r=5 m) and becomes more important with increasing heating time. They are detected in the in-situ measurements be the negative temperature gradient extended below the depth that corresponds to the last 5 m of the heated borehole.

The bedrock in this case study consists of shale and siltstone interbedded with sandstone. Based on fiber optics temperature profiles of the recovery phase in the heated BHE, the variation of the effective thermal conductivity with depth can be detected. The higher heat transfer rate along the sandstone/siltstone layers (thickness>1.2 m), compared to the shale/siltstone layers, is displayed as local minima at the temperature profiles. This is also observed in the profiles after the two heat input interruptions and after the 7-days DTRTs in the other BHEs (Chapter 5). The higher heat transfer rate along the sandstone/siltstone layers is also displayed in the rock mass temperature field, indicated as local maxima in the corresponding profiles during the whole heating phase. These results indicate that heterogeneity effects could be also important for the study of the thermal interaction between BHEs.

It is, therefore, possible to conclude that obtaining the temperature profile 4 h after the beginning of the recovery phase can allow to detect layers with high heat transfer rate. Based on the measurements of this case study, this seems to be invariant to the duration of the heating phase (investigated range of 7 d to 7 months), the grouting thermal conductivity (investigated range of 1.0 W/mK - to 1.8 W/mK) or the U-pipe configuration (single-U or double-U). The resolution of the applied procedure is limited by the measurement parameters, spatial resolution and sampling interval. The fiber optic recovery profiles in this study were obtained for sampling interval of 20 cm and spatial resolution of 2 m. Lower spatial resolution and sampling interval could improve the resolution of the results. Though this is not the case for a longer heating duration of the test. Alternatively to fiber optic cables, a temperature sensor (e.g. thermocouple element, resistance temperature detector) can simply be lowered down into the pipe to obtain the temperature profiles. This approach is cost-effective and easy to implement and would give valuable information about the rock nature and stratification, as well as about the rock geothermal reservoir potential. It would contribute to the optimal design of the system in terms of the required number and length of BHEs. This proposition is in good agreement with the study of Liebel et al. (2011) in non-grouted wells in Norway, where groundwater effects are dominant. They argued that taking temperature measurements 4 h to 5 h after the beginning of the recovery phase allows to locate high heat transfer rate zones related to hydraulically active fractures and upcoming groundwater flow from confined artesian aquifers.

Laboratory measurements conclude that foliated rocks display an anisotropic thermal behaviour depending on the direction of the heat flow with regard to the foliations orientation (Popov et al., 1999; Eppelbaum et al., 2014). In this case study, the relative position of the four boreholes, allows to investigate the in-situ anisotropy along two different heat flow directions: parallel to the bedding planes and at an angle of approximately 45° with regard to the bedding planes. Based on the comparison between the numerical and experimental data and given the accuracy of the in-situ measurements , the shale anisotropic thermal behaviour has an insignificant effect on the thermal behaviour of the bedrock. However, it should be noted that the anisotropy effect could be more important in the case of greater difference between the effective shale thermal conductivity along the two directions (e.g. parallel and perpendicular to the foliations) and of higher ratio of shale to sandstone layers.

Chapter 7: Conclusions and perspectives

7.1 Summary

This thesis focuses on the influence of the in-situ characteristics on the design and the behaviour of Borehole Heat Exchangers (BHEs), at the borehole scale as well as at the surrounding ground, based on an in-situ case study of an heterogeneous bedrock in a semi-urban environment. The experimental site consists of four double-U BHEs, of about 100 m long, installed over a surface area of 32 m² on the campus of the University of Liege (Liege, Belgium). The BHEs were equipped with fiber optic cables along the outer surface of the pipe loops and a detailed bedrock characterisation was achieved based on borehole televiewer measurements in the four boreholes. Several temperature measurements were conducted in a period of four years: during hardening of the grouting material, at the undisturbed state and during the heating and the recovery phase of Distributed Thermal Response Tests (DTRTs) of a duration of 7 days. Moreover, a long-duration DTRT (heating phase of 7 months) was conducted in one of the BHEs. During this test, temperature was measured by the fiber optics during the heating and the recovery phase in all the four BHEs. These measurements create a unique data set, that allows to investigate the BHE behaviour for longer heating periods and to investigate the effect of various factors on the thermal plume in the heterogeneous bedrock at the in-situ scale. The in-situ tests were simulated with numerical modelling, which allowed to further investigate the measured temperature profiles and to detect the effect of in-situ characteristics on the temperature field at different conditions (undisturbed, heating, recovery). The results of all the measured profiles analyses are consistent with each other, as well as with the bedrock characterisation results from the borehole televiewer measurements interpretation.

In this case study, the undisturbed ground temperature profiles are characterised by an elevated temperature and a negative temperature gradient. These profiles can be the result of the ground heating by structures located close to the boreholes (feeder pipe at a distance of 6.6 m and the building of SEGI at a distance of 15 m), as verified by the numerical model analysis compared to the analytical predictions. The heat loss into the subsurface, through the

feeder pipe shell (150 W/m length) and through the SEGI basement (4 W/m²), has a significant effect on the maximum extracted power of the BHE and on the heat pump COP.

In BHEs, water circulation in the pipe loops allows to determine the depth-average ground temperature. The equipment's pipework is usually insulated to minimize air temperature effects. This study highlights the importance of the rig insulation for the accurate estimation of the ground temperature, based on measurements of five tests. Despite the pipe insulation, the measurements analysis indicates the heat transfer between the ambient air and the water during its circulation inside the rig. The maximum ground temperature overestimation is 1.7 °C and corresponds to air temperature 18 °C higher than the ground temperature. This results in an overestimation of the maximum extracted power of the BHE of 14%.

In the cuttings thermal conductivity measurements, the transition of one formation to another and the layer dipping is indicated, since in this case their different mineral composition results in a different thermal conductivity. This approach is easy to implement and can provide information on the bedrock heterogeneity, but is not applicable if a limited quantity of cuttings is available. These measurements indicate a possible varying effective thermal conductivity of the rock mass in-situ, due to alternation of different rock layers through depth, with enhanced heat transfer rate at mainly sandstone layers. Based on the dry cuttings measurements in this study, the mean bedrock thermal conductivity is equal to 1.6 W/mK, lower of 45% than the one estimated based on the TRTs conducted in-situ (2.88±0.16 W/mK).

The fiber optic profiles of the heating phase are characterised by temperature oscillations along the whole pipe length including overlapping of the downward and upward measured temperature. This could be mainly attributed to the exact position of the cable at the outer surface of the pipes, which varies through depth in this case study, in combination with the non-uniform temperature distribution inside the borehole.

Obtaining the temperature profile 4 h after the beginning of the recovery phase can allow to detect layers with high heat transfer rate. Based on the measurements of this case study, this seems to be invariant to the duration of the heating phase (investigated range of 7 d to 7 months), the grouting thermal conductivity (investigated range of 1.0 W/mK - to 1.8 W/mK)

or the U-pipe configuration (single-U or double-U). Layers thinner than 1.2 m were not identified by this procedure. The resolution of the applied procedure is limited by the measurement parameters, spatial resolution (2 m in this study) and sampling interval (20 cm in this study). Though this is not the case for a longer heating duration of the test. Comparison of the boreholes recovery temperature profiles can result in determination of the layer dipping. Moreover, temperature profiles during hardening of the grouting material allow to locate extended fracture zones, more than 1 m thick in this case study. These zones are characterised by a lower thermal diffusivity, due to air or grouting material filling the fractures, compared to the surrounding less/non fractured rock.

TRT data are widely analysed by applying the simple, analytical solution of the ILS model. In this case study, the importance of a sufficiently insulated TRT equipment for a steady heat input is highlighted. The ILS model results (ground thermal conductivity and borehole thermal resistance) are quite sensitive to the heat input oscillations. This sensitivity increases for late starting times and for short data time windows. The data were evaluated by avoiding late starting times and by increasing gradually the length of the time window. This approach was applied to the in-situ TRT measurements and the proposed results were verified by numerical simulations of the in-situ TRTs.

The in-situ grouting thermal conductivity was estimated lower than the one proposed by the producers (maximum difference of 0.8 W/mK), based on inverse numerical modelling results. This could be mainly attributed to the water fraction applied in-situ for the preparation of the admixtures, which was higher than the one proposed by the producers. For the given BHE geometry, this could have an important effect on the borehole thermal resistance for grouting thermal conductivity values lower than 2 W/mK.

The long-duration DTRT was simulated by numerical modelling, considering the surrounding ground a homogenous, isotropic material. The applied ground thermal conductivity was taken equal to the one estimated by the ILS interpretation of the TRT. The numerical results are in good agreement with the measured water temperature evolution and with the measured depth-average ground temperature evolution in the rock mass (DT<0.15°C) for the heating and the recovery phase. Moreover, the measured temperature distribution along the pipes of the heated BHE remains constant with time during the heating phase. These results indicate that,

in this case study, the heat transfer in the surrounding bedrock does not vary significantly with time and that variations of the effective thermal conductivity along a layer (eg. due to variation of the mineral composition or the density) do not have a dominant effect on the BHE behaviour. Moreover, groundwater effects are not dominant, since they would have resulted to a varying effective ground thermal conductivity during the test.

The effect of the distance to the heating source is a controlling factor for the temperature evolution in the surrounding bedrock, as indicted by the numerical results and verified by the fiber optic measurements of the three observation boreholes. This is also the case for the temperature distribution at the borehole cross-section of the heated BHE during the heating phase. The temperature at the borehole cross section can vary in order of 5 °C (steady-state heat transfer) based on the numerical results and the non-uniform temperature distribution can explain the measured temperature oscillations along the pipe loops.

The effect of the ambient air temperature variations during the heating phase is limited to the top 2 m, as far as the pipe temperature evolution of the heated BHE is concerned. However, this effect dominated the temperature distribution in the first 18 m in the measurements at the surrounding boreholes. This is also the case during the recovery period at the borehole and the rock mass scale. Given the good agreement between the measured and the numerical water temperature evolution, where the air temperature variations are not simulated, this effect does not seem to have an important influence on the BHE behaviour during the whole test duration. This effect could be more important for shorter BHE and especially for the operation of horizontal systems.

The influence of the thermal effects at the bottom end on the borehole wall temperature distribution have been highlighted in several studies. The results of the present study indicate that these effects are non-negligible also at the rock mass temperature distribution and that the assumption of the BHE as an infinite heating source is not valid in the ground surrounding the bottom of the borehole. The influence of the end effects are observed not only close to the borehole (eg. r=0.2 m), but also at greater distance (eg. r=5 m) and becomes more important with increasing heating time. They are detected in the in-situ measurements be the negative temperature gradient extended below the depth that corresponds to the last 5 m of the heated borehole.

The effect of the bedrock heterogeneity is displayed in the rock mass temperature field during the long-duration DTRT. The higher heat transfer rate along the sandstone/siltstone layers, compared to the shale/siltstone layers is indicated as local maxima in the corresponding profiles during the whole heating phase.

Laboratory measurements conclude that foliated rocks display an anisotropic thermal behaviour depending on the direction of the heat flow with regard to the foliations orientation. In this case study, the relative position of the four boreholes, allows to investigate the in-situ anisotropy along two different heat flow directions: parallel to the bedding planes and at an angle of approximately 45° with regard to the bedding planes. Based on the comparison between the numerical and experimental data and given the accuracy of the in-situ measurements , the shale anisotropic thermal behaviour has an insignificant effect on the thermal behaviour of the bedrock. However, it should be noted that the anisotropy effect could be more important in the case of greater difference between the effective shale thermal conductivity along the two directions (eg. parallel and perpendicular to the foliations) and of higher ratio of shale to sandstone layers.

7.2 Recommendations for BHE installations in practise

The in-situ characteristics are often not adequately considered for the BHEs design and operation in practise. This can result in increased capital costs or to malfunctions and short life spans, overwhelming the potential and the applicability of these systems and prohibiting their wide application. This section presents recommendations that can be applied in practise prior to the operation of the system and could optimise its design and operation, based on the conclusions of this in-situ case study.

- It would be of interest in any BHE to measure the temperature along the borehole length at the undisturbed state, during hardening of the grouting material and after 4h of recovery. Alternatively to fiber optic cables, a temperature sensor (e.g. thermocouple element, resistance temperature detector) can simply be lowered down into the pipe to obtain the temperature profiles. This approach is cost-effective, easy to implement, does not delay the installation or require a pre-installed equipment and would give valuable information about

the rock nature and stratification, as well as about the geothermal reservoir potential. It would allow to detect layers of enhanced heat transfer and contribute to the optimal design of the system in terms of the required number and length of BHEs.

- Given the importance of the undisturbed ground temperature for the design of BHEs, it is recommended during the TRT not only to insulate the connecting pipes but also the test rig wall. This allows to avoid a significant overestimation of the extracted power of the BHEs, in the case of high ambient air temperature during the test, as well as an underestimation of the extracted power, in the case of low ambient air temperature. Moreover, an insufficient test rig insulation results in heat input oscillations during the heating phase of the TRT, which is critical in the case that the data are analysed by applying the simple analytical solution of the ILS model. The sensitivity of the ILS model results increases for late starting times and for short data time windows. It could be, therefore, proposed to evaluate the data of the in-situ TRTs by increasing gradually the length of the time window. The choice of the starting time of the evaluated data is limited by the required time for the heat transfer inside the borehole to reach the steady-state phase, equal to 1 h -12 h for normal borehole sizes and ground conditions (Spitler and Gehlin, 2015), and should fulfil the mathematical limitation of the simplified ILS formulation, $t \geq 5 r_b{}^2 / \alpha$, where r_b is the borehole radius (m) and α the ground thermal diffusivity (m²/s). However, later starting times should be avoided to decrease the sensitivity of the ILS model results to the heat input oscillations. Moreover, a longer than the typical duration of the TRT (50 h) might be necessary in order to obtain accurate results, in the case of heat input oscillations and of the interpretation of the data by the ILS model.

- Cuttings measurements should be studied qualitatively for extrapolating them to in-situ conditions and cannot replace the TRT. Cuttings contain no information on the rock mass fracturing, the degree of saturation, possible groundwater effects and the thermal interaction between different layers, parameters that influence the effective in-situ thermal conductivity. However, studying cuttings thermal conductivity measurements qualitatively can provide information on the bedrock heterogeneity and on the possible varying thermal conductivity with depth in-situ.

- The in-situ grouting thermal conductivity depends on the water fraction applied for the preparation of the admixtures. A water fraction higher than the one proposed by the

producers should be avoided if possible, since it can result in a significantly lower than the proposed grouting thermal conductivity, and especially lower than 2 W/mK. This value is indicated by guidelines as the minimum required grouting thermal conductivity in-situ (NF X 10-970) and below this limit the borehole thermal resistance varies significantly with varying grouting thermal conductivity, for the BHE geometry investigated in this study.

7.3 Perspectives for future research

The experimental site presented in this study has a great potential. The BHEs are equipped with fiber optic cables which provide continuous high-resolution temperature profiles along the boreholes length. The relative position between the different BHEs makes it possible to investigate the temperature field evolution in the rock mass during different modes. The BHEs are installed in a heterogeneous bedrock and a detailed geological description of the rock mass is available, which allows to study heterogeneity effects at the in-situ scale and correlate geological characteristics with the obtained temperature profiles. Moreover, it is located in a semi-urban environment (campus of the University of Liege), where the urbanisation effect in the subsurface is present, and could also provide the possibility the BHEs to be connected to a building for further investigating the behaviour of the system during real operation conditions. The analyses of the so far conducted measurements open up new questions for future research, that could be investigated in-situ and/or with numerical modelling.

- This study indicates that heat loss through buildings foundations and underground structures (feeder pipes, sewage pipes etc.) can have an important effect on the design and the long-term operation of BHEs, since it recharges the geothermal reservoir. Taking the effect of this continuous phenomenon into account could contribute to a sustainable geothermal reservoir management in a city scale, as well as to an optimisation of the geothermal systems design. In this context, it would be interesting to develop a 3D numerical model including the heat loss through structures and to investigate the influence of this effect on the performance of geothermal systems during their lifespan. Given that the ground temperature field is significantly affected close to the structures, the case of energy piles would be particularly interesting, since they are located underneath the building and are usually shorter than BHEs.

- This study presents the potential of the temperature profiles during hardening of the grouting material on the detection of fractured zones in the surrounding bedrock. A continuous monitoring during this process could provide information on the behaviour of different grouting materials during hardening, as well as on the required time for the temperature to retrieve its initial profile after the BHE installation. The latter is crucial for the reliability of the TRT results, which control the design of closed-loop systems. Moreover, a study of the thermal response during hardening of the grouting material, which is an exothermic process, could provide information on the possible varying heat transfer rate with depth.

- The long-duration DTRT was simulated by numerical modelling considering the ground an homogeneous medium. This allowed to detect the effect of the bedrock heterogeneity on the temperature field evolution, based on the comparison between the numerical results and the in-situ measurements. It would be interesting to estimate the transferred heat along each layer and their thermal conductivity by inverse numerical modelling, in order to quantify the varying heat transfer rate through depth and to provide an indication of the potential of the thermal energy storage of different formations.

- The question arises, at which distance from the BHE the existence of structures or heterogeneities can affect the temperature field evolution during the typical operation of the system (cycling thermal loading). This could be further investigated by numerical modelling, including the heat loss into the subsurface by existing structures and a cyclic thermal loading applied at the BHE. Moreover, repeating a long-duration test, during which a cycling thermal loading is applied to one of the BHEs and measuring the temperature by the fiber optics in all the four boreholes, could significantly contribute to this direction. The comparison between the experimental data of both long-duration tests would allow to detect the factors that influence the behaviour of the system and the temperature field evolution in the surrounding ground under different modes.

- The ground temperature close to the surface is influenced by air temperature variations, as observed in the in-situ measurements. During the long-duration DTRT, this effect does not seem to have an important influence on the BHE behaviour during the whole test duration. However, in practise, the BHEs are connected to the building through pipes embedded in the

top meters of the ground, which can have a length of several meters, especially in the case of collective buildings where several BHE are required. It would be interesting to investigate if a significant heat transfer occurs between the circulating fluid and the ground in the case of typically insulated connecting pipes and what is the influence of the air temperature variations to the final performance of the system. However this requires particular conditions, since BHE installations should be connected to a building and a monitoring system should be available that would allow temperature logging along the boreholes and the connecting pipes. The experimental site of the present study provides this potential. The BHEs could be connected to the university building located close to them (distance of 15 m) and the remaining part of the fiber optic cables, i.e the part that is not installed inside the boreholes, can be attached along the connecting pipes. This would allow to investigate the air variations effect under real operating conditions. Moreover, given the close distance between the four BHEs, operating only two of the installed BHEs would allow to investigate the thermal interaction between them at the in-situ scale, as well as to monitor the temperature field evolution in the surrounding rock mass.

References

Acuña, J. (2010). *Improvements of U pipe Borehole Heat Exchangers*. Doctoral dissertation, KTH School of Industrial Engineering and Management, Stockholm, Sweden

Acuña, J., Morgesen, P. and Palm, B. (2009). Distributed thermal response test on a U-pipe borehole heat exchanger. In: *EFFSTOCK Conference Proceedings 2009*, Stockholm, Sweden, 14-17 June

Alonso-Sánchez, T., Rey-Ronco, M.A., Carnero-Rodríguez, F.J., and Castro-García, M.P. (2012). Determining ground thermal properties using logs and thermal drill cutting analysis. First relationship with thermal response test in principality of Asturias, Spain. *Applied Thermal Engineering*, 37, 226–234

ASTM D 5334-00 (2000): *Standard Test Method for Determination of Thermal Conductivity of Soil and Soft Rock by Thermal Needle Probe Procedure*. ASTM International, West Conshohocken, PA 19428-2959, 04.08

Banks, D. (2009). An introduction to 'thermogeology' and the exploitation of ground source heat. *Quarterly Journal of Engineering Geology and Hydrogeology*, 42 (3), 283–293

Banks, D., Gandy, C.J., Younger, P.L., Withers, J. and Underwood, C. (2009). Anthropogenic thermogeological 'anomaly' in Gateshead, Tyne and Wear, UK. *Quarterly Journal of Engineering Geology and Hydrogeology*, 42, 307-312

Barla, M., Di Donna, A. and Perino, A. (2016). Application of energy tunnels to an urban environment. *Geothermics*, 61, 104-113

Bayer, P., Saner, D., Bolay, S., Rybach, L. and Blum, P. (2012). Greenhouse gas emission savings of ground source heat pump systems in Europe: A review. *Renewable and Sustainable Energy Reviews*, 16, 1256-1267

Blum, P., Campillo, G. and Kölbel, T. (2011). Techno-economic and spatial analysis of vertical ground source heat pump systems in Germany. *Energy*, 36 (5), 3002-3011

Brandl, H. (2006). Energy foundations and other thermo-active ground structures. *Geotechnique*, 56 (2), 81-122

Buckley, C., Pasquali, R., Lee, M., Dooley, J. and Williams, T.H. (2015). *'Ground Source Heat' & 'Shallow Geothermal Energy', Homeowner Manual.* Geothermal survey of Ireland

Bultynck, P., Coen-Aubert, M., Dejonghe, L., Godefroid, J., Hance, L., Lacroix, D., Preat, A., Stainier, P., Steemans, P., Streel, M. and Tourneur, F. (1991). *Les formations du Dévonien Moyen de la Belgique.* Mémoires pour servir à l'explication des Cartes Géologiques et Minières de la Belgique, 30. Ministère des affaires économiques (Bruxelles)

Calembert, L., Monjoie, A. and Polo-Chiapolini, Cl., préface par De Beer, E. (1975). *Carte géotechnique prototype du Sart Tilman.* Annales des Travaux Publics de Belgique, N° 5

Calembert, L., Pel, J. and Brumagne, D. (1964). *Géologie*. Extrait du 2ième cahier du Sart Tilman, Publication no25, Laboratoires de Géologie de la Fac. des Sc. Appl.,Université de Liège

Carslaw, H.S. and Jaeger, J.C. (1959). *Conduction of Heat in Solids, second edition*. New York: Oxford University Press

Cataldi, R. and Chiellini, P. (1995). Geothermal Energy in the Mediterranean before the Middle Ages, A review. In: *Proceedings of the World Geothermal Congress, 1995*, IGA, Florence, Italy, 18-31 May, 373-380

Cerfontaine, B., Radioti, G., Collin, F. and Charlier, R. (2016). Formulation of a 1D finite element of heat exchanger for accurate modelling of the grouting behaviour: Application to cyclic thermal loading. *Renewable Energy*, 96, 65-79

Chalhoub, M., Chéry, C., Maragna, C. and Philippe, M. (2014). *Plate-Forme expérimentale pour les pompes à chaleur géothermiques - Tranche 3*. Rapport final. BRGM/RP-63742-FR. 53 p., 27 fig., 2 tabl., 2 ann.

Charlier, R., Radu, J.-P. and Collin, F. (2001). Numerical modelling of coupled transient phenomena. *Revue Française de Génie Civil*, 5(6), 719-741

Choi, W. and Ooka, R. (2016a). Effect of disturbance on thermal response test, part 1: Development of disturbance analytical model, parametric study, and sensitivity analysis. *Renewable Energy*, 85, 306-318

Choi, W. and Ooka, R. (2016b). Effect of disturbance on thermal response test, part 2: Numerical study of applicability and limitation of infinite line source model for interpretation under disturbance from outdoor environment. *Renewable Energy*, 85, 1090-1105

Clauser, C. (2006). Geothermal Energy. In: *K. Heinloth (ed), Landolt-Börnstein, Group VIII: Advanced Materials and Technologies, Vol 3: Energy Technologies, Subvol. C: Renewable Energies*. Heidelberg-Berlin, Springer Verlag

Clauser, C. and Huenges, E. (1995). Thermal Conductivity of Rocks and Minerals. In: *Rock Physics and Phase Relations - a Handbook of Physical Constants*. AGU Reference Shelf, 3, 105-126

Climate-data.org: Climate data for cities worldwide. Last accessed 15-10-2015, http://en.*climate-data.org*/

Collin, F., Li, X.L., Radu, J.-P. and Charlier, R. (2002). Thermo-hydro-mechanical coupling in clay barriers. *Engineering Geology*, 64, 179-193

Corteel, C., Van Den Houte, P. and Verniers, J. (2004). New sedimentological and petrographical observations on the Devonian Burnot Formation in the Belgian Rhenohercynian basin. *Geologica Belgica*, 7, 41–53

CREGE, Laboratoire de géothermie, Université de Neuchâtel, Suisse. Last accessed June 2016, http://crege.ch/

Davies, J.H. and Davies, D.R. (2010). Earth's surface heat flux. *Solid Earth*, 1, 5-24

Dehkordi, S.E. and Schincariol, R.A. (2014). Effect of thermal-hydrogeological and borehole heat exchanger properties on performance and impact of vertical closed-loop geothermal heat pump systems. *Hydrogeology Journal*, 22, 189-203

Delaleux, F., Py, X., Olives, R. and Dominguez, A. (2012). Enhancement of geothermal borehole heat exchangers performances by improvement of bentonite grouts conductivity. *Applied Thermal Engineering*, 33-34 (1), 92-99

Earthtest Energy. *Ground source heat pumps use renewable energy*. Last accessed June 2016, http://www.earthtestenergy.com/commercial-ground-source-heat.html

Eppelbaum, L., Kutasov, I. and Pilchin, A. (2014). *Applied Geothermics, Lecture Notes in Earth System Sciences*, Springer-Verlag Berlin Heidelberg

Erol, S. and François, B. (2014). Efficiency of various grouting materials for borehole heat exchangers. *Applied Thermal Engineering*, 70, 788–799

European Commission - Fact Sheet (2016). *Towards a smart, efficient and sustainable heating and cooling sector*, Brussels, 16 February 2016. Retrieved online: http://europa.eu/rapid/press-release_MEMO-16-311_en.htm

Ferguson, G. and Woodbury, A.D. (2007). Urban heat island in the subsurface. *Geophysical research letters*, 34 (23), L23713

Florides, G. and Kalogirou, S. (2007). Ground heat exchangers-A review of systems, models and applications. *Renewable Energy*, 32 (15), 2461-2478

Florides, G. and Kalogirou, S. (2008). First in situ determination of the thermal performance of a U-pipe borehole heat exchanger, in Cyprus. *Applied Thermal Engineering*, 28, 157-163

Fujii, H., Okubo, H., and Itoi, R. (2006). Thermal Response Tests Using Optical Fiber Thermometers. *GRC Transactions*, 30, 545-51

Fujii H., Okubo H., Nishi K., Itoi R., Ohyama K. and Shibata, K. (2009). An improved thermal response test for U-tube ground heat exchanger based on optical fiber thermometers. *Geothermics*, 38, 399-406

Gehlin, S. (2002). *Thermal Response Test - Method, Development and Evaluation.* Doctoral dissertation, Luleå University of Technology, Sweden

Gehlin, S.E.A. and Nordell, B. (2003). Determining undisturbed ground temperature for thermal response test. *ASHRAE Transactions*, 109, 151-156

Hanson, J. L., Neuhaeuser, S. and Yesiller, N. (2004). Development and Calibration of a Large-Scale Thermal Conductivity Probe. *Geotechnical Testing Journal*, ASTM, 27, 393-403

Hausner, M.B, Suarez, F., Glander, K.E., van de Giesen, N., Selker, J.S. and Tyler, S.W. (2011). Calibrating single-ended fiber-optic raman spectra distributed temperature sensing data. *Sensors*, 11, 10859-10879

Hellström, G. (1991). *Ground heat storage: thermal analyses of duct storage systems.* Doctoral dissertation, University of Lund, Sweden

Hermans, T., Nguyen, F., Robert, T. and Revil, A. (2014). Geophysical Methods for Monitoring Temperature Changes in Shallow Low Enthalpy Geothermal Systems. *Energies,* 7, 5083–5118

Hillel, D. (1980b). *Applications of soil physics*. Academic Press, New York

Hoffmann, L., Müller, M. S., Krämer, S., Giebel, M., Schwotzer, G. and Wieduwilt, T. (2007). Applications of Fibre Optic Temperature Measurement. *Proc. Estonian Acad. Sci. Eng.,* 13 (4), 363-378

Johansen, O. (1975). *Thermal conductivity of soils*. Doctoral dissertation, Norwegian University of science and Technology, Trondheim, Norway (CRREL draft transl. 637, 1977)

Jaudin, F., Angelino, L., Annunziata, E., Van Beek, D., Benson, J., Bezelgues, S., Croufer, M., Cucueteanu, D., Cuevas, J., Frey, M., Godschalk, B., Goumas, A., Jardeby, A., Nielsen, A.M., Pasquali, R., Poux, A., Räftegård, O., Rizzi, F. and Sanner, B. (2013). D2.2 General Report of the current situation of the regulative framework for the SGE systems. In: *Overview of shallow geothermal legislation in Europe*. Retrieved from ReGeoCities Project website: http://regeocities.eu/wp-content/uploads/2012/12/D2.2.pdf

Kavanaugh, S.P., Xie, L. and Martin, C. (2001). Investigation of methods for determining soil and rock formation thermal properties from short-term field tests. *ASHRAE 1118-RP*, Atlanta, Georgia

Kaye, G.W. C. and Laby, T. H. (1978). *Table of Physical and Chemical Constants and Some Mathematical Functions*, Longman, New York

Kayode Coker, A. (2010). *Ludwig's Applied Process Design for Chemical and Petrochemical Plants*, Elsevier, 4th ed., Oxford

Kepinska, B. (2003). *Lectures on geothermal resources and utilization in Poland and Europe*, United Nations University - Geothermal Training Programme, Iceland, report 2, 1-27

Keys, W.S. (1990). Borehole Geophysics Applied to Ground-water Investigations. In *U.S. Geological Survey Techniques of Water-Resources Investigations*. Retrieved from U.S. Geological Survey website: http://pubs.usgs.gov/twri/twri2-e2/

Kömle, N.I. , Huetter, E.S. and Feng, W.J. (2010). Thermal conductivity measurements of coarse-grained gravel materials using a hollow cylindrical sensor. *Acta Geotechnica*, 5, 211–223

Kurevija, T., Vulin D. and Macenić, M. (2014). Impact of geothermal gradient on ground source heat pump system modeling. *Rudarsko Geolosko Naftni Zbornik*, 28, 39-45

Laloui, L. and Di Donna, A. (2013). *Energy Geostructures: Innovation in Underground Engineering*, Vol. 304. ISTE Ltd and John Wiley & Sons Inc.

Liebel, H.T., Huber, K., Frengstad, B.S., Kalskin Ramstad, R. and Brattli, B. (2010). Rock core samples cannot replace thermal response tests - A statistical comparison based on thermal conductivity data from the Oslo Region (Norway). In: *Proceedings of Renewable Energy Research Conference*, Trondheim, Norway, 145-154

Liebel, H.T., Huber, K., Frengstad, B.S., Ramstad, R.K. and Brattli, B. (2011). Temperature footprint of a thermal response test can help to reveal thermogeological information. *Norges geologiske undersøkelse Bulletin*, 451, 20-31

Loveridge, F., Holmes, G., Powrie, W. and Roberts, T. (2013). Thermal response testing through the Chalk aquifer in London, UK. *Proceedings of the Institution of Civil Engineers: Geotechnical Engineering*, 166 (2), 197-210

Lund, J.W., Freeston, D.H. and Boyd, T.L. (2005). Direct application of geothermal energy: 2005 Worldwide review. Geothermics, 34 (6), 691-727

Lund, J.W., Freeston, D.H. and Boyd T.L. (2011). Direct utilization of geothermal energy 2010 worldwide review. *Geothermics*, 40 (3), 159-180

Luo, J., Rohn, J., Xiang, W., Bertermann, D. and Blum, P. (2016). A review of ground investigations for ground source heat pump (GSHP) systems. *Energy and Buildings*, 117, 160-175

MCS 022 (2008): *Ground heat exchanger look-up tables. Supplementary material to MIS 3005*. Department of Energy and Climate Change, London

Menberg, K., Bayer, P., Zosseder, K., Rumohr, S. and Blum, P. (2013). Subsurface urban heat islands in German cities. *Science of the Total Environment*, 442, 123-133

MIS 3005 (2008): *Requirements for MCS contractors undertaking the supply, design, installation, set to work, commissioning and handover of microgeneration heat pump systems*. Department of Energy and Climate Change, London

Mogensen, P. (1983). Fluid to Duct Wall Heat Transfer in Duct System Heat Storages. *Proceedings of the International Conference on Subsurface Heat Storage in Theory and Practice*, Stockholm, Sweden, June 6-8, 652-657

Monier-Williams, M.E., Davis, R.K., Paillet, F.L., Turpening, R.M., Sol, S.J.Y and Schneider, G.W. (2009). *Review of Borehole Based Geophysical Site Evaluation Tools and Techniques* (Rep. NWMO TR-2009-25). Retrieved from Nuclear Waste Management Organization website: http://www.nwmo.ca/uploads_managed/MediaFiles/1770_nwmotr-2009-25boreholebasedgeophysicaltools_r0d.pdf

Nguyen, D. and Lanini, S. (2012). *Projet Solargeotherm: modélisations numeériques de transferts thermiques dans le dispositif souterrain d'échange de chaleur.*BRGM/RP-59697-FR, 91 p., 63 ill, 5 ann., don't ann. 5 sur DVD

Paillet, F.L., Barton, C., Luthi, S., Rambow, F. and Zemanek, J.R. (1990). Borehole imaging and its application in well logging - an overview. In: *Borehole Imaging*. Society of Professional Well Log Analysts, 3-23

Pechnig, R., Mottaghy, D., Arnold, J., Koch, A. and Jorand, R. (2010). *Thermal properties of paleozoic rocks from the Rhenish Massif*. European Geoscience Union, General Assembly, Vienna, 02-07 May

Petitclerc, E. and Vanbrabant, Y. (2011). *Développement de la plate-forme Géothermique de la Wallonie*. Rapport final, DGO4. Retrieved online: http://energie.wallonie.be/fr/la-geothermie-profonde.html?IDC=6173

Philippe, M., Bernier, M. and Marchio, D. (2009). Validity ranges of three analytical solutions to heat transfer in the vicinity of single boreholes. *Geothermics*, 38 (4), 407–413

Philippe, M. (2010). *Développement et validation expérimentale de modèles d''echangeurs géothermiques horizontaux et verticaux pour le chauffage de bâtiments résidentiels*. Doctoral dissertation, Chemical and Process Engineering. École Nationale Supérieure des Mines de Paris, France

Popiel, C.O., Wojtkowiak, J. and Biernacka, B. (2001). Measurements of temperature distribution in ground. *Experimental Thermal and Fluid Science*, 25, 301-309

Popov, Y. A., Pribnow, D.F.C., Sass, J.H., Williams, C.F. and Burkhardt, H. (1999). Characterization of rock thermal conductivity by high-resolution optical scanning. *Geothermics*, 28, 253-276

Preene, M. and Powrie, W. (2009). Ground energy systems: From analysis to geotechnical design. *Geotechnique*, 59 (3), 261-271

Quick, H., Michael, J., Huber, H. and Arslan, U. (2010). History of International Geothermal Power Plants and Geothermal Projects in Germany. In: *Proceedings World Geothermal Congress 2010*, IGA, Bali, Indonesia, 25-29 April

Radioti, G., Charlier, R., Nguyen, F. and Radu, J.-P. (2013). Thermal Response Test in Borehole Heat Exchangers Equipped with Fiber Optics. In: *Proceedings, International Workshop on Geomechanics and Energy: The Ground as Energy Source and Storage,* EAGE, Lausanne, Switzerland, 96-100

Radioti, G., Delvoie, S., Radu, J.-P., Nguyen, F. and Charlier, R. (2015a). Fractured bedrock investigation by using high-resolution borehole images and the Distributed Temperature Sensing technique. In: *ISRM Congress 2015 Proceedings - Int'l Symposium on Rock Mechanics*, ISRM, Montreal, Canada

Radioti, G., Delvoie, S., Sartor, K., Nguyen, F. and Charlier, R. (2015b). Fiber-optic temperature profiles analysis for closed-loop geothermal systems: a case study. In: *Proceedings, Second EAGE Workshop on Geomechanics and Energy: The Ground as Energy Source and Storage*, EAGE, Celle, Germany

Radioti, G., Delvoie, S., Charlier, R., Dumont, G. and Nguyen, F. (2016a). Heterogeneous bedrock investigation for a closed-loop geothermal system: A case study. *Geothermics*, 62, 79-92

Radioti, G., Delvoie, S., K. Sartor, Nguyen, F. and Charlier, R. (2016b). Fiber-optic temperature measurements in closed-loop geothermal systems: a case study in heterogeneous bedrock. In: *Proceedings of 1st International Conference on Energy Geotechnics ICEGT 2016*, Kiel, Germany

Rainieri, S., Bozzoli, F. and Pagliarini, G. (2011). Modeling approaches applied to the thermal response test: A critical review of the literature. *HVAC&R Research*, 17 (6), 977-990

Rybach, L. (2010). CO_2 Emission Mititation by Geothermal Development - Especially with Geothermal Heat Pumps. In: *Proceedings World Geothermal Congress 2010*, IGA, Bali, Indonesia, 25-29 April

Sanner, B. (2001). Some history of shallow geothermal energy use. *Proceedings of International Summer School on Direct Application of Geothermal Energy*, UNESCO/IGA, Bad Urach, Germany

Sanner, B., Angelino, L., De Gregorio, M., Février, N., Haslinger, W., Kujbus, A., Landolina, S., Sparber, W., Stryi-Hipp, G., Van Helden, W. and Weiss, W. (2013). *Strategic Research and Innovation Agenda for Renewable Heating & Cooling*. Retrieved from the European Technology and Innovation platform website: http://www.rhc-platform.org/fileadmin/user_upload/members/RHC_SRA_0418_lowres.pdf

Sartor, K., Quoilin, S. and Dewallef, P. (2014). Simulation and optimization of a CHP biomass plant and district heating network. *Appied Energy*, 130, 474–483

Self, S.J, Reddy, B.V. and Rosen, M.A. (2013). Geothermal heat pump systems: Status review and comparison with other heating options. *Applied Energy*, 101, 341-348

Selker, J.S., Thévenaz, L., Huwald, H., Mallet, A., Luxemburg, W., van de Giesen, N., Stejskal, M., Zeman, J., Westhoff, M. and Parlange, M.B. (2006). Distributed fiber-optic temperature sensing for hydrologic systems. *Water Resources Research*, 42 (12)

Singorelli, S., Bassetti, S., Pahud, D. and Kohl, T. (2007). Numerical evaluation of thermal response tests. *Geothermics*, 36, 141-166

Smolarczyk, U. (2003). *Geotechnical Engineering Handbook*, Vol.2: Procedures, Berlin

Soldo, V., Borović, S., Lepoša, L. and Boban, L. (2016). Comparison of different methods for ground thermal properties determination in a clastic sedimentary environment. *Geothermics*, 61, 1-11

Spitler, J.D. and Gehlin, S. (2015), Thermal response testing for ground source heat pump systems-An historical review. *Renewable and Sustainable Energy Reviews*, 50, 1125-1137

Stober, I. and Bucher, K. (2013). History of Geothermal Energy Use. In: *Geothermal Energy - From Theoretical Models to Exploration and Development*, Springer Berlin Heidelberg, 15-24

ThinkGeoEnergy. *Enel inaugurates National Museum of Geothermal Energy in Italy*. Last accessed June 2016, http://www.thinkgeoenergy.com/enel-inaugurates-national-museum-of-geothermal-energy-in-italy/

Tinti, F. (2012). *The probabilistic characterization of underground as a tool for the optimization of integrated design of shallow geothermal systems*. Doctoral dissertation, University of Bologna, Italy

VDI 4640 (2001). *Thermal use of the underground - GSHP systems*. Verain Deutscher Ingenieure, VDI-Verlag, Düsseldorf

Wagner, R. and Clauser., C. (2005). Evaluating thermal response tests using parameter estimation for thermal conductivity and thermal capacity. *Journal of Geophysics and Engineering*, 2 (4), 349-356

Wikipedia contributors, "Roman Baths (Bath)" *Wikipedia, The Free Encyclopedia.* Last accessed June 2016, https://en.wikipedia.org/w/index.php?title=Roman_Baths_(Bath)&oldid=739971901

Williams, J.H. and Johnson, C.D. (2004). Acoustic and optical borehole-wall imaging for fractured-rock aquifer studies. *Journal of Applied Geophysics*, 55 (1-2), 151-159

Witte, J.J.L., Van Gelder, G.J. and Spitler, J.D. (2002). In situ measurement of ground thermal conductivity: A dutch perspective. ASHRAE Transactions, 108 (1), 263-272

Yamano, M., Goto, S., Miyakoshi, A., Hamamoto, H., Lubis R.F., Monyrath, V. and Taniguchi, M. (2009). Reconstruction of the thermal environment evolution in urban areas from underground temperature distribution. *Science of the Total Environment*, 407, 3120-3128

Zemanek, M.D., Glenn, E.E., Norton, L.J. and Caldwell, R.L. (1970). Formation Evaluation by Inspection with the Borehole Televiewer. *Geophysics*, 35, 254-269

Zhu, K., Blum, P., Ferguson, G., Balke, K.D. and Bayer, P. (2010). The geothermal potential of urban heat islands. *Environmental Research Letters*, 5, 044002

Appendix A: Drilling parameters logs for the four boreholes

ULg-Sart-Tilmant

Date	: **06/06/2013**	Machine :	**KLEMM 805-2W**	Méthode :	**DTH**	Outil :	**DTH**	Profondeur : **0.00 - 101.16 m**
Heure début :	**10:51**			Fluide :	**Eau+mousse**	Diamètre :	**132mm**	
Heure fin :	**10:01**			Tubage :	**150mm**	Volumes :	**0, 0.00 m³**	

1/100

Forage : B1

Vitesse d'avancement (m/h) — Pression de poussée (bar) — Pression d'injection (bar) — Couple de rotation (bar)

ULg-Sart-Tilmant

B1

Vitesse d'avancement (m/h)	Pression de poussée (bar)	Pression d'injection (bar)	Couple de rotation (bar)
0 125 250	0 100 200	0 50 100	0 100 200
101	101	101	101
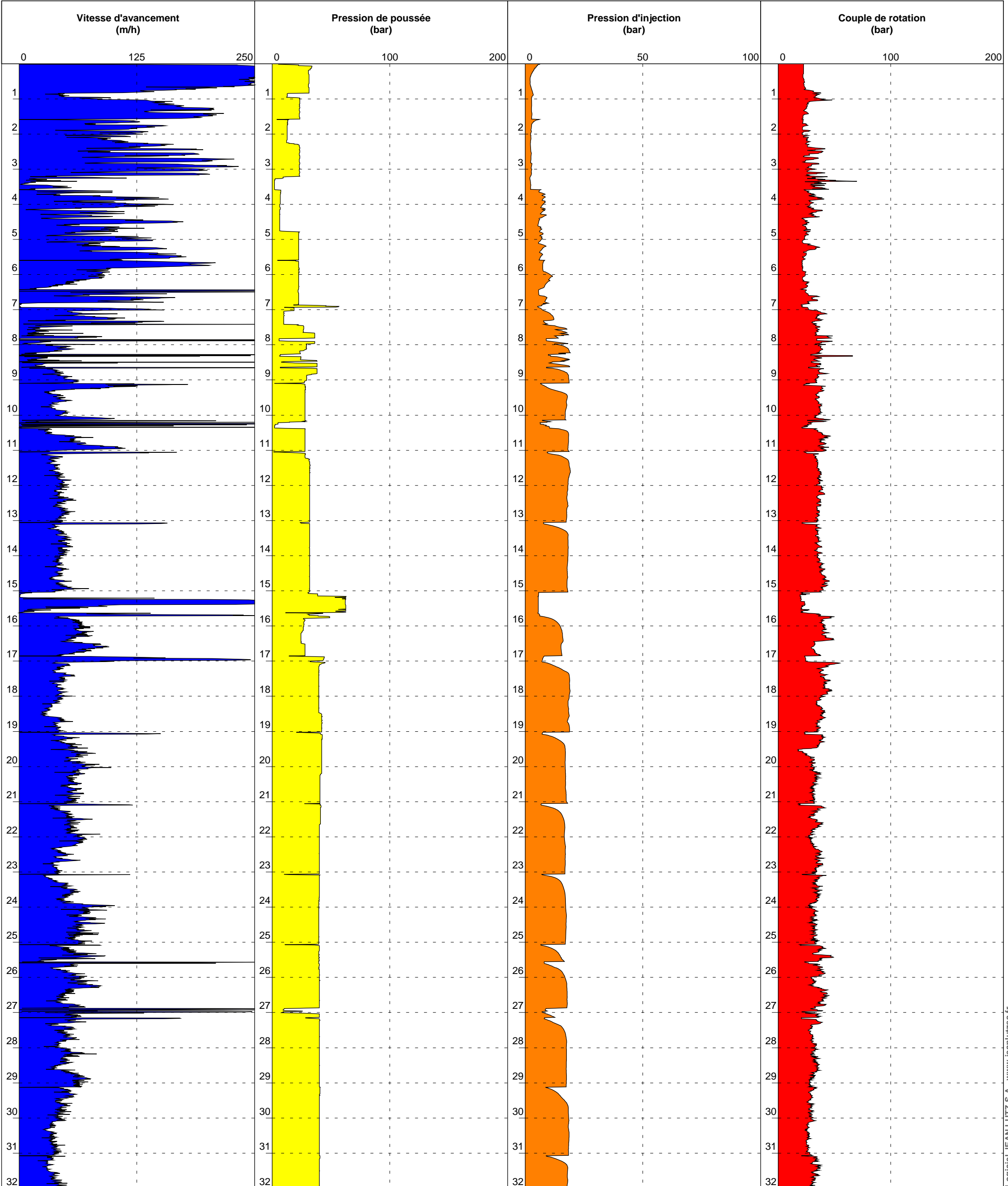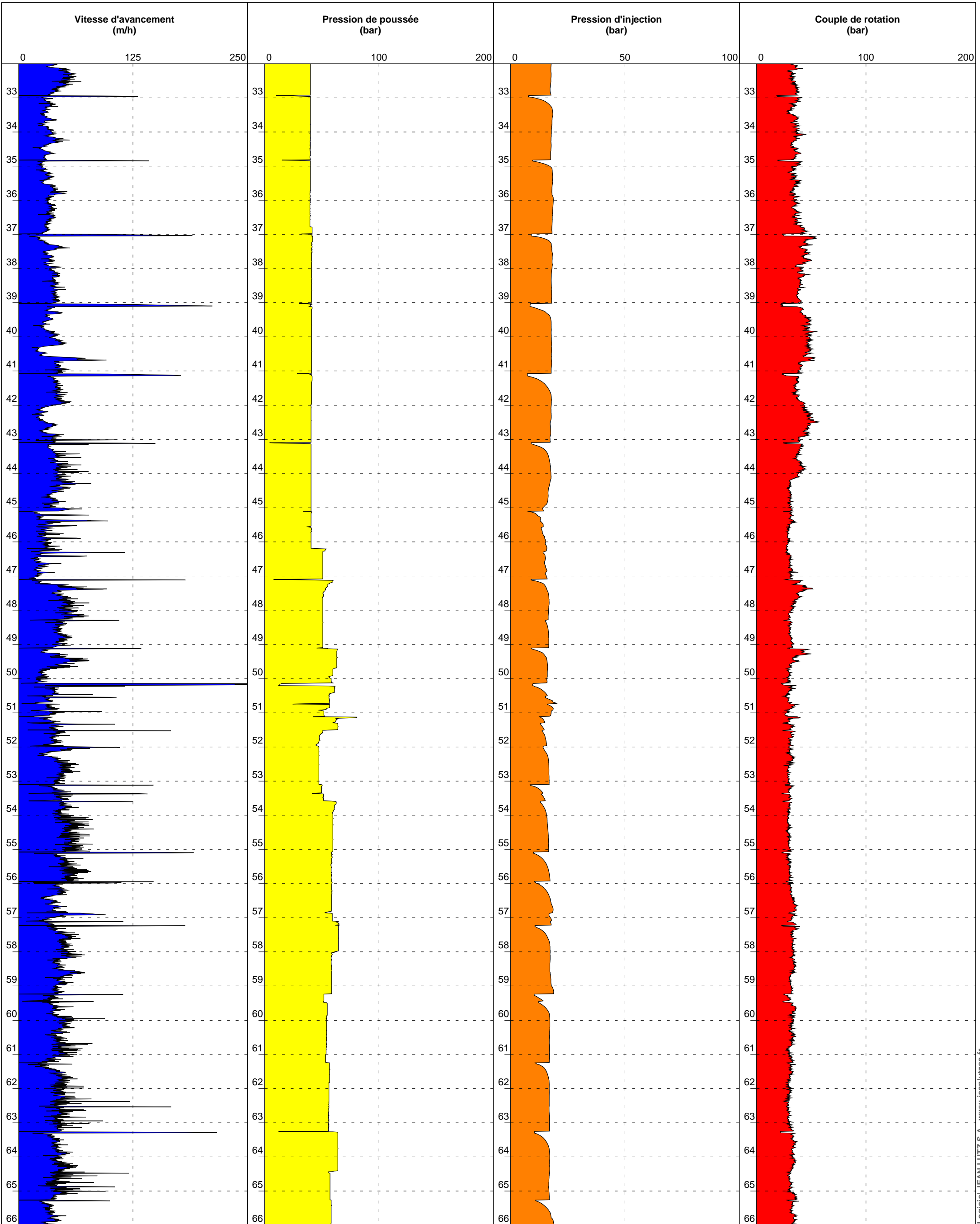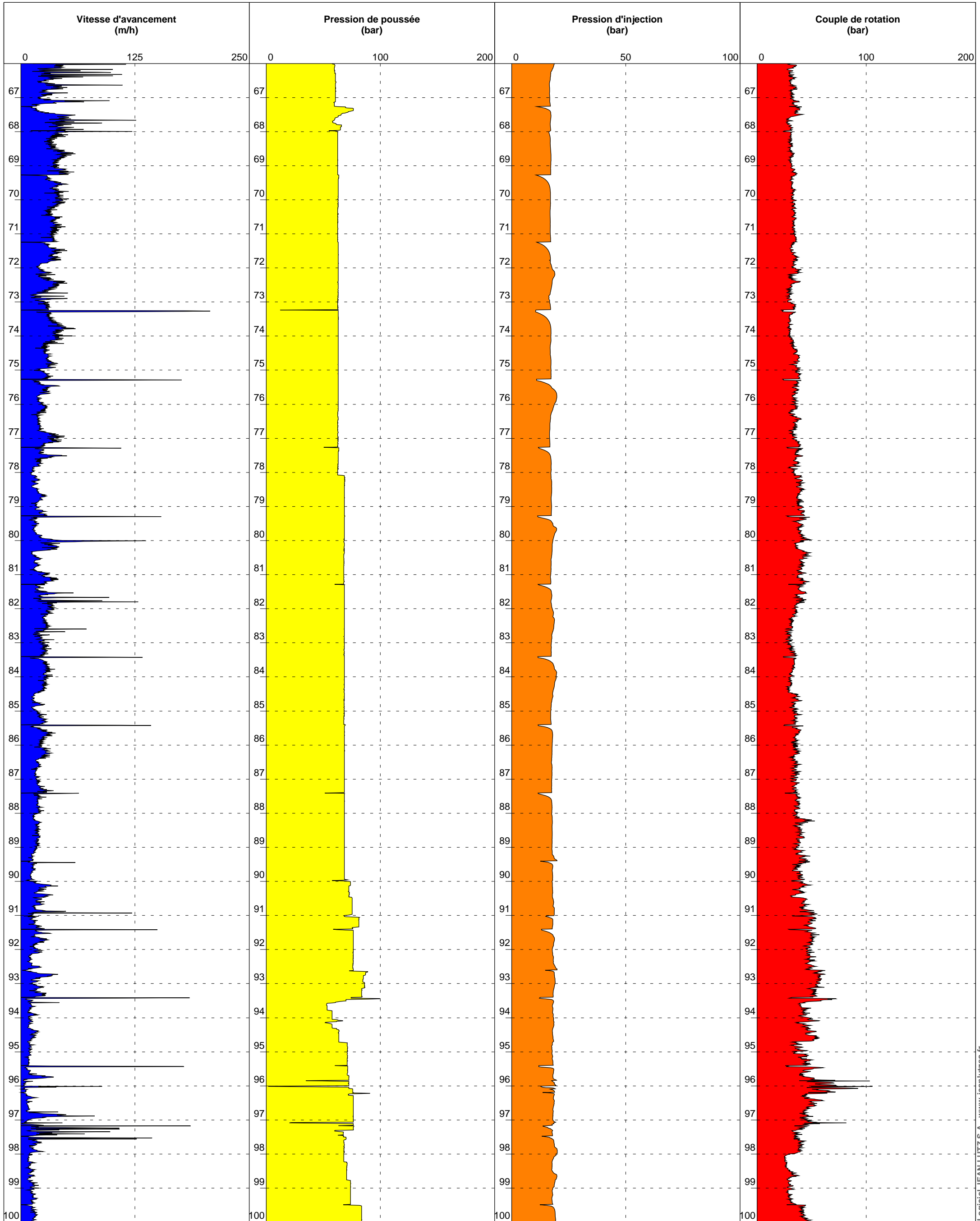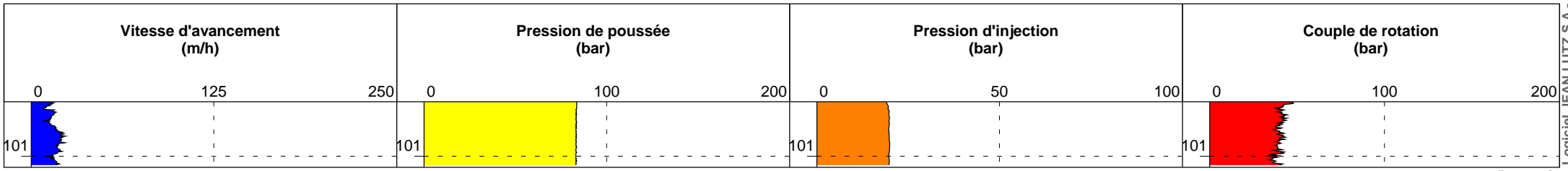
ULg-Sart-Tilmant

Date	:	**10/06/2013**	Machine :	**KLEMM 805-2W**	Méthode :	**DTH**	Outil	:	**DTH**	Profondeur :	**0.00 - 101.16 m**
Heure début	:	**10:56**			Fluide	:	**Eau+mousse**	Diamètre :	**132mm**		
Heure fin	:	**12:40**			Tubage	:	**150mm**				

1/100

Forage : B2

Vitesse d'avancement (m/h)	Pression de poussée (bar)	Pression d'injection (bar)	Couple de rotation (bar)
0 125 250	0 50 100	0 50 100	0 100 200
101	101	101	101
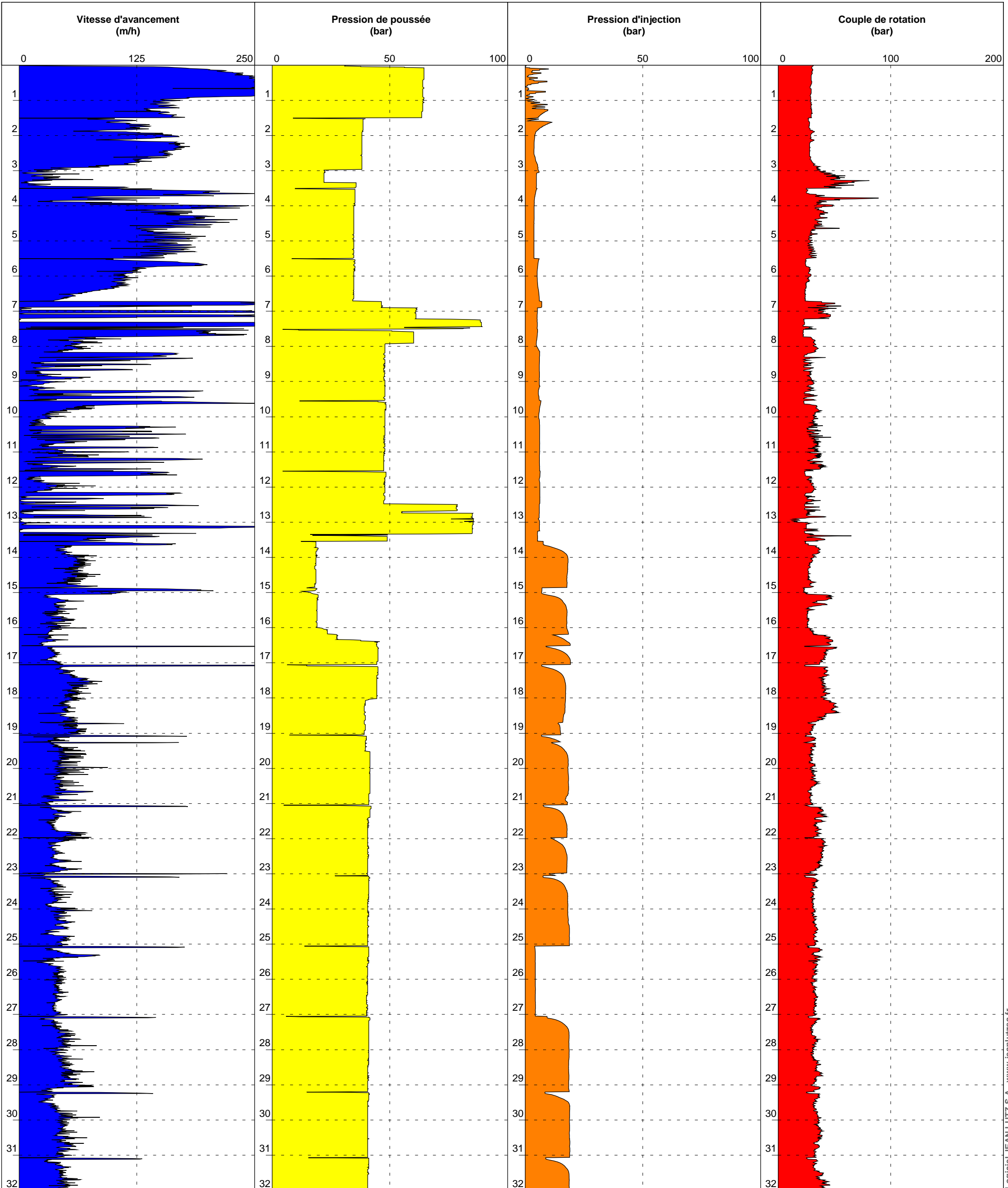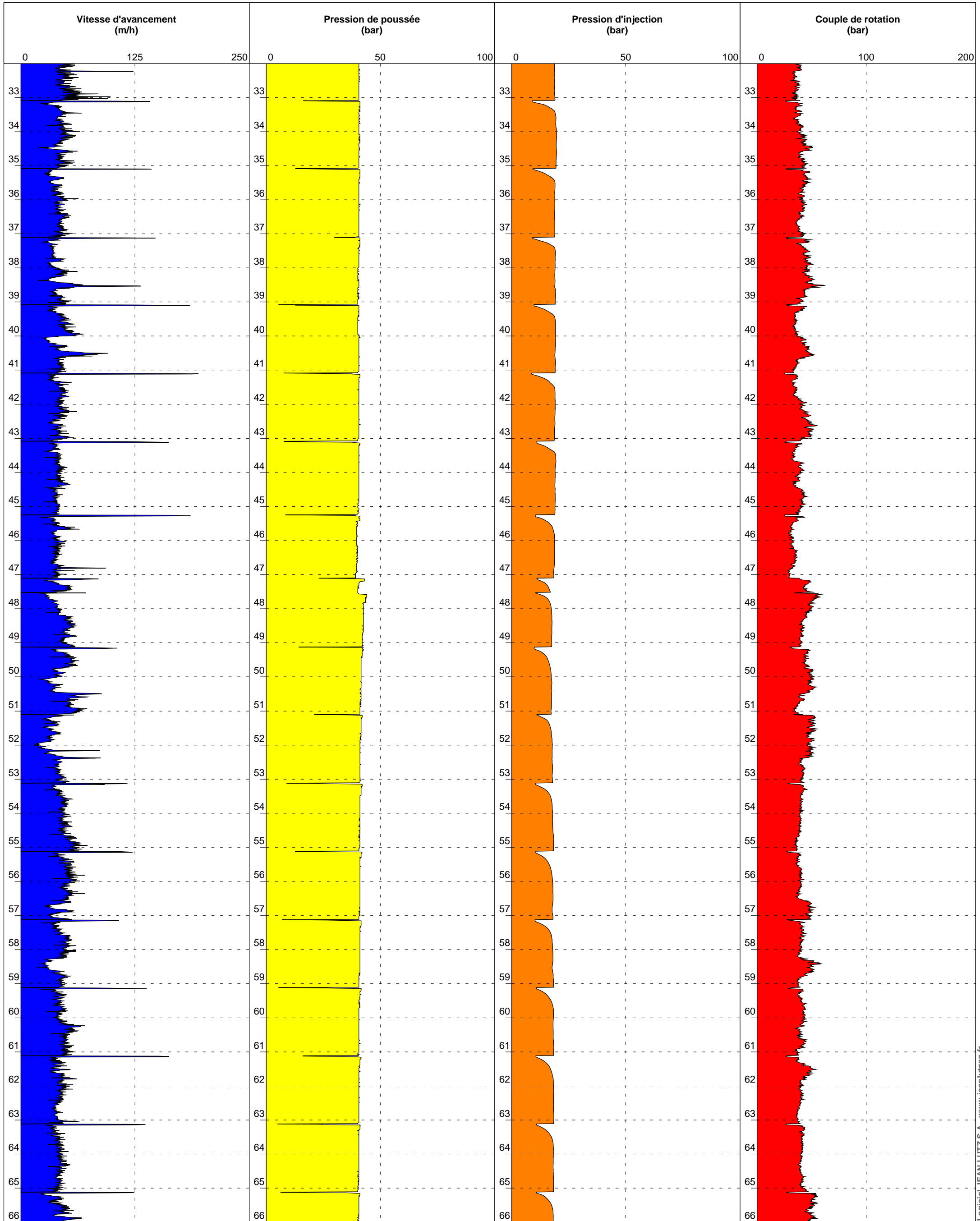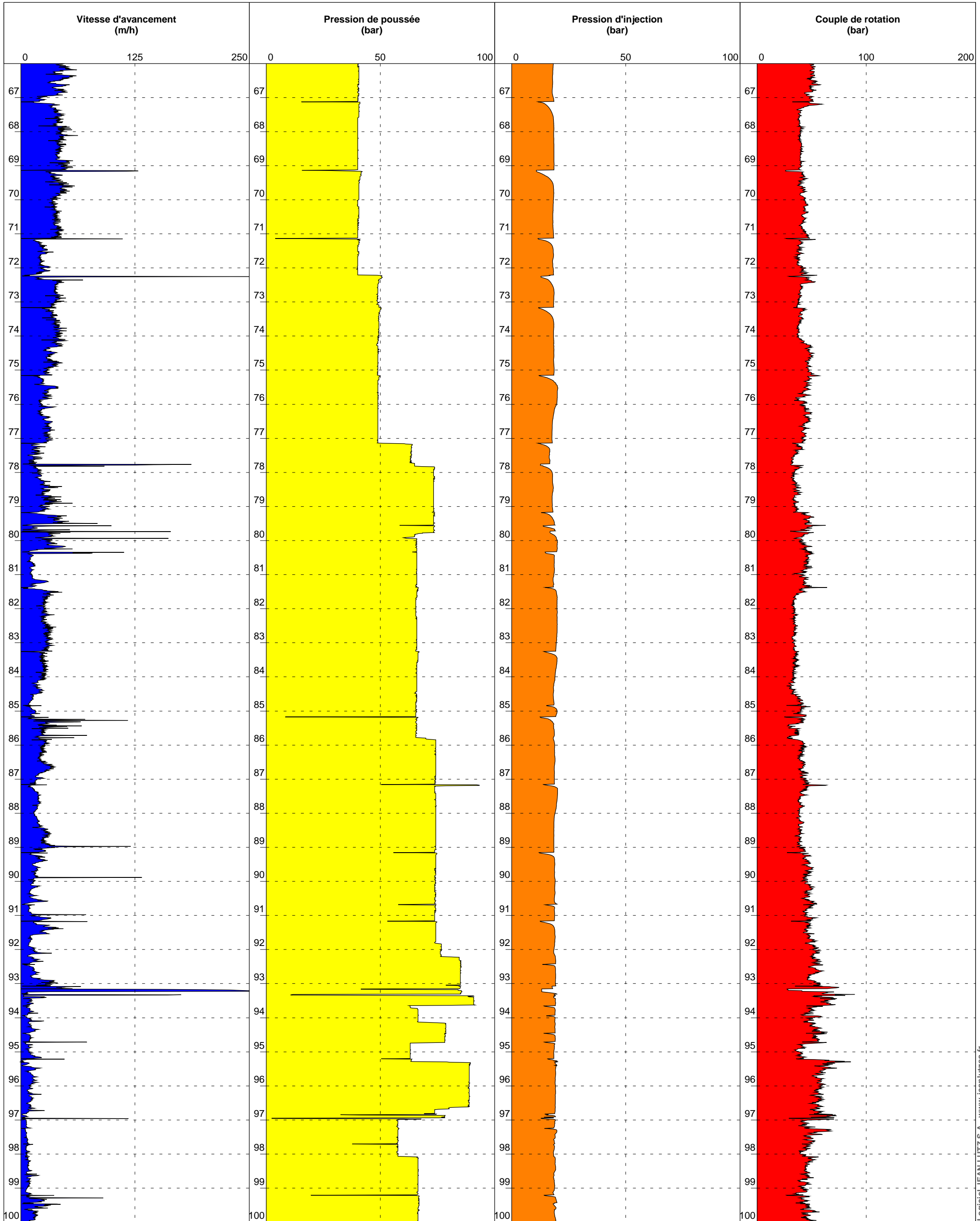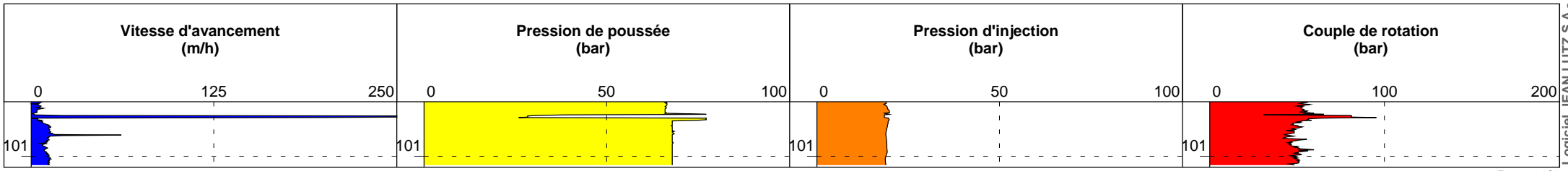
ULg-Sart-Tilmant

Date	: **04/07/2013**	Machine :	**KLEMM 805-2W**	Méthode :	**DTH**	Outil :	**DTH**

Profondeur : **0.00 - 101.13 m**

Heure début :	**09:57**
Heure fin :	**12:04**

Fluide : **Eau+mousse**   Diamètre : **132mm**

Tubage : **150mm**

1/100

Forage : B3

Vitesse d'avancement (m/h) — Pression de poussée (bar) — Pression d'injection (bar) — Couple de rotation (bar)

Vitesse d'avancement (m/h)	Pression de poussée (bar)	Pression d'injection (bar)	Couple de rotation (bar)

Vitesse d'avancement (m/h)	Pression de poussée (bar)	Pression d'injection (bar)	Couple de rotation (bar)
0　　125　　250	0　　100　　200	0　　50　　100	0　　100　　200
101	101	101	101
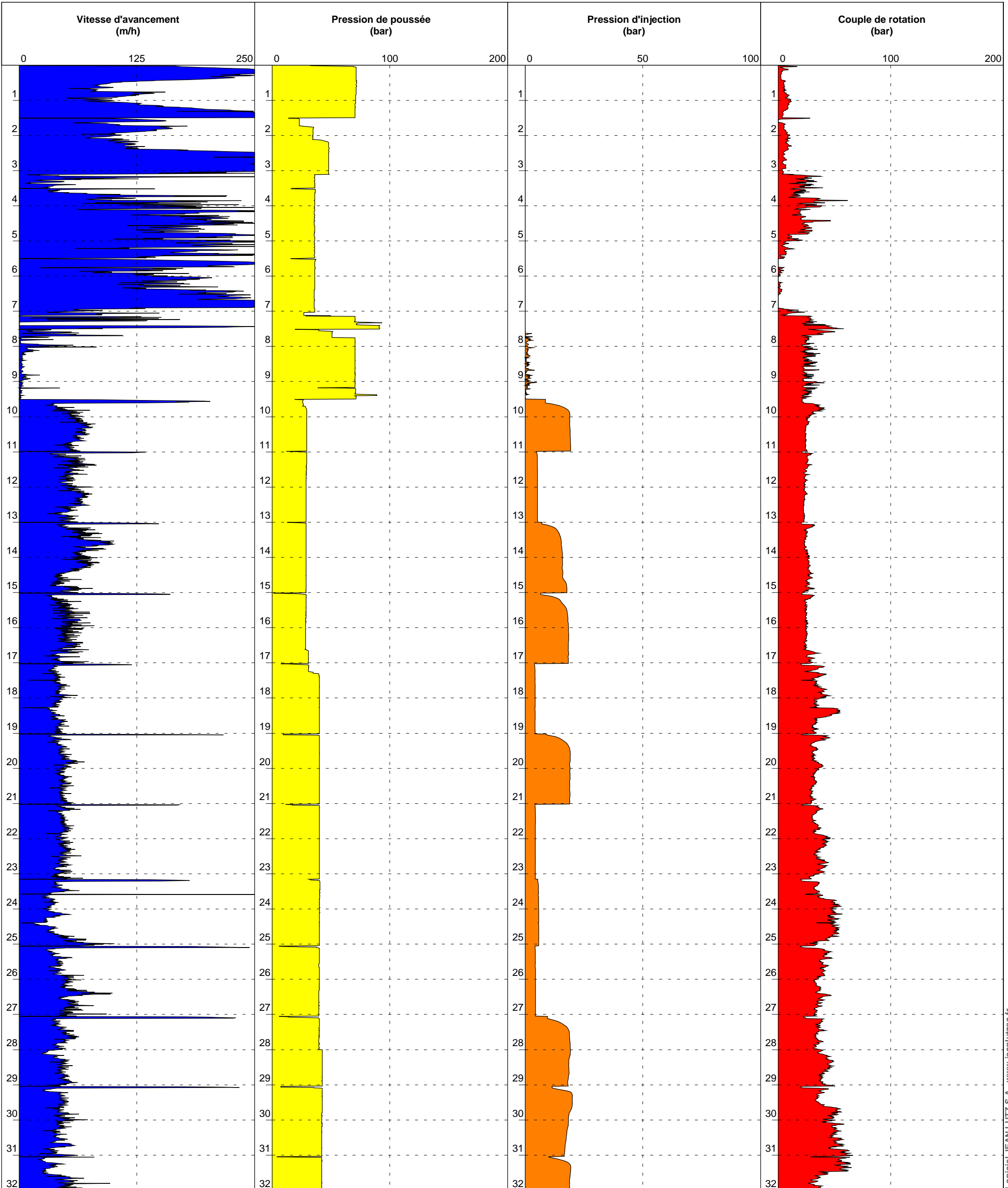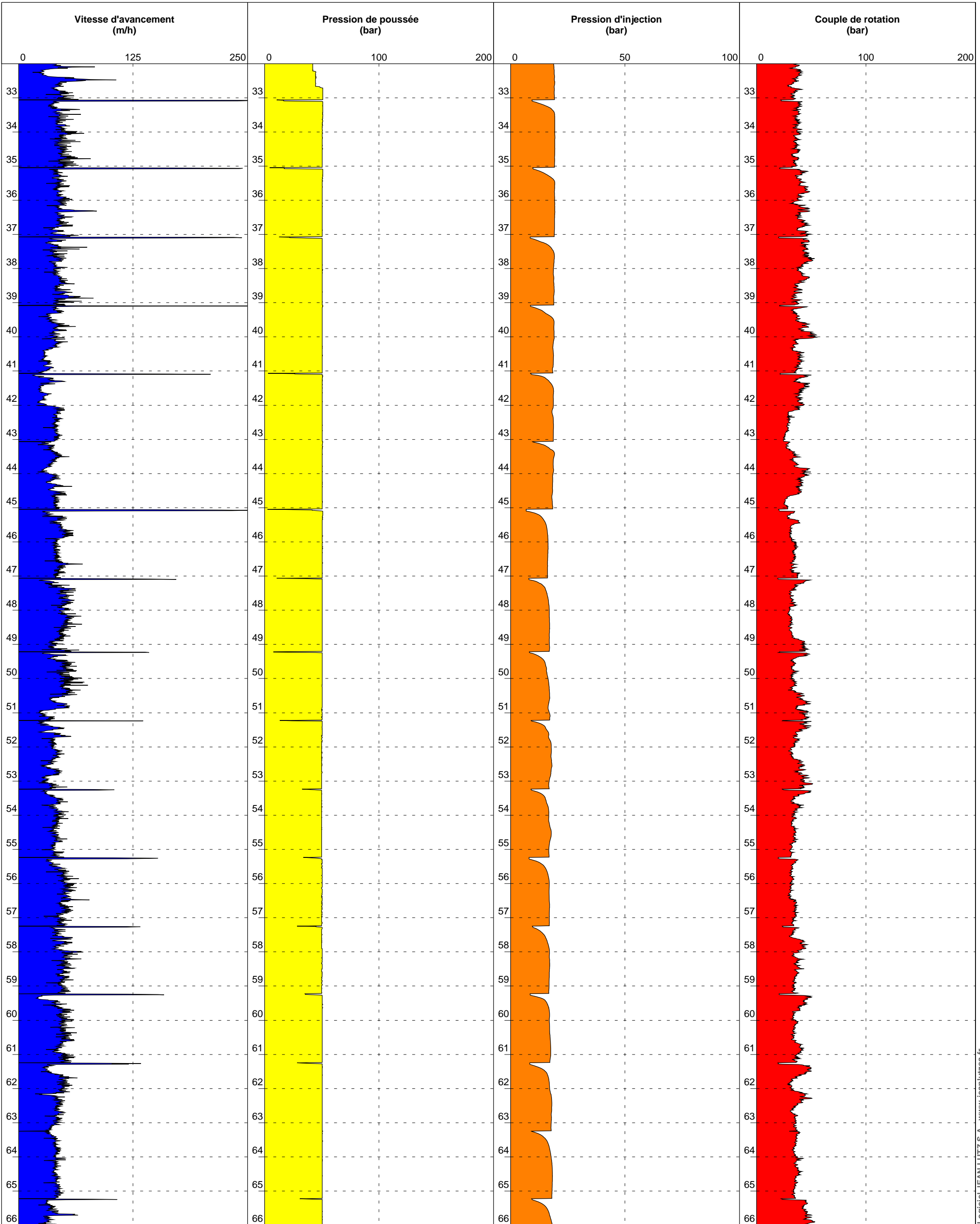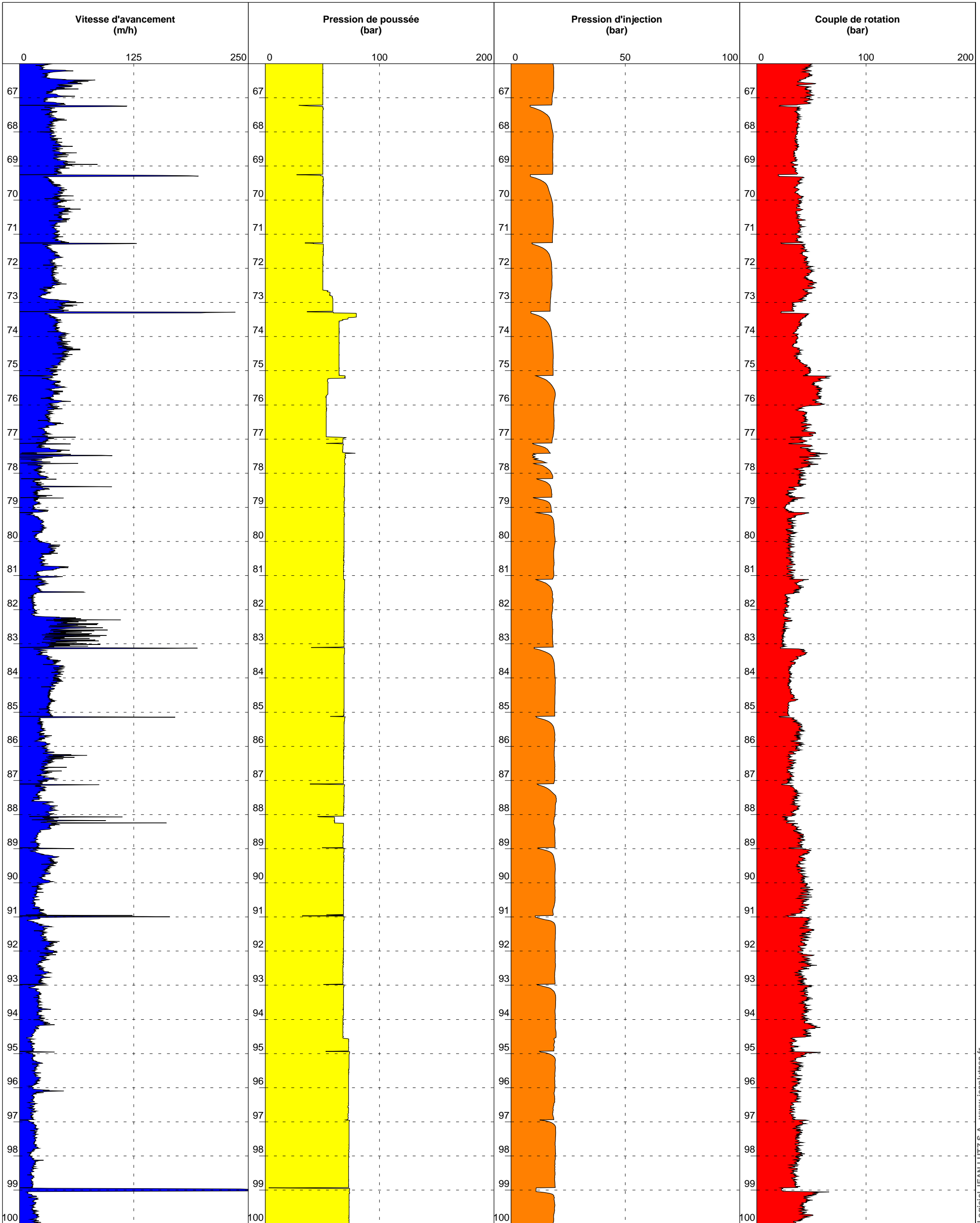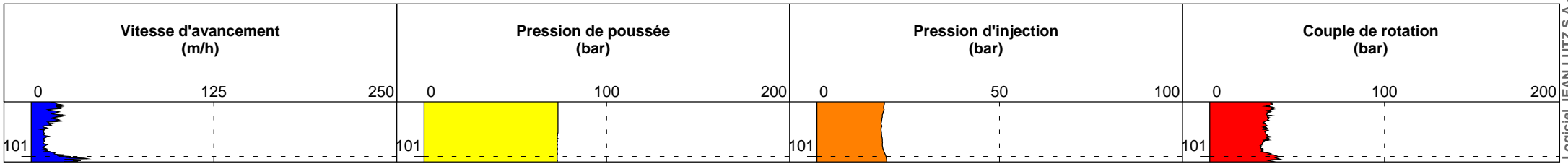
ULg-Sart-Tilmant

Date	: **20/06/2013**	Machine : **KLEMM 805-2W**	Méthode : **DTH**	Outil : **DTH**	Profondeur : **0.00 - 100.87 m**
Heure début : **09:55**			Fluide : **Eau+mousse**	Diamètre : **132mm**	
Heure fin : **10:46**			Tubage : **150mm**	Volumes : **0, 0.00 m³**	

1/100

Forage : B4

Vitesse d'avancement (m/h)	Pression de poussée (bar)	Pression d'injection (bar)	Couple de rotation (bar)

Vitesse d'avancement (m/h)	Pression de poussée (bar)	Pression d'injection (bar)	Couple de rotation (bar)

Vitesse d'avancement (m/h)	Pression de poussée (bar)	Pression d'injection (bar)	Couple de rotation (bar)
0　　　125　　　250	0　　　100　　　200	0　　　50　　　100	0　　　100　　　200
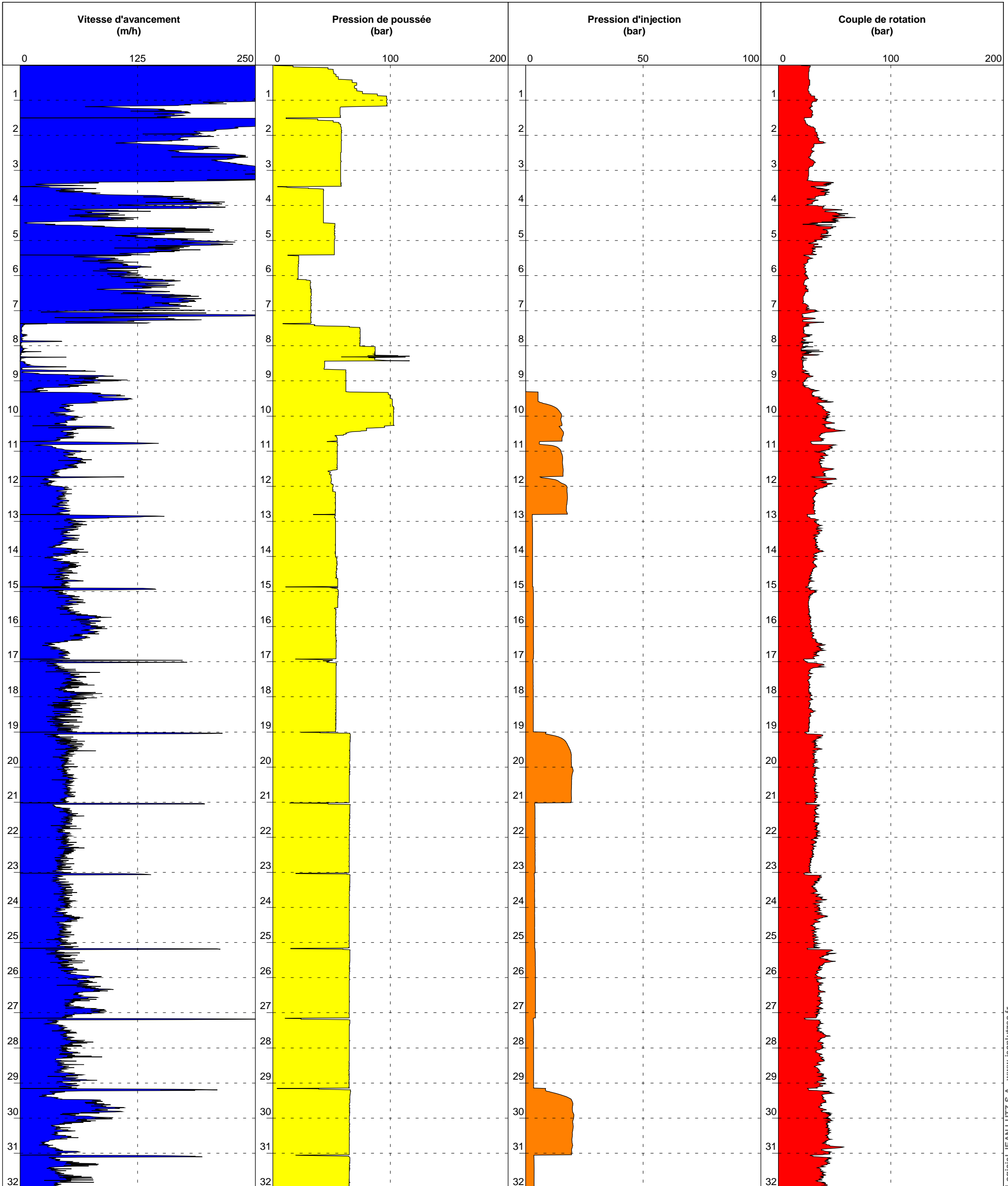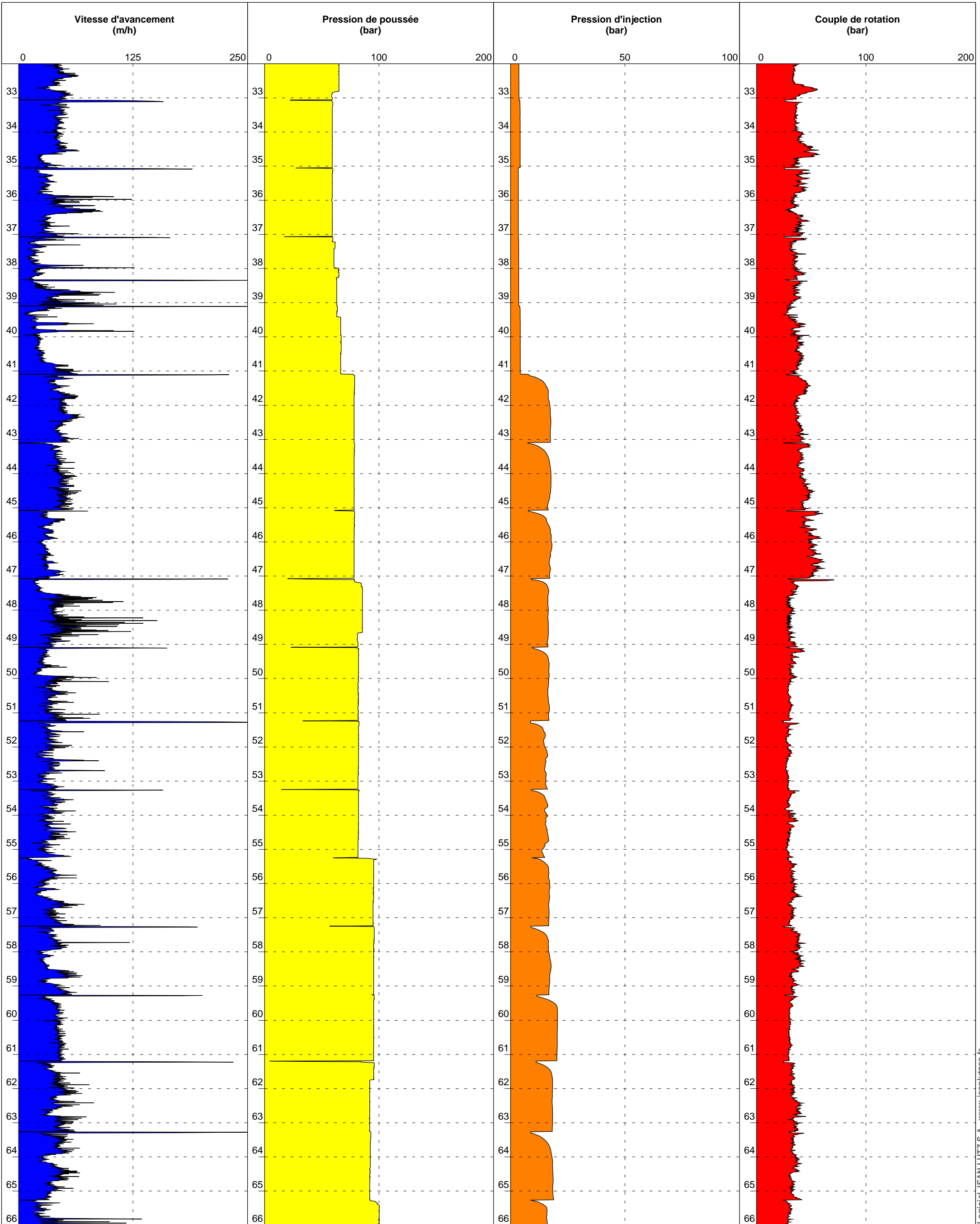
Appendix B: Formulation of a 1D finite element of heat exchanger for accurate modelling of the grouting behaviour: Application to cyclic thermal loading

Formulation of a 1D finite element of heat exchanger for accurate modelling of the grouting behaviour: Application to cyclic thermal loading

CrossMark

B. Cerfontaine [a, *], G. Radioti [a, b], F. Collin [a], R. Charlier [a]

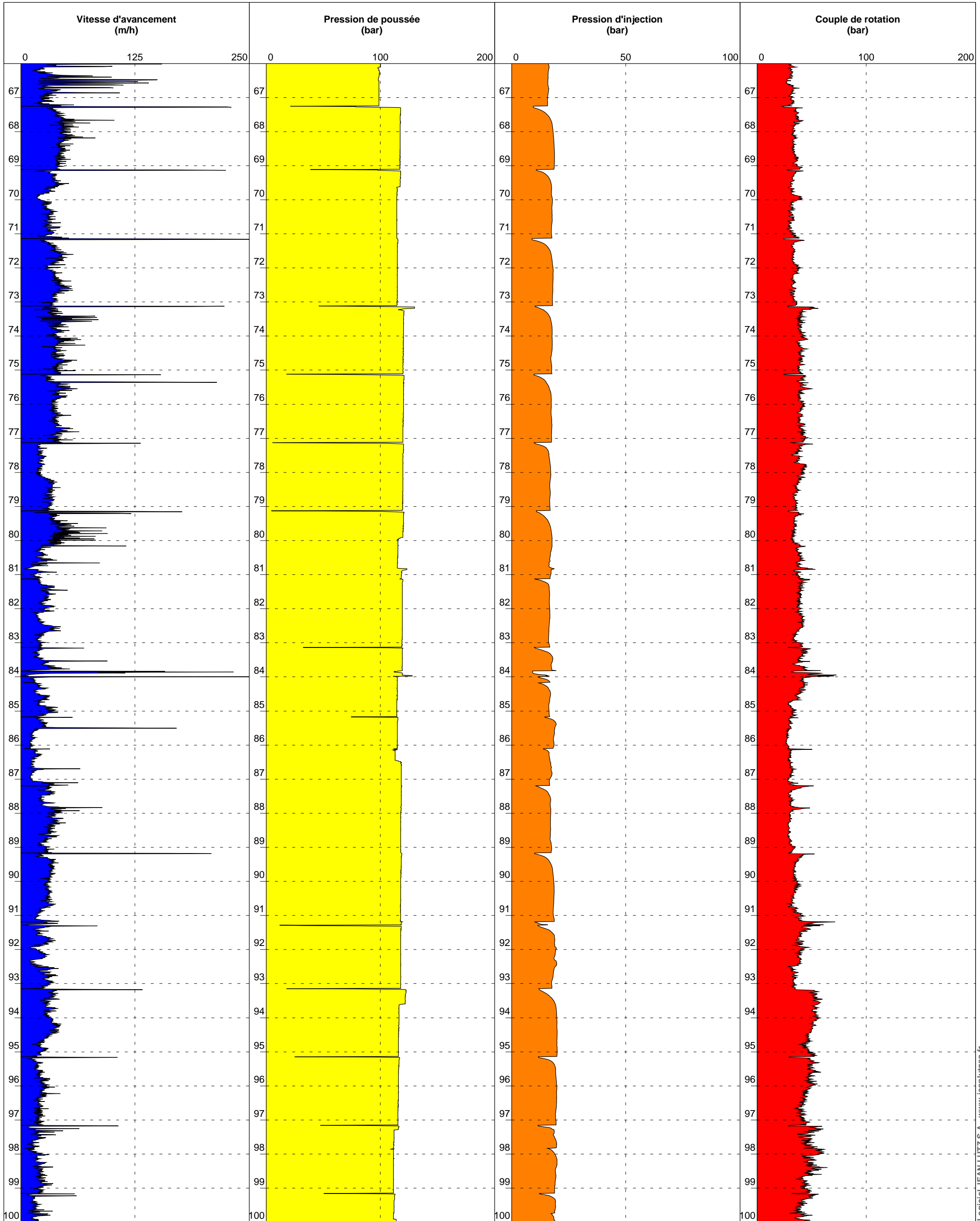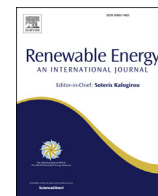[a] University of Liege, Geomechanics and Engineering Geology, Chemin des chevreuils, Liege, Belgium
[b] F.R.I.A., Fonds de la Recherche Scientifique - FNRS, Brussels, Belgium

ABSTRACT

This paper presents a comprehensive formulation of a finite element for the modelling of borehole heat exchangers. This work focuses on the accurate modelling of the grouting and the field of temperature near a single borehole. Therefore the grouting of the BHE is explicitly modelled. The purpose of this work is to provide tools necessary to the further modelling of thermo-mechanical couplings.

The finite element discretises the classical governing equation of advection-diffusion of heat within a 1D pipe connected to ground nodes. Petrov-Galerkin weighting functions are used to avoid numerical disturbances. The formulation is able to capture highly transient and steady-state phenomena.

The proposed finite element is validated with respect to analytical solutions. An example consisting of a 100 m depth U-pipe is finally simulated. A first continuous heating simulation highlights the non-symmetric distribution of temperature inside and near the borehole. An estimation of the error on the results as a function of the resolution parameters is also carried out. Finally simulations of cyclic thermal loading exhibit the need to take into account all daily variations if the grouting behaviour must be modelled. This is true especially in case of freeze-thaw damaging risk.

© 2016 Elsevier Ltd. All rights reserved.

1. Introduction

Among the different possibilities that geothermal energy offers, energy extraction through geothermal heat pumps is the most frequent worldwide application and increasing over the last years [1]. Shallow geothermal heat pump systems exchange heat with the ground either by circulating the groundwater through two separate wells (open-loop) or by using heat exchangers embedded in the ground mass (closed-loop). Vertical closed-loop geothermal systems, also known as Borehole Heat Exchangers (BHEs), are widely used since they have a small footprint at the surface for installation and can be applied in many hydrogeological contexts [2,3]. BHEs consist typically of one or two loops of high-density polyethylene pipes installed in a borehole. A heat carrier fluid is circulated in the pipe loop and heat is transferred between the fluid and the surrounding ground. A grouting material is usually injected in the borehole to enhance the heat transfer between the

circulating fluid and the surrounding ground and to prevent environmental risks. These systems are widely used for heating and cooling of buildings and small compounds [4]. In winter heat is extracted from the ground (heating of the building) while in summer heat is injected in the ground (cooling of the building).

The long-term use of BHE may have many technical and environmental consequences [5] such as the influence on groundwater quality or the reduction of efficiency of the injection/extraction process. Sustainability of BHE is a crucial issue [6]. This consists in finding the maximum level of energy production allowing a constant production for a very long time. Therefore the optimisation of single or fields of BHE is carried out in order to limit their impact or increase their efficiency [7–9]. Limitations of temperature variations within the soil, the carrier fluid and the grouting is another constraint. Indeed the freeze-thaw cycles may affect the thermal properties of the grouting [10–12] or the shallow aquifer quality [5]. The evaluation of these consequences requires the development of analytical and numerical models able to capture all the features of BHE-ground interactions.

Analytical and semi-analytical solutions are widely used for the BHE design and optimisation [7–9] especially due to their low

---

* Corresponding author.
E-mail address: b.cerfontaine@ulg.ac.be (B. Cerfontaine).

computational cost. Early solutions are developed to analyse the long-term behaviour of BHE [13,14]. They are limited to conduction only and drop vertical effects or pipe interactions [15]. extend one of these methods to take into account short-term behaviour which is proven important for some applications. The basic infinite line source, finite line source and infinite cylindrical source models are compared in Ref. [16] and their applicability is classified with respect to the duration of the simulation.

Refinements of analytical methods are more and more developed. Heat advection in the surrounding soil is taken into account in Ref. [17] despite the proposed solution is in 2D. The interaction between pipes is included in Ref. [18–20]. propose a model dealing with vertical conduction as well as advection-diffusion in the soil and discontinuous loading. A classification procedure of these models is proposed in Ref. [21].

Finally some other authors try to better estimate the variation of temperature within the pipe only in order to simplify the resistance parameter identification procedure. For instance [22] propose to use a so called p-approximation of the temperature profile within U-pipes [23,24]. develop other analytical solutions taking into account interactions between the pipes. However despite the high efficiency of all these methods, they are still limited in geometry, soil configuration and complexity of couplings.

The last decade gives birth to a large number of different numerical models of BHE. These models allow more flexibility on thermal properties distribution within the soil, modelling of an advection flow around the BHE, varying geometries, short-term description of the temperature variations … They could be classified with respect to different criteria [25].

1. numerical method: finite element (most of the following papers), finite differences [26,27], finite volumes [25,28];
2. 2D or 3D simulations;
3. treatment of circulating fluid transport;
4. representation of the grouting;
5. possible advection in the soil [29];
6. single or multiple borehole(s).

Fully coupled 3D models of BHE are most of the time very computationally demanding. However the continuous increase of computational power allows their intensive use. Indeed, many case studies are inherently 3D, especially when multiple boreholes are involved, the soil is heterogeneous or in case of waterflow in the ground.

Advection of heat within the pipe and diffusion within the soil are two phenomena with distinct time constant and numerical requirements (time step or mesh limitations). A pioneering work of [30] and [31] early distinguishes the BHE from the soil finite elements. In this model, the BHE (including one or two U-pipes and the grouting) is modelled as a 1D finite element. This was extended to higher number of pipes in the grouting [32,33] or to multiple dof representing the grouting [34]. This decomposition of the pipes and the volume element becomes classical in the modelling of BHE. Another model describes the BHE as an assembling of resistances and thermal capacity [26,35]. The enumeration of the different models is not the purpose of this paper but interested reader should refer to [25] as a starting point.

Many models deal with steady-state solutions for the temperature distribution within the pipe. However it appears that the dynamic modelling of BHE is a crucial issue in their design [36–39]. conclude that alternative and discontinuous operation modes can strongly increase the heat transfer efficiency. Heat pump are often used in alternative modes and periods ranging from a year to less than a day. In the first case, heat extraction (winter) and injection (summer) modes alternate over a year [40,25]. In the second case,

the heat pump may work only for a part of the day and be switched off otherwise [41,19]. Subsequently there is a need of a model able to reproduce highly transient effects with a minimum error and computer cost. Indeed, the error accumulation may be a critical issue [42] in case of cycle thermal loading.

The objective of the paper is to present the formulation of a versatile finite element of heat exchanger. The classical basic idea consists in dissociating the advective problem within the pipes and the dispersive problem within the grouting and the soil. The focus is placed here not on the large-scale modelling of multiple BHE but on the accurate modelling of a single BHE in the near and far fields. The grouting around the pipes is then explicitly modelled in order to well reproduce the gradients of temperature inside it and to avoid any hypothesis on the grouting thermal resistance or the interaction between different pipes. The geometry of the grouting section may also evolves with depth due to the heterogeneity of the soil. The model must accurately reproduce long and short term variations of temperature around the borehole.

The finite element is implemented in the non-linear finite element code LAGAMINE developed at the University of Liege [43,44]. This software is able to take into account all thermo-hydro-mechanical couplings in a fully coupled manner. However only thermal effects are considered here. The formulation of the element is adapted to highly transient simulations. Moreover the error control is a major concern. Indeed, the integration scheme and parameters are of crucial importance for advection problem.

In the following, the coupled heat exchanger finite element is firstly described in a general manner. It is validated on a classical example and verified with respect to a line source analytical solution. Numerical examples are then presented. A short-term heat injection scenario is investigated to prove the capabilities of the model and to estimate the error due to time integration parameter. A short-period discontinuous heat extraction scenario is presented and the influence of the operation scheme is analysed. Finally a one year simulation is carried out taking into account daily variations of the thermal demand.

2. Heat exchanger finite element

In the following it is decided to represent the pipe inside the BHE as a 1D finite element. Contrary to many models, the 1D finite element only models the flow into the pipes and does not include the grouting. This allows a very flexible formulation where the number, the disposition and the interaction of the pipes inside the borehole is arbitrary. The fluid flow is supposed to be in steady-state and the fluid velocity is constant all along the pipes.

Each node of the pipe element is related to a node, representative of the surrounding ground temperature. Here the ground is a generic denomination of the volume surrounding the pipe irrespectively of its actual nature (grouting, soil …). The volume 8-node finite elements describing the ground are classical and defined in Ref. [45] for thermo-hydro-mechanical couplings. They take into account thermal conduction into the soil and could also deal with advection, despite this is not considered in the following.

2.1. Governing equations

Let us assume a pipe is embedded into a ground volume of arbitrary shape, as depicted in Fig. 1. A fluid is circulating within the pipe and there is a difference of temperature between the fluid and the surrounding ground. It is assumed that the cross-section of the pipe is constant all over the pipe. Moreover the temperature of the fluid is assumed uniform over each cross-section and the velocity of the fluid is constant all along the pipe. The incoming longitudinal heat flux q_z [W/m^2] into the pipe is composed of a conduction and
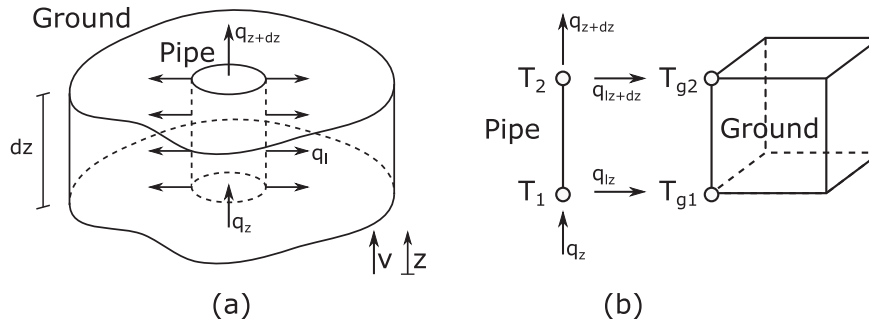
Fig. 1. (a) Sketch of the control volume, (b) idealisation of the problem.

an advection terms such that

$$q_z = -k \frac{\partial T}{\partial z} + v \rho c_p \left(T - T_{ref} \right), \tag{1}$$

where k [W/m/K] is the thermal conductivity, v [m/s] is the velocity of the fluid, ρ [kg/m^3] is the mass density of the fluid, c_p [J/kg/K] is the specific heat of the fluid, T [K] is the temperature of the fluid and T_{ref} [K] is a reference temperature. The outcoming heat flux q_{z+dz} is derived from

$$q_{z+dz} = q_z + \frac{\partial q_z}{\partial z} dz. \tag{2}$$

It is assumed that the convective heat exchange through the lateral surface of the pipe q_l [W/m^2] depends on the difference of temperature between the temperature of the fluid and the representative temperature of the ground T_g [K], leading to

$$q_l = h \left(T_g - T \right), \tag{3}$$

where h [W/m^2/K] is the convective heat coefficient. This coefficient rules the exchange of heat between the fluid and the wall of the pipe but may also include the thermal resistance of the pipe. Considering the control volume represented in Fig. 1 (a), the heat balance equation for the pipe is expressed as

$$\rho c_p S dz \frac{\partial T}{\partial t} = S (q_z - q_{z+dz}) + h P dz (T_g - T) \tag{4}$$

where P [m] is the circumference of the pipe and S [m^2] its section. Introducing Eqs. (1) and (2) into Eq. (4) yields to the governing equation of the heat flux within the pipe

$$\rho c_p S dz \frac{\partial T}{\partial t} + S \left(-k \frac{\partial^2 T}{\partial z^2} + v \rho c_p \frac{\partial T}{\partial z} \right) dz - h P dz (T_g - T) = 0. \tag{5}$$

2.2. Initial and boundary conditions

Initially at time $t = 0$, the temperature within the soil is set equal to the representative temperature of the ground T_g at the beginning, such that

$$T(z, 0) = T_g(z, 0). \tag{6}$$

Two types of boundary conditions can be imposed on surfaces normal to the axis of the pipe: essential (Dirichlet) and natural (Neumann) conditions. The first condition consists in imposing the temperature of the fluid. For instance imposing the temperature at

the beginning of the pipe reads

$$T_{z_{in}, t} = T_{in}, \tag{7}$$

where z_{in} is the position of the pipe's inlet and T_{in} the imposed temperature.

The Neumann condition imposes a heat flux on the inlet or outlet surface of the pipe. The heat flux in any cross-section is computed according to Eq. (1). A first condition applied in the following consists in a "free flow", which allows the heat to go out of the pipe. In this case, the q_{out} flow is imposed on the outlet cross-section such that

$$q_{out} = -k \frac{\partial T}{\partial z} + v \rho c_p \left(T - T_{ref} \right). \tag{8}$$

The carrier circulating fluid often describes a loop and is heated by a heat at the top of a U-pipe. In this case, the free-flow condition is applied to the outlet section and the q_{in} flow is applied at the inlet cross-section according to

$$q_{in} = -k \frac{\partial T}{\partial z} + v \rho c_p \left(T - T_{ref} \right) + \frac{Q_p}{S}, \tag{9}$$

where Q_p [W] is a power provided to the fluid.

2.3. Weak formulation of the problem

The exact residual Eq. (5) is numerically solved over an arbitrary domain by the weighted residual method [46]. The following equation holds over a 1D domain of length L

$$S \int_0^L W(z) \rho c_p \frac{\partial T}{\partial t} dz - S \int_0^L W(z) k \frac{\partial^2 T}{\partial z^2} dz + S \int_0^L W(z) v \rho c_p \frac{\partial T}{\partial z} dz$$

$$- P \int_0^L W(z) h (T_g - T) dz = 0 \tag{10}$$

where $W(z)$ is an arbitrary weighting function. Eq. (10) is integrated by parts and the resulting weak formulation of the problem is then provided by,

$$S \int_0^L W(z) \, \rho \, c_p \, \frac{\partial T}{\partial t} \, dz - S \int_0^L k \, \frac{\partial W(z)}{\partial z} \, \frac{\partial T}{\partial z} \, dz$$

$$+ S \int_0^L W(z) \, v \, \rho \, c_p \, \frac{\partial T}{\partial z} \, dz - P \int_0^L W(z) \, h \, (T_g - T) dz$$

$$= \left[k \, W(z) \, \frac{\partial T}{\partial z} \right]_0^L, \tag{11}$$

where the right-hand term is a boundary condition term.

2.4. Space discretisation of the problem

The field of temperature in the pipe is discretised by two-node isoparametric finite elements as described in Fig. 1. A mapping described by the Jacobian matrix **J** rules the change of variable from global coordinates (x,y,z) to local coordinate (ξ). Therefore the continuous field of temperature T is described over an element by

$$T(\xi) = \mathbf{N}^T \, \tilde{\mathbf{T}}, \tag{12}$$

where $\tilde{\mathbf{T}}^T = [\tilde{T}_1, \tilde{T}_2]$ is the vector of nodal temperatures and $\mathbf{N}^T = [N_1(\xi), N_2(\xi)]$ is the vector of shape functions related to these nodes. They are defined according to

$$N_1(\xi) = \frac{1}{2} \, (1 - \xi), \tag{13}$$

$$N_2(\xi) = \frac{1}{2} \, (1 + \xi). \tag{14}$$

The field of representative ground temperature parallel to the pipe is described similarly,

$$T_g(\xi) = \mathbf{N}^T \, \tilde{\mathbf{T}}_g, \tag{15}$$

but the shape functions are related to nodes of the ground $\mathbf{T}_g = [T_{g1}, T_{g2}]^T$ in Fig. 1.

Galerkin finite elements where the weighting functions are identical to the shape functions are classically used. However for advection-diffusion problems, it is shown that spurious oscillations may appear [47]. A lot of attention has been paid to this problem over the years. One solution is to use Petrov-Galerkin weighting functions [48,49]. Such a solution is already adopted for BHE in Refs. [30,32]. The weighting functions related to the pipe nodes are gathered into the vector $\mathbf{W}^T = [W_1(\xi), W_2(\xi)]$,

$$W_1(\xi) = \frac{1}{2} \, (1 - \xi) - \frac{3}{4} \, \beta \, \left(1 - \xi^2\right) \tag{16}$$

$$W_2(\xi) = \frac{1}{2} \, (1 + \xi) + \frac{3}{4} \, \beta \, \left(1 - \xi^2\right), \tag{17}$$

where β is a parameter depending on the Peclet number Pe such that

$$\beta = \coth(Pe) - \frac{1}{Pe}, \tag{18}$$

and the Peclet is defined according to

$$Pe = \frac{v \, \Delta z}{k}, \tag{19}$$

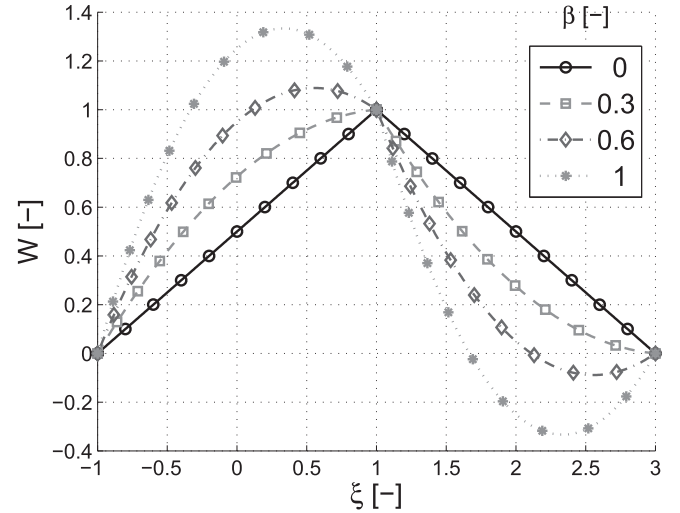where Δz is the length of the 1D finite element. The weighting

Fig. 2. Petrov-Galerkin weighting functions.

functions are represented in Fig. 2 for different values of β. This represents the functions related to a node centred in Ref. $\xi = 1$ for two adjacent elements. The speed of the flow is oriented towards positive axis. These functions simply give more weight to information coming from the direction of the flow.

Injecting Eqs. (16) and (17) into Eq. (11) leads after some algebra (dropping boundary terms $\tilde{\mathbf{W}}$) to a residual equation

$$\mathbf{F}_p^e = S \int_{-1}^1 \rho \, c_p \, \mathbf{W} \, \frac{\partial T}{\partial t} \, |\mathbf{J}| \, dz - S \int_{-1}^1 k \, \left[\frac{\partial \mathbf{W}}{\partial z}\right] \frac{\partial T}{\partial z} |\mathbf{J}| \, dz$$

$$+ S \int_{-1}^1 \mathbf{W} v \, \rho \, c_p \, \frac{\partial T}{\partial z} |\mathbf{J}| \, dz - P \int_{-1}^1 \mathbf{W} \, h \, (T_g - T) \, |\mathbf{J}| \, dz \tag{20}$$

where $|\mathbf{J}|$ is the determinant of the Jacobian matrix **J**, equal to $L/2$. Vector $\mathbf{F}_p^e$ is also termed vector of energetically equivalent nodal forces. It is an elementary vector related only to nodes of the pipe. The solution is in equilibrium if $\left\| \mathbf{F}_p^e \right\| = 0$. Otherwise, there are out of balance forces that should be reduced. This formulation is general and remains valid even if thermal properties varies with temperature. This vector is defined individually for each finite element.

The lateral heat flux Eq. (3) consists of a source term for the ground domain around the pipe. Therefore energetically equivalent nodal forces on the ground side, $\mathbf{F}_g^e$, are defined similarly such that

$$\mathbf{F}_g^e = P \int_{-1}^1 \mathbf{N}^T \, h \, (T_g - T) \, |\mathbf{J}| \, dz. \tag{21}$$

Only the heat exchange between the pipe and the ground is taken into account. In this case, the weighting functions are identical to the shape ones in order to be consistent with the ground finite elements [30,31].

Eqs. (20) and (21) are defined at the level of a single element. The last step is the assembling of a global vector of energetically equivalent nodal forces, **F**. This step is somehow classical and not detailed here.

2.5. Resolution of the problem

The time continuum is discretised in different time steps of

duration Δt_n such that

$$t_{n+1} = t_n + \Delta t_n. \tag{22}$$

The duration of the time steps may evolve during the simulation. It is supposed that the nodal unknowns vary linearly over a time step such that

$$\tilde{\mathbf{T}}_{n+\theta} = (1-\theta)\tilde{\mathbf{T}}_n + \theta\,\tilde{\mathbf{T}}_{n+1} \qquad \theta \in [0,1]. \tag{23}$$

Therefore the out of balance nodal forces can be computed for any θ. Solving the problem consists in finding the final nodal temperature vector $\tilde{\mathbf{T}}_{n+1}$ at the end of the time steps ensuring the out of balance forces $\mathbf{F}_{n+\theta}(\mathbf{T}_{n+\theta})$ are equal to zero. If the θ parameter is equal to 0, the integration is explicit. Otherwise the resolution is implicit. The fully implicit scheme corresponds to $\theta=1$ and $\theta=0.5$ is the so called Crank-Nicholson scheme.

If the problem is linear and the time step constant the elementary stiffness matrix $\mathbf{K}^k$ is unique and comes from

$$\mathbf{K} = \frac{\partial \mathbf{F}_{n+\theta}}{\partial \tilde{\mathbf{T}}_{n+1}} = \frac{\partial \mathbf{F}_{n+\theta}}{\partial \tilde{\mathbf{T}}_{n+\theta}} \frac{\partial \tilde{\mathbf{T}}_{n+\theta}}{\partial \tilde{\mathbf{T}}_{n+1}} = \theta\,\frac{\partial \mathbf{F}_{n+\theta}}{\partial \tilde{\mathbf{T}}_{n+\theta}}. \tag{24}$$

Finally, the heat storage is considered as a component of the out of balance forces. It is assumed that $\partial\mathbf{T}/\partial t$ is constant over the time step and

$$\frac{\partial \tilde{\mathbf{T}}}{\partial t}\Big|_{n+\theta} = \frac{\tilde{\mathbf{T}}_{n+\theta} - \tilde{\mathbf{T}}_n}{\theta\Delta t}. \tag{25}$$

The expression of the elementary stiffness matrix related to nodal unknowns $[\tilde{T}_1, \tilde{T}_2, \tilde{T}_{g1}, \tilde{T}_{g2},]^T$ is then summarised into the expression,

$$\mathbf{K}^e = \begin{bmatrix} \mathbf{K}_{pp} & \mathbf{K}_{pg} \\ \mathbf{K}_{gp} & \mathbf{K}_{gg} \end{bmatrix}, \tag{26}$$

where the p subscript corresponds to the pipe and g to the ground. For instance the definition of the pipe-pipe component reads

$$\mathbf{K}_{pp} = \frac{S}{\theta\,\Delta t}\int_{-1}^{1}\mathbf{W}\,\rho\,c_p\cdot\mathbf{N}^T\,|\mathbf{J}|\,\mathrm{d}z - S\int_{-1}^{1} k\,\frac{\partial \mathbf{W}}{\partial z}\cdot\left[\frac{\partial \mathbf{N}}{\partial z}\right]^T |\mathbf{J}|\,\mathrm{d}z$$
$$+ S\int_{-1}^{1} v\,\rho\,c_p\,\mathbf{W}\cdot\left[\frac{\partial \mathbf{N}}{\partial z}\right]^T |\mathbf{J}|\,\mathrm{d}z + P\int_{-1}^{1} h\,\mathbf{W}\cdot\mathbf{N}^T\,|\mathbf{J}|\,\mathrm{d}z \tag{27}$$

The explicit definition of all components is provided in Appendix B for temperature independent thermal properties. Finally all the elementary stiffness matrices are assembled to the global stiffness matrix that will be solved.

3. Validation of the finite element

In the following section, the developed finite element is validated with respect to analytical solutions. A simplified geometry is considered in order to stay as close as possible to the hypotheses of the analytical solution.

3.1. Problem investigated

The geometry of the problem is illustrated in Fig. 3. The geometry consists of a single pipe coupled to a sector (opening of 10°) of ground. This ground represents a unique material whose properties are given in Table 1. The validity of the coupling with a 3D domain is
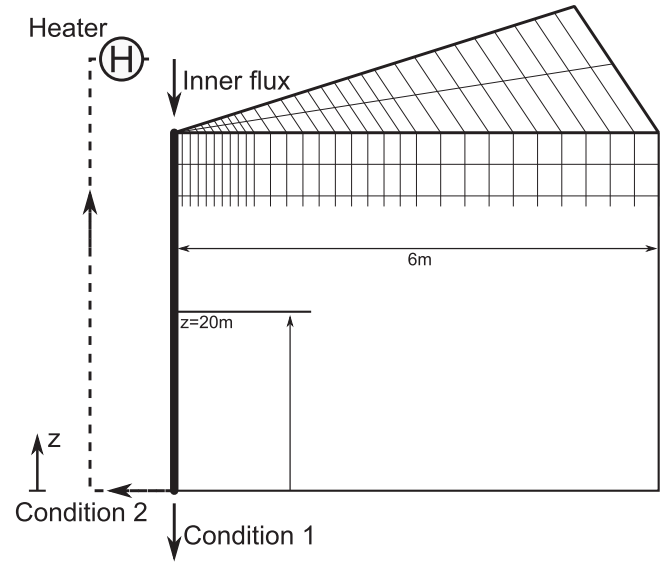
Fig. 3. Sketch of the mesh and parameters for the validation of coupled finite elements.

Table 1
Material parameters of the sector problem.

	1D pipe	Ground
ρ [kg/m^3]	1000	2500
c_p [kJ/kg/K]	4.185	0.92
k [W/m/K]	0.58	2.94
v [m/s]	0.3	/
r [m]	0.0131	/
μ [N.s/m^2]	1.002E-3	/
h [W/m^2/K]	1500	

shown but the computational time is limited. The external radius of the sector (ground domain) is equal to 6 m and its depth to 40 m. The mesh is laterally refined near the centre and more spaced further. It is uniformly discretised over the depth ($\Delta z = 1$ m). The carrier circulating fluid is supposed to be pure water.

The top boundary of the pipe condition consists of an imposed temperature or an imposed flux. The bottom condition is either an open pipe (the fluid goes away) or a loop condition (the fluid is heated and injected back to the top). This latter condition is non-realistic since the fluid is instantaneously transported. However this condition better suits the analytical line source solution, namely there is a single pipe. The ground domain is supposed to be in adiabatic conditions. The temperature is recorded in the pipe and in a cross-section at mid-depth as depicted in Fig. 3.

The rigorous choice of a time step to solve a transient problem depends on physical and numerical parameters. It is known that there is a critical time step that should not be overpassed in order to ensure the stability of the simulation, especially if the solution scheme is explicit. This conditions for convection dominated 1D problems is summarised into the Courant number condition [50,47],

$$\frac{v\,\Delta t}{\Delta z} \le 1. \tag{28}$$

This involves that the time step between two successive computations of a solution must be less than the time required for the perturbation to travel across the length of a finite element. The maximum time step of the simulation is equal to 3 s in order to fulfil

the Courant requirement such that

$$\frac{v \, \Delta t}{\Delta z} = 0.9 \le 1. \tag{29}$$

The convective heat transfer coefficient h is calculated according to

$$h = \frac{Nu \, k_w}{D_h}, \tag{30}$$

where D_h [m] is the hydraulic diameter of the pipe ($=2r$), k_w [W/m/K] the fluid thermal conductivity and Nu [−] the Nusselt number obtained from the classical correlation [51],

$$Nu = \frac{(f/8)(Re - 1000) \, Pr}{1 + 12.7(f/8)^{1/2}(Pr^{2/3} - 1)}, \qquad 0.5 < Pr < 200,$$
$$3000 > Re > 5 \cdot 10^6. \tag{31}$$

This relation depends on the Reynolds number Re [−],

$$Re = \frac{\rho \, v \, D_h}{\mu}, \tag{32}$$

where ρ [kg/m³] is the density of the fluid, v [m/s] the average velocity and μ [Pa.s] is the dynamic viscosity. The Prandtl number Pr [−] is defined as

$$Pr = \frac{c_p \, \mu}{k} \tag{33}$$

where c_p [J/kg/K] is the specific heat. Finally the Darcy friction factor f [−] is computed according to

$$f = (0.79 \ln(Re) - 1.64)^{-2} \tag{34}$$

for smooth pipes. The final convective heat transfer coefficient h computed is equal to 1500 W/m/K. It is related to parameters provided in Table 1 for the 1D pipe.

3.2. Constant soil temperature

The steady-state solution of the advection-diffusion problem in the pipe is easily obtained if the soil is assumed to have a constant temperature. The analytical solution of the temperature profile in the pipe is provided by Ref. [52].

$$T(z) = T_g - (T_g - T_i) \exp\left(\frac{-2\pi \, r \, z}{\pi \, r^2 \, v \, \rho \, c_p} \, h\right) \tag{35}$$

where T_i [K] is the imposed temperature at the beginning of the pipe. A numerical simulation is run where the initial inlet temperature is instantaneously heated from the initial temperature of 285 K–300 K. Numerically there is a first short transient phase where the perturbation propagates inside the pipe. The vertical distributions of temperature along the pipe at different time steps are provided in Fig. 4.

For the first time step, there is a small non-physical oscillation located around z = 35 m after 10 s. This is simply due to a mesh too coarse to exactly reproduce a very steep propagation front. After more than 90 s, the numerically computed distribution of temperature in the pipe perfectly matches the analytical steady-state solution.
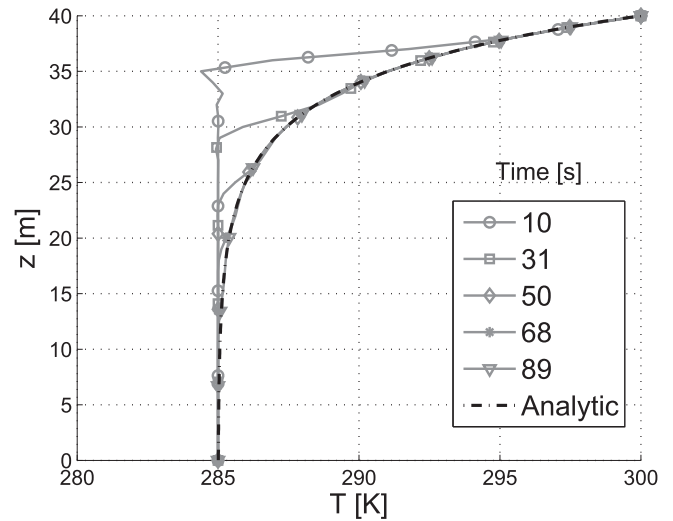

Fig. 4. Distribution of the temperature in the pipe at difference time steps, constant soil temperature.

3.3. Variable soil temperature

In the following, a heating test is simulated. It is assumed that the fluid going out of the pipe (z = 0 m) is instantaneously injected at its beginning (z = 40 m) and heated by a power Q_p of 2 kW. This leads to an average heating flux of the BHE q_{av} equal to 50 W/m. The evolution of the temperature in three sections of the pipe is provided in Fig. 5. The log scale is chosen to distinguish between transient and stationary phases. Temperature is constant until the incoming heated fluid reaches the observation point. Temperature is continuously increasing afterwards since the fluid describes a loop.

The distribution of temperature within the pipe at different time steps is provided in Fig. 6. Results on the left of the figure depicts the transient phase of the temperature evolution. The temperature profile is curved and temperature is higher at the top of the pipe. After few hours, the temperature profile has a constant shape that is simply shifted. This is a kind of stationary phase despite the evolution of temperature is still ongoing.

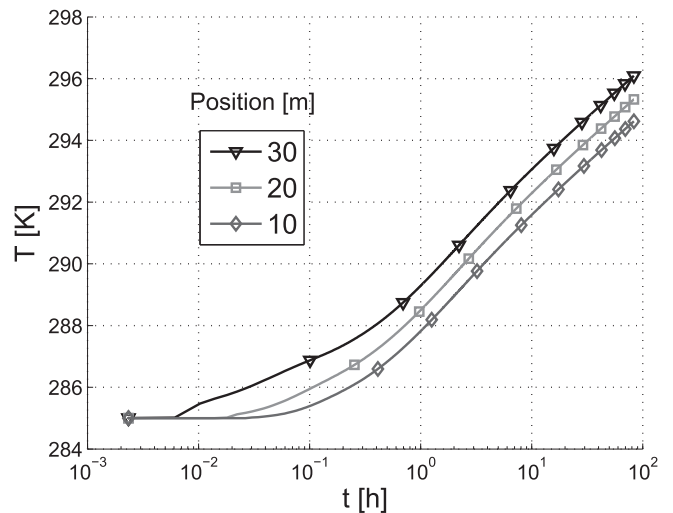The evolution of convective fluxes corresponding to Eq. (3) in

Fig. 5. Time evolution of the temperature in the pipe at three vertical positions.
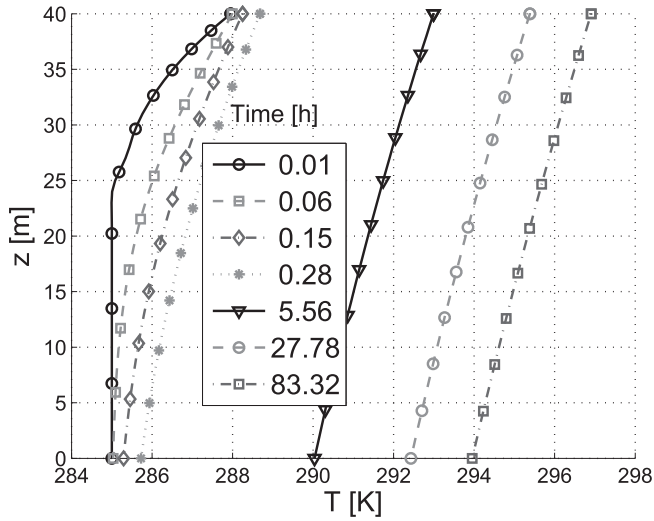
Fig. 6. Distribution of the temperature in the pipe at difference time steps.

the three cross-sections is depicted in Fig. 7. They are quite different during the first hour but almost converge towards the average value at the end. At the beginning the heat flux is the highest near the inlet of the pipe where the fluid has the highest temperature. Consequently the ground is heated, which progressively decreases the heat flux. Indeed the difference of temperature between the fluid and the ground is reduced. This highly transient phase is roughly limited to less than an hour. Afterwards the heat flux stabilises.

The line source model is frequently used to validate results of transient simulations of heat exchanger [31]. It consists of the heating of a semi-infinite medium where the heating fluxes are normal to a vertical line. The initial temperature in the ground and the pipe is uniform at the beginning. The radial distribution of temperature within the soil follows

$$T = T_{g0} + \frac{q}{2\pi k} \int_{\varepsilon}^{\infty} \frac{\exp\left(-\xi^2\right)}{\xi} d\xi, \tag{36}$$
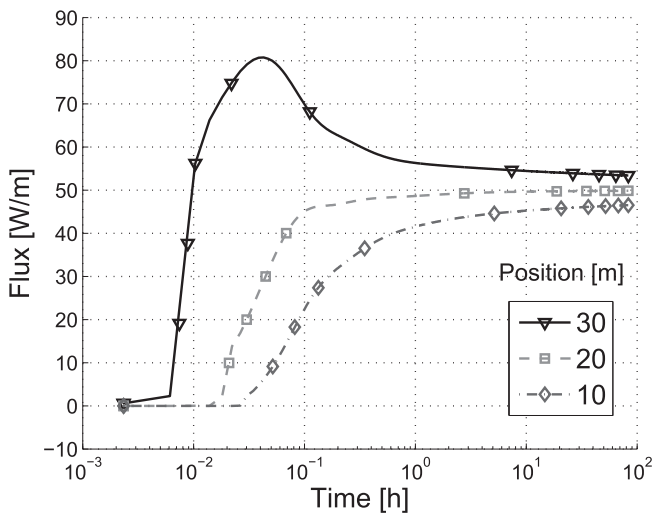

Fig. 7. Time evolution of the pipe-soil heat convective flux at three vertical depths.

$$\varepsilon = \frac{r}{2\sqrt{\alpha \, t}}, \tag{37}$$

where T_{g0} [K] is the initial temperature of the ground, q [W/m] is the average heat flux per meter length of the borehole, r [m] the radial distance to the source $\alpha = k/\rho/c_p$ [s^{-1}] is the thermal diffusivity of the soil and t [s] the time. An analytical solution of the integrand of Eq. (36) is provided if $\varepsilon < 0.2$ [53],

$$I(\varepsilon) = \ln\frac{1}{\varepsilon} + \frac{\varepsilon^2}{2} - \frac{\varepsilon^4}{8} - 0.2886. \tag{38}$$

The accuracy of that solution is then a function of position and time. The correct solution for a point lying far from the heating source is only available for a long time operation.

The mid-depth section is the point where the lateral heat flux is the closest from the average value. Therefore the horizontal temperature profile in the ground at this depth is compared with the line source solution in Fig. 8. Three time steps are investigated. Numerical and analytical solutions present a very good agreement. They slightly diverge but this could be explained by the non-constant heat flux over the depth and time, the mesh discretisation at the centre of the sector and vertical diffusion.

According to the line-source model, the conductivity of the soil can be estimated according to [52,27].

$$k_{est} = \frac{q}{4\pi} \frac{\log(t_{n+1}) - \log(t_n)}{T_{n+1} - T_n}. \tag{39}$$

The time-evolution of this estimated conductivity computed using the evolution of fluid temperature at three depths is provided in Fig. 9. The estimated value at the beginning of the simulation has no meaning since it lies in the highly transient phase where the heat fluxes are not stabilised. Moreover this phase is mainly controlled by the grouting properties. Finally the back-calculated values tend to the imposed values.
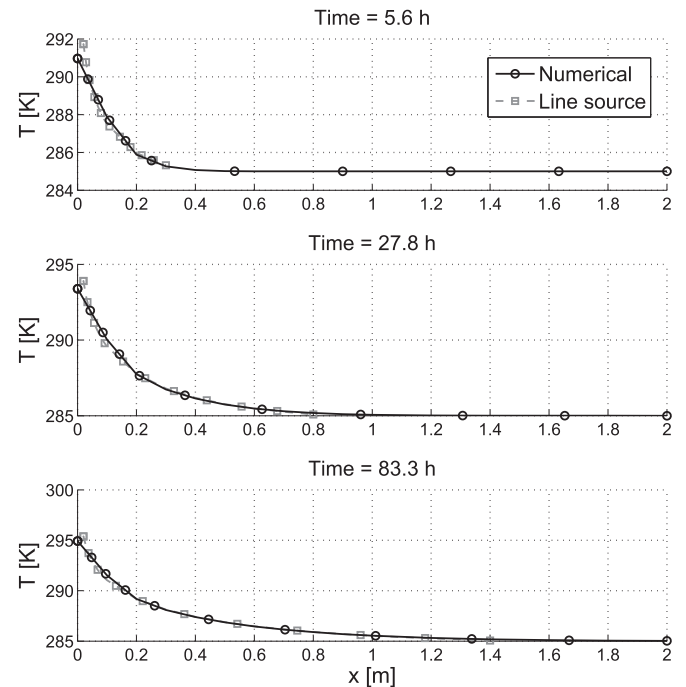

Fig. 8. Distribution of the temperature in the soil at difference time steps at $z = 20$ m, comparison between infinite line-source and numerical results.
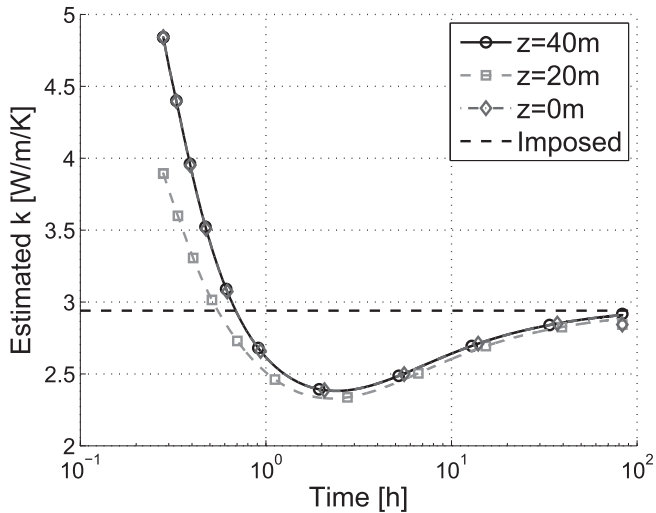
Fig. 9. Time evolution of the conductivity estimated in the soil from the temperature evolution at the end of the pipe.

4. Numerical examples

In this section, the capabilities of the model are described by different examples. A real case study is investigated where a U-pipe of 100 m is modelled. Short- and long-term simulations are presented. The 3D simulations are cpu time consuming. Therefore the time steps of the simulations are frequently chosen much higher than what is required by the Courant condition for advection-diffusion problems. The influence of the maximum time step of the simulation on the error is investigated. A cyclic example combining transient and long term phenomena is also presented. Finally a one year simulation exhibits differences in results due to daily or annual variations of thermal demand.

4.1. Problem investigated

The geometry consists of a single U-tube embedded in a bore-hole of radius equal to 6.8 cm as shown in Fig. 10. Both pipes of
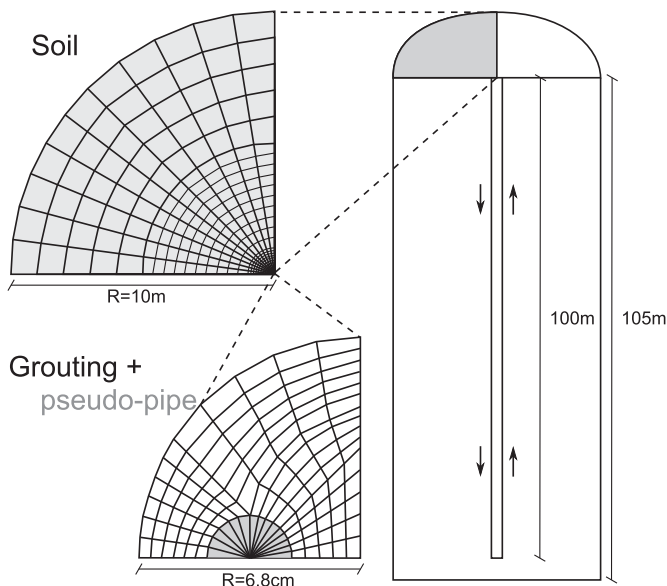

Fig. 10. Sketch of the mesh of the Upipe problem.

Table 2
Material parameters of the U-pipe problem.

	1D pipe	Pseudo-pipe	Grouting	Soil
ρc_p [MJ/^{3}/K]	4.18	0	1.62	2.3
k [W/m/K]	0.58	200	2.35	2.94

radius equal to 1.31 cm are separated by 6.8 cm. The grouting is explicitly modelled.

The 1D finite element of pipe that is used does not occupy any volume, by definition. However the pipe are physically embedded in the grouting and fill a volume [54]. propose to use a pseudo-pipe material to discretise this volume. This method is adopted here as shown in Fig. 10. This material has a high conductivity in order to not introduce an additional thermal resistance. However contrary to [54] there is no heat capacity assigned to the material to avoid the introduction a spurious transient phase within the pipe cross-section where temperature is supposed to be constant.

The 1D pipe element is connected to the central node the pseudo-pipe's volume. The pipe material is not represented here but the geothermal resistance could be included in the convective heat transfer coefficient h. The different material parameters are provided in Table 2. The vertical direction is discretised in 105 slices with a height of 1 m. The total size of the mesh is equal to almost 95000 unknowns. The simulations are run in adiabatic conditions and the initial temperature is uniform and equal to 285 K.

4.2. Heating simulation

The first simulation consists of a thermal response test during 50000 s (13.89 h). The time step is equal to 3 s. The fluid describes a loop and is heated continuously. Temperature profiles within the pipe are provided in Fig. 11 in order to describe the behaviour of the installation. The observed distribution of temperature quickly reaches its steady state where a similar V shape profile is progressively translated towards higher temperatures.

Different cross-sections of the grouting and the pseudo pipes at the end of the heating are depicted in Fig. 12. Temperature over the pseudo-pipe material is almost constant which was intended. On the contrary, temperature distribution in the grouting is everything but uniform.

The highest gradients of temperature within the grouting are observed in z = 100 m, which is the section closest to the pipe inlet.
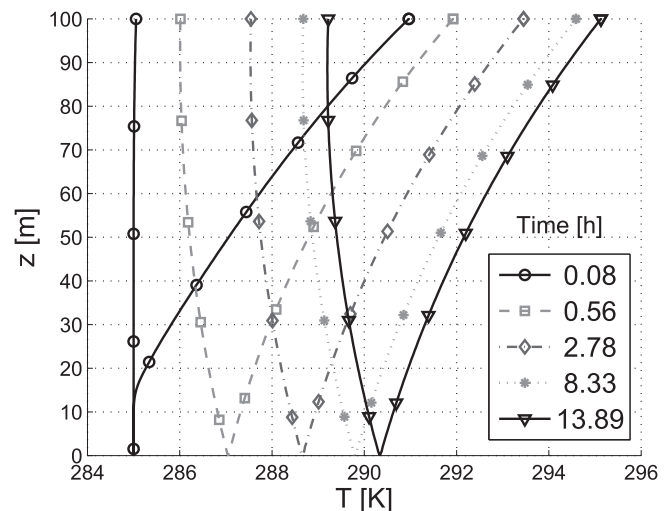

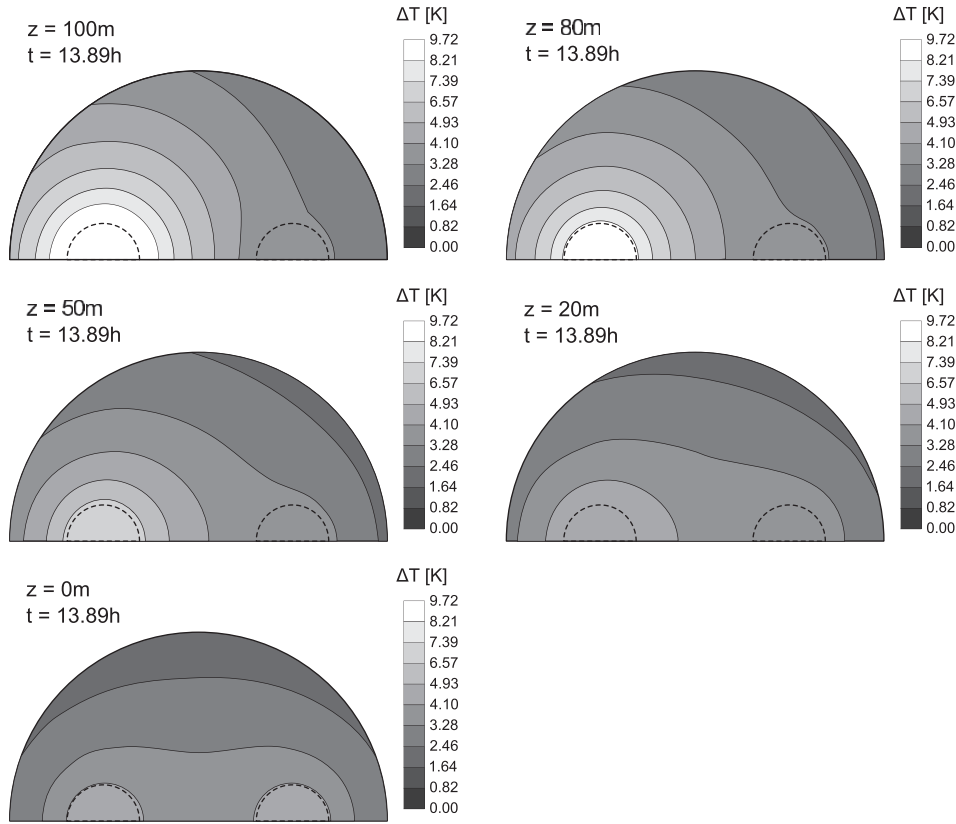**Fig. 11.** Distribution of temperature in the pipe of the BHE.

Fig. 12. Cross-section within grouting and pseudo-pipes at the end of the heating (t = 13.89 h).

This is consistent with the temperature profile distribution in Fig. 11 since the difference of temperature is the highest. On the contrary, the distribution of temperature is symmetric at the bottom of the borehole, where the temperature is identical in both pipes. The accurate simulation of the temperature gradient is crucial for their sustainability since the induced thermal stresses may degrade the grouting [11,12,20]. The mechanical degradation of the grouting is correlated with a decrease of its thermal properties and then its efficiency.

Fig. 13 exhibits the temperature distribution in the very near area around the grouting at the end of the simulation. Indeed, the distribution is non-symmetric around the borehole due to the downstream and upstream pipes. However the symmetry of the temperature profile fast becomes symmetric at a radial distance lower than 50 cm. Moreover, the symmetry also increases with depth. Therefore from a practical point of view, the line source like

Fig. 13. Cross-section within grouting, the pseudo-pipes and the soil at the end of the heating, (z = 100 m, t = 13.89 h).

models are sufficient to study the long-term behaviour of BHE for homogeneous soils without waterflow.

4.3. Error assessment

In many applications, the duration of the simulation ranges from days to years [27,28,31]. Large time steps are commonly carried out to spare cpu time and the fully implicit method is mainly adopted. However as previously mentioned in Section 3.1, the time step in advection-diffusion problems is classically limited by the Courant number. Moreover the θ parameter defined in Eq. (23) is known to affect the results [55,46]. A θ parameter equal to 0.5 limits numerical diffusion and provides a second order accuracy scheme for small time steps. However $\theta=1$ is known to provide a better precision for large time steps [56]. Therefore it is interesting to assess the error arising from the choice of a time step and an integration scheme.

An error indicator must be found to summarise the error of the results. It is chosen to focus on the temperature distribution within the pipe. The following error deals with the variation of temperature rather than its absolute value as proposed in Refs. [39,16]. The relative error at node i of the pipe and time t is defined according to

$$err(i,t) = \frac{T_i(t) - T_{ref,i}(t)}{T_{ref,i}(t) - T_0} \tag{40}$$

where $T_i(t)$ [K] is the temperature of the fluid in the current simulation at node i, $T_{ref,i}(t)$ [K] is the temperature of the fluid at the same node in the reference simulation and T_0 [K] is the initial temperature. The reference simulation is the thermal response test. The reference time step is equal to 3 s and the Crank-Nicholson integration scheme is adopted. The average error over the pipe at
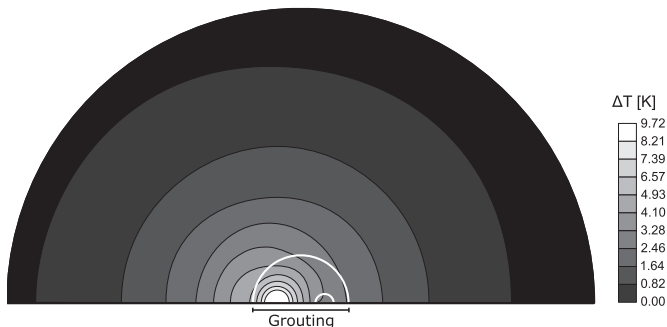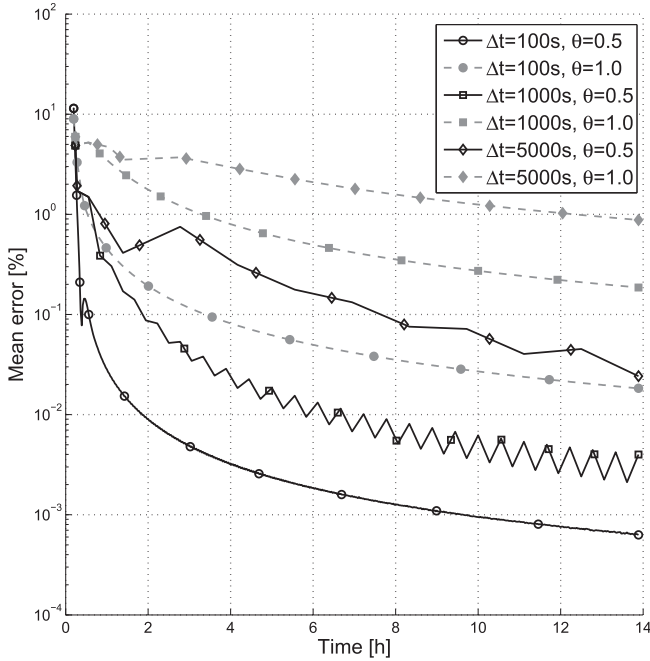
Fig. 14. Mean error as a function of the time step Δt and the integration parameter θ.

time t is defined such that

$$err_{av}(t) = \frac{1}{n_{nodes}} \sum_{i=1}^{n_{nodes}} err(i,t) \qquad (41)$$

where n_{nodes} is the number of nodes of the pipe where the temperature variation is different from zero.

Simulations are carried out for three time steps ($\Delta t = 100, 1000, 5000$ s) and two integration schemes: Crank Nicholson ($\theta = 0.5$) and fully implicit ($\theta = 1.0$). The evolution of the error with respect to the reference simulation is provided in Fig. 14. The first 700 s are

not provided because the error is very huge. Indeed, this corresponds to the highly transient phase and the propagation of a heat front which is not well captured but was not intended to be for larger time steps.

The error increases obviously with the size of the time step. However it can be observed that it decreases with time and is under 1% at the end of all simulations. For a given time step size, the error of the Crank-Nicholson integration is lower than the fully implicit one. However some oscillations appear for time steps equal to 1000 or 5000 s. This reflects oscillations in the solution. The occurrence of oscillations has been detailed in Ref. [55] and is a consequence of the too high time step. Therefore it is decided in the following to adopt a fully implicit scheme.

4.4. Typical thermal cyclic behaviour

The cyclic thermal loading of the borehole heat exchanger is based on the assumption that the maximum power should not necessary be maintained during a long period. For instance in office buildings or house, the human presence and use of heavy equipments is often non-continuous over a day. Therefore in the following a period of full operation ($Q_p = Q_{p,max}, v = v_{max}$) alternates with a period of recovery ($Q_p = 0, v = 0$). The duration of each period is equal to 12 h. The only additional hypothesis is that the convective heat transfer coefficient h remains constant during the recovery phase even if v is equal to zero.

The evolution of the temperature in a cross-section at position $z = 80$ m is provided in Fig. 15. The first cycle of heating/recovery is depicted on the left of the figure. There is a sharp cooling (starting from 285 K) of the fluid followed by a slower decrease of temperature. The shape of the results is similar when the pump is switched off. However the initial temperature is not totally recovered at the end of the recovery phase which was already observed [6,19,57,58]. Therefore cycle after cycle, the average temperature decreases as shown in Fig. 15 on the right. This cumulated decrease of temperature is marked at the beginning but tends to slow down.

The evolution of temperature is the superposition of two distinct processes characterised by a time-scale and a zone of influence. The first is the oscillatory variation of temperature due to
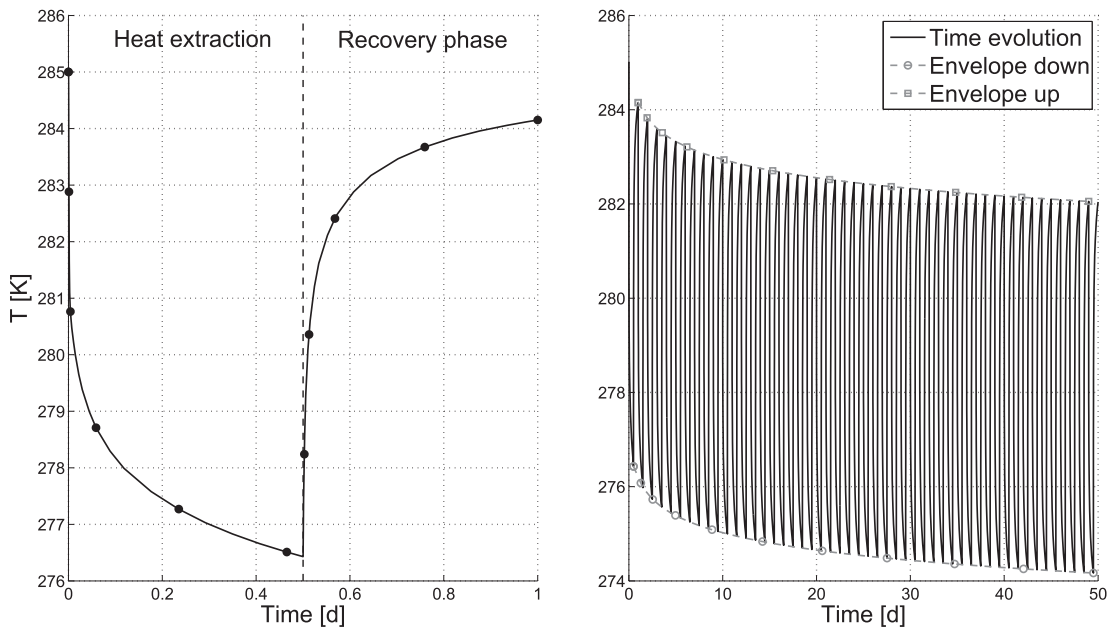

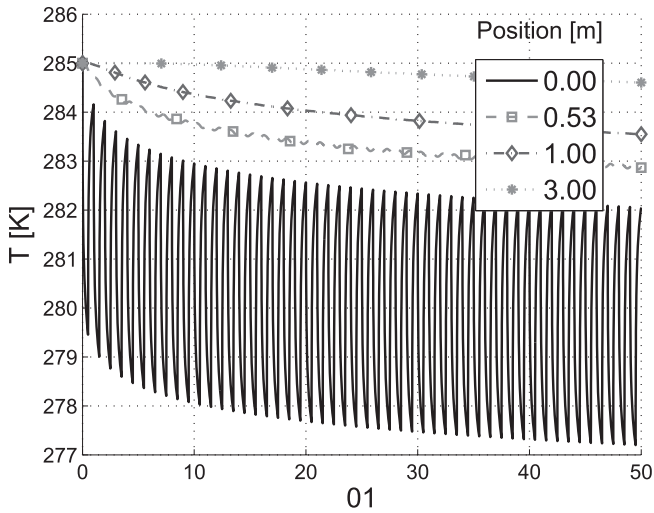**Fig. 15.** Time evolution of the temperature ($z = 80$ m).

Fig. 16. Time evolution of the temperature in the soil (z = 80 m) at different radial positions x.

Fig. 18. Daily operation schemes: operation/recovery duration.

the alternative power. It is cyclic and has a period of 1 day. The second is the residual variation of temperature which accumulates slowly. In order to simplify the reading of the results, the time evolution signal is described by its envelope curve, that is the locus of the local minima or maxima, as shown in Fig. 15 on the right.

Time evolution of temperature at different points of an horizontal (z = 80 m) cross-section are provided in Fig. 16. It can be observed that the temperature cyclic amplitude is lower in the centre of the borehole (position = 0 m) than in the pipe. However the trend is clearly towards freezing point. The amplitude is also smoothed with the distance from the borehole. This variation of temperature within the grouting may be a starting point for the study of its thermo-mechanical analysis.

Fig. 17 presents horizontal cross sections within the soil at different depths on the downstream or upstream pipe side. In this Figure, only the last 12 h of the 50th days are presented, that is only the recovery phase of the last thermal cycle is depicted. As previously mentioned, the oscillations are attenuated with distance from the borehole, depicted by the vertical dashed line. This figure clearly shows that the period of influence of the thermal cyclic
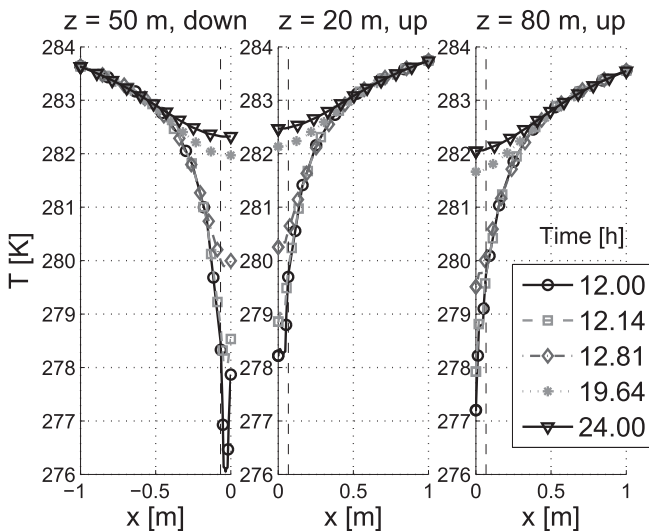
loading is limited to 50 cm. However the long-term influence is much larger and equal to almost 6 m after 50 days.

4.5. Daily operation scheme

The following simulations investigate the influence of the daily operation scheme of the borehole heat exchanger. Three hypothetical schemes are considered in which the operating duration of the pump is respectively 8 h, 12 h or 16 h. The pump is switched off during the remaining time of the day. The same total energy is supposed to be extracted each day, that is to say, the power is equal to 6 kW, 4 kW or 3 kW as shown in Fig. 18.

The envelope of the time evolution of the temperature at the beginning of the downstream pipe (z = 100 m) is provided in Fig. 19. This section is the most critical since the lowest temperature of the circulating fluid is reached there. The tendency of the time evolution of the temperature is identical for all simulations and tends towards a decreasing temperature. However there is a clear difference between the local maxima and local minima envelopes.

The temperature recovered at the end of the off-period almost does not depend on the operating scheme. It was nevertheless observed that the dispersion increases slightly with depth. On the contrary, the lowest part of the envelope exhibits a strong dispersion. In this case, the lower the cooling power, the lower the minimum temperature. Indeed, the conduction of the soil limits the amount of heat that can be extracted from it. Therefore, for an imposed power of the pump, heat is extracted from the fluid and only partly recovered during a loop. This results has practical purpose since the lowest temperature of the fluid is limited by the

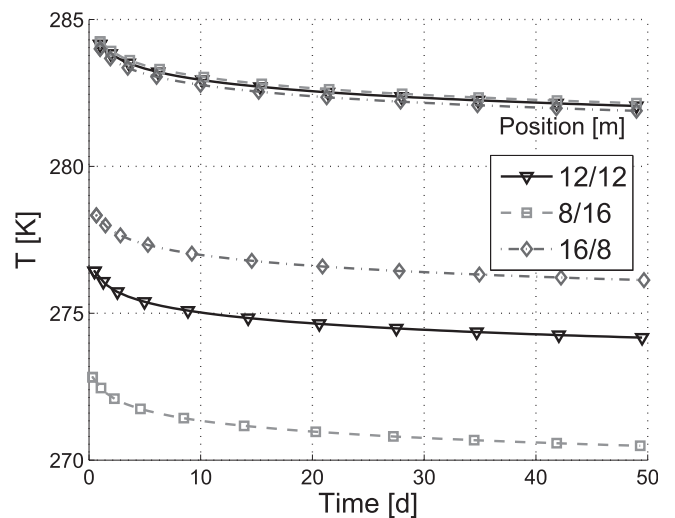**Fig. 17.** Distribution of temperature in the soil at different depths, recovery phase of the 50th day.

Fig. 19. Envelope curves of the time evolution of the temperature in the pipe (z = 80 m).

freezing point of the circulating fluid. The evolution in the grouting is similar.

This result shows that the simulation of continuous heat extraction at an average cooling power is insufficient to study the sustainability of the grouting or the risk of freezing of the circulating fluid. Indeed, an average simulation would have provided an identical temperature evolution for all the previously mentioned simulations while the actual locus of minimal peaks strongly differ. These minimum values are important for the design of the BHE.

4.6. Annual simulation

In the following, a synthetic thermal load described in Ref. [22] is used to simulation a one year operation scheme. This expression includes daily variations of the thermal demand and reads

$$Q_p(t) = A - B \cos\left(\frac{t}{8760} 2\pi\right) - C \cos\left(\frac{t}{24} 2\pi\right)$$
$$- D \cos\left(\frac{t}{24} 2\pi\right)\left(\frac{2\,t}{8760} 2\pi\right), \qquad (42)$$

where A [W] controls the annual load unbalance, B [W] is the half amplitude of the annual load variation, C and D [W] rule the half amplitude of the daily variations and t [d] is the time starting at mid-winter. The ratio C/D controls the damping of daily amplitude at mid-season with respect to winter or summer. Parameters used in this simulation are provided in Table 3 and the full thermal signal is depicted in Fig. 20. A second thermal load profile is considered. It does not take into account the daily variations but only the annual one, as shown in Fig. 20. It describes the annual trend of the full load signal.

The annual power demand evolves from negative power (heat extraction) to positive power (heat injection) but there is no exact compensation between heat extraction and injection as shown by the annual trend curve in Fig. 20. The power amplitude variation is also set up higher in winter and in summer than at mid-seasons.

Table 3
Parameters used for the synthetic thermal load.

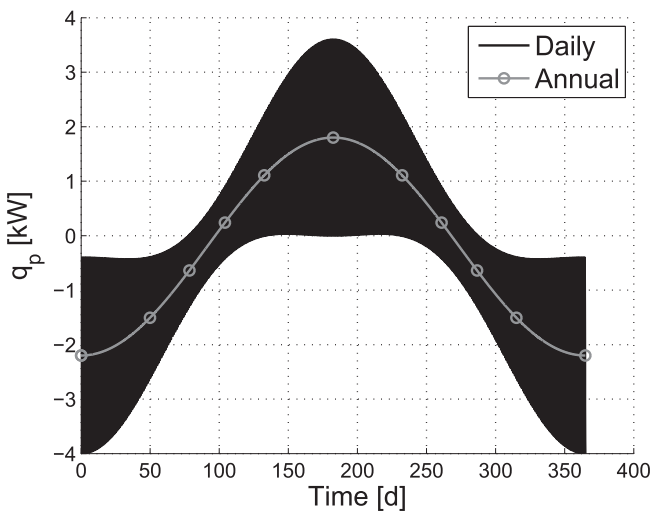| A [kW]	B [kW]	C [kW]	D [kW]
−0.2	2.0	1.2	0.6

Fig. 20. Annual power use including daily variations.

The time step of the daily simulation is set to 2 h in order to well capture the variations. On the contrary the time step of the annual simulation is set up to one day.

Fig. 21 depicts the time evolution of the temperature at the inlet of the pipe. The trend of the daily simulation is well represented by the annual one. However the amplitude of variations may be not negligible around this trend. They are equal to almost 4 K at peak. Therefore if the thermal behaviour of the circulating carrier fluid should be investigated, using only an average thermal load misses the lower/upper bound of the fluid temperature.

The daily variations of temperature are also illustrated in the centre of the borehole, as shown in Fig. 22 at a depth of 80 m. The amplitude of variations is lower than in the pipe. However temperature also oscillates between lower and upper bounds which could influence the thermo-mechanical behaviour of the grouting.

On the contrary, daily variations in the soil are much more damped. They almost disappear after 50 cm from the centre of the borehole which was already mentioned in a previous section. Therefore if only the long term behaviour of the soil must be investigated, only the annual load signal can be used. The main advantage is the higher time step that can be used since it has been
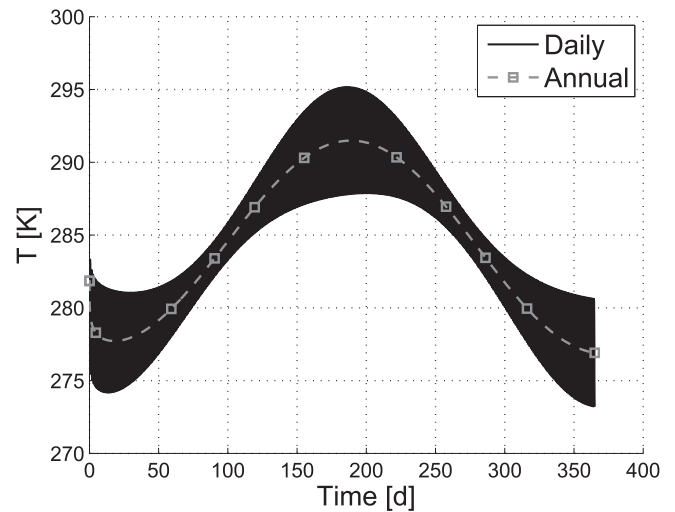

Fig. 21. Temperature evolution at the inlet of the pipe (z = 100 m), daily and annual simulations at different radial positions.
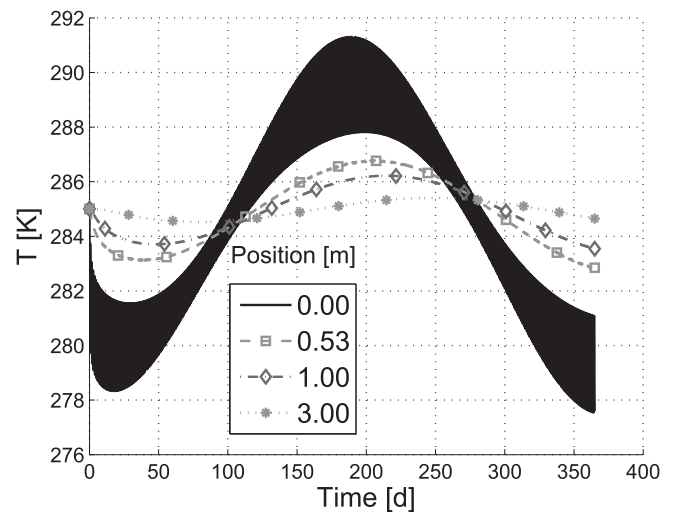

Fig. 22. Temperature evolution in an horizontal cross-section (z = 80 m), daily simulation only.

shown that the error remains negligible. Therefore the total cpu time is considerably decreased.

5. Conclusion

The aim of this paper is to formulate a finite element of heat exchanger in order to accurately model the behaviour of borehole heat exchangers. The element developed must be as flexible as possible and must reproduce transient and steady-state phases, near and far field distributions of temperature, and short- and long-term solutions. The focus is placed on the accurate modelling of a single BHE rather than the ability to optimise a field of BHE.

The finite element is developed in the framework of the non-linear finite element code LAGAMINE for multiphysical couplings. The advection-diffusion problem in the pipe is simplified into a 1D problem. Assuming the temperature is uniform in each cross-section, a convective exchange between the fluid inside the pipe and a temperature representative of the ground around the pipe is modelled. The weighted residual method with Petrov-Galerkin functions is adopted to solve the problem and avoid spurious oscillations. The analytical formulation of elementary out of balance force vector and stiffness matrix are provided.

The element formulation is validated by comparison with analytical solutions. Transient distributions of temperature are compared to a steady-state solution in a simplified problem where the ground temperature is fixed. Furthermore, the field of temperature within the ground is compared with the infinite line source model. Finally the back-calculation of the conductivity of the ground is carried out and compared with the imposed one.

A realistic case study is finally investigated. It consists of a single U-pipe embedded in a 100 m depth borehole. Firstly a 50000s heating simulation is carried out in order to highlight the capabilities of the model. The V-shape steady-state of the temperature distribution is fast reached. Temperature distributions in cross-sections of the grouting are shown to be non-uniform over the main part of the borehole. The highest gradients of temperature are particularly visible at its top. Therefore an explicit modelling of the grouting is necessary if its thermo-mechanical behaviour is investigated. This is particularly important when there is a risk of freeze-thaw damaging. For instance this is particularly important for energy piles.

The choice of the time step and the time integration scheme on the error is further investigated. It is shown that the Crank-Nicholson integration scheme leads to the lowest error for a given time step. However oscillations are likely to appear if the time step is chosen too high. On the contrary a fully implicit scheme avoids the generation of oscillations. Whatever the time step, the error is proven to decrease progressively and finally reach less than 1%.

The simulation of an alternating operation scheme is simulated afterwards. A period of full operation of the BHE (heat extraction) is systematically followed by a recovery period where the pump is switched off. Results exhibit the superposition of a short-term recoverable variation of temperature on a decreasing trend of the temperature within the pipe, the grouting and the soil. The influence of the cycles is limited to 50 cm around the centre of the borehole while the long-term influence reaches 6 m after 50days of simulation.

The influence of the operation scheme on the results is considered. An identical amount of energy is extracted over a varying operating period (8 h/12 h/16 h) while the recovery period is equal to 16 h/12 h/8h. It is shown that the temperature at the end of the recovery period is almost identical. However the minimum temperature at the end of the heat extraction much more varies. If the operation period is equal to 8 h, the fluid temperature decreases

down to almost 270 K while it remains over 276 K if this period is equal to 16 h.

A final one-year simulation considering both annual and daily variations in the power demand is finally run. It is shown that the annual variation of the power is sufficient to study the long term and far-field evolution of temperature within the soil. However hourly simulations with daily variations of the power are necessary if the thermo-mechanical behaviour of the grouting must be investigated. Indeed, these variations may lead to non negligible oscillations of the temperature around its trend.

Appendix A. Force vectors

The out of balance equivalent nodal forces related to the pipe part are computed according to

$$\mathbf{F}_p^e = S \int_{-1}^{1} \rho \, c_p \, \mathbf{W} \, \frac{\partial T}{\partial t} \, |J| \, dz - S \int_{-1}^{1} k \left[\frac{\partial \mathbf{W}}{\partial z}\right] \frac{\partial T}{\partial z} |J| \, dz$$
$$+ S \int_{-1}^{1} \mathbf{W} v \, \rho \, c_p \, \frac{\partial T}{\partial z} |J| \, dz - P \int_{-1}^{1} \mathbf{W} \, h \, (T_g - T) \, |J| \, dz.$$

(A.1)

The exact solution of this equation is provided hereafter, assuming that thermal properties do not depend on temperature and using weighting and shape functions respectively defined in Eqs. (13)–(17),

$$\mathbf{F}_p^e = |\mathbf{J}| \, S \, \rho \, c_p \begin{bmatrix} \frac{2}{3} - \frac{\beta}{2} & \frac{1}{3} - \frac{\beta}{2} \\ \frac{1}{3} + \frac{\beta}{2} & \frac{2}{3} + \frac{\beta}{2} \end{bmatrix} \cdot \begin{bmatrix} \frac{\partial \tilde{T}_1}{\partial t} \\ \frac{\partial \tilde{T}_2}{\partial t} \end{bmatrix} - \frac{S \, k}{2 \, |\mathbf{J}|} \begin{bmatrix} 1 & -1 \\ -1 & 1 \end{bmatrix} \cdot \begin{bmatrix} \tilde{T}_1 \\ \tilde{T}_2 \end{bmatrix}$$
$$+ \frac{S \, v \, \rho \, c_p}{2} \begin{bmatrix} -1 + \beta & 1 - \beta \\ -1 - \beta & 1 + \beta \end{bmatrix} \cdot \begin{bmatrix} \tilde{T}_1 \\ \tilde{T}_2 \end{bmatrix}$$
$$- P \, h |\mathbf{J}| \begin{bmatrix} \frac{2}{3} - \frac{1}{2}\beta & \frac{1}{3} - \frac{1}{2}\beta & -\frac{2}{3} + \frac{1}{2}\beta & -\frac{1}{3} + \frac{1}{2}\beta \\ \frac{1}{3} + \frac{1}{2}\beta & \frac{2}{3} + \frac{1}{2}\beta & -\frac{1}{3} - \frac{1}{2}\beta & -\frac{2}{3} - \frac{1}{2}\beta \end{bmatrix} \cdot \begin{bmatrix} \tilde{T}_1 \\ \tilde{T}_2 \\ \tilde{T}_{g1} \\ \tilde{T}_{g2} \end{bmatrix}$$

(A.2)

where $\tilde{T}_1$ and $\tilde{T}_2$ are the nodal temperatures on the pipe side and $\tilde{T}_{g1}$ and $\tilde{T}_{g2}$ are the nodal temperatures on the ground side. The out of balance vector related to the ground nodes is defined similarly but only convective exchange matters. It is equal to

$$\mathbf{F}_g^e = P \, h |\mathbf{J}| \begin{bmatrix} \frac{2}{3} - \frac{1}{2}\beta & \frac{1}{3} - \frac{1}{2}\beta & -\frac{2}{3} + \frac{1}{2}\beta & -\frac{1}{3} + \frac{1}{2}\beta \\ \frac{1}{3} + \frac{1}{2}\beta & \frac{2}{3} + \frac{1}{2}\beta & -\frac{1}{3} - \frac{1}{2}\beta & -\frac{2}{3} - \frac{1}{2}\beta \end{bmatrix} \cdot \begin{bmatrix} \tilde{T}_1 \\ \tilde{T}_2 \\ \tilde{T}_{g1} \\ \tilde{T}_{g2} \end{bmatrix}.$$

(A.3)

Appendix B. Stiffness matrices

The elementary stiffness matrix (size 4×4) is decomposed into different components (sizes 2×2) such that

$$[\mathbf{K}^e]_{4\times 4} = \begin{bmatrix} [\mathbf{K}_{pp}]_{2\times 2} & [\mathbf{K}_{pg}]_{2\times 2} \\ [\mathbf{K}_{gp}]_{2\times 2} & [\mathbf{K}_{gg}]_{2\times 2} \end{bmatrix}, \tag{B.1}$$

where the subscript p is related to the pipe unknowns $[\tilde{T}_1 \quad \tilde{T}_2]^T$ and g to the ground unknowns $[\tilde{T}_{g1} \quad \tilde{T}_{g2}]^T$. These components are easily obtained from Eqs. (A.2) and (A.3) such that,

$$\mathbf{K}_{pp} = |\mathbf{J}| \frac{S}{\theta \Delta t} \rho c_p \begin{bmatrix} \frac{2}{3} - \frac{\beta}{2} & \frac{1}{3} - \frac{\beta}{2} \\ \frac{1}{3} + \frac{\beta}{2} & \frac{2}{3} + \frac{\beta}{2} \end{bmatrix} - \frac{S k}{2 |\mathbf{J}|} \begin{bmatrix} 1 & -1 \\ -1 & 1 \end{bmatrix}$$
$$+ \frac{S v \rho c_p}{2} \begin{bmatrix} -1 + \beta & 1 - \beta \\ -1 - \beta & 1 + \beta \end{bmatrix} - P h |\mathbf{J}| \begin{bmatrix} \frac{2}{3} - \frac{1}{2}\beta & \frac{1}{3} - \frac{1}{2}\beta \\ \frac{1}{3} + \frac{1}{2}\beta & \frac{2}{3} + \frac{1}{2}\beta \end{bmatrix}, \tag{B.2}$$

$$\mathbf{K}_{pg} = -P h |\mathbf{J}| \begin{bmatrix} -\frac{2}{3} + \frac{1}{2}\beta & -\frac{1}{3} + \frac{1}{2}\beta \\ -\frac{1}{3} - \frac{1}{2}\beta & -\frac{2}{3} - \frac{1}{2}\beta \end{bmatrix}, \tag{B.3}$$

$$\mathbf{K}_{gp} = P h |\mathbf{J}| \begin{bmatrix} \frac{2}{3} - \frac{1}{2}\beta & \frac{1}{3} - \frac{1}{2}\beta \\ \frac{1}{3} + \frac{1}{2}\beta & \frac{2}{3} + \frac{1}{2}\beta \end{bmatrix}, \tag{B.4}$$

$$\mathbf{K}_{gg} = P h |\mathbf{J}| \begin{bmatrix} -\frac{2}{3} + \frac{1}{2}\beta & -\frac{1}{3} + \frac{1}{2}\beta \\ -\frac{1}{3} - \frac{1}{2}\beta & -\frac{2}{3} - \frac{1}{2}\beta \end{bmatrix}. \tag{B.5}$$

References

[1] J. Lund, D. Freeston, T. Boyd, Direct utilization of geothermal energy 2010 worldwide review, Geothermics 40 (3) (2011) 159–180, http://dx.doi.org/10.1016/j.geothermics.2011.07.004.

[2] G. Florides, S. Kalogirou, Ground heat exchangers - a review of systems, models and applications, Renew. Energy 32 (15) (2007) 2461–2478, http://dx.doi.org/10.1016/j.renene.2006.12.014.

[3] H. Yang, P. Cui, Z. Fang, Vertical-borehole ground-coupled heat pumps: a review of models and systems, Appl. Energy 87 (1) (2010) 16–27, http://dx.doi.org/10.1016/j.apenergy.2009.04.038.

[4] P. Bayer, D. Saner, S. Bolay, L. Rybach, P. Blum, Greenhouse gas emission savings of ground source heat pump systems in Europe: a review, Renew. Sustain. Energy Rev. 16 (2) (2012) 1256–1267, http://dx.doi.org/10.1016/j.rser.2011.09.027.

[5] S. Hähnlein, P. Bayer, G. Ferguson, P. Blum, Sustainability and policy for the thermal use of shallow geothermal energy, Energy Policy 59 (2013) 914–925, http://dx.doi.org/10.1016/j.enpol.2013.04.040.

[6] L. Rybach, W. Eugster, Sustainability aspects of geothermal heat pump operation, with experience from Switzerland, Geothermics 39 (4) (2010) 365–369, http://dx.doi.org/10.1016/j.geothermics.2010.08.002.

[7] M. de Paly, J. Hecht-Méndez, M. Beck, P. Blum, A. Zell, P. Bayer, Optimization of energy extraction for closed shallow geothermal systems using linear programming, Geothermics 43 (2012) 57–65, http://dx.doi.org/10.1016/j.geothermics.2012.03.001.

[8] J. Hecht-Méndez, M. De Paly, M. Beck, P. Bayer, Optimization of energy extraction for vertical closed-loop geothermal systems considering groundwater flow, Energy Convers. Manag. 66 (2013) 1–10, http://dx.doi.org/10.1016/j.enconman.2012.09.019.

[9] P. Bayer, M. de Paly, M. Beck, Strategic optimization of borehole heat exchanger field for seasonal geothermal heating and cooling, Appl. Energy 136

[10] (2014) 445–453, http://dx.doi.org/10.1016/j.apenergy.2014.09.029.

[10] L. Laloui, M. Nuth, L. Vulliet, Experimental and numerical investigations of the behaviour of a heat exchanger pile, Int. J. Numer. Anal. Methods Geomech. 30 (8) (2006) 763–781, http://dx.doi.org/10.1002/nag.499.

[11] H. Anbergen, J. Frank, L. Müller, I. Sass, Freeze-thaw-cycles on borehole heat exchanger grouts: impact on the hydraulic properties, Geotech. Test. J. 37 (4) (2014) 639–651.

[12] S. Erol, B. François, Freeze-thaw damage of grouting materials for borehole heat exchanger: experimental and analytical evaluations, Geomech. Energy Environ. 5 (2016) 29–41.

[13] P. Eskilson, Thermal analysis of Heat Extraction Boreholes, Lund University, 1987.

[14] G. Hellström, Ground Heat Storage : Thermal Analyses of Duct Storage Systems, Ph.D. thesis, Lund University, 1991.

[15] C. Yavuzturk, J. Spitler, A short time step response factor model for vertical ground loop heat exchangers, ASHRAE Trans. 105 (2) (1999) 475–485.

[16] M. Philippe, M. Bernier, D. Marchio, Validity ranges of three analytical solutions to heat transfer in the vicinity of single boreholes, Geothermics 38 (4) (2009) 407–413, http://dx.doi.org/10.1016/j.geothermics.2009.07.002.

[17] N. Diao, Q. Li, Z. Fang, Heat transfer in ground heat exchangers with groundwater advection, Int. J. Therm. Sci. 43 (12) (2004) 1203–1211, http://dx.doi.org/10.1016/j.ijthermalsci.2004.04.009.

[18] L. Lamarche, S. Kajl, B. Beauchamp, A review of methods to evaluate borehole thermal resistance in geothermal heat-pump systems, Geothermics 39 (2) (2010) 187–200, http://dx.doi.org/10.1016/j.geothermics.2010.03.003.

[19] S. Erol, M. Hashemi, B. François, Analytical solution of discontinuous heat extraction for sustainability and recovery aspects of borehole heat exchangers, Int. J. Therm. Sci. 88 (2015) 47–58, http://dx.doi.org/10.1016/j.ijthermalsci.2014.09.007.

[20] S. Erol, B. François, Thermal stresses in borehole heat exchangers, Int. J. Numer. Anal. Methods Geomech. 39 (2015) 1450–1470, http://dx.doi.org/10.1002/nag.

[21] R. Al-Khoury, S. Focaccia, A spectral model for transient heat flow in a double U-tube geothermal heat pump system, Renew. Energy 85 (2016) 195–205, http://dx.doi.org/10.1016/j.renene.2015.06.031.

[22] D. Marcotte, P. Pasquier, On the estimation of thermal resistance in borehole thermal conductivity test, Renew. Energy 33 (11) (2008) 2407–2415, http://dx.doi.org/10.1016/j.renene.2008.01.021.

[23] R. Beier, J. Acuña, P. Mogensen, B. Palm, Vertical temperature profiles and borehole resistance in a U-tube borehole heat exchanger, Geothermics 44 (2012) 23–32, http://dx.doi.org/10.1016/j.geothermics.2012.06.001.

[24] R. Beier, J. Acuña, P. Mogensen, B. Palm, Borehole resistance and vertical temperature profiles in coaxial borehole heat exchangers, Appl. Energy 102 (2013) 665–675, http://dx.doi.org/10.1016/j.apenergy.2012.08.007.

[25] S. Rees, M. He, A three-dimensional numerical model of borehole heat exchanger heat transfer and fluid flow, Geothermics 46 (2013) 1–13, http://dx.doi.org/10.1016/j.geothermics.2012.10.004.

[26] D. Bauer, W. Heidemann, H.-J. Diersch, Transient 3D analysis of borehole heat exchanger modeling, Geothermics 40 (4) (2011) 250–260, http://dx.doi.org/10.1016/j.geothermics.2011.08.001.

[27] T. Ozudogru, O. Ghasemi-Fare, C. Olgun, P. Basu, Numerical modeling of vertical geothermal heat exchangers using finite difference and finite element techniques, Geotech. Geol. Eng. 33 (2015) 291–306, http://dx.doi.org/10.1007/s10706-014-9822-z.

[28] S. Rees, An extended two-dimensional borehole heat exchanger model for simulation of short and medium timescale thermal response, Renew. Energy 83 (2015) 518–526, http://dx.doi.org/10.1016/j.renene.2015.05.004.

[29] L.H. Dai, Y. Shang, X.L. Li, S.F. Li, Analysis on the transient heat transfer process inside and outside the borehole for a vertical U-tube ground heat exchanger under short-term heat storage, Renew. Energy 87 (2016) 1121–1129.

[30] R. Al-Khoury, P. Bonnier, R. Brinkgreve, Efficient finite element formulation for geothermal heating systems. part i: steady state, Int. J. Numer. Methods Eng. 63 (7) (2005) 988–1013.

[31] R. Al-Khoury, P. Bonnier, Efficient finite element formulation for geothermal heating systems. part ii: transient, Int. J. Numer. Methods Eng. 67 (5) (2006) 725–745.

[32] H.-J. Diersch, D. Bauer, W. Heidemann, W. Rühaak, P. Schätzl, Finite element modeling of borehole heat exchanger systems, Part 1. Fundamentals, Comput. Geosci. 37 (8) (2011) 1136–1147, http://dx.doi.org/10.1016/j.cageo.2010.08.002.

[33] H.-J. Diersch, D. Bauer, W. Heidemann, W. Rühaak, P. Schätzl, Finite element modeling of borehole heat exchanger systems, Part 2. Numerical simulation, Comput. Geosci. 37 (8) (2011) 1136–1147, http://dx.doi.org/10.1016/j.cageo.2010.08.002.

[34] J. Wooszyn, A. Goaś, Experimental verification and programming development of a new MDF borehole heat exchanger numerical model, Geothermics 59 (2016) 67–76, http://dx.doi.org/10.1016/j.geothermics.2015.10.006.

[35] D. Bauer, W. Heidemann, H. Müller-Steinhagen, H.-J. Diersch, Experimental investigation of an adsorptive thermal energy storage, Int. J. Energy Res. 35 (March/2011), http://dx.doi.org/10.1002/er, 135–312–320.

[36] M. Kummert, M. Bernier, Sub-hourly simulation of residential ground coupled heat pump systems, Build. Serv. Eng. Res. Technol. 29 (1) (2008) 27–44, http://dx.doi.org/10.1177/0143624407087286.

[37] V. Partenay, P. Riederer, T. Salque, E. Wurtz, The influence of the borehole short-time response on ground source heat pump system efficiency, Energy

Build. 43 (6) (2011) 1280—1287, http://dx.doi.org/10.1016/j.enbuild.2011.01.009.

[38] P. Hein, O. Kolditz, U.-J. Görke, A. Bucher, H. Shao, A numerical study on the sustainability and efficiency of borehole heat exchanger coupled ground source heat pump systems, Appl. Therm. Eng. 100 (2016) 421—433.

[39] P. Cui, H. Yang, Z. Fang, Numerical analysis and experimental validation of heat transfer in ground heat exchangers in alternative operation modes, Energy Build. 40 (2008) 1060—1066, http://dx.doi.org/10.1016/j.enbuild.2007.10.005.

[40] S. Lazzari, A. Priarone, E. Zanchini, Long-term performance of BHE (borehole heat exchanger) fields with negligible groundwater movement, Energy 35 (12) (2010) 4966—4974, http://dx.doi.org/10.1016/j.energy.2010.08.028.

[41] R. Al-Khoury, T. Kölbel, R. Schramedei, Efficient numerical modeling of borehole heat exchangers, Comput. Geosci. 36 (10) (2010) 1301—1315, http://dx.doi.org/10.1016/j.cageo.2009.12.010.

[42] C. Lee, A modified three-dimensional numerical model for predicting the short-time-step performance of borehole ground heat exchangers, Renew. Energy 87 (2016) 618—627, http://dx.doi.org/10.1016/j.renene.2015.10.052.

[43] F. Collin, R. Chambon, R. Charlier, A finite element method for poro mechanical modelling of geotechnical problems using local second gradient models, Int. J. Numer. Methods Eng. 65 (11) (2006) 1749—1772.

[44] P. Gerard, R. Charlier, R. Chambon, F. Collin, Influence of evaporation and seepage on the convergence of a ventilated cavity, Water resources research 44 (5).

[45] F. Collin, X.-L. Li, J.-P. Radu, R. Charlier, Thermo-hydro-mechanical coupling in clay barriers, Eng. Geol. 64 (2) (2002) 179—193.

[46] O. Zienkiewicz, R. Taylor, The Finite Element Method, the Basis, fifth ed., McGraw-hill, London, 2000.

[47] O. Zienkiewicz, R. Taylor, The Finite Element Method, Fluid Dynamics, fifth ed., McGraw-hill, London, 2000.

[48] A.N. Brooks, T.J. Hughes, Streamline upwind/petrov-galerkin formulations for convection dominated flows with particular emphasis on the incompressible navier-stokes equations, Comput. Methods Appl. Mech. Eng. 32 (1) (1982) 199—259.

[49] J. Heinrich, P. Huyakorn, O. Zienkiewicz, A. Mitchell, An upwindfinite element scheme for two-dimensional convective transport equation, Int. J. Numer. Methods Eng. 11 (1) (1977) 131—143.

[50] R. Courant, K. Friedrichs, H. Lewy, On the partial difference equations of mathematical physics, IBM J. Res. Dev. 11 (2) (1967) 215—234.

[51] V. Gnielinski, New equations for heat and mass transer in turbulent pipe and channel flow, International Journal of Chemical Engineering 16.

[52] R. Al-Khoury, Computational Modeling of Shallow Geothermal Systems, CRC Press, 2011.

[53] L. Ingersoll, O. Zobel, A. Ingersoll, Heat Conduction with Engineering and Geological Applications, in: International Series in Pure and Applied Physics, McGraw-Hill, 1948.

[54] T. Ozudogru, C. Olgun, a. Senol, 3D numerical modeling of vertical geothermal heat exchangers, Geothermics 51 (2014) 312—324, http://dx.doi.org/10.1016/j.geothermics.2014.02.005.

[55] K.-J. Bathe, M. Khoshgoftaar, Finite element formulation and solution of nonlinear heat transfer, Nucl. Eng. Des. 51 (3) (1979) 389—401.

[56] W. Wood, R. Lewis, A comparison of time marching schemes for the transient heat conduction equation, Int. J. Numer. Methods Eng. 9 (3) (1975) 679—689.

[57] S. Signorelli, Geoscientific Investigations for the Use of Shallow Low-enthalpy Systems, Ph.D. thesis, Eidgenössische Technische Hochschule ETH Zürich, Diss., 2004.

[58] M. Fossa, F. Minchio, The effect of borefield geometry and ground thermal load profile on hourly thermal response of geothermal heat pump systems, Energy 51 (0) (2013) 323—329, http://dx.doi.org/10.1016/j.energy.2012.12.043.